

IONOSPHERIC SOUNDING USING FARADAY ROTATION OF  
SIGNALS OF OPPORTUNITY

Ionospheric Sounding Using Signals Of Opportunity

SONDAGE IONOSPHERIQUE UTILISANT LA ROTATION DE  
FARADAY DES TRANSMISSIONS D'OPPORTUNITÉES

Sondage ionosphérique utilisant des transmissions d'opportunités

A Thesis Submitted

to the Division of Graduate Studies of the Royal Military College of Canada

by

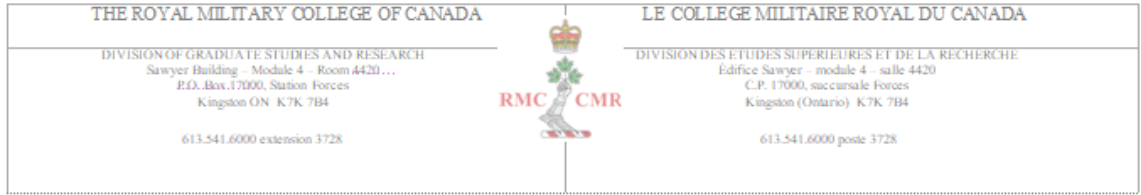
Alex Clay Cushley, B.Sc., B.Ed., M.Sc., RMC, OCT

In Partial Fulfillment of the Requirements for the Degree of

Doctorate of Philosophy

November 2019

© This thesis may be used within the Department of National  
Defence but copyright for open publication remains the property of the author.



This is to certify that the thesis prepared by / Ceci certifie que la thèse rédigée par

**ALEX C. CUSHLEY**

entitled / intitulée

**IONOSPHERIC SOUNDING USING FARADAY ROTATION OF SIGNALS OF OPPORTUNITY**  
**SONDAGE IONOSPHERIQUE UTILISANT LA ROTATION DE FARADAY DES TRANSMISSIONS D'OPPORTUNITÉS**

complies with the Royal Military College of Canada regulations and that it meets the accepted standards of the Graduate School with respect to quality and originality for the degree of  
satisfait aux règlements du Collège militaire royal du Canada et qu'elle respecte les normes acceptées par la Faculté des études supérieures quant à la qualité et l'originalité pour le diplôme de

**Doctorate (PhD) / Doctorat (PhD.)**

Signed by the final examining committee 21 Nov 2019:

Signé par les membres du comité examinateur de la soutenance de la thèse 21 Nov 2019:

Professor Ali Ghanbarpour-Dizboni:

Chair / Président

Dr. Glenn Hussey (University of Saskatchewan):

Examiner External to RMC / Examineur externe au CMR

Dr. Manish Jugroot:

Examiner External to the department and internal to RMC /  
Examineur externe au département et interne au CMR

Dr. Jennifer Shore:

Examiner Internal to the department / Examineur interne au département

Dr. Jean-Marc Noël:

Supervisor(s) / Directeur(s) du mémoire/de thèse

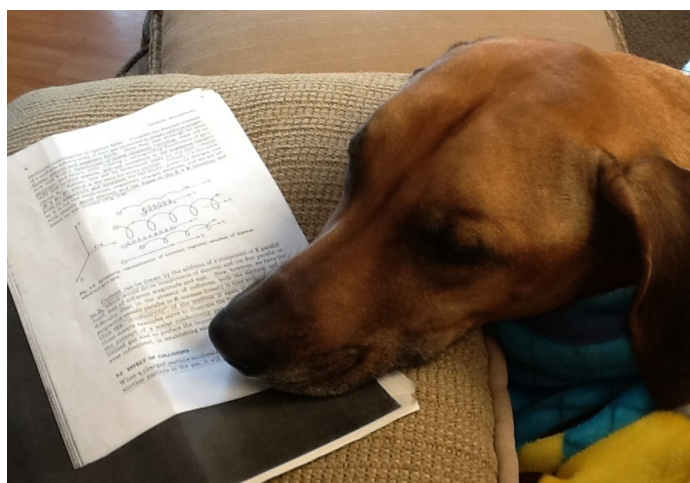
Dr. Jean-Marc Noël:

Approved by the Head of Department / Approuvé par le Directeur du Département

To the Librarian: This thesis is not to be regarded as classified.  
Au Bibliothécaire: Cette thèse n'est pas considérée comme à publication restreinte.



*For my late grandmother Bernadine Anne Cushley, and my “research associate” Gypsy.*



## Declaration of authorship

I, A.C. Cushley, declare that this dissertation titled, 'IONOSPHERIC SOUNDING USING FARADAY ROTATION OF SIGNALS OF OPPORTUNITY' and the work presented in it are my own. I confirm that:

- This work was done wholly or mainly while in candidature for a research degree at the Royal Military College of Canada.
- Where any part of this dissertation has previously been submitted for a degree or any other qualification at this University or any other institution, this is clearly stated.
- Where I have consulted the published work of others, this is always clearly attributed.
- Where I have quoted from the work of others, the source is always given. With the exception of such quotations, this dissertation is entirely my own work.
- I have acknowledged all the main sources of help.
- Where the thesis is based on work done by me in collaboration with others, I clearly state exactly what was done by others and what my contribution was.

Signed:

Date:

## Acknowledgements

I would sincerely like to thank my thesis supervisor, Dr. Jean-Marc Noël, for his guidance, support, and all of the opportunities he's given me throughout the past several years. I have come to know him not only as a supervisor, but as a friend.

I would also like to thank Dr. Konstantin Kabin for his encouragement and support as a mentor and collaborator. I would like to express my personal thanks to Dr. Robert Gillies for access to the ray-trace program used for his research with ePOP and the SuperDarn Radar. Additionally, Dr. Joe Buckley and Dr. Jennifer Shore for their continued assistance with various aspects of computer programming.

I thank past and current graduate students, technical staff, researchers and faculty members in the Department of Physics and Space Science at the RMC and elsewhere who have provided generous advice, assistance and interesting discussions, including Alex Willison, Pete Snell, Dave Watts, Dr. Albert Russell, Maj. Patrick Perron, Maj. John de Boer and Dr. Ron Vincent. I extend my appreciation to the Natural Sciences and Engineering Council of Canada (NSERC) for their financial assistance for publications and conference attendance.

Additionally, I express a personal thank you to my family and friends, especially Martha Deeks and my Modo family for supporting me throughout my postgraduate studies, and especially during the writing of my dissertation. Without their ongoing friendship and support, these past few years would have been far less fulfilling and all the more challenging.

Finally, an enormous THANK YOU to my parents Mark and Donna, who have selflessly encouraged and supported me in all my endeavours, and providing the opportunities and experiences that have made me who I am today. Their love and support during challenging times has kept me on track. This journey would not have been possible if not for them.

## Abstract

Cushley, Alex Clay. Ph.D. Royal Military College of Canada, November 2019. *IONOSPHERIC SOUNDING USING FARADAY ROTATION OF SIGNALS OF OPPORTUNITY: Ionospheric Sounding Using Signals Of Opportunity*. Supervised by Dr. Jean-Marc Noël, Ph.D.

Ionospheric sounding using signals of opportunity is the practice of using any type of signal that is intended for another purpose to measure parameters that characterize the ionosphere. Numerical modelling has demonstrated that Automatic Dependent Surveillance-Broadcast (ADS-B) and Automatic Identification System (AIS) signals are subject to Faraday rotation (FR) as they pass through the ionosphere. Ray tracing techniques were used to determine the characteristics of individual waves, including the wave path and the state of polarization. The modelled FR was computed and used to infer the total electron content (TEC) along the paths. TEC data was used as input for computerized ionospheric tomography (CIT) in order to reconstruct electron density maps of the mid-latitude ionosphere. A technique is also developed to obtain a more realistic value for the average parallel component of the magnetic field along the path. This improves the estimation of TEC from FR (and vice-versa). Another method to create an electron density profile using three tunable parameters and independent FR and TEC measurements is also presented.

**Keywords:** Automatic Dependent Surveillance-Broadcast (ADS-B), Automatic Identification System (AIS), Faraday rotation, electromagnetic (EM) waves, radio frequency (RF) propagation, ionosphere (auroral, irregularities, instruments and techniques), electron density profile, total electron content (TEC), computer ionospheric tomography (CIT), algebraic reconstruction technique (ART), single frequency.

## Résumé

Cushley, Alex Clay. Ph.D. Collège militaire royal du Canada, Novembre, 2019.  
*SONDAGE IONOSPHERIQUE UTILISANT LA ROTATION DE FARADAY DES TRANSMISSIONS D'OPPORTUNITÉES: Sondage ionosphérique utilisant des transmissions d'opportunités.* Thèse dirigée par Dr. Jean-Marc Noël, Ph.D.

Le sondage ionosphérique à l'aide de signaux d'opportunité est la pratique qui consiste à utiliser tout type de signal destiné à mesurer les paramètres caractéristiques de l'ionosphère. La modélisation numérique a démontré que les signaux de surveillance dépendante automatique en mode diffusion (ADS-B) et de système d'identification automatique (AIS) sont soumis à la rotation de Faraday (FR) lorsqu'ils traversent l'ionosphère. Les techniques de traçage de rayons ont été utilisées pour déterminer les caractéristiques des ondes individuelles, y compris le trajet des ondes et l'état de polarisation. Le FR modélisé a été calculé et utilisé pour déduire le densité électronique total (TEC) le long des trajectoires. Les données TEC ont été utilisées pour la tomographie ionosphérique informatisée (CIT) afin de reconstruire les cartes de densité électronique de l'ionosphère aux latitudes moyennes. Une technique est également développée pour obtenir une valeur plus réaliste de la composante parallèle moyenne du champ magnétique le long du trajet. Cela améliore l'estimation de TEC à partir de FR (et vice-versa). Une autre méthode pour créer un profil de densité électronique utilisant trois paramètres réglables et des mesures indépendantes de FR et TEC est également présentée.

**Mots clés :** L'ADS-B, L'AIS, rotation de Faraday, ondes électromagnétiques, propagation radioélectrique, l'ionosphère (auroral, irrégularités, instruments et techniques), le profil de densité d'électrons, contenu électronique total (TEC), tomographie informatisée ionosphérique, technique de reconstruction algébrique, fréquence unique.

# Table of Contents

<b>Declaration of authorship</b> . . . . .	iv
<b>Abstract</b> . . . . .	vi
<b>Résumé</b> . . . . .	vii
<b>List of Tables</b> . . . . .	x
<b>List of Figures</b> . . . . .	xi
<b>Nomenclature</b> . . . . .	xvi
<b>Chapter 1. Introduction</b> . . . . .	1
1.1. Thesis Aim . . . . .	1
1.2. Chapter Overview . . . . .	3
1.3. Introduction to the Ionosphere . . . . .	4
1.3.1. Context of the Problem: Earth’s Ionosphere . . . . .	12
1.4. Introduction to Computerized Tomography (CT) . . . . .	19
1.4.1. Computerized Ionospheric Tomography (CIT) . . . . .	23
1.5. Thesis Outline . . . . .	27
<b>Chapter 2. Theoretical Considerations</b> . . . . .	31
2.1. Overview . . . . .	31
2.2. The Ionosphere . . . . .	32
2.2.1. Regions of the Ionosphere . . . . .	34
2.2.2. Why Study the Ionosphere? . . . . .	36
2.3. Plasma Interaction with EM-Wave Propagation . . . . .	36
2.3.1. Wave Polarization . . . . .	37
2.3.2. Radio Waves in a Magnetized Plasma . . . . .	38
2.3.3. Faraday Rotation (FR) . . . . .	44
<b>Chapter 3. Application</b> . . . . .	48
3.1. Overview . . . . .	48
3.2. Signals of Opportunity . . . . .	48
3.2.1. Automatic Dependent Surveillance Broadcast (ADS-B) . . . . .	48
3.2.2. Automatic Identification System (AIS) . . . . .	57
3.2.3. Automatic Packet Reporting System (APRS) . . . . .	58
3.3. Ray Tracing . . . . .	61
3.4. Reconstruction . . . . .	64
3.4.1. The Inverse Problems . . . . .	64
3.4.2. Computer Tomography (CT) . . . . .	66
3.4.3. Computerized Ionospheric Tomography (CIT) . . . . .	66



3.4.4.	Algebraic Reconstruction Technique (ART) . . . . .	68
3.4.5.	Ambiguity of FR Measurements . . . . .	83
<b>Chapter 4.</b>	<b>Ionospheric tomography using ADS-B signals . . . . .</b>	<b>87</b>
4.1.	Overview . . . . .	87
4.2.	The Study . . . . .	87
4.3.	Published Paper . . . . .	93
<b>Chapter 5.</b>	<b>Faraday rotation of Automatic Dependent Surveillance-Broadcast (ADS-B) signals as a method of ionospheric characterization . . . . .</b>	<b>109</b>
5.1.	Overview . . . . .	109
5.2.	The Study . . . . .	109
5.3.	Published Paper . . . . .	111
<b>Chapter 6.</b>	<b>Faraday Rotation, total electron content, and their sensitivity to the average parallel component of the magnetic field . . . . .</b>	<b>120</b>
6.1.	Overview . . . . .	120
6.2.	The Study . . . . .	120
6.3.	Published Paper . . . . .	122
<b>Chapter 7.</b>	<b>Ionospheric sounding and tomography using Automatic Identification System (AIS) and other signals of opportunity . . . . .</b>	<b>138</b>
7.1.	Overview . . . . .	138
7.2.	The Study . . . . .	138
7.3.	Accepted Paper . . . . .	140
<b>Chapter 8.</b>	<b>Conclusions and Future Work . . . . .</b>	<b>177</b>
8.1.	Overview . . . . .	177
8.2.	Summary . . . . .	177
8.3.	Key Findings . . . . .	182
8.3.1.	Summary of Important Results . . . . .	185
8.4.	Future Work . . . . .	186
<b>References</b>	. . . . .	<b>190</b>
<b>Appendix A.</b>	<b>Copyright Agreements . . . . .</b>	<b>210</b>
<b>CURRICULUM VITAE</b>	. . . . .	<b>230</b>

## List of Tables

Table 1.1. The variability in ionospheric peak density, MUF and TEC over the diurnal and solar cycle [ <i>Anderson and Fuller-Rowell</i> , 1999]. . . . .	13
Table 3.1. FR as a TEC observable; a comparison of the expected FR from Eqn. 2.11 for ADS-B, GPS L1 and L2, AIS ( 161.975 MHz (ch 87) and 162.025 MHz (ch 88)) and APRS. . . . .	85

## List of Figures

Figure 1.1. On a global scale, the aurora takes the form of an oval centred on the Earth’s magnetic poles and are called the <i>auroral oval</i> due to its shape [Perron, 2014]. Figure adapted from <i>Aurora Service</i> [2016]. . . .	5
Figure 1.2. Typical mid-latitude IED profiles for day and night, maximum and minimum sunspot conditions. Solid lines are for high solar activity. Dotted lines are for solar minima. The red line is the typical altitude ( $\sim 300$ km) of the maximum electron number density. Adapted from a wall-chart by W. Swider entitled <i>Aerospace Environment</i> , US Air Force Geophysics Laboratory, Hanscom Air Force Base, Massachusetts. . . . .	7
Figure 1.3. Structure of the neutral atmosphere and ionosphere adapted from Kelley [1989]; Anderson and Fuller-Rowell [1999]. The plasma density of the ionospheric regions varies greatly, as shown in the right panel. The predominant ion populations are shown for the <i>E</i> - and <i>F</i> -regions as well as the topside. Lighter ions tend to dominate higher altitudes [Cushley and Noël, 2014]. . . . .	9
Figure 1.4. An ionogram is the visual product of ionosonde data. It is a plot of the time between when the signal is transmitted and received as a function of frequency. The time of propagation is related to the vertical height that the wave is reflected by the ionosphere. Each layer is represented by a smooth curve, separated from other layers by an asymptote at the critical frequency of that layer. Ionograms can also be converted into electron density profiles. Image provided by National Centers for Environment Information. . . . .	10
Figure 1.5. Comparison of the MUF and LUF over a 24 hour duration, during which a solar X-ray event with a sudden onset at 07h00 took place. The event caused the LUF to exceed the MUF, signifying an HF signal blackout until $\sim 08h00$ [Anderson and Fuller-Rowell, 1999]. . . . .	14
Figure 1.6. The time delay due to the ionosphere increases as a function of TEC and decreases as a function of frequency for several values of the TEC	16
Figure 1.7. An example of the type of vertical TEC (VTEC) maps produced regularly from GNSS and used to assess the state of the ionosphere and propagation conditions, available from <i>NASA Jet Propulsion Laboratory California Institute of Technology</i> [2014]. Stations used are shown as red dots. . . . .	17
Figure 1.8. The location of all CORS stations (whether operational or not) [National Geodetic Survey, 2015] . . . . .	18

Figure 1.9. The largest and densest network of GNSS receivers for TEC measurement is in Japan, called GEONET. The locations of the 1200 ground receivers are shown as red dots [Saito]. . . . .	19
Figure 1.10. An example of the type of VTEC maps produced using IRI model, available from Bilitza [2007]; Bilitza et al. [2011]; Compston [2012]. . . . .	20
Figure 1.11. Numerous ionospheric experiments have been performed using a similar apparatus in order to obtain sufficient data to reconstruct the ionosphere using limited viewing angle CT. . . . .	24
Figure 1.12. In this <i>inverted</i> CIT apparatus, the location of the transmitter(s) and receivers have been exchanged. The amateur radio APRS stations are the transmitters and the satellite is the receiver. The satellite is also now a low Earth orbit (LEO) satellite and creates a synthetic bank of receivers during the course of a line-of-sight (LOS) pass. . . . .	26
Figure 2.1. Photoionization occurs when an atom absorbs an EM photon of sufficiently high frequency (e.g. solar UV, X-Ray and shorter wavelength radiation) [Jahn, 1968]. . . . .	33
Figure 2.2. Some examples of electron number density profiles measured at different times by the EISCAT incoherent scatter radar 13 Mar 2013. . . . .	33
Figure 2.3. Periodic electromagnetic wave, $\vec{E} = E\hat{x}$ is the electric field vector, $\vec{B} = B\hat{y}$ is the magnetic field vector. The wave travels in the $\vec{E} \times \vec{B}$ ( $\hat{k}$ ) direction. . . . .	37
Figure 2.4. Typical elliptical polarization state of an EM-wave. $\psi$ is the orientation angle, $a$ is the semi-major axis, $b$ is the semi-minor axis, and $\theta$ is the aspect angle. . . . .	38
Figure 2.5. Squared refractive index values for the O-mode (solid curve) and the X-mode (dashed curve) as a function of $X$ for constant aspect angle ( $40^\circ$ ), external magnetic field ( $6.0 \times 10^{-5} \text{T}$ ), and frequency (15 MHz) EM-wave. Adapted from [Gillies, 2010]. . . . .	42
Figure 2.6. Top: a linear EM-wave as the superposition of the left-hand circular polarized (LHCP) and right-hand circular polarized (RHCP) waves. Bottom: after traversing some distance in the plasma the RHCP has returned to its initial orientation after $N$ -cycles, but the LHCP wave has relatively advanced in phase and the plane of polarization is seen to rotate. Adapted from Chen [2006]. . . . .	44
Figure 3.1. Main; shows Ikhana, NASA's unmanned ADS-B equipped aircraft test flight with the placement of two ADS-B antennas indicated by black arrows. Inset; shows the most widely adopted aircraft ADS-B antenna [Turner, 2012]. . . . .	50
Figure 3.2. The positions of aircraft plotted from data provided by crowd-sourced ADS-B receivers, courtesy of Fredrik Lindahl, Flightradar24. The data represents 1040 unique aircraft signals received for one second as an indication of the amount of data available. Note that the data received by ground based receivers do not have polar or oceanic coverage. . . . .	52

Figure 3.3. Nav Canada Radar (green) and ADS-B (yellow). Coverage reproduced from Nav Canada website: [ <i>NavCanada</i> , 2011]. . . . .	53
Figure 3.4. APRS-IS tracking the author VA3CUS (red dots) December 2014. Only a subset of other permanent stations that received signals directly from VA3CUS are shown along with VA3CUS. Mobile stations are not shown. For a complete legend, please refer to <i>www.aprs.fi</i> . . . . .	60
Figure 3.5. Various standard forms of sparse matrices: (a) band diagonal, (b) block triagonal, (c) block tridiagonal, (d) singly bordered block diagonal, (e) doubly bordered block diagonal, (f) singly bordered block triangular, (g) bordered band-triangular, (h) singly bordered band diagonal, (i)doubly bordered band diagonal, (j) and (k) other! [ <i>Tewarson</i> , 1973; <i>Press et al.</i> , 2007] . . . . .	65
Figure 3.6. CIT imaging geometry. Adapted from <i>Na</i> [1996] . . . . .	67
Figure 3.7. Implementation of the ART Algorithm. Note that $M = \rho$ in Eqn. 3.1 . . . . .	70
Figure 3.8. Shepp-Logan Phantom image available through MATLAB <sup>®</sup> ; a numerical computing environment and programming language, created by Mathworks. . . . .	72
Figure 3.9. Left: a Sudoku puzzle with 20 given values. The integral of each row and column is 45. The integral along each diagonal is shown with a different line and text color for each. Right: The solution to the Sudoku puzzle shown on the left. . . . .	74
Figure 3.10. Diagram showing the sampling of a square grid containing 3x3 unknown pixels. Red lines show direction sampled and total value attenuated. See Appendix A for the solution to $x_i$ . . . . .	75
Figure 3.11. An illustration of a signal ray path passing through illuminated pixels (blue) within a portion of the 2D reconstruction grid (yellow). . .	78
Figure 3.12. Faraday rotation rate . . . . .	84
Figure 7.1. Geometry of single layer ionosphere model for mapping STEC to VTEC [ <i>Musa</i> , 2007; <i>Royal Observatory of Belgium</i> , 2014]. . . . .	140
Figure 7.2. The multiplication factor used to convert STEC to VTEC for a selected range of mean ionospheric heights from 300 to 400 km. At 25 degrees elevation, the time delay calculated for zenith would be approximately doubled due to the greater TEC encountered along an oblique path. Adapted from <i>Klobuchar et al.</i> [1973]. . . . .	141
Figure 8.1. 3D reconstruction in slices of longitude. . . . .	187
Figure 8.2. Diagram showing the problem with the formation of the geometry matrix using a logical index. . . . .	188

## List of Acronyms

2D	Two-dimensional
ADS-B	Automatic Dependent Surveillance Broadcast
AIS	Automatic Identification System
AOI	Area of Interest
APRS	Automatic Packet Reporting System
APRS-IS	Automatic Packet Reporting System Internet System
ART	Algebraic Reconstruction Technique
ASL	Above Sea Level
ATC	Air Traffic Control
CAT	Computer Assisted Tomography or Computer Axial Tomography
CF	Canadian Forces
CIT	Computerized Ionospheric Tomography
CMEs	Coronal Mass Ejections
CSDC	Canadian Satellite Design Competition
CT	Computerized Tomography
DART	Decomposed Algebraic Reconstruction Technique
DRDC	Defence Research and Development Canada
<i>dTEC</i>	Differential Total Electron Content
DX	Distant Earth Communications
EM	Electromagnetic
ePOP	Enhanced Polar Outflow Probe
Eqn.	Equation
ES	Extended Squitter
EUV	Extreme Ultraviolet
FFT	Fast Fourier Transform
FL	Flight Level
FLOAT	Flying Laboratory for the Observation of ADS-B Transmissions
FOV	Field-of-view
FR	Faraday Rotation
ft	feet
GNSS	Global Navigation Satellite System
GPS	Global Positioning System
HF	High-frequency
IED	Ionospheric Electron Density
IGRF	International Geomagnetic Reference Field
IRI	International Reference Ionosphere
ISR	Incoherent Scatter Radar
LHCP	Left-hand Circular Polarized
LAN	Local Area Network
LEO	Low Earth Orbit
LOS	Line of sight
LUF	Lowest Usable Frequency

MART	Multiplicative Reconstruction Technique
MEO	middle-Earth Orbit
Mode-S	Mode Select
MUF	Maximum Usable Frequency
Nav Canada	Navigation Canada
$n_e$	Electron Density
PCA	Polar Cap Absorption
PNT	Positioning, Navigation, and Timing
QL	Quasi-longitudinal
QT	Quasi-transverse
RHCP	Right-hand Circular Polarized
RMC	Royal Military College of Canada
RRI	Radio Receiver Instrument
SABRE	Space ADS-B Receiver Experiment
S-AIS	Satellite-AIS
SART	Simultaneous Algebraic Reconstruction Technique
SIM	Subscriber Identification Module
SIRT	Simultaneous Iterative Reconstruction Technique
SMAD	Space Mission Analysis and Design
STEC	Slant TEC
STK	Satellite Tool Kit
TEC	Total Electron Content
TECu	Total Electron Content Units
TNC	Terminal Node Controller
UTIAS	University of Toronto Institute for Aerospace Studies
UV	Ultraviolet
VDL	VHF Data Link
VHF	Very High Frequency
UAT	Universal Access Transceiver
UHF	Ultra High Frequency
USA	United States of America

## Nomenclature

$\chi$	.....	The ellipticity angle (rad)
$\Delta\phi$	.....	The phase difference (rad)
$\Delta N$	..	The difference between the measured value and the integrated value of the pixels along the same path (electrons·m <sup>-3</sup> )
$\Delta_i$	.....	The uncertainty associated with pixels $j$ for ray path $i$ (electrons·m <sup>-2</sup> )
$\epsilon_0$	.....	The permittivity of free space ( $8.85418782 \times 10^{-12} \text{C}^2/\text{N}\cdot\text{m}^2$ )
$\lambda$	.....	The wavelength of the EM wave (m)
$\lambda_k$	.....	The relaxation parameter (dimensionless)
$\Omega$	.....	The Faraday rotation of an EM wave (rad)
$\omega$	.....	The angular radio wave frequency (rad·s <sup>-1</sup> )
$\omega_c$	.....	The angular gyrofrequency (rad·s <sup>-1</sup> )
$\omega_p$	.....	The angular plasma frequency (rad·s <sup>-1</sup> )
$\phi_n$	.....	The $n^{\text{th}}$ carrier phase (rad)
$\psi$	.....	Orientation angle (rad)
$\rho$	.....	The number of pixels in the reconstruction grid (dimensionless)
$\tau$	.....	The tolerance (electrons·m <sup>-2</sup> )
$\theta$	.....	Aspect angle (rad)
$\vec{B}$	.....	The magnetic field vector of the EM-wave (nT)



$\vec{E}$	.....	The electric field vector of the EM-wave (N·C <sup>-1</sup> )
$\vec{p}$	.....	The vector of the measured, integrated quantity (electrons·m <sup>-2</sup> )
$\vec{x}$	.....	The vector of unknown values (electrons·m <sup>-3</sup> )
$A$	.....	The geometry matrix (m)
$a$	.....	The semi-major axis (m)
$B$	.....	The magnetic field strength (T)
$b$	.....	The semi-minor axis (m)
$B_{\parallel}(z)$	....	The parallel component of the magnetic field at a point along path $z$ (T)
$B_{avg}$	.....	The average magnetic field (nT)
$c$	.....	The speed of light in a vacuum ( $3 \times 10^8$ m·s <sup>-1</sup> )
$d_{ij}$	.....	The contribution to pixel $j$ from ray $i$ in the logical matrix $D$ (m)
$D_i$	.....	The $i^{th}$ row of $D$ (m)
$dt$	.....	The change in time
$e$	.....	The charge of an electron ( $1.60217657 \times 10^{-19}$ C)
$E_L$	.....	The left-hand circular polarized electric vector of the wave (N·C <sup>-1</sup> )
$E_R$	.....	The right-hand circular polarized electric vector of the wave (N·C <sup>-1</sup> )
$E_x$	.....	The $x$ component of the electric vector of the wave (N·C <sup>-1</sup> )
$E_y$	.....	The $y$ component of the electric vector of the wave (N·C <sup>-1</sup> )
$E_{i \times 1}$	.....	The column vector of $i$ error values (electrons·m <sup>-2</sup> )
$el$	.....	The elevation angle (degrees)
$f$	.....	The radio wave frequency (Hz)

$f_c$	.....	The gyrofrequency (Hz)
$f_n$	.....	The $n^{th}$ carrier frequency (Hz)
$f_p$	.....	The plasma frequency (Hz)
$i$	.....	The imaginary component of the complex number ( $i^2=-1$ dimensionless)
$j$	.....	The pixel number (dimensionless)
$k$	.....	The iteration number (dimensionless)
$l$	.....	The path length (m)
$m$	.....	The mass of a charged particle (kg)
$m_e$	.....	The mass of an electron ( $9.10938291 \times 10^{-31}$ kg)
$MF_I(el)$	.....	The mapping function is a function of the elevation angle (dimensionless)
$n$	.....	Index of refraction (dimensionless)
$N^{k+1}$	.....	The vector of the modified pixel values $n_j^{k+1}$ for the next iteration (electrons·m <sup>-3</sup> )
$N^k$	.....	The vector of pixels $n_j^k$ for the iteration (electrons·m <sup>-3</sup> )
$n_e$	.....	The electron density (electrons·m <sup>-3</sup> )
$n_e(z)$	.....	The electron density at a point along path $z$ (electrons·m <sup>-3</sup> )
$n_0$	.....	The pixel value for the first iteration (electrons·m <sup>-3</sup> )
$n_{ej}$	.....	The brightness of pixel $j$ (electrons·m <sup>-3</sup> )
$N_e(j)$	.....	The electron density as a function of pixel $j$ (electrons·m <sup>-3</sup> )
$N_e^{new}$	.....	The vector of pixels $n_j^k$ for the next iteration (electrons·m <sup>-3</sup> )
$N_e^{old}$	.....	The vector of pixels $n_j^k$ for the iteration (electrons·m <sup>-3</sup> )

$N_{j \times 1}$	.....	The column vector of $j$ unknown pixel values (electrons·m <sup>-3</sup> )
$n_j^{k+1}$	.....	The brightness of pixel $j$ for the next iteration (electrons·m <sup>-3</sup> )
$n_j^k$	.....	The brightness of pixel $j$ for the iteration $k$ (electrons·m <sup>-3</sup> )
$n_x$	..	The number of pixels in the horizontal ( $x$ ) dimension of the reconstruction grid (dimensionless)
$n_y$	..	The number of pixels in the horizontal ( $y$ ) dimension of the reconstruction grid (dimensionless)
$p$	.....	The wave polarization ratio (dimensionless)
$q$	.....	The charge of a particle (C)
$r$	.....	The gyroradius of a particle (m)
$R_e$	.....	The radius of an electron ( $2.81794 \times 10^{-15}$ m)
$RM$	.....	The measured Faraday rotation between consecutive epochs (rad·m <sup>-2</sup> )
$STEC$	.....	The slant $TEC$ (as opposed to vertical $TEC$ ) (electrons·m <sup>-2</sup> )
$STEC_{i \times 1}$	.....	The column vector of $i$ measurements (electrons·m <sup>-2</sup> )
$STEC_i$	.....	The $STEC$ measurement for the $i^{th}$ ray-path (electrons·m <sup>-2</sup> )
$t$	.....	The time (s)
$t_{d_i}$	.....	Time delay due to the ionosphere (s)
$TEC$	.....	Total electron content (1TECu = $10^{16}$ electrons·m <sup>-2</sup> )
$v$	.....	The velocity of a particle (m·s <sup>-1</sup> )
$v_\phi$	.....	The phase velocity (rad·s <sup>-1</sup> )
$VTEC$	.....	The vertical TEC (electrons·m <sup>-2</sup> )
$X$	..	Squared ratio of plasma frequency to radio wave frequency (dimensionless)

$Y$  .....Ratio of gyrofrequency to radio wave frequency (dimensionless)  
 $z'$  ..... The ionospheric zenith angle (degrees)  
 $D_{i \times j}$  ..... The geometry matrix (m)



## Chapter 1

# Introduction

### 1.1 Thesis Aim

The goal of this thesis is to investigate the feasibility of ionospheric sounding using signals of opportunity. More specifically, the feasibility of using two different signals, namely 1090 MHz Automatic Dependent Surveillance Broadcast (ADS-B) signals from aircraft and  $\sim 162$  MHz Automatic Identification System (AIS) signals from ships, to estimate total electron content (TEC) along the signal paths, and to create two-dimensional (2D) ionospheric electron density (IED) maps. Consequently, this research demonstrates the dual-purpose of a single payload for improving air/nautical traffic management and for scientific observation of the ionosphere.

As electromagnetic (EM) waves propagate through the electrically charged ionosphere in the near-Earth space environment they are modulated and can provide an opportunity to model the medium through which they have passed. Modelling the IED of Earth's ionosphere (and plasmasphere) in general is essential in determining the state of ionospheric activity, as is discussed more in Chapter 2. This information can be used to correct for propagation delays in satellite communications, predicting space weather, and ionospheric disturbances due to geomagnetic storms and solar flares [*Jin et al.*, 2006].

The 1090 MHz ADS-B signal was proposed in support of research conducted in space mission analysis and design (SMAD) at the Royal Military College of Canada (RMC) pioneering the use of ADS-B in space due to its global adoption as the standard mode of ADS-B, especially for larger aircraft *Tremblay et al.* [2009]. Moreover, for this research, the ADS-B signal was selected for several other reasons: this frequency allows for robust operational communications yet measurable perturbation due to ionospheric effects, the spatially dense dataset that was estimated by the geometry between multiple transmitting aircraft and the passive satellite receiver(s),

and to support the expedition of an operational ADS-B constellation.

The  $\sim 162$  MHz AIS signal was selected to compliment and compare ADS-B data. AIS signals transmitted by ships are received by a satellite constellation and relayed to a ground network in near real-time. The AIS constellation provides updated information on identified vessels, including their respective locations and a wide range of other relevant maritime geospatial information at least once per hour. This same space mission analysis and design architecture was the inspiration for a proposed deployment of space-borne ADS-B transceivers to monitor air traffic [*Francis et al.*, 2011].

Although there are satellites currently carrying ADS-B and AIS receivers, data for ionospheric sounding is not available. For this reason, “synthetic” data was used for these studies as a proof of concept for real data. This work communicates the importance and feasibility of using signals of opportunity, specifically linearly polarized single frequency signals for ionospheric sounding. It is assumed in these simulations that a double-dipole or quad monopole satellite antenna configuration capable of measuring the FR to within  $1^\circ$  has been deployed. It is important to note, both as an engineering challenge and design requirement for future satellites, that the orientation of the satellite must be known to achieve this accuracy.

At the time this research was initiated, the primary benefit of ADS-B was to improve Canada’s flight safety and efficiency by providing timely, cost-effective wide-area surveillance over the Hudson Bay region, with the eventual expansion to global real-time air-traffic control (ATC). Since the scientific model presented in this thesis cannot be used until the concept demonstrator or the dedicated ADS-B satellite was in orbit, the primary objective of the research was to support the immediate use of ADS-B ATC from space.

ADS-B signals were first detected at 35 km, well above commercial flight level ( $\sim 10$  km) by a high altitude balloon mission, which successfully demonstrated the reception of ADS-B signals from near space, paving the way to the development of a space-based ADS-B system [*Francis et al.*, 2011]. Since that time, ADS-B receivers have been flown on satellite demonstrators, including the CanX-7 nano-satellite [*University of*

*Toronto Institute for Aerospace Studies Space Flight Laboratory*, 2014], however data has not been made available and is only being used for ATC, its intended purpose.

The topic of ionospheric modelling within the scope of ADS-B has not been explored prior to the work by *Cushley* [2013]. All previous work surrounding ADS-B technologies by *Tremblay et al.* [2009]; *Francis* [2009]; *Francis et al.* [2011]; *Castillo et al.* [2012]; *Van Der Prys* [2014]; *Van Der Prys and Vincent* [2015a,b, 2016]; *Vincent and Van Der Prys* [2017]; *Freitag* [2017] were oriented towards the feasibility of the signal for operational communications, not the potential secondary scientific benefits, which is the focus of this thesis. The motivation for this study is to investigate the potential exploitation of ADS-B operational data to contribute to current methods of IED mapping, primarily at high latitudes and oceanic regions.

In order to characterize the ionospheric electron content under different geometric, geomagnetic and solar conditions, this research combines knowledge extracted from EM-wave propagation theory, IED and geomagnetic models, to produce independent static data of the wave properties received at the satellite receiver using a ray tracing model. The synthetic data produced by ray tracing is what the satellite ought to measure and this data was applied to the techniques and findings in the published papers presented in Chapters 4 – 7.

## 1.2 Chapter Overview

In this chapter, we introduce some elements of the Sun–Earth environment and plasma physics as they relate to the ionosphere as background to the specific ionospheric research described by this thesis. To remain concise, we only touch upon a few of the solar-terrestrial relationships, features and properties relevant to this research, particularly those which influence the IEDs in the high-latitude  $F$ -region ionosphere. We will also discuss ionospheric sounding and mapping of TEC and IED. Particular detail will be given to a remote sensing technique that has been used to study the complex plasma structures in the ionosphere among many other applications in different fields such as computerized tomography (CT). In the final section, the problem is described



with a brief introduction to an inverted computerized ionospheric tomography (CIT) system, and how the remainder of the thesis will be organized.

### 1.3 Introduction to the Ionosphere

The Earth's ionosphere is a region of Earth's upper atmosphere between approximately 60-1000 km altitude, comprised of free electrons, different molecular ions and neutral particles, where photoionization by solar extreme ultraviolet (EUV) and X-ray radiation/photons, and impact ionization by charged particles causes ionization. Typically, on a macroscopic scale the ionosphere contains an equal number of electrons and ions, a property of a quasi-neutral plasma. Plasmas do not occur spontaneously in nature. They are created from initially neutral, un-ionized molecules by radiation, heating and collisions. [*Rose and Clark Jr.*, 1963; *Jahn*, 1968; *St-Maurice*, 1998; *Schunk and Nagy*, 2000; *Bellan*, 2008]

Although the plasma state of matter is not found in abundance on Earth (with exceptions such as lightning, arcs from welding or plasma cutters, sparks from static discharge or electrical outlets), in fact greater than 99 % of the visible universe is in a plasma state [*Chen*, 1984]. Plasmas are abundant in the universe, including the majority of our solar system. Life on Earth is a rare exception, however all matter above  $\sim 80$  km altitude must be treated using plasma-physical methods [*Treumann and Baumjohann*, 1996].

At high latitudes and above an altitude of  $\sim 80$  km there is another example of a well-known terrestrial plasma, a well-known and often observable phenomenon occurs namely the Aurora Borealis (northern lights) in the northern hemisphere and the Aurora Australis (southern lights) in the southern hemisphere. The aurora is caused by electrons (and protons, although they only produce diffuse aurora that are not easily detected by the naked eye) striking the atmosphere at high speed. The particles originate from the magnetosphere and spiral down Earth's magnetic field lines. These particles produce a spectacular array of light, and when they strike the atmosphere they can also produce ionization. The auroral oval is named because

of its shape (see Fig. 1.1). It exists in both hemispheres above about 60 degrees geomagnetic latitude [Anderson and Fuller-Rowell, 1999].

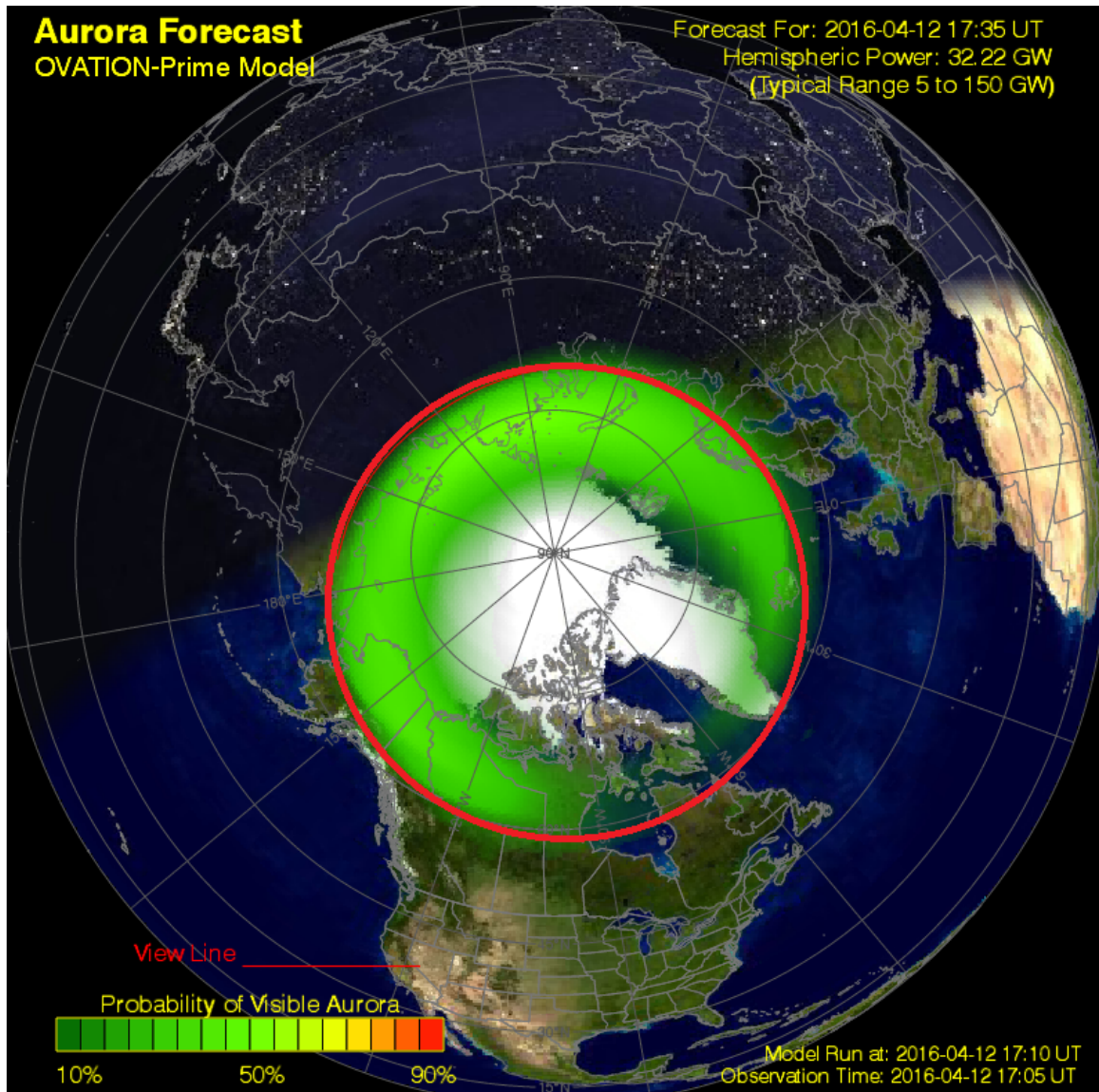


Figure 1.1: On a global scale, the aurora takes the form of an oval centred on the Earth's magnetic poles and are called the *auroral oval* due to its shape [Perron, 2014]. Figure adapted from *Aurora Service* [2016].

At altitudes above  $\sim 90$  km the Earth is surrounded by a plasma of higher density than auroral altitudes [Gurnett and Bhattacharjee, 2005]. Considering that the universe is predominantly in a plasma state, it is surprising that the mass of the particles that comprise it make up less than 1 % of the mass of the atmosphere above 100 km

[*Anderson and Fuller-Rowell, 1999*]. Despite this fact, the ionosphere is significant due to the effect it has on radio wave propagation above  $\sim 30$  MHz [*Tucker, 1998*]. The ionosphere also has a significant effect on the processes governing atmospheric electricity, and forms the inner edge of the magnetosphere.

Space weather links the Sun, the Earth, and the space environment in between. Space weather systems can generate interplanetary storms of immense size and energy that can envelop whole planet(s) such as Earth [*Birkeland, 1908; Kleimenova et al., 2011*]. Typically sub-storms last 1-5 hours and disturb the magnetic field of Earth's magnetosphere 1–4 times per day, making them (along with geomagnetic storms) the primary mechanism by which magnetic energy from the Sun is transported through the magnetosphere and into the auroral ionosphere [*Tanskanen et al., 2005*]. Such storms can adversely affect complex and expensive technological systems that provide much of the infrastructure that allows modern society to function. Therefore, studying the Earth's ionospheric plasma content is an important endeavour that has a direct input into space situational awareness and applications that exploit this knowledge [*Perron, 2014; Frisell et al., 2014*].

The ionosphere can be regarded initially as a neutral gas. As solar radiation irradiates the chemical constituents that compose the ionosphere, electrons become dislodged from atoms and molecules producing ionization [*Anderson and Fuller-Rowell, 1999*]. The radiation received, and consequently the amount of ionization is also perturbed by geographical location (polar, auroral, mid-latitude, or equatorial region) sunspot cycles, and solar flares. For example, the local winter hemisphere is tipped away from the Sun, thus receiving less solar radiation.

Other mechanisms which disturb the ionosphere activity, but are less predictable are: solar flares, coronal mass ejections (CMEs) and other cosmic releases of charged particles into the continuous radiation throughout the EM spectrum from the Sun, called *solar wind*. The solar wind reaches the Earth and interacts with the geomagnetic field, distorting the magnetosphere which shields Earth from this solar radiation [*Chen, 1984*].

Ionization is primarily dependent on solar activity, although some high energy

cosmic particles reaching Earth's atmosphere can also contribute. Since the amount of ionization is governed mainly by the Sun, there is a great deal of variation due to the amount of solar radiation reaching Earth. This results in diurnal and seasonal variations shown in Fig. 1.2. It is evident that the solar dependence means that day-side electron densities are typically much greater than those on the night-side. Ionization occurs mostly on the sunlit side of the Earth, while recombination processes dominate on the night-side [Cushley, 2013].

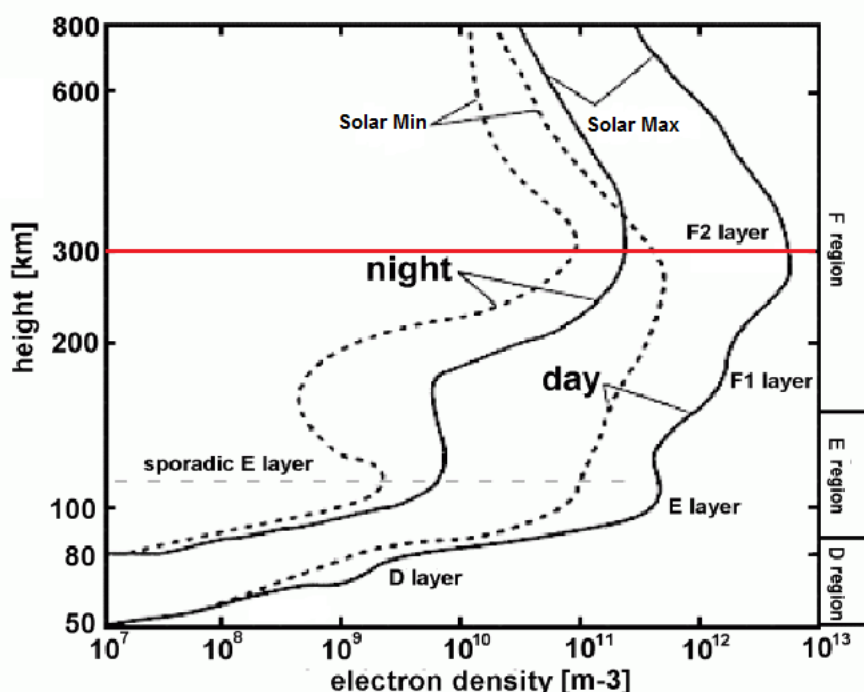


Figure 1.2: Typical mid-latitude IED profiles for day and night, maximum and minimum sunspot conditions. Solid lines are for high solar activity. Dotted lines are for solar minima. The red line is the typical altitude ( $\sim 300$  km) of the maximum electron number density. Adapted from a wall-chart by W. Swider entitled *Aerospace Environment*, US Air Force Geophysics Laboratory, Hanscom Air Force Base, Massachusetts.

The altitude and densities of all ionospheric layers are highly variable depending on season and solar activity. The complex composition of the ionosphere complicates matters further. The ionosphere is dominated by different species at different altitudes (see the right panel of Fig. 1.3) and these species have different ionization and recombination rates. The total or net ionization is determined by the difference between the ionization and recombination reactions. For example, diurnal variations

can cause the *D* and *F1* layers to vanish at night, whereas the *E* and *F2* layers tend to persist. Following local sunset the *D*- and *E*-regions reduce and often disappear completely on the night side, particularly at high latitudes due to molecular recombination.

The radiative recombination rates for  $\text{O}_2^+$  and  $\text{NO}^+$  are on the order of  $\sim 10^{-7}$ . In the higher altitude *F*-region, the number of  $\text{O}^+$  decrease and lighter ions such as hydrogen ( $\text{H}^+$ ) and helium ( $\text{He}^+$ ) dominate the reaction rates of ionization and recombination which are on the order of  $\sim 10^{-12}$  [Schunk and Nagy, 2000]. *F*-region altitudes are also illuminated longer after local sunset than lower altitudes. Since the recombination rates for the dominant constituents of the *D*- and *E*- region are  $10^5$  higher, combined with lower ionization levels after sunset where ionization is primarily due to residual levels of far-field cosmic sources of radiation, recombination becomes the predominant mechanism at night.

The *D*-region (60-90 km) is the most chemically complex because ionization levels are quite low and its properties can vary significantly compared to the weakly collisional *E*-region (105-150 km) and the quasi-collisionless *F*-region (>150 km) [Schunk and Nagy, 2000; Kelley, 2009]. Below 150 km  $\text{NO}^+$  and  $\text{O}^+$  dominate the plasma composition, behaviour and interactions, whereas the *F*-region is composed mostly of atomic oxygen. The *D*-region can play a critical role in ionospheric physics (e.g. turbulence) because of these neutral atmospheric interactions. On much shorter time scales, the variation in the *D*- and *E*-region ionization can change dramatically due to solar flares release of excess X-ray radiation.

The presence of these charged particles in the ionosphere allows electric current to flow which helps explain how the propagation of radio waves are facilitated by the ionospheric plasma, and its adverse effects on radio frequency (RF) EM wave propagation. Interestingly, the Earth's ionosphere was discovered by observing radio waves being reflected by an unknown layer. The waves properties could only be explained by the presence of a reflecting layer composed of electrons and positive ions [Lodge, 1902; Ratcliffe, 1967]. The letter designations *D*-, *E*- and *F*- (*F1* and *F2*) came from the successive plateaus in radio sounding; a ground based transmitter

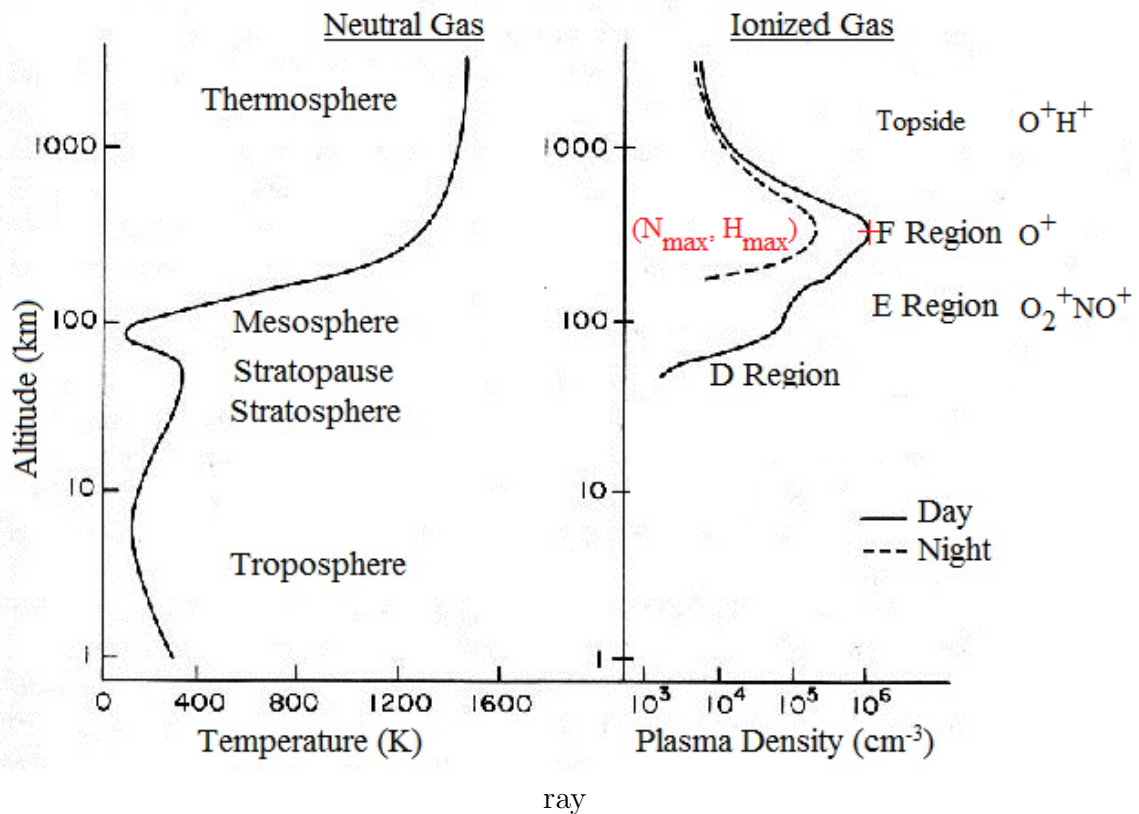


Figure 1.3: Structure of the neutral atmosphere and ionosphere adapted from *Kelley* [1989]; *Anderson and Fuller-Rowell* [1999]. The plasma density of the ionospheric regions varies greatly, as shown in the right panel. The predominant ion populations are shown for the *E*- and *F*-regions as well as the topside. Lighter ions tend to dominate higher altitudes [*Cushley and Noël*, 2014].

swept through multiple frequencies to observe the critical frequency at which the radio wave was reflected. The *E*-layer was the first to be discovered and labelled as such for being the layer which reflected the E-vector of the radio wave (see Fig. 1.4). The lower *D*-, and higher *F*-layers were discovered later and named according to their ascending relationship with the predefined *E*-layer [*Bauer*, 1973; *Schunk and Nagy*, 2000; *Kelley*, 2009]. The *F*-region is further subdivided into two sub-regions: *F1* (160-180 km) and *F2* (with peak density at approximately 300 km).

The existence of different ionospheric regions is caused mainly by the complex composition of the neutral atmosphere and partly due to hydrostatic balance [*Huba et al.*, 2014]. It is a mixture of gases that differ in their susceptibility to ionizing

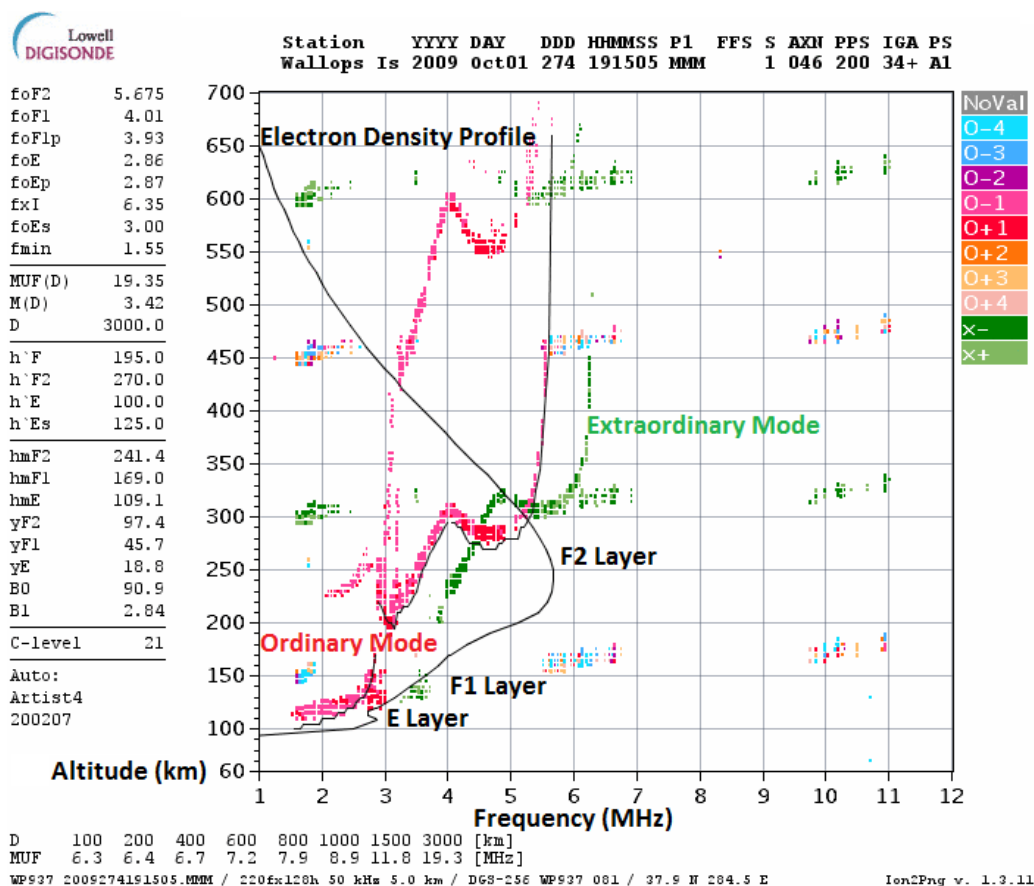


Figure 1.4: An ionogram is the visual product of ionosonde data. It is a plot of the time between when the signal is transmitted and received as a function of frequency. The time of propagation is related to the vertical height that the wave is reflected by the ionosphere. Each layer is represented by a smooth curve, separated from other layers by an asymptote at the critical frequency of that layer. Ionograms can also be converted into electron density profiles. Image provided by National Centers for Environment Information.

radiation, and thus produce maximum ionization at different altitudes.

The ionosphere is a dynamic system controlled by many parameters including acoustic motions of the atmosphere, electromagnetic emissions, and variations in the geomagnetic field. Any atmospheric disturbance affects the distribution of the ionization. As a result, the boundaries of the ionosphere and its regions are not particularly well defined. Various scientific literature sources such as: *Chen* [1984]; *Kelley* [1989]; *Schunk and Nagy* [2000]; *Hunsucker and Hargreaves* [2003] give various boundaries for the lower and upper ionosphere, ranging from 60–100 km and 1000–2000 km respectively. Realistically, there is no physical boundary separating the layers

of the neutral atmosphere, including the ionospheric plasma, from the plasmasphere and magnetosphere at the outer reaches of Earth's magnetic field.

The ionosphere also interacts with the composition of the thermosphere and thermospheric winds. The composition affects the rate that ions and electrons recombine, while the thermospheric winds tend to push the ionosphere along the inclined magnetic field lines to a different altitude [*Anderson and Fuller-Rowell, 1999; Pokhotelov et al., 2008; Saranya et al., 2015*]. During geomagnetic storms, the energy input at high latitudes produces waves in the thermospheric winds and changes in the composition. This causes both increases (positive phases) and decreases (negative phases) in the electron concentration [*Anderson and Fuller-Rowell, 1999; Hanslmeier, 2007*]. These features are otherwise known as blobs or enhancements and troughs or depletions when examining multi-dimensional maps of the electron concentration.

The ionospheres dynamics are not only a function of latitude. Otherwise there would exist hemispheric symmetry. Continuous observations of mid-latitude plasma structures in the American sector have shown that they do not always fully map to the opposite hemisphere [*Martinis et al., 2011*]. Structures that regularly appear in one hemisphere do not necessarily occur in the other hemisphere or at least not to the same extent and/or exact latitude. However, some conjugacy exists. In addition to the variation of characteristic regions of the ionosphere, entire vertical profiles of the ionosphere also exhibit a large degree of variation. This comes from main two sources of ionization (aurora and thermospheric winds) in addition to the response to changes of the neutral and upper atmosphere in which it is embedded [*Anderson and Fuller-Rowell, 1999*]. For example, during a geomagnetic storm the auroral ionization increases and expands to lower latitudes. In the most extreme cases, the respective aurora of one hemisphere can be seen in the other hemisphere. The most devastating coronal mass ejection (CME) in recorded history occurred 1-2 September 1859. The Carrington Event shorted telegraph wires, starting fires in North America and Europe, and caused bright aurorae (northern and southern lights). The aurora Borealis was seen as far South as Cuba and Hawaii while the aurora Australis was seen as far north as Brisbane [*Carrington, 1859; BBC News, 2013*]. Low latitude plasma bubbles



can reach mid latitudes, not only during magnetically disturbed conditions, but also during quiet epochs [McClure *et al.*, 1977; Comberiate and Paxton, 2009; Abdu, 2012].

Mapping the ionosphere electron content is important for scientific study, research and application development. The ionosphere offers a globally accessible plasma laboratory from which observations, measurement and validation of theory can be performed and extended to other less accessible systems (distant or difficult to contain). This natural laboratory offers naturally occurring EM fields and events such as lightning strikes and the aurora that would otherwise be difficult to synthetically produce. For example, lightning strikes cause the electron density to significantly change by heating electrons, making ionization and dissociative attachment dominant processes [Taranenko *et al.*, 1993].

### 1.3.1 Context of the Problem: Earth's Ionosphere

The atmosphere, ionosphere, and its layers are shown in Fig. 1.3. The peak density altitude can be seen typically at  $\sim 300$  km, in the  $F$ -region, but with a high degree of variation (see Fig. 1.2). The practical importance of studying the ionosphere, is that it has a sufficient electron density to adversely effect EM-wave propagation for satellite communications and distant Earth communications [Rawer, 1993]. The most important layer from a navigation and communications perspective is the  $F2$  layer, where the electron content reaches peak density. The  $F$ -layer is present on both the day- and night-side ionosphere and is the layer principally responsible for the refraction of radio waves [Hunsucker and Hargreaves, 2003].

The ionosphere plays a critical role in satellite communication, military communication and space science. Satellite signals passing through the ionosphere can be delayed and refracted to such a degree that these effects cannot be ignored. The delay and refraction are to the first order inversely proportional to the square of the frequency of the signal. Specifically, the extent to which the signal is affected is proportional to the amount of ionised gas or equivalently the number of free electrons or TEC in the ionosphere along a ray path of unit cross-section from the transmitter to the receiver. If the state of the ionosphere, particularly the distribution of the elec-

tron density is known, the influence and consequential effects on radio propagation and communications systems can be quantified [*van der Merwe, 2011*].

For high frequency (HF) communication, the propagation path of interest is a sky-wave; radio waves are reflected off the ionosphere to another location on Earth's surface. In this case, the parameters of interest are the maximum/lowest usable frequency (MUF/LUF respectively) that the ionosphere can reflect. The MUF depends on the peak density in the  $F$ -region and angle of elevation of the incident EM wave. Since the degree of ionization is sensitive to EUV radiation, the ionosphere varies over a 24 hour period (day and night) as shown in Fig. 1.2. Similarly, ionospheric variations are affected by the solar sunspot cycle ( $\sim 11$  years). As a result, these parameters can change over the solar cycle, diurnally and due to solar and geomagnetic disturbances that are difficult to account for (in models) or predict. Table 1.1 shows the diurnal variation and change in the peak density ( $N_{max}$ ), MUF and TEC over one solar cycle.

Ionospheric Parameter	Diurnal (Mid-Latitude)	Solar Cycle (Daytime)
$N_{max}$	$1 \times 10^5$ to $1 \times 10^6$ electrons/cm <sup>3</sup> Factor of 10	$4 \times 10^5$ to $2 \times 10^6$ electrons/cm <sup>3</sup> Factor of 5
Maximum Usable Frequency (MUF)	12 to 36 MHz Factor of 3	21 to 42 MHz Factor of 2
Total Electron Content	5 to $50 \times 10^{16}$ electrons/m <sup>2</sup> Factor of 10	10 to $50 \times 10^{16}$ electrons/m <sup>2</sup> Factor of 5

Table 1.1: The variability in ionospheric peak density, MUF and TEC over the diurnal and solar cycle [*Anderson and Fuller-Rowell, 1999*].

The LUF is dependent on the degree to which the  $D$ - and  $E$ -region absorb the radio wave and therefore it is significantly affected by solar X-ray events as shown by Fig. 1.5 [*Anderson and Fuller-Rowell, 1999; Zolesi and Cander, 2013*].

Ionospheric altitudes encompass a region that is higher than aircraft fly, and only the topside ionosphere is at satellite orbital altitudes. Intermittent scientific rocket campaigns [*Burchill et al., 2004; Sangalli et al., 2009; Abe and Moen, 2011*] and *high altitude* balloon experiments [*Francis et al., 2011*] in the lower ionosphere and occasional space shuttle voyages through the ionosphere are the only sources of in-situ

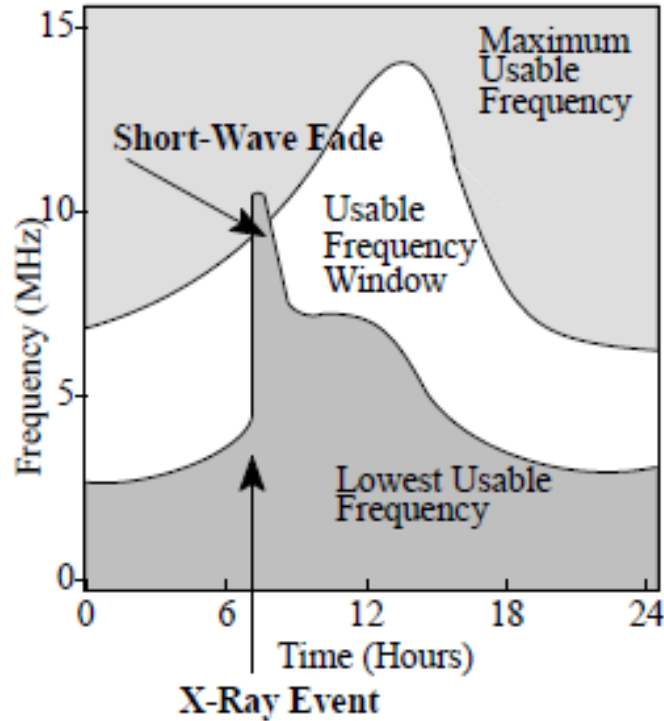


Figure 1.5: Comparison of the MUF and LUF over a 24 hour duration, during which a solar X-ray event with a sudden onset at 07h00 took place. The event caused the LUF to exceed the MUF, signifying an HF signal blackout until  $\sim 08\text{h}00$  [Anderson and Fuller-Rowell, 1999].

measurement. Sparse datasets (time and place of launch) exist at best. Therefore satellite remote sensing techniques are used to provide more widely distributed measurements for global studies.

Remote sensing techniques acquire information about the physical parameters of an object without being in direct physical contact with it [Elachi and van Zyl, 2006]. Measurements of changes caused by the object on its surrounding fields (e.g. electromagnetic waves emitted or reflected, acoustic waves reflected or perturbed, magnetic potential due to objects presence) provides information about the object itself or the emissivity of the medium through which the EM energy propagates through from the source to the sensor.

In the past, the scientific community has developed several methods and instruments for observing the IED distribution; examples include vertical incidence sounders [Mushini et al., 2009], incoherent scatter radar (ISR) [Lilensten et al., 2005], spaceborne topside sounders [Chen et al., 2011], in-situ rocket and satellite data and oc-

cultation measurements [Burchill *et al.*, 2004; Sangalli *et al.*, 2009; Abe and Moen, 2011]. Another common method for the wide-area observation of mesoscale ionospheric structures (features ranging from 100 km to 1000 km in horizontal extent) is the reception of signals on the ground from satellite radio beacons such as Global positioning System (GPS). This method allows large segments of the ionosphere to be observed in a relatively short period of time due to the motion of the satellite(s) [Yizengaw *et al.*, 2004]. These signals can be used to reconstruct the electron content using techniques from CT.

Tomography has proven to be a useful tool in the development of Global Navigation Satellite Systems (GNSS). These systems are affected by variations of IEDs, particularly those that do not follow predictable patterns [Mitchell *et al.*, 1997a; Kunitsyn and Tereschenko, 2003; Max van de Kamp, 2012]. In CIT, the TEC measurements are inverted and the resulting image is the reconstructed electron content of the ionosphere. Although this method seems indirect, it is capable of yielding multi-dimensional images. This is an obvious advantage over direct measuring techniques such as in-situ  $n_e$  measurement using meteorological balloons, sounding rockets, and vertical sounders which give only localized data for a specific time and location [Max van de Kamp, 2012; Cushley, 2013].

### 1.3.1.1 TEC

Total electron content ( $TEC$  in Eqn. 1.1) is a parameter that can be used to describe the state of ionospheric activity and characterize propagation conditions, from the navigation perspective in particular. The TEC along the path or within the plasma column of unit cross-section is defined by:

$$TEC = \int_0^l n_e dl \quad (1.1)$$

where  $TEC$  is the integrated electron density  $n_e$  along the path length  $l$ . GPS satellites orbit at 22 200 km altitude and the signals received (by millions of users) to determine position must be corrected to account for propagation delays due to electron density variations over different paths through the ionosphere. The accuracy

to which the propagation delay can be accounted directly correlates to the degree of positional accuracy provided by a GPS receiver [Anderson and Fuller-Rowell, 1999].

Signal phase measurements suffer a negative delay and the code measurements a positive delay from propagation through the ionosphere. To the first order, the propagation delay can be calculated as a function of TEC and frequency. The propagation time delay due to the ionosphere  $t_{d_i}$  is proportional to the TEC and inversely proportional to the square of the frequency as shown in Fig. 1.6. This relationship is given by Eqn. 1.2 [Marković, 2014; Subirana et al., 2016].

$$t_{d_i} = \frac{e^2}{8\pi^2 m_e \epsilon_0 f^2} \int_0^l n_e dl = 40.3 \frac{TEC}{f^2} \quad (1.2)$$

where  $e = 1.602 \times 10^{-19}$  C is the elementary charge,  $m_e = 9.109 \times 10^{-31}$  kg is the mass of an electron, and  $\epsilon_0 = 8.854 \times 10^{-12}$  C<sup>2</sup>/N · m<sup>2</sup> is the permittivity of free space. For example, a very high frequency (VHF) radar operating at 430 MHz may experience a time delay that ranges from 36 to 363 ns for a target at zenith for the TEC range given by Table 1.1 of 5–50 TECu (1TECu =  $10^{16}$  electrons·m<sup>-2</sup>).

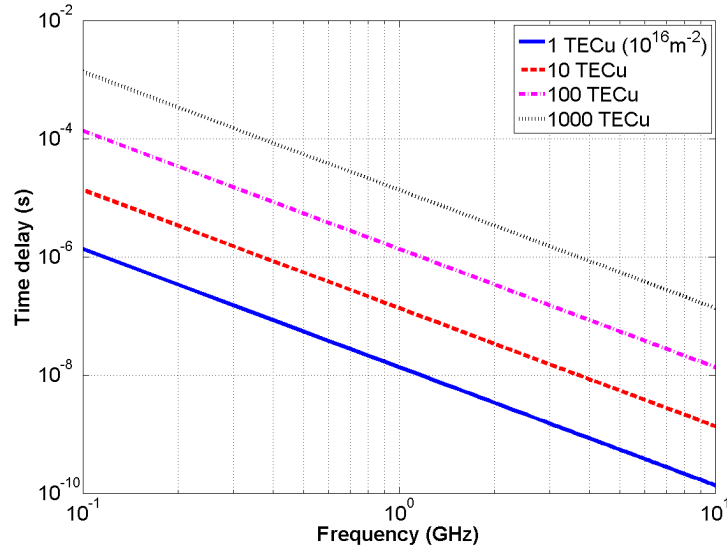


Figure 1.6: The time delay due to the ionosphere increases as a function of TEC and decreases as a function of frequency for several values of the TEC

GNSS data consisting of carrier phase and code range measurements in support of autonomous three-dimensional Geo-spatial positioning is available from several networks. These networks of ground-based GNSS receivers are used to produce maps

such as that shown in Fig. 1.7. The National Geodetic Survey is an office of the National Oceanic and Atmospheric Administration (NOAA) National Ocean Service that manages such a network, called Continuously Operating Reference Stations (CORS) [National Geodetic Survey, 2015]. The location of these stations (whether operational or not) are shown in Fig. 1.8.

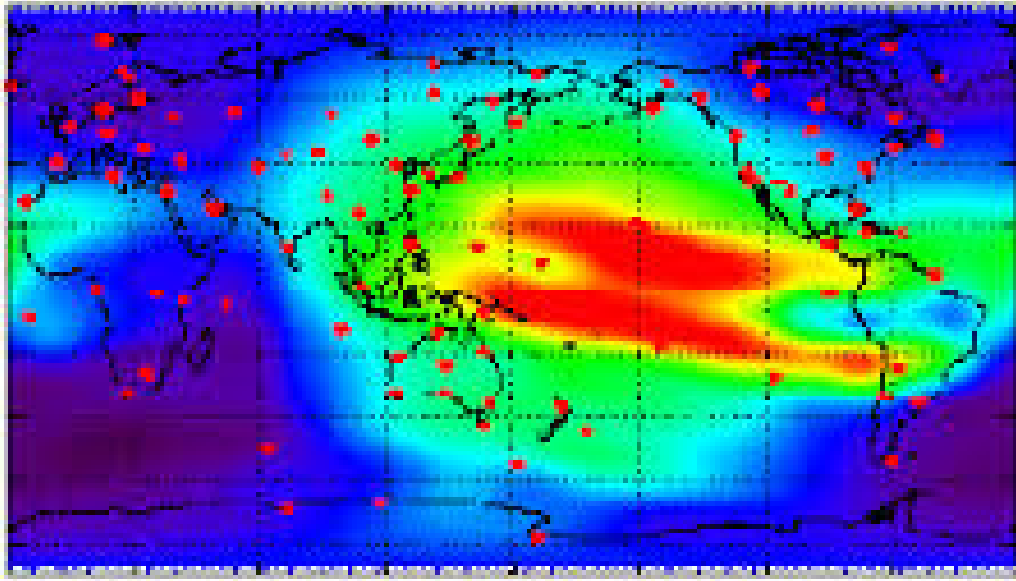


Figure 1.7: An example of the type of vertical TEC (VTEC) maps produced regularly from GNSS and used to assess the state of the ionosphere and propagation conditions, available from *NASA Jet Propulsion Laboratory California Institute of Technology* [2014]. Stations used are shown as red dots.

The stations are located on land, mostly at equatorial, low- and mid-latitudes. The high latitude domain and oceanic regions do not have coverage except from a few ground stations in the Canadian Arctic [Jayachandran *et al.*, 2009] and on islands such as Hawaii. The largest (1200 stations shown in Fig. 1.9) and densest network of receivers is the GNSS Earth Observation Network System (GEONET), located in Japan primarily to monitor movement of the land mass. Observation data are made available for actual survey works and for studies of earthquakes and volcanic activities. It is evident that GNSS receiving stations suffer the same constraints as those discussed for Automatic Dependent Surveillance Broadcast (ADS-B) and other ground-based receiving architectures [Cushley and Noël, 2014].

Despite their limited coverage, these networks are the source of current global

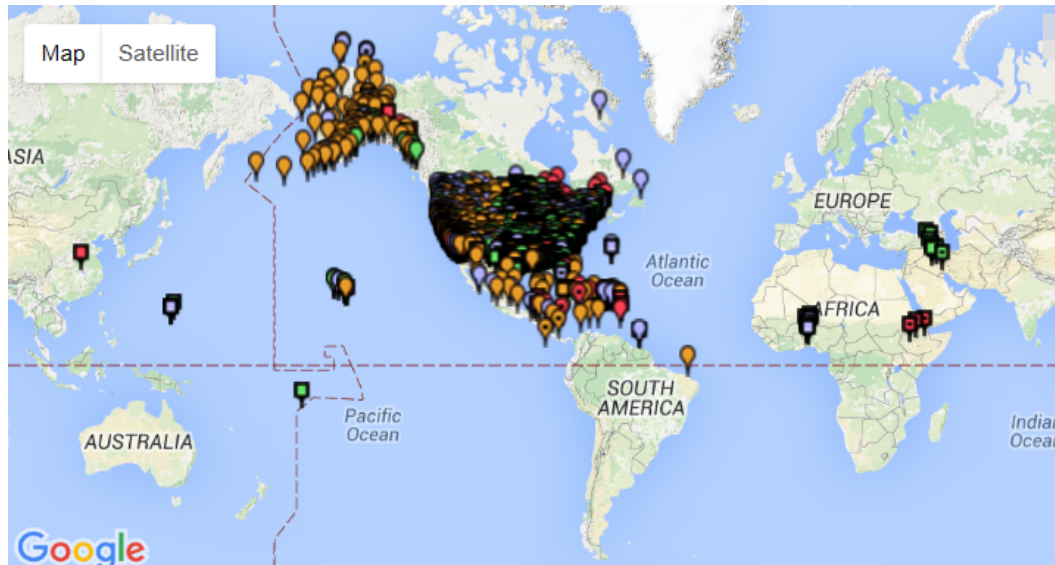


Figure 1.8: The location of all CORS stations (whether operational or not) [National Geodetic Survey, 2015]

ionospheric maps (GIMs) of vertical TEC (VTEC) shown in Fig. 1.7. By examining the raw data, it is evident that the coverage used to produce the GIM are not in fact globally distributed and often rely on models or interpolation techniques to fill the gaps in coverage. The models generally rely on data from instruments such as ionosondes, ISR and GPS TEC and therefore do not accurately model the TEC at high latitudes, where data is unavailable and short time scale events tend to disrupt the ionosphere more due to the converging magnetic field. For example, see Fig. 1.10 for the VTEC produced by the International Reference Ionosphere (IRI). Empirical models represent long-term averaged data, neglecting specific events. While models have proven to be useful for the general behaviour of the ionosphere and even show diurnal variation quite well, they cannot be used for the analysis of sporadic short time-scale (minutes to hours) events [Cushley, 2013]. Sometimes they do not even show well-known ionospheric features such as the equatorial ionization anomaly that is shown in Fig. 1.7 (red region on either side of the equator).

Coverage from another source that is capable of measuring the ionospheric TEC, particularly over oceanic regions and at high latitudes would be beneficial to eliminate gaps in coverage and supplement GNSS data where coverage is available.

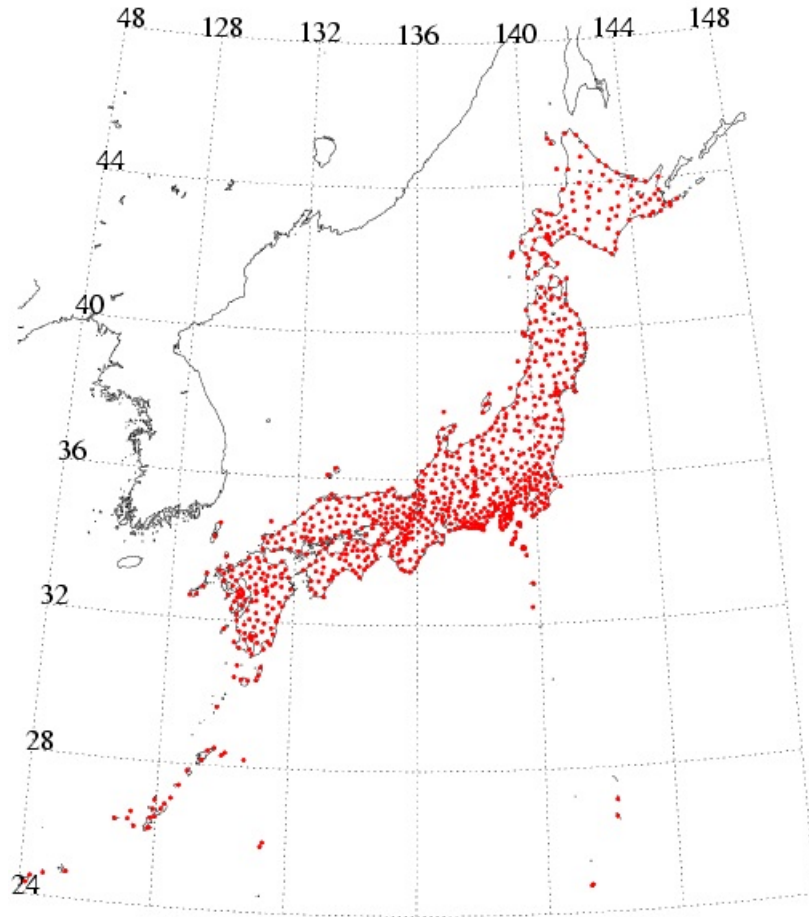


Figure 1.9: The largest and densest network of GNSS receivers for TEC measurement is in Japan, called GEONET. The locations of the 1200 ground receivers are shown as red dots [Saito].

#### 1.4 Introduction to Computerized Tomography (CT)

Tomography is an image reconstruction technique that is based on large scale numerical optimization of large sparse matrices, particularly linear algebra. It has a wide range of applications in medicine (CT-scans), industry (non-destructive testing) and science (3D imaging of nano-materials). CT is a non-invasive technique used to image the interior of objects. The word tomography comes from the Greek words *tomos* meaning ‘slice’ and *graphein* ‘to write’. It refers to the manner in which the resulting image is reconstructed; images are created in 2D slices, which can then be combined to give a 3D structure if required. Information from different propagation paths are combined to give a representative picture of a slice through the body with



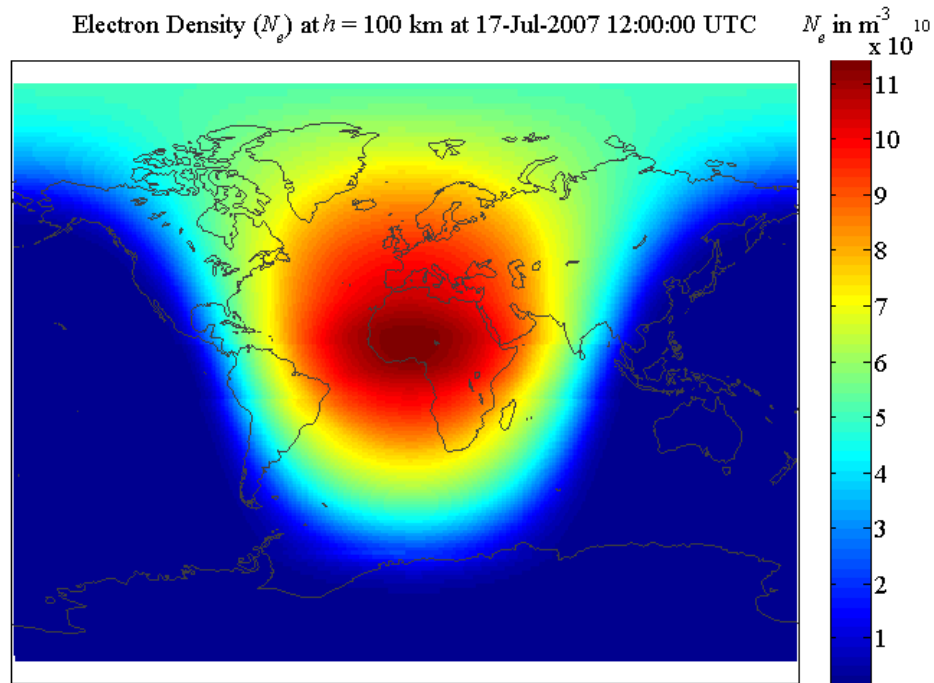


Figure 1.10: An example of the type of VTEC maps produced using IRI model, available from *Bilitza* [2007]; *Bilitza et al.* [2011]; *Compston* [2012].

quantitative absorption of different density media.

The best known application of CT is in medical imaging, often referred to as computed axial tomography, computer assisted tomography or CAT-scans; using X-rays passed through a patient to detect such things as cancer. The credit for the pioneering work in CT was the 1979 Nobel Prize in Medicine, “for the development of computer assisted tomography” by G.N Hounsfield and A.M. Cormack in the 1950s and ’60s. Prior to the simultaneous independent research of Hounsfield and Cormack others had developed the same mathematical techniques for a variety of other applications, but they failed to grasp its critical application which illustrated the significance of their work [*Gbur*, 2008; *Cushley*, 2013]. The technique has gained popularity within the ionospheric imaging community since *Austen et al.* [1986, 1988] first demonstrated that CT techniques developed extensively in medical physics could also be applied to

the ionosphere electron content. CIT experiments using RF measurements as input have demonstrated the capability of applying tomographic methods to image various ionospheric structures *Andreeva et al.* [2001].

Several physical constraints of the imaging system restrict the quantity of data collected and consequently the quality of the reconstructed image. An ideal tomographic apparatus requires a finite-sized object distribution, densely packed ray paths passing at all possible angles through it, and a dense chain of coplanar receivers [*Na and Lee*, 1994; *Na et al.*, 1995; *Biswas and Na*, 1998]. For the typical CIT apparatus (e.g. GPS), unlike other applications of CT, a complete set of projection data is not available. A measurement for every sensor position moved in equal increments, whether equiangular or equidistant, at a fixed distance (or altitude in the case of CIT) is not controlled in the CIT apparatus, as with most applications of CT. For example, the nature of a satellite pass where the data is collected in fixed increments of time will not be equidistant, nor equiangular. In CT, an instrument may be built to satisfy these specifications, but in applications like CIT there are a great deal of other restricting considerations.

Although an extension of the CT theory would appear quite easy there are many additional factors that must be taken into consideration. Inversion procedures that work for CT would work well if the data were available at regularly spaced intervals, in all directions. Given orbital geometry consideration for a satellite, and LOS conditions throughout a satellite pass, it is not possible to acquire data from all viewing angles. Unlike medical imaging, there are no defined space for the object, and free-space separation, making the *a priori* guess more difficult. Generally, models are used for the initial guess, unless the receivers are collocated with other instruments that can provide information for the real-time ionosphere.

There are three primary differences between CIT and CT. The first is that the medium through which the EM wave propagates is quite different and therefore a different frequency must be used. For example, X-rays that are used in medical CT scans would propagate with very little measurable attenuation through the ionosphere.

The second difference, is that unlike most applications of CT, the apparatus is not

designed specifically for the application and as a consequence, measurements are not equidistant, equiangular, or measured from all angles because of the constraints in satellite geometry. Any satellite that is not in a perfectly circular orbit (eccentricity equal to 0) will not maintain a constant altitude above the Earth's surface and the distance between the transmitter and receiver will vary. The velocity of the satellite will change (fastest at perigee and slowest at apogee) and therefore transmissions at equal time intervals will not be equally spaced in terms of their angular separation or distance between along-track satellite positions.

The height of the unknown ionization may be predictable, but it is certainly not known and constrained within the centre of an immobile apparatus as is typically the case in most other applications of CT (e.g. brain scans, nano materials). Projections are taken using a transmitter and multiple opposing receivers rotated by no more than  $180^\circ$  or  $\pi$  radians. The Earth blocks views of projections and we cannot sample through  $180^\circ$ . At best, using a flat horizon and an elevation cut-off below  $10^\circ$  where communications are more sporadic, we can sample through  $\sim 160^\circ$ . Rays at low elevations go undetected because of the continuity of the ionosphere, curvature of the Earth-atmosphere system, and limited number of ground receivers [Na and Lee, 1994; Biswas and Na, 1998]. Each overpass accounts for only about  $40^\circ$  to  $60^\circ$  latitudinal coverage, which is equivalent to only  $45^\circ$  to  $50^\circ$  tomographic angular coverage. According to the principles of tomographic inversion, this diminishes the vertical information content of the reconstruction image [Kak and Slaney, 1988].

The third difference is the gradients of the features we wish to image. For example, in medical CT scans some rays will miss the object completely thus yielding sharp edges of the skull, (inner, and outer) among other features with steeply varying densities. Bones, organs, tissue, and tumours all absorb X-rays by a different amount. This is not the case for CIT. Even enhanced regions of the ionosphere will generally have much lower tapering gradients towards the quiet neighbouring (latitude or longitude) profiles. The fact that the measurement is the integrated electron density over the complete path also smooths the gradients of individual features.

### 1.4.1 Computerized Ionospheric Tomography (CIT)

The CIT technique used to map the IEDs involves the transmission of RF beacon signals through the ionospheric plasma, typically from a transmitting satellite to ground-based receiver(s) or a satellite receiver at a lower altitude. Measurement of ionospheric effects such as phase delay or Faraday rotation (FR) on the transmission of beacon radio signals through the complex dielectric plasma medium composing the ionosphere can be used to determine the TEC along the signal path. The TEC measurement and ray-path geometry between the transmitter and receiver for each respective value are inputs to a CT algorithm, which reconstructs maps of the electron density [Selcher, 2007]. The principal advantage of this technique is the capacity for rapid, efficient, extensive geographic coverage and its cost efficiency [Biswas and Na, 1998].

Traditionally, CIT has been implemented to observe naturally occurring large-scale ionospheric structures [Pryse and Kersley, 1992; Kersley et al., 1993; Pryse et al., 1993.]. Other work has investigated small-scale spatial resolution from relatively high data rate receivers at a rate sufficient to resolve structures of interest to a degree comparable to one kilometre. Figure 1.11 shows a typical CIT imaging system which employs a chain of ground stations to receive signals transmitted from geostationary satellites to dual-frequency ground-based receivers [Leitinger, 1994; Choi et al., 2006; Selcher, 2007; Max van de Kamp, 2012].

A typical CIT apparatus uses a chain or array of receivers (e.g. GPS/GLONASS, CERTO, SBAS). An array can be used to form a dense, high resolution ( $m \times n$ ) matrix, which has the added advantage of being able to either reconstruct multiple parallel chains that are each oriented approximately along a line of longitude, or using data from all receivers to map in three or more dimensions. An array also has the benefit of allowing observations of phenomena (e.g. changes in a cavity) both parallel and perpendicular to magnetic field lines.

Logistically speaking, a typical CIT experiment often forces the receiver geometry to have fewer than eight irregularly spaced stations spanning  $15^\circ$  to  $40^\circ$  in latitu-

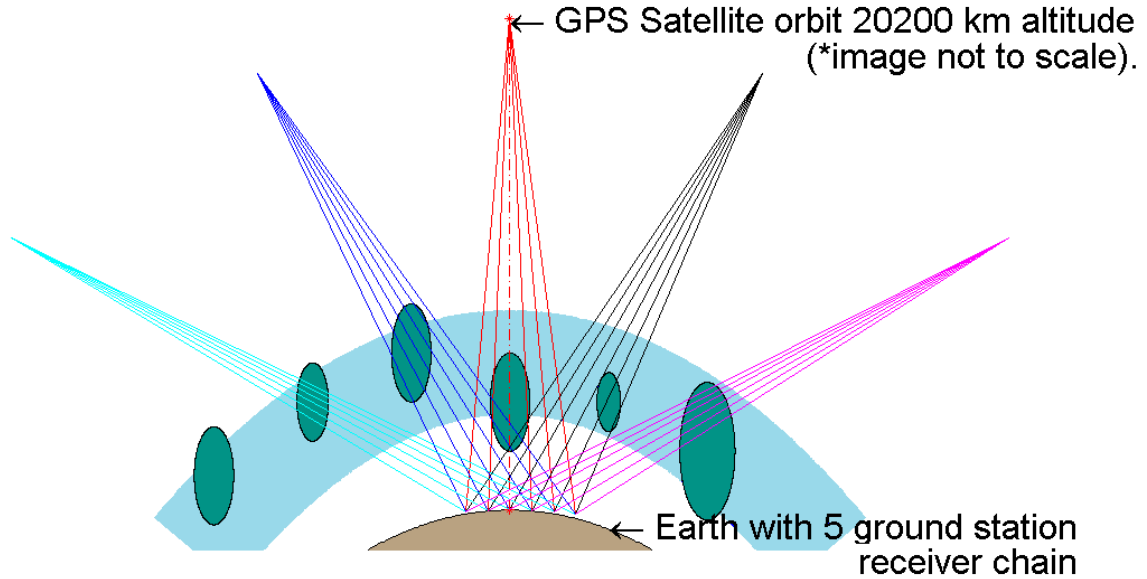


Figure 1.11: Numerous ionospheric experiments have been performed using a similar apparatus in order to obtain sufficient data to reconstruct the ionosphere using limited viewing angle CT.

dinal extent and displaced by  $2^\circ$  to  $10^\circ$  in terms of longitude from the orbital plane [Biswas and Na, 1998]. Inverted systems such as ADS-B, AIS and Automatic Packet Reporting System (APRS) will typically experience more irregular transmitter distributions, but technically could control these distributions (e.g. formation flight) in a more timely manner using air and marine assets as opposed to deploying ground based receivers.

For 3D reconstructions, CIT experimental systems use multiple north-south oriented chains spanning  $20^\circ$  to  $25^\circ$  longitude [Biswas and Na, 1998]. Consequently, the irregularly space measurements, limited angle visibility and non-coplanar receiver geometry result in limited projection domain information. To overcome these physical constraints *a priori* information about the ionospheric electron distribution is often used to aid the inversion/reconstruction process.

Several CIT inversion algorithms incorporate *a priori* information from models based on the dynamics of electron distribution in the upper atmosphere or data from another source when available to guide the reconstruction process towards a convergent and feasible solution [Raymund, 1994; Sutton and Na, 1996; Na and Biswas, 1996; Biswas and Na, 1998]. Most algorithms provide this *a priori* information as an

initial guess [*Pryse and Kersley, 1992; Raymund, 1994*] for an iterative algebraic reconstruction process based on standard tomographic principles or as statistical [*Fre-mouw et al., 1992*] or structural constraints such as smoothness [*Sutton and Na, 1996b*], maximum entropy [*Frougere, 1995*] and cross entropy [*Kuklinsky, 1997*] for achieving minimum-norm least squares solutions using pseudo-inversion of system matrices [*Kak and Slaney, 1988; Biswas and Na, 1998*]. These iterative algorithms associate a distance with each law and associated equation(s) with the composition, updated continuously to minimize the distance until the largest distance is zero or some other stopping condition is met.

During the actual implementation of the image reconstruction algorithm(s), one must decide on a source of projection data, how to approximate the projection operator, what inversion algorithm to employ and how to include and control the ancillary data and constrain the reconstructed image. For example, electron densities cannot be negative. Each decision may yield a reconstructed image that is compatible with the projection data, but the resulting images may differ depending on the choices made in terms of attendant artefacts and distortions [*Andreeva et al., 2001*].

From a tomographic perspective, the restricted viewing angles of the imaging system, combined with irregularity and sparsity of ground based receiver(s) chain, makes it inherently prone to data insufficiency and the inversion process one of the most challenging examples of limited data tomography [*Yeh and Raymund, 1991*]. In Figure. 1.12, one (or more) low-orbit satellites may receive signals transmitted by multiple amateur radio ground stations (or aircraft as will be discussed shortly). Rather than the satellite transmitting to ground stations whose positions are restricted and confined to the surface of the Earth, the location of the transmitter(s) and receivers have been exchanged and the CIT apparatus is inverted. It should be noted that the TEC calculated along a ray path does not depend on the direction of propagation.

The work discussed here makes use of pre-existing radio beacon signals that have been deployed for a dedicated purpose other than science (e.g. autonomous Geospatial positioning and tracking services), that indicate the potential for exploitation using the CIT technique. These signals all use a single respective carrier frequency

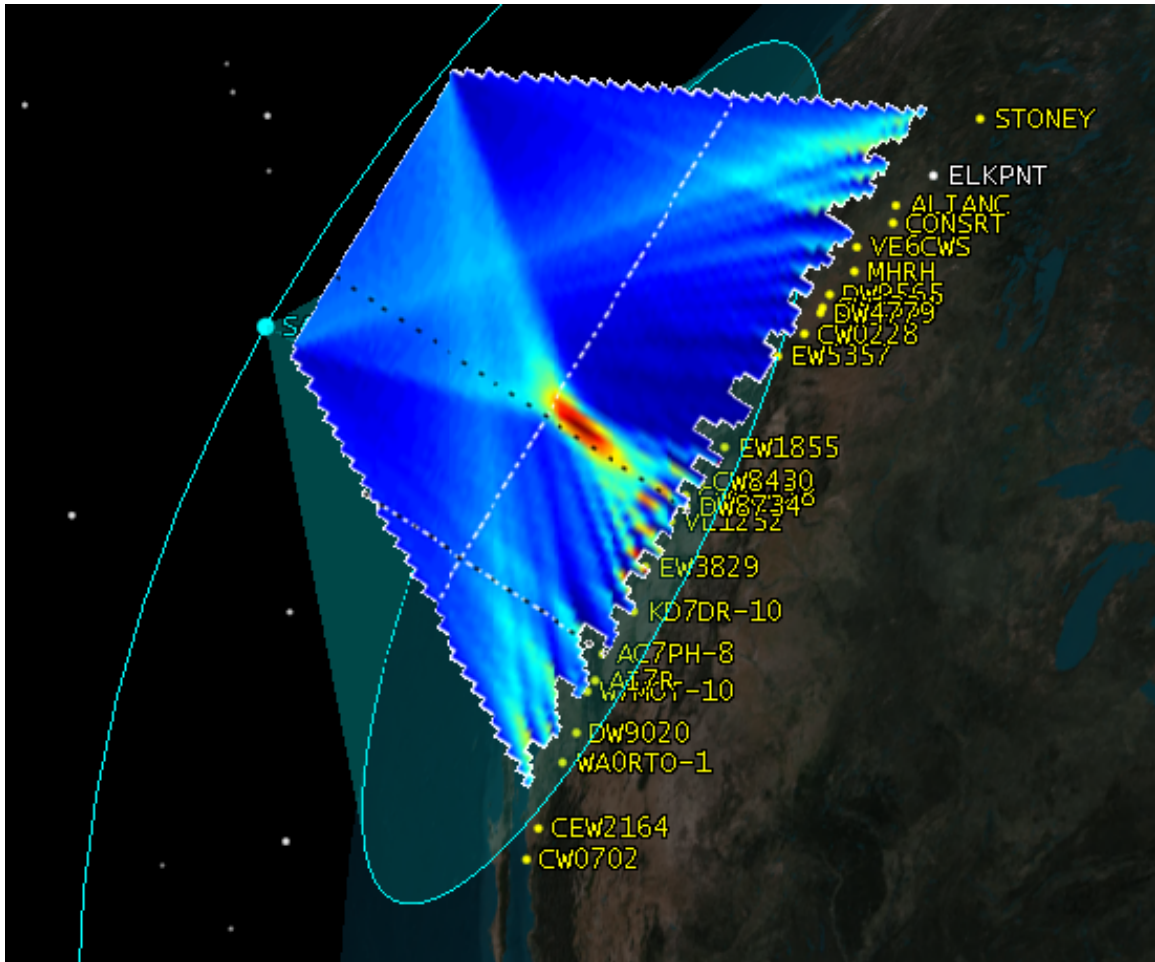


Figure 1.12: In this *inverted* CIT apparatus, the location of the transmitter(s) and receivers have been exchanged. The amateur radio APRS stations are the transmitters and the satellite is the receiver. The satellite is also now a low Earth orbit (LEO) satellite and creates a synthetic bank of receivers during the course of a line-of-sight (LOS) pass.

to satisfy the dedicated purpose for which they were intended and therefore is not possible to extract the TEC using the dual-frequency method. Instead, the FR of individual signals is used to determine the TEC between the transmitter and receiver locations.

Although the inverted CIT systems (e.g using ADS-B, AIS or APRS) will encounter the same three main issues with the traditional CIT apparatus, there are also several advantages imparted by inverting the system and using ground based transmitters with a mobile receiver.

Generally, a ground-based campaign can only deploy to a specific location. There-

fore, observations are confined, and many regions such as oceanic and polar regions have been neglected. Reconstructions from an orbital platform over time can be made for various regions and may indicate areas of interest of most probable occurrence to prioritize other fixed ground-based instrument campaigns (e.g., ISR) [Cushley and Noël, 2014].

The work presented in this thesis explores the feasibility of using two of these signals; ADS-B and AIS, and two other aspects related to the problem of using FR of these signals as input to CIT. As will be discussed shortly, the TEC can be calculated from FR measurements, but this estimation requires accurate magnetic field information along the path. The sensitivity of the FR and TEC to different methods to obtain the parallel component of the magnetic field along a path was investigated by Cushley *et al.* [2018]. Improving the accuracy of this calculation reduces the uncertainties introduced to the CIT and propagation of these errors to the final reconstruction. As briefly discussed previously, CIT generally uses an *a priori* guess for the first iteration to guide the reconstruction process towards a reasonable solution. Models do not represent sporadic events so it is better to use data from another source whenever possible. The research by Cushley *et al.* [2017] presents a method that could be considered using independent TEC and FR measurements for this purpose, however the papers presented in Chapters 4 and 7 do not use this method since no *a priori* information was used. This was done to preserve the integrity of the reconstruction to evaluate the feasibility of CIT using only the data from these new potential sources without bias from the *a priori* information.

## 1.5 Thesis Outline

This thesis explores the concept of ionospheric sounding and tomographic reconstruction of 2D IED profiles using ADS-B, AIS and other linearly polarized signals of opportunity. Chapter 2 of the thesis elaborates on a more detailed discussion of the structure of the ionosphere and ionospheric EM-wave propagation theory as it relates to this research. The first section of Chapter 3 introduces the functionality and operational principle of three types of beacon signals; ADS-B, AIS and APRS.



The second section of Chapter 3 describes how a ray trace model used to simulate the data used throughout this thesis. The last section of Chapter 3 compiles a literature survey of relevant CIT research related to this thesis and describes the experimental design with respect to data collection and the ADS-B *apparatus* for CIT.

This thesis has been written in the article-based format. Chapters 4 through 6 each consist of a paper published in *Radio Science*. Chapter 7 consists of a paper manuscript which has been accepted by *Radio Science*. Each of Chapters 4 through 7 also contains a short overview and results section explaining the significance of the paper and the relation to the rest of the thesis.

- Chapter 4: Cushley, A. C., and J.-M. Noël, Ionospheric tomography using ADS-B signals, *Radio Sci.*, 49, 2014.
- Chapter 5: Cushley, A. C., Kabin, K., & Noël, J.-M.. Faraday rotation of Automatic Dependent Surveillance-Broadcast (ADS-B) signals as a method of ionospheric characterization. *Radio Sci.*, 52, 2017.
- Chapter 6: Cushley, A. C., Noël, J.-M., & Kabin, K., Faraday rotation, total electron content, and their sensitivity to the average parallel component of the magnetic field. *Radio Sci.*, 53., 2018.
- Chapter 7: Cushley, A. C. & Noël, J.-M., Ionospheric sounding and tomography using Automatic Identification System (AIS) and other signals of opportunity. Submitted to *Radio Sci.*, Accepted 11 December 2019.

Chapter 4 presents a study of the FR of ADS-B signals and estimation of slant TEC (STEC) that will be detected using an ADS-B receiver on an orbital platform. It deals with reconstruction of the IED by means of CIT using synthetic ADS-B data for a simulated ionosphere and estimated aircraft distribution in preparation for the launch of (a constellation of) satellites equipped with ADS-B receivers. The study describes the ADS-B system, mathematical basis for the FR and its proportionality to TEC, and the mathematics of the tomographic analysis. The paper presents a

technique to determine electron density maps of the ionosphere using ADS-B radio beacon signals which are transmitted by aircraft.

Due to the relevance of the geomagnetic field to FR measurements and using such measurements to estimate the TEC, or as direct input to CIT, Chapter 5 describes a method for using linearly polarized ultra high frequency (UHF) signals from existing transmitting aircraft to existing receiving spacecraft to measure FR and TEC, thereby creating a wide data base upon which the distribution of IED can be modelled. Using as a first approximation vertical propagation at a frequency of 1090 MHz from a transmitter in the ADS-B system, candidate orbital receivers in LEO spacecraft capable of polarization measurement, and using a 3-parameter Epstein ionospheric density model, FR values under a variety of physical conditions are computed using a ray trace model. With the cited existing infrastructure, this paper demonstrated encouraging accuracy or precision of the proposal at mid latitudes. These ADS-B devices are installed on most aircraft and transmit linear polarized waves automatically which can be measured by orbiting satellites. In particular, the FR of these signals can be measured and used in conjunction with separate TEC measurements. The vast number of independent FR measurements that can be made along several paths with this technique provides great potential for ionospheric characterization. Since FR is dependent on magnetic field geometry (which varies as a function of altitude) as well as electron density, it provides additional information about the shape of the IED profile.

Chapter 6 presents a comparison of techniques for the determination of the average parallel component of the geomagnetic field given independent FR and TEC measurements. This paper addresses the question, “what is the appropriate estimator of parallel magnetic field to use when calculating FR in the ionosphere, given TEC, or using FR to determine TEC. The purpose of this comparison was to determine which technique produces the most consistent results and introduces the smallest uncertainty when estimating STEC from FR and vice versa. This knowledge can later be applied to problems which determine TEC only from FR and average magnetic field values, such that the most appropriate magnetic field value may be chosen. It

is related to the paper presented in Chapter 4 because this technique can be used to improve the estimation of the STEC values derived from FR observations, that are used as input to CIT. Improving this estimation reduces the uncertainties that would be propagated by the CIT algorithm to the final reconstruction. This technique can also be used for other applications including correction of polarized signals, for example in radio astronomy and radar polarimetry. The various techniques compared in this paper are evaluated with respect to a benchmark solution based off of integrated values from the International Geomagnetic Reference Field (IGRF) model.

Chapter 7 presents a similar study to Chapter 4 but for AIS signals. In this paper a simulation of AIS signals in the Phillippine Sea region was undertaken. This area was chosen because it has one of the highest density of ships and marine traffic. This study is similar to that conducted in *Cushley and Noël* [2014] for ADS-B; which begins by comparing the same cases as those presented in *Cushley and Noël* [2014] for ADS-B before proceeding to investigating a new region where the AIS data density is much greater. The same ionospheric profiles were used to provide a comparison of AIS to those ADS-B reconstructions as well as comparisons of AIS simulations using time delay in addition to those using FR.

Finally, Chapter 8 will summarize the main findings of each chapter and discuss the overall conclusions of this work. Possibilities for future work in this area of research are also discussed.

In this thesis it was shown that FR measurements from the received aircraft and ship signals are detectable, and can be used to calculate the TEC along the ray paths. These integrations through various 3D input electron density profiles served as the basis for modelling the expected TEC data collected by space-borne ADS-B and AIS receivers, revealing important features of the input profile such as ionization troughs, localized enhancements, and other large and small scale ionization irregularities.

## Theoretical Considerations

### 2.1 Overview

In this chapter, we present a qualitative treatment of several topics in order to proceed with our study of ionospheric sounding and CIT using new sources of ionospheric sounding data. In this chapter, we briefly describe the ionosphere, its respective layers and its importance, specifically why it is important to be studied and how this information can be used operationally. Finally, the theory pertaining to magneto-ionic wave propagation, including the decomposition of an EM wave into two propagation modes when they traverse a birefringent medium such as the ionosphere and how waves interact with the geomagnetic field is reviewed. Finally, the observable, FR, that is used to sound the ionosphere and as input to CIT later in Chapters 4 to 7 is discussed. This chapter describes the mathematical basis for the FR and its proportionality to TEC and the mathematics of the tomographic analysis. These topics are discussed in more detail in Chapters 4 to 7 as they relate to the specific research topics presented in these publications.

It should be noted that in this work, the collisions between neutral and charged particles are neglected. In the  $E$ -region, collisions can effect the propagating EM-wave, however for the 1090 MHz ADS-B carrier the effect of collisions can be ignored in the  $E$ -region, which contains only a small portion of the wave path. The majority of the EM-wave modifications occur in the  $F$ -region where the electron density peak occurs. The collision frequency for both electrons and ions can be considered negligible at altitudes above the  $E$ -region (  $10^3$  Hz, compared to  $10^9$  Hz for ADS-B) [*Budden*, 1961; *Gillies*, 2006] .

## 2.2 The Ionosphere

The Earth's ionosphere is generally regarded as the region of the upper atmosphere extending between 60–1000 km above Earth's surface where unbound or *free* particles are ionized by solar radiation to form a plasma [Kelley, 1989]. An unbound electron is any electron which is not bound to an ion, atom or molecule and is *free* to move under the applied force of an electric or magnetic field [William Collins Sons & Co. Ltd 1979, 2003]. In the weakly ionized ionospheric plasma the temperature is typically 0.1 eV (1160 K) and the free electrons and positive ions are attracted to one another by the chemical processes of ionization and recombination [Chen, 1984]. The resulting balance between the two processes determines the electron number density [Schunk and Nagy, 2000].

The number of free electrons in the ionosphere is sufficient to affect radio wave propagation. The ionosphere encompasses portions of the mesosphere, thermosphere and exosphere, and is generally further subdivided into regions; *D*, *E* and *F*. The atmosphere, ionosphere, and its layers are shown in Fig. 1.3. It should be noted that the altitude and electron density of the ionospheric layers vary with different solar conditions, diurnal variation, geomagnetic variation and latitude.

The lowest portion of the atmosphere is called the troposphere. It extends from Earth's surface to approximately 10 km altitude. Above 10 km is the stratosphere, where incoming solar radiation at very short ultra-violet (UV) wavelengths ( $\sim 315$  nm) forms the ozone layer. Above 80 km, the atmosphere has very low density such that free electrons exist for short periods of time, before being bonded to a nearby positive ion. This portion of the atmosphere is ionized forming a plasma, thus called the ionosphere [Kelley, 1989].

The ionosphere owes its formation to the extreme solar UV, X-Ray, and shorter wavelength radiation that has enough energy to break chemical bonds. Photons at these high frequencies are energetic enough to dislodge electrons from a neutral gas atom or molecule upon absorption (see Fig. 2.1).

The reverse process of ionization is recombination. In the upper ionosphere the

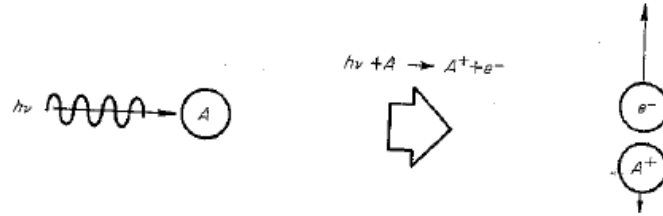


Figure 2.1: Photoionization occurs when an atom absorbs an EM photon of sufficiently high frequency (e.g. solar UV, X-Ray and shorter wavelength radiation) [Jahn, 1968].

main loss process is dissociative recombination. A less common process called radiative recombination is whereby a free electron is captured by an ion spontaneously occurring in photon emission, called airglow, or afterglow [Chen, 1984]. At lower altitudes, the electron density is much lower and diffusion and attachment are the dominating processes because the gas molecules and ions are closer together.

The electron number density changes with altitude above the Earth's surface. As previously mentioned, the ionosphere is further subdivided into regions with letter designations: *D*, *E*, and *F* (*F1* and *F2*) as was shown in Fig. 1.2 for long-term modelled variation, and Fig. 2.2 for measured hourly variation.

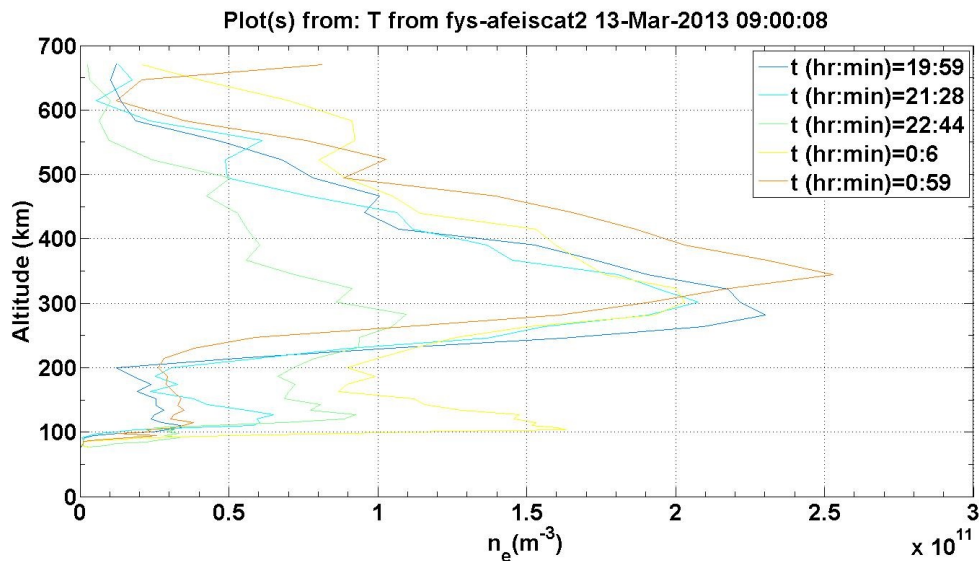


Figure 2.2: Some examples of electron number density profiles measured at different times by the EISCAT incoherent scatter radar 13 Mar 2013.

The distinct development of the ionospheric regions can be summarized as follows:

1. solar radiation of different wavelengths deliver energy to different altitudes depending on the absorption characteristics of the atmosphere at a given region, or particular altitude,
2. the physics of recombination depends on the atmospheric density, and
3. the changing composition of the atmosphere with altitude. Different governing physical and chemical processes cause the formation of the four distinct layers; *D*, *E*, *F1*, and *F2*.

The physics, rather than simple alphabetic height division, is the basis for labelling these regions and extending the same labels to ionospheric regions of other planets [Schunk and Nagy, 2000].

### 2.2.1 Regions of the Ionosphere

The *D*-region, the innermost region  $\sim 60$ -90 km above Earth's surface, coincides with the region where the most penetrating cosmic radiation produces free electron pairs sufficient to affect radio-wave propagation [Rishbeth *et al.*, 1996]. Ionization in this region is due to Lyman series alpha hydrogen radiation at 121.5 nm wavelength, ionizing nitric oxide (NO), producing an abundance of nitrogen oxide ( $\text{NO}^+$ ), oxygen ions ( $\text{O}_2^+$ ), and negative ions [Kelley, 2009]. Additionally, with high Solar activity hard X-rays ( $\leq 1$  nm) may ionize Nitrogen ( $\text{N}_2$ ), and Oxygen ( $\text{O}_2$ ). After sunset the *D*-region reduces significantly but on the night-side, cosmic rays produce residual levels of ionization. The peak density of the *D*-region is generally located at 90 km altitude.

With the high rate of recombination in the *D*-region, the net ionization effect is low, but loss of energy is great due to the frequent ( $10/\text{msec}$ ) collision rate of electrons. As these ions are much heavier than electrons, they have even lower gyrofrequencies and higher collision frequencies as a result they are considered to be unmagnetized. Essentially, neutral chemistry and dynamics governs the *D*-region as the electron density is actually too low for the *D*-region to be considered a plasma

[*Treumann and Baumjohann, 1997*]. These low electron densities result in a critical plasma frequency ( $f_p$  in Eqn 2.5) on the order of 300-900 kHz. Consequently, HF radio waves are not reflected by the *D*-region, but the waves suffer propagation loss due to absorption, particularly for frequencies below 10 MHz. The absorption is progressively smaller with higher frequency. With the process of ionization mainly dependent on the Sun, this effect is observed to be greatest around local midday, and least on the night-side.

Modelling the ionosphere becomes particularly important when considering the effect on HF communications. At these altitudes, the electron density results in a high collision rate between unbound electrons and neutral particles. The absorption of HF radio waves is dependent on both collision frequency and electron density, thus during disturbed conditions, the electron density of the *D*-region can be increased by high ionization sources, penetrating to these relatively low altitudes. Under such conditions, waves of these frequencies may be completely absorbed in the *D*-region and/or lower portion of the *E*-region [*Hunsucker and Hargreaves, 2003*].

A well known, and easily demonstrable example is the loss of reception of distant AM radio stations during the daytime. Another more rare example, known as Polar Cap Absorption (PCA), occurs during solar proton events, causing unusually high levels of ionization over high and polar latitudes. The effects of such events can last between 24–48 hours and decrease the radio communications link margin by many tens of decibels absorbing most, if not all, trans-polar radio communications. This is certainly important to many organizations, including the Canadian Forces (CF) as HF is the alternative to communications in maintaining Canadian sovereignty should satellite communications ever be compromised.

Above the *D*-region is the *E*-region; the *E*-region generally extends from 90 km to 150 km in altitude above Earth with peak densities during the day time at about 110 km [*Kelley, 1989*]. Ionization is due to soft X-ray and far UV solar radiation ionization of O<sub>2</sub>. At oblique incidence, generally frequencies below 10 MHz are reflected but with active events frequencies up to 50 MHz and higher may also be reflected by the *E*-layer [*El-Naggar, 2011*].



Above the  $E$ -region is the  $F$ -region, subdivided into  $F_1$  and  $F_2$  layers, from 150 km to 180 km and greater than 180 km, respectively. Peak density altitude can be found at 180 km for the  $F_1$  peak and 300 km for the  $F_2$  peak, but with a high degree of variation. At night the  $F$ -layer is the only layer of significant ionization present, with extremely low rates of ionization in the  $D$ , and  $E$ -regions. During the day all layers:  $D$ ,  $E$  and  $F$  have increased ionization rates but the  $F$ -layer develops a weaker layer known as the  $F_1$  layer. The  $F$ -layer is present on both the day and night-side ionosphere and is the layer principally responsible for the refraction of radio waves [Hunsucker and Hargreaves, 2003].

### 2.2.2 Why Study the Ionosphere?

The electron density varies with time (sunspot cycle, seasonally, and diurnally), with geographical location, and with certain solar-related ionospheric disturbances. The two primary sources which produces and sustains the ionizations level are solar X-ray and EUV radiation and by corpuscular radiation from the Sun. Although the Sun is the largest contributor toward the ionization, cosmic rays also make small contributions; moreover any atmospheric disturbance affects the distribution of the ionization. Because of its extreme sensitivity to changes in solar conditions, the ionosphere is a very sensitive monitor of atmospheric events. The electron density,  $n_e$ , is an important physical parameter in the ionosphere as these fluctuations cause undesirable effects on radio waves propagation as will be discussed in the following section.

## 2.3 Plasma Interaction with EM-Wave Propagation

EM-waves are time varying, coupled electric ( $\vec{E}$ ) and magnetic ( $\vec{B}$ ) fields that travel perpendicular to one another. Fig. 2.3 shows a periodic EM-wave travelling in the positive  $z$  or  $\vec{E} \times \vec{B}$  ( $\hat{k}$ ) direction. This is the same direction in which energy is propagating, which is called the Poynting vector.

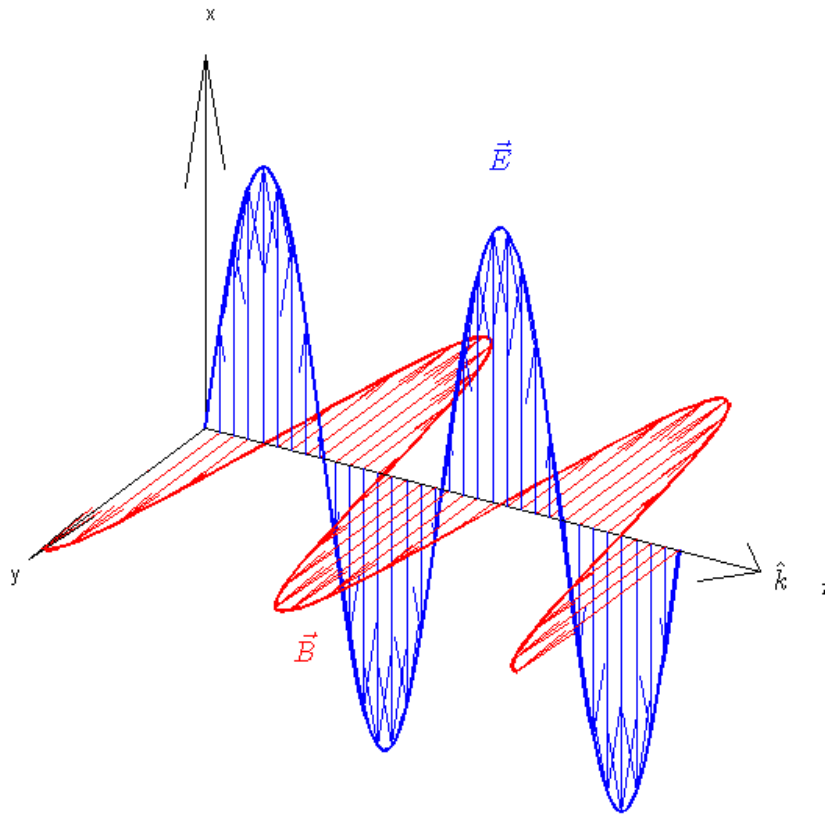


Figure 2.3: Periodic electromagnetic wave,  $\vec{E} = E\hat{x}$  is the electric field vector,  $\vec{B} = B\hat{y}$  is the magnetic field vector. The wave travels in the  $\vec{E} \times \vec{B}$  ( $\hat{k}$ ) direction.

### 2.3.1 Wave Polarization

One of the primary signal characteristics which defines the propagation of an EM-wave, and that can be measured is the polarization. The polarization state of a wave is given by the shape that  $\vec{E}$  forms as it propagates. The propagation is shown by convention in the  $\vec{E} \times \vec{B}$  direction with the external magnetic field (such as Earth's) in the  $x$ - $z$ -plane.

The general case is elliptical as shown in Fig 2.4. The shape can also be linear (ellipticity of  $0^\circ$ ) or circular (ellipticity of  $\pm 45^\circ$ ), however these are special cases of ellipticity. The shape of the polarization ellipse is given by the relationship of the ellipticity angle  $\chi$  to the semi-major and semi-minor axes,  $a$  and  $b$  respectively

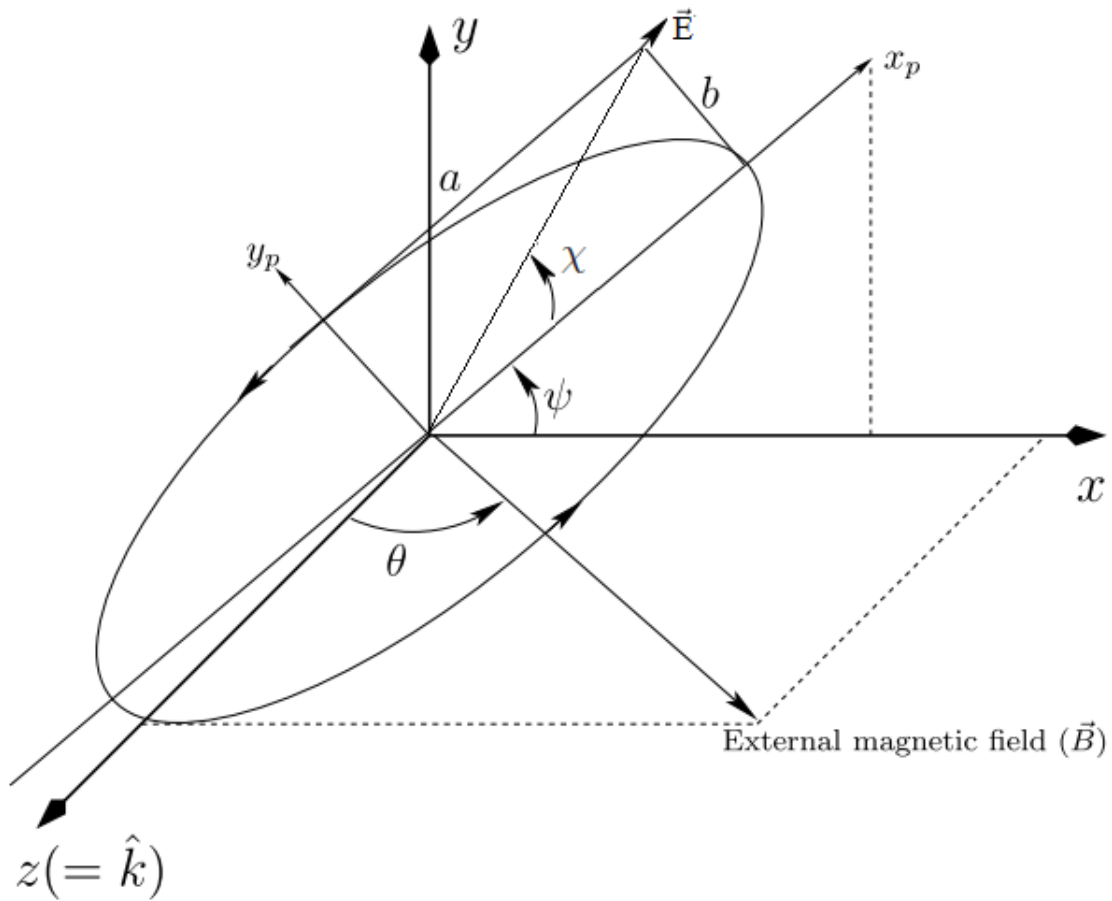


Figure 2.4: Typical elliptical polarization state of an EM-wave.  $\psi$  is the orientation angle,  $a$  is the semi-major axis,  $b$  is the semi-minor axis, and  $\theta$  is the aspect angle.

[Gillies, 2010]

[Canada Centre For Remote Sensing, 2007; Budden, 1961]:

$$\chi = \pm \arctan \frac{b}{a} \quad (2.1)$$

The polarization ellipse can be fully defined by  $\chi$  and the orientation angle  $\psi$ , defined as the angle between the  $x$ -axis and the semi-major axis.

### 2.3.2 Radio Waves in a Magnetized Plasma

An EM-wave propagating through a magnetised plasma decomposes into two propagation modes which have different indices of refraction and polarizations due to the external magnetic field. The two modes are called the ordinary and extraordinary

modes or O-mode and X-mode respectively. When collisions between neutral and charged particles are neglected, the refractive indices of the two modes are given by the Altar-Appleton-Hartree dispersion relation [*Hartree, 1929; Appleton and Builder, 1933; Gillmor, 1982*]:

$$n^2 = 1 - \frac{X}{1 - \frac{Y^2 \sin^2 \theta}{2(1-X)} \pm \sqrt{\frac{Y^4 \sin^4 \theta}{4(1-X)^2} + Y^2 \cos^2 \theta}} \quad (2.2)$$

where  $\theta$  is the aspect angle of the wave,  $X$  and  $Y$  are the ratios of the plasma frequency  $\omega_p$ , and gyrofrequency  $\omega_c$  to the radio wave frequency  $\omega$  respectively [*Schunk and Nagy, 2000*] namely,

$$X = \left(\frac{\omega_p}{\omega}\right)^2, \quad Y = \frac{\omega_c}{\omega} \quad (2.3)$$

The aspect angle is defined with respect to the external magnetic field. It is the angle formed between the wave propagation vector  $\vec{k}$  and the external magnetic field  $\vec{B}$ .

The plasma frequency, also called the critical frequency, describes the oscillation of the electron density for a cold neutral plasma. If thermal motion is neglected, and electrons are displaced with respect to the relatively heavy ions, the Coulomb force acts as a restoring force. This relationship is given by, among others [*Schunk and Nagy, 2000*].

$$\omega_p = \sqrt{\frac{n_e e^2}{m_e \epsilon_0}}. \quad (2.4)$$

By substituting for angular frequency ( $\omega = 2\pi f$ ) the plasma frequency can be written as:

$$f_p = \frac{e}{2\pi} \sqrt{\frac{n_e}{m_e \epsilon_0}} = 9\sqrt{n_e} \quad (2.5)$$

where  $n_e$  is the electron density per cubic metre and  $f_p$  is the limiting frequency in Hz at, or below which radio waves will be reflected by an ionospheric layer at vertical incidence.

This relationship assumes the following approximations [*Chen, 1984; Schunk and Nagy, 2000*]:

- the plasma is *quasi-neutral*; meaning the electron density is approximately equal to the ion density over large volumes of the plasma ( $n_e \sim n_i$ );
- the *cold plasma approximation*, which assumes the electron temperature to be zero ( $T_e=T_i=0$ ), and the dispersion relation for electron plasma waves ( $\omega^2=\omega_p^2$ ) which describes the plasma oscillations;
- ions can be considered as stationary when  $\omega \geq \omega_p$ ; a local disturbance in the plasma does not propagate to other regions of the plasma, but remains a local disturbance because the frequency is too high to affect the ions due to their inertia.

A typical approximation in SI-units is that the plasma frequency is nine times the square root of the electron density. Using a typical value for the ionospheric maximum electron density of  $10^{12}$  electrons per cubic metre gives a plasma frequency of 9 MHz. This computed value represents the lowest frequency that will propagate through the ionosphere without being reflected. Using the range of values of the maximum electron density from Table 1.1 gives the typical range of 2.85 – 12.73 MHz for the plasma frequency of the ionosphere. Since the electron density varies with altitude, the critical frequency also increases as the electron density increases allowing higher frequencies to penetrate further into the ionosphere before being reflected.

The gyrofrequency, or cyclotron frequency is the frequency of a charged particle of mass  $m$  (in kg), charge  $q$  (in C), moving with velocity  $v$  in a circular path (in  $\text{m}\cdot\text{s}^{-1}$ ) and gyroradius  $r$  (m) in a uniform magnetic field  $B$  (T), and can be obtained from:

$$\frac{mv^2}{r} = qBv. \quad \Rightarrow v = \frac{qBr}{m} \quad (2.6)$$

The cyclotron frequency is defined as:

$$f_c = \frac{v}{2\pi r} = \frac{1}{2\pi} \frac{qB}{m}. \quad (2.7)$$

A typical value for the gyrofrequency in the ionosphere can be found using Eqn. 2.6. Note that while the plasma frequency is proportional to the electron density, the gyrofrequency is proportional to the magnetic field. Using a value of 0.5 Gauss

( $5 \times 10^{-5}$  T) for the magnetic field gives a gyrofrequency of  $8.8 \times 10^6$  rad/s which is equivalent to 1.4 MHz.

Examining the cases when propagation of the wave is parallel or anti-parallel to the external magnetic field (i.e. the aspect angle  $\theta = 0^\circ$  or  $\theta = 180^\circ$  or is *field aligned*) the index of refraction for each mode is given by [Chen, 1984],

$$n^2 = \frac{c^2}{v_{\phi(O)}^2} = 1 - \frac{\omega_p^2/\omega^2}{1 + \omega_c/\omega} \quad (\text{O - mode}) \quad (2.8)$$

$$n^2 = \frac{c^2}{v_{\phi(X)}^2} = 1 - \frac{\omega_p^2/\omega^2}{1 - \omega_c/\omega} \quad (\text{X - mode}) \quad (2.9)$$

where  $c = 3 \times 10^8$  m/s is the speed of light in a vacuum. This indicates the X-mode is affected more by the plasma and will always have a smaller refractive index than the O-mode [Chen, 1984; Gillies, 2010].

The Earth's magnetic field in the ionosphere does not vary a great deal over a short time period, therefore the variable of interest in Eqn. 2.3 is  $X$  due to variability of the electron density of the plasma. As the electron density and the ratio of  $X$  increases, the refractive index for the two modes decreases and separation between the two modes of propagation increases (see Fig. 2.5). When the wave frequency is equal to the plasma frequency and since  $\omega_p \gg \omega_c$  the O-mode refractive index goes to zero and the wave is reflected. This is the basis on which ionosondes operate.

In the standard treatment of magneto-ionic theory, the effect of collisions is taken into account by assuming that an electron experiences a retarding force proportional to its velocity [Budden, 1965]. Eqn. 2.2 was derived using the effective collision frequency in the frictional term of the equations of motion for electrons as a constant, independent of energy [Setty, 1972]. Pure electron modes, also known as cold plasma modes, like the upper hybrid frequency, are modes in which the frequency is sufficiently high that the motion of ions may be neglected [Stix, 1992]. Other research by Molmud [1959]; Sen and Wyller [1960]; Budden [1965] have included the collision term in the derivation of Eqn. 2.2, however the effect of collisions in the  $F$ -region are quite low in comparison to the  $D$ - and  $E$ - regions and therefore are not a significant source for modification of  $F$ -region electron densities. Budden [1965] concludes that

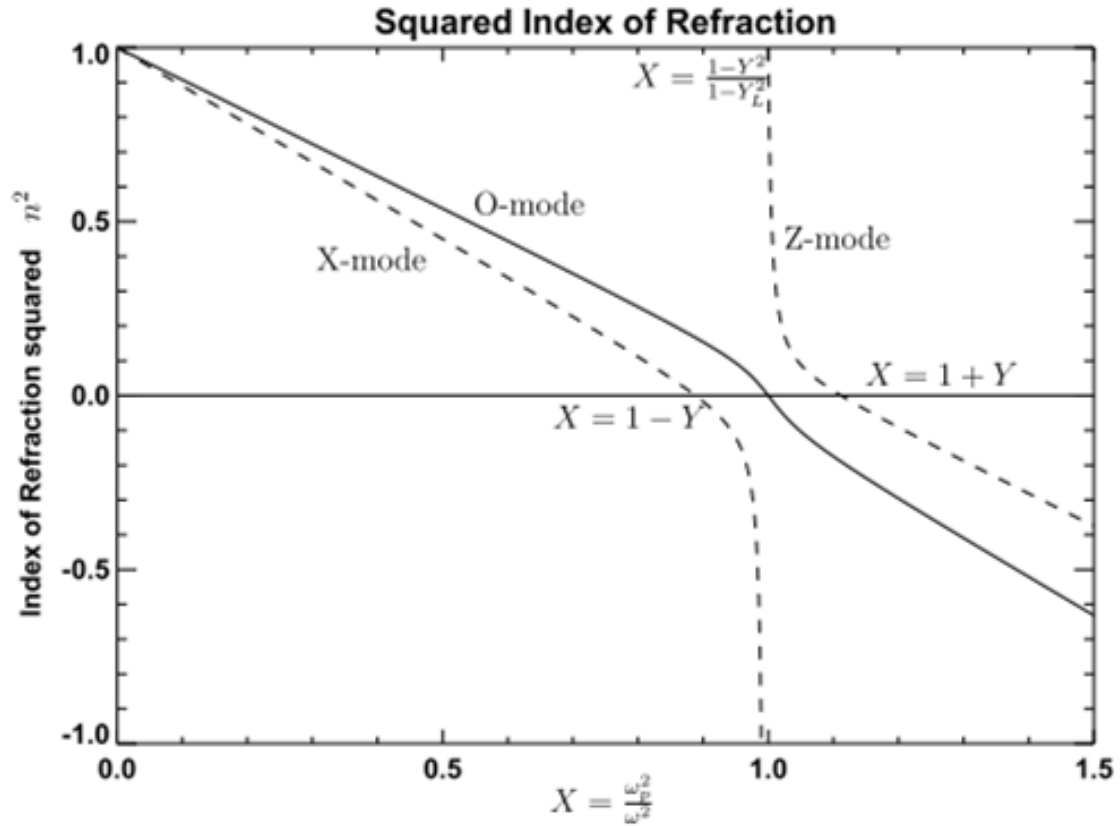


Figure 2.5: Squared refractive index values for the O-mode (solid curve) and the X-mode (dashed curve) as a function of  $X$  for constant aspect angle ( $40^\circ$ ), external magnetic field ( $6.0 \times 10^{-5} \text{T}$ ), and frequency (15 MHz) EM-wave. Adapted from [Gillies, 2010].

the standard Appleton-Hartree formula can be used without modification for nearly all radio propagation problems in the ionosphere, provided that the correct effective value of the collision frequency is used and that the modified formula may only be important for wave interaction theory and waves of very low frequency whose wave normals are perpendicular to the Earth's magnetic field.

The polarization of a propagating wave is found using the wave polarization ratio  $p$  [Budden, 1961]. The polarization ratio for the two modes of propagation, given a set of propagation conditions, is calculated using the following equation [Budden, 1961; Gillies, 2010]:

$$p = \frac{E_y}{E_x} = i \frac{(Y \sin \theta)^2}{2Y \cos \theta (1 - X)} \pm i \sqrt{\frac{(Y \sin \theta)^4}{4(Y \cos \theta)^2 (1 - X)^2} + 1}. \quad (2.10)$$

where  $E_x$  and  $E_y$  are the  $x$ - and  $y$ -components of the electric vector of the wave. The direction of rotation and the shape of the ellipse is determined by the sign and magnitude of  $p$  respectively.

In the absence of collisions, the semi-major axis of the O-mode wave is oriented parallel to the  $x$ -axis and parallel to the magnetic field in the plane of polarization. The semi-major axis of the X-mode wave is oriented parallel to the  $y$ -axis or perpendicular to the external magnetic field in the plane of polarization.

An absolute value greater than unity of  $p$  occurs when the magnitude of  $E_x$  is less than  $E_y$  and corresponds to the X-mode of propagation. Conversely, a value of  $p$  less than unity corresponds to O-mode propagation, when  $E_x$  is greater than  $E_y$ . The resulting polarization of a propagating wave will be the superposition of that of the two modes.

The polarization of a wave is dependent on the propagation direction relative to the external magnetic field. A wave which propagates mostly parallel or anti-parallel which corresponds to an aspect angle of either  $0^\circ$  or  $180^\circ$  to the external magnetic field lines, and  $p = \pm i$  is called quasi-longitudinal (QL) propagation and the polarization ellipse of the two modes are circular with opposite sense of rotation. Conversely, if the wave propagation is mostly perpendicular to the external magnetic field is called quasi-transverse (QT) propagation. If the magnitude of the two circular waves are equal, the resulting superposition of the EM-wave is linear [Budden, 1961; Gillies, 2010].

The refractive index for the two modes is determined by the positive (O-mode) and negative (X-mode) sign of the denominator in Eqn. 2.2 (see Eqns. 2.8 and 2.9). Because the refractive index is different for the two wave components, the phase difference between the two modes will increase along the propagation path.

The resulting imbalance between the phase velocities ( $v_\phi$ ) produces a change in the major axis of the polarization ellipse of the radio wave, which is formed by the sum of the two components. The orientation angle of the polarization ellipse [Budden, 1961; Canada Centre For Remote Sensing, 2007] will rotate by half the phase difference between the components, which is known as FR. Without a magnetic field, there is



only be one refractive index, there is no separation between the modes, and FR does not occur *Chen* [1984].

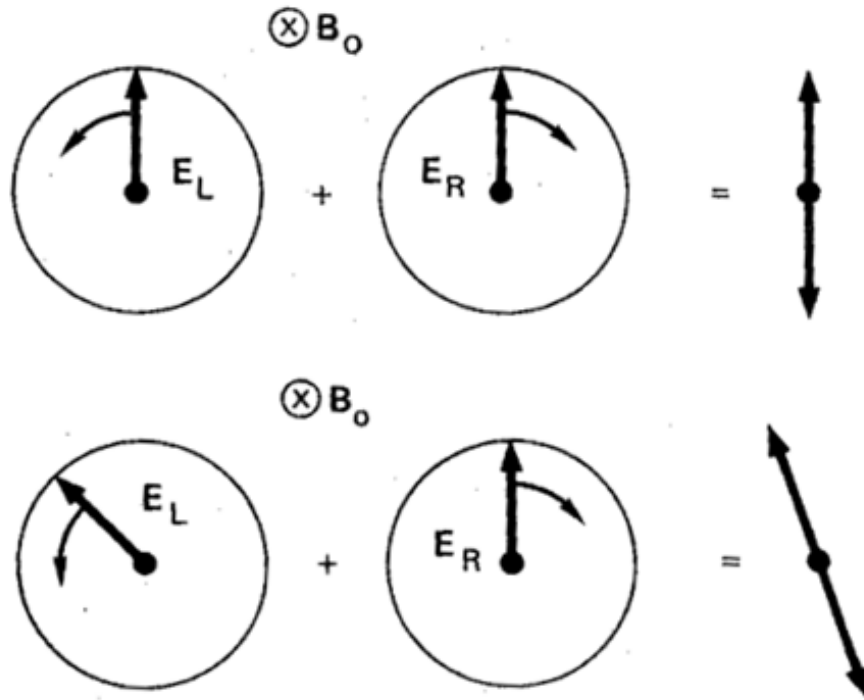


Figure 2.6: Top: a linear EM-wave as the superposition of the left-hand circular polarized (LHCP) and right-hand circular polarized (RHCP) waves. Bottom: after traversing some distance in the plasma the RHCP has returned to its initial orientation after  $N$ -cycles, but the LHCP wave has relatively advanced in phase and the plane of polarization is seen to rotate. Adapted from *Chen* [2006].

### 2.3.3 Faraday Rotation (FR)

A plane polarized wave propagating through a plasma, parallel to a magnetic field, suffers a gradual rotation of its plane of polarization due to the presence of the geomagnetic field and the anisotropy of the plasma medium. FR is principally due to a plane polarized wave being the sum or superposition of two equal-amplitude circularly polarized waves at the same frequency, opposite handedness, and different phase.

When a linearly polarized wave reaches the ionosphere, it is split into two independent components, or modes of propagation that take different paths/branches

through the plasma [Stix, 1992]. These are two elliptically (or potentially circularly) polarized waves with electric vectors  $\vec{E}$  that are in-phase at the vertical (if vertical linear transmitted polarization) position, but rotating in opposite directions.

After a certain number of cycles the E vectors of the two modes will return to the initial position, however at distance  $d$  the X- and O-modes have undergone a different number of cycles, since they require different time to cover the same distance provided  $n_e$  varies on length scales which are large compared to the wavelength of the radiation.

Two conditions are required for FR to occur. The wave must propagate in the QL regime and the relative amplitude or power of the two propagation modes must be mostly equal. The situation is further complicated when the relative amplitude or power of the two modes of propagation is not equal, as is often the case.

The ionosphere is assumed to be a birefringent medium due to the Earth's terrestrial magnetic field [Hartmann and Leitinger, 1984; Orfanidis, 2008]. Any EM-wave propagating through a magnetised plasma decomposes into two propagation modes which have different indices of refraction and polarizations due to the magnetic field. Two modes of propagation, called the ordinary and extraordinary modes or O-mode and X-mode respectively, exist in the ionosphere [Chen, 1984].

Since a plasma, and particularly the ionosphere, is a circular birefringent medium the two modes take a different time to propagate through the same medium due to the different phase velocities. The effect of the relative phase shift between the R- and L-waves induced by the Faraday effect is to rotate the orientation of the wave's linear polarization shown in Fig. 2.6.

The magnitude of the rotation is proportional to the integrated product of the electron density,  $n_e(l)$ , along the ray path or plasma column and the strength of the parallel component of the magnetic field  $B_{||}(z)$ . It is inversely proportional to the square of the frequency as follows, [Budden, 1961; Kraus, 1966; Gurnett and Bhattacharjee, 2005]

$$\Omega = \frac{e^3}{8\pi^2\epsilon_0 m_e^2 c f^2} \int n_e(z) B_{||}(z) dz \quad (2.11)$$

where the FR,  $\Omega$  is measured in radians and  $m_e = 9.109 \times 10^{-31}$  kg is the mass of an electron. The magnetic field  $b_{||}$  is in tesla. In the absence of a magnetic field,

$\omega_c = 0$ , therefore  $Y = 0$  and there is only one refractive index. As a result, there is no separation of the modes and there is no difference in the rate of change in the orientation angle and hence FR does not take place *Chen* [1984].

Independent of frequency, this relationship can be expressed as Eqn 2.12 and 2.13.

$$\Omega = \lambda^2 RM; \quad (2.12)$$

$$RM = 2.63 \times 10^{-6} B_{avg} TEC. \quad (2.13)$$

where RM is the rotation measure,  $\lambda$  is the wavelength of the EM-wave and  $B_{avg}$  is the average  $z$ -component of the magnetic field in tesla. For higher frequencies the O-mode propagates faster than the X-mode.

Although the integral is evaluated over the total path length from transmitter to receiver, only the frequency dependent refractive index contributes to the result [*Max van de Kamp*, 2012]. This is an integral, where separate functions combine, which can be separated into their components  $n_e(l)$  and  $b_z(l)$  for tomography by transforming the space into one where the integral becomes a multiplication.

Using the ADS-B and AIS wavelengths ( $\lambda = 1.85085$  m for 161.975 MHz AIS) in Eqn. 2.11, the FR can be written for AIS as,

$$\begin{aligned} \Omega_{AIS} &= 9.007 \times 10^{-13} \int n_e(z) b_{\parallel}(z) dz. \\ &= 9.007 \times 10^{-13} B_{avg} TEC. \end{aligned} \quad (2.14)$$

and for ADS-B as

$$\begin{aligned} \Omega_{ADS-B} &= 1.989 \times 10^{-14} \int_0^l n_e b_z dl. \\ &= 1.989 \times 10^{-14} B_{avg} TEC. \end{aligned} \quad (2.15)$$

where  $n_e$  is in  $\text{m}^{-3}$  with 1 TECu equivalent to  $10^{16}$  electrons  $\text{m}^{-2}$ . In Eqn. 2.15 the vertical component  $b_{\parallel}$ , is assumed to be a constant value  $B_{avg}$  [*Wright et al.*, 2003; *Sheriff and Hu*, 2003; *Ippolito*, 2008; *Jehle et al.*, 2009]. The average magnetic field  $B_{avg}$  is obtained from the IGRF model [*International association of geomagnetism and aeronomy, Working Group V-MOD*, 2010] for the simulations. The TEC values are computed using Eqn. 2.15 for the simulated FR. The TEC values and ray endpoints

are used as the input to CIT in order to reconstruct the resulting electron density maps.

For VHF the signal may rotate over  $180^\circ$  resulting in a  $n\pi$  ambiguity in the RM. For UHF frequencies such as that used for ADS-B the rotation will be much less; on the order of 8-25 degrees for propagation from ground to a LEO satellite at 1000 km.

The integral of the electron density over the path in Eqn. 2.15, for an average magnetic field  $B_{avg}$ , is the number of free electrons in a plasma column of unit cross-section area from the transmitting aircraft to the satellite receiver, or TEC, given by Eqn. 1.1. The TEC is the density over the entire plasma column or ray-path from source to observer, which smooths out the structures.

## Chapter 3

# Application

### 3.1 Overview

In this chapter, we briefly introduce the functionality and operational principle of three types of beacon signals. The primary signal of interest for this research is ADS-B. Canadian implementation of ADS-B, including contributions from research at the RMC are discussed along with the exact benefits of space-based ADS-B and how this system can also be used to obtain scientific data. Two other systems; APRS and AIS are also briefly introduced. The ray trace model used to simulate the data is described.

This chapter outlines the experimental procedures that are used for CT as well as CIT image reconstruction. A brief literature review of CT is included from its origins in medical physics, consideration of the ionosphere, EM-wave interactions, the specific CT algorithm used and its extension to GPS CIT, and finally the method used CIT using ADS-B and AIS signals. This chapter describes how IED maps are produced using FR from the modelled ray-trace output.

### 3.2 Signals of Opportunity

#### 3.2.1 Automatic Dependent Surveillance Broadcast (ADS-B)

ADS-B is a technology developed to track the position and movement of aircraft through intermittent broadcasts of their identity, itinerary and position state vectors to ground based receivers and other aircraft within range. The system is intended to augment radar as the standard for air traffic control by providing an enhanced ranging and separation distinction capability with a reduced footprint for ground support infrastructure [*Marsh, 2006; Brown and Hendricks, 2011; ADS-B-Technologies, 2011; Cushley and Noël, 2014*]

While current radar networks provide aircraft positional information to air traffic control (ATC) centres, the use of ADS-B imparts the added capability of providing that information, in real time, to aircraft in their operational area as well as to ground controllers. With this information, aircraft crews are able to actively monitor their immediate airspace and quickly react to emerging situations. The ADS-B communications link also provides for additional potential future capability, such as weather and flight information updates. The ADS-B system utilizes three distinct components to achieve its purpose [*Tremblay et al.*, 2009; *Francis et al.*, 2011; *Castillo et al.*, 2012]:

1. A high integrity GPS installed on ADS-B equipped aircraft to accurately determine their position. GPS is a mature and reliable technology capable of providing real-time positional information for users with sufficient accuracy for use in air traffic control functions;
2. An ADS-B data link to communicate with the overall network. There are three types of ADS-B transmissions; 1090 MHz Extended Squitter (ES) for large commercial aircraft, the 978 MHz Universal Access Transceivers (UAT) for general aviation, and the VHF Data Link (VDL) Mode 4 that operates between 108 and 137 MHz in Europe. While the technology allows for two-way communications, the option exists for users to operate on a lower level and simply provide position information for airspace controllers providing a baseline capability similar to radar; and
3. A receiver network to provide a communications link between ground operators and aircraft. This network serves as the backbone of the ADS-B system and distributes operational flight data to aircraft operators and ground-based controllers.

ADS-B is an automatically operating, passive system whereby accuracy is limited only by that of the aircraft navigational system to which it is linked. It can therefore significantly surpass the accuracy of radar. Update rates are higher, terrain masking problems are avoided and coverage is maintained below radar cut-off heights in mountainous terrain [*Marsh*, 2006].

Required transmitter power for the ADS-B signal varies as a function of aircraft category. For smaller aircraft, a minimum transmission power of 75 W is specified, while larger aircraft require a minimum power of 125 W or 200 W with a maximum

output power for all classes of 500 W. Any aircraft that is capable of operating at altitudes greater than 15,000 ft (4570 m) above sea level (ASL), or with cruising speeds above 175 kts (324 km/h), are required to transmit at a minimum of 125 W. Aircraft transmit vertically polarized signals using two quarter-wave monopole antennas mounted to the top and bottom of the aircraft, shown in Fig. 3.1 [NavCanada, 2008; Francis et al., 2011].



Figure 3.1: Main; shows Ikhana, NASA's unmanned ADS-B equipped aircraft test flight with the placement of two ADS-B antennas indicated by black arrows. Inset; shows the most widely adopted aircraft ADS-B antenna [Turner, 2012].

### 3.2.1.1 Why use ADS-B for ATC?

Modern methods of air traffic management have traditionally relied on radar systems for positional information of aircraft. Typical civilian radar surveillance cannot track aircraft over the horizon, causing traffic over large unpopulated expanses such as ocean or the polar regions to take indirect, inefficient, and imprecise routes to ensure adequate safe separation of aircraft. Continuous surveillance in this airspace would increase safety and security of air traffic, in addition to permitting aircraft to follow more direct routes, saving time, fuel and consequently, reducing engine emissions.

An alternative method of acquiring aircraft position data is by ADS-B. As opposed to bouncing radio waves from a fixed terrestrial antenna off airborne targets

and interpreting the data received, ADS-B capable aircraft use a conventional GNSS receiver such as GPS, or Galileo to derive its navigational information and broadcast it along with other aircraft discretely such as speed, heading, altitude, flight number, ascent/descent rate, etc.

Unlike radar, ADS-B has the advantage of low cost remote installations as they are much less complex and have much lower power requirements [*Francis et al.*, 2011]. This consequently reduces systems and maintenance costs, environmental impact, as well as allowing for their deployment in remote areas where a radar installation is impossible. Even in regions where long-range radar is a possibility, the accuracy of ADS-B does not critically degrade with range, atmospheric conditions, or target altitude and update intervals do not depend on the rotational speed and reliability of mechanical antennas [*ADS-B-Technologies*, 2011]. ADS-B can yield a much better dataset within these long-range regions than radar. ADS-B is lower cost than conventional radar and permits higher quality surveillance of airborne and surface movements [*AirNav-Systems*, 2008]. This in turn allows airspace controllers to utilize reduced intra-aircraft spacing, enabling operators to reduce fuel consumption through the use of more direct flight plans.

ADS-B networks that monitor air traffic have already been deployed around the world in high volume air-traffic areas, however ground stations cannot be installed mid-ocean and are difficult to maintain in the Arctic, leaving coverage gaps for oceanic and high latitude airspace (see Fig. 3.2). The lack of coverage over oceanic and high latitude airspace has hampered further development. *Francis et al.* [2011] have suggested that ADS-B receivers could be deployed on a constellation of satellites to allow for worldwide tracking of aircraft, alleviating this problem.

There are far too many other benefits to the use of ADS-B to discuss within the scope of this brief literature review, however to list a few: flight safety, economic, environmental, efficiency, and automation of some aspects of ATC. For example, discrepancies between radar and ADS-B datasets may be used to automatically alert ATC for priority assistance with procedural flight path, and verification of instrumentation functionality. To briefly summarize the reason ADS-B should be used



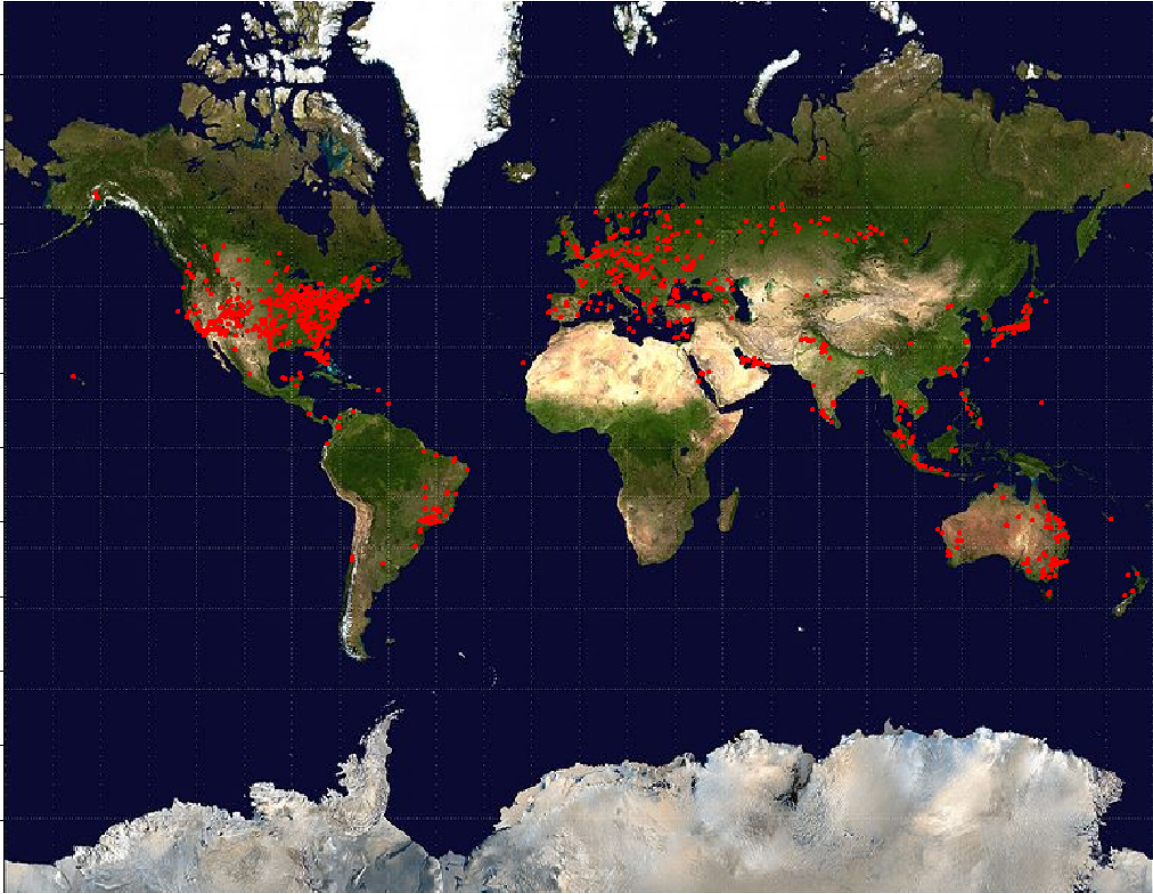


Figure 3.2: The positions of aircraft plotted from data provided by crowd-sourced ADS-B receivers, courtesy of Fredrik Lindahl, Flightradar24. The data represents 1040 unique aircraft signals received for one second as an indication of the amount of data available. Note that the data received by ground based receivers do not have polar or oceanic coverage.

globally:

“If only three percent of flights were equipped with ADS-B and were able to alter their speed and altitude in a manner to increase efficiency, 2.7 million litres of fuel, and emittance of approximately 7200 tons of greenhouse gases would be saved annually.”

-Rudy Kellar, NAV CANADA Vice president of operations [*NavCanada*, 2010].

### 3.2.1.2 Canadian Implementation

Navigation Canada (Nav Canada) is one organization that has pioneered the integration of ADS-B to enhance aircraft separation and flight safety in remote areas of Canada's North. The majority of these flights link Europe and North America, while many others transit to Asia, including those using polar routes [NavCanada, 2011].



Figure 3.3: Nav Canada Radar (green) and ADS-B (yellow). Coverage reproduced from Nav Canada website: [NavCanada, 2011].

Implementation of ADS-B surveillance in Canadian airspace, notably over the Hudson Bay area since January 2009, uses the 1090 MHz ES [ADS-B-Technologies, 2011; NavCanada, 2011]. The 1090 MHz ES transmissions were selected for worldwide interoperability given lineage to Mode Select (Mode-S) transponders carried on all commercial airlines and on many business and charter aircraft. These aircraft and any other aircraft that fly in (Class A) high altitude airspace are required to install a 1090 MHz ES transmitter as a minimum.

The 1090 MHz ES ADS-B message is a 120 bit transmission that contains the aircraft identification, position, velocity and status. The message is broadcast on

a period which ranges randomly between 0.4 and 0.6 seconds. This randomization function is designed to prevent aircraft from having synchronized transmissions on the same frequency, and thus interfering with each other's transmissions. Other studies by *Van Der Prys* [2014]; *Van Der Prys and Vincent* [2015a,b, 2016] have investigated the effects of ADS-B signal collision, bit-swapping, and other undesirable effects.

ADS-B is also being adopted by air traffic service organizations in other countries. A collaboration with the European community and United States of America (USA) was announced 10 January 2011 with the initiation of an international program called "ENGAGE" to reduce the amount of fuel and greenhouse gases released in the oceanic space of the North Atlantic. Seven new generation ADS-B installations in Northern Canada provide coverage improving the capacity, efficiency, and security of air traffic during polar and international flights. With 350 000 flights over the North Atlantic airspace each year, it is the busiest in the world [*Tremblay et al.*, 2009; *NavCanada*, 2010].

### 3.2.1.3 Satellite Augmentation of ADS-B/ Current platforms carrying ADS-B

A potential solution for worldwide tracking of aircraft is to monitor aircraft transmitted ADS-B signals using satellite-borne receivers. Such a system would be particularly useful for monitoring aircraft over oceanic regions but also could be used over land, for example in Canada's high Arctic, where large areas are without air traffic surveillance [*Francis et al.*, 2011].

To investigate this possibility, a high altitude balloon experiment was carried out in June 2009 to determine if ADS-B signals could be detected from near space. The Flying Laboratory for the Observation of ADS-B Transmissions (FLOAT) was the first stratospheric platform to collect ADS-B data [*Francis et al.*, 2011]. The FLOAT mission successfully demonstrated the reception of ADS-B signals from near space, paving the way to the development of a space-based ADS-B system.

Since the FLOAT mission, a significant amount of interest has been received from government agencies as well as the private sector. The FLOAT balloon mission was a success and subsequently led to RMC's entry into the Canadian Satellite Design

Challenge (CSDC) [Rubio, 2010], the Space ADSB Receiver Experiment (SABRE) [Castillo et al., 2012]. Regretfully the SABRE satellite never flew, however another high altitude balloon mission tested the satellite payload and as a result of these efforts, the payload was integrated onto the CanX-7 satellite in conjunction with COM DEV, University of Toronto Institute for Aerospace Studies (UTIAS) and Defence Research and Development Canada (DRDC) [University of Toronto Institute for Aerospace Studies Space Flight Laboratory, 2014].

CanX-7 was a nano-satellite equipped with an ADS-B receiver launched into a 690 km sun synchronous orbit on 26 September 2016 to validate this idea. CanX-7 was a demonstration mission that demonstrated a lightweight, deployable drag sail to achieve the de-orbit requirements of the Inter-Agency Space Debris Coordination Committee [Inter-Agency Space Debris Coordination Committee, 2007; National Aeronautics and Space Administration, 2012]. While the primary mission of CanX-7 was to demonstrate de-orbiting technology, it was also used to evaluate an ADS-B receiver in space [Shmuel et al., 2012; University of Toronto Institute for Aerospace Studies Space Flight Laboratory, 2014; Bennett and Zee, 2016; Freitag, 2017; Vincent and Van Der Pryn, 2017]. Prior to deploying its four drag-sails, CanX-7 was among the first satellites in the world to evaluate the use of an ADS-B receiver in space [Shmuel et al., 2012; University of Toronto Institute for Aerospace Studies Space Flight Laboratory, 2014]. CanX-7 received ADS-B signals from various aircraft distributions and geometries with slant ranges in excess of 2000 km and up to 3300 km at look angles (off-nadir) of  $\sim 64^\circ$  [Kelly Freitag - personal communication, Vincent and Van Der Pryn [2017]].

Regretfully, useful data for ionospheric sounding was not available since the purpose of the demonstration satellite was to receive ADS-B and the antenna configuration and sampling were not amenable to ionospheric measurement. This research communicates the requirements for future operational ADS-B satellites as well as other satellite systems that use linearly polarized radio signals, which could be considered for the secondary scientific purpose of ionospheric sounding in addition to their intended purpose. These include an appropriate antenna configuration, capabil-

ity of measuring the complete waveform, and accurate satellite attitude determination and control.

There are other organizations that are interested in space-based air traffic monitoring using ADS-B including the European Space Agency Proba-V mission [*Francois et al.*, 2014] and GomSpace GomX-1 [*Alminde et al.*, 2012]. The Proba-V missions are a series of space-flight opportunities for new technologies from European companies (especially small and medium enterprises) to help boost Europe’s competitiveness in global markets [*European Space Agency*, 2013b]. One technology of interest for Proba-V has been an ADS-B receiver contributed by the (Deutsches Zentrum für Luft- und Raumfahrt e.V. abbreviated DLR) German Aerospace Center. DLR is working with industrial partner Société Européenne des Satellites Astra on a constellation of satellites for global coverage – one of a number of such initiatives in the planning stages around the world [*European Space Agency*, 2013a]. GomX-1 is a collaboration between Gomspace, DSE Airport Solutions, Aalborg University and funding from the Danish National Advanced Technology Foundation to launch GomX-1; a 2U nanosatellite mission with a software defined radio emphasis on receiving ADS-B signals [*GomSpace*, 2013; *Alminde et al.*, 2014].

ADS-B (and AIS) receivers have also been integrated as hosted secondary payloads on the Iridium Next constellation, Iridium’s second generation 66 satellite LEO constellation [*Aireon*, 2015; *de Selding*, 2015]. The Iridium satellite constellation has provided global L-band voice and data coverage to satellite phones, pagers and integrated transceivers since 2002. Iridium has recently replaced its existing constellation by sending 75 Iridium NEXT satellites into space over 8 different launches from 2017–2019. Although the primary mission of the Iridium NEXT satellites is to provide global satellite telecommunications, these new generation satellites also carry other payloads such as ADS-B and AIS receivers which provide additional capabilities while utilizing the benefit of integrated commercial satellite communications downlink. The contract awarded to Harris Corporation by Aireon LLC (a joint venture between Iridium and Nav Canada) represents the largest implementation of a commercially hosted payload solution to date. The first-ever global aircraft tracking

capability will play a key role in the modernization of global air traffic management infrastructure [*Harris Corporation*, 2012, 2014].

### 3.2.2 Automatic Identification System (AIS)

Ship detection has been made possible by a combination of remote sensing data and data from other sources such as AIS [*Greidanus*, 2005]. AIS is a marine vessel tracking technology used to monitor and control marine traffic, particularly in high traffic areas such as ports and harbours.

exactEarth is a Canadian company that has pioneered global maritime vessel data monitoring using spaceborne AIS receivers for ship tracking and maritime situational awareness. Since its establishment in 2009, exactEarth has provided a powerful maritime surveillance tool called Satellite-AIS (S-AIS), which has provided regional and global maritime pictures of the world's oceans, unrestricted by the terrestrial limitations encountered using ground based techniques. exactEarth's infrastructure is composed of an operational data processing supply chain involving a constellation of satellites, receiving ground stations, patented decoding algorithms and advanced "big data" processing and distribution facilities. This system provides the most comprehensive picture of the location of AIS equipped maritime vessels throughout the world and allows exactEarth to deliver data and information services characterized by high performance, reliability, security and simplicity to large international markets [*exactEarth*, 2015].

This is achieved in a similar manner to the method that was discussed previously with respect to the implementation of space-based ADS-B. The SMAD architecture was the inspiration for the deployment of space-borne ADS-B transceivers to monitor air traffic in a similar manner. Ships transmit beacons that include state vectors derived from on-board GPS receivers and other instrumentation. These signals are received by a satellite constellation and relayed to a ground network in near real-time. The AIS constellation can provides updated information on identified vessels, including their respective locations and a wide range of other relevant maritime geospatial information at least once per hour.

exactEarth utilizes a network of high data rate ground stations to enable rapid distribution of the data to global customers. To briefly summarize the benefits of AIS, equipping larger vessels has led to improved capabilities in maritime traffic picture monitoring, control and consequently maritime safety and security, particularly in high traffic regions such as ports. By equipping smaller vessels with inexpensive AIS transceivers, including fishing fleets, AIS can be used as an important tool for fisheries management and to combat piracy. The AIS satellites orbit the equator every 97 minutes, making the constellation of polar orbiting satellites capable of providing adequate coverage, particularly for busy tropical shipping regions of the world with high density maritime traffic [*exactEarth*, 2015].

In 2015, exactEarth announced the successful launch of its ninth AIS satellite, exactView-9 (EV9) to expand and compliment the constellation currently being used for global vessel monitoring. EV9 employs a next generation AIS payload that supports exactEarth’s patented ground-based AIS spectrum processing technology in order to deliver superior detection performance. EV9 is also capable of providing high performance detection of low power class B AIS transceivers, for the small vessel market [*exactEarth*, 2015].

These additional transmitters and ray paths will improve the spatial sampling suitability for the CT methods that will be described in Section 3.4.

AIS is another hosted payload on 58 of the Iridium Next constellation in order to provide unprecedented real-time global marine vessel tracking. This new AIS system has inter-satellite cross-links for continuous communication with the existing ground stations to provide an average global revisit time of less than one minute [*exactEarth*, 2016]. This may also offer the opportunity to study conjunctions between AIS and ADS-B datasets.

### 3.2.3 Automatic Packet Reporting System (APRS)

Finally, other signals of opportunity were considered for example APRS [*Cushley and Noël*, 2015]. APRS is a linearly polarized beacon signal that could also be considered in addition to ADS-B and AIS, but it was not explored in any great detail in this

thesis other than to examine the FR due to APRS to compared it with AIS and ADS-B.

APRS is a radio-based digital communication protocol developed and utilized by the amateur radio community to report and track the position and status of APRS-equipped stations. There are both ground and space-borne digital repeaters, including Psat (launched 20 May 2015) and on the International Space Station (ISS).

APRS was developed by *Bruninga (WB4APR)* [1992], a hand amateur (HAM) radio operator and instructor at the United States Naval Academy in Annapolis, to report and track the position and status of APRS-equipped stations. Initial testing was performed to track the midshipmen travelling from Annapolis to Philadelphia ( $\simeq$  150 km) for the Army/Navy football game. A football helmet was packed with a GPS receiver, a radio modem and transmitter operating on the VHF HAM band. This experiment was performed during a time before cell phones were popular and when GPS receivers were a novelty for civilians and still relatively expensive. The true innovation was to plot the automatic position reports on a computer map display to graphically track the station [Mills, 2010]. Figure 3.4 shows an example for the station VA3CUS (red dots) travelling round-trip from Kingston, ON to Fredericton, NB in December 2014. A subset of the permanent stations (e.g. weather, CW, hospitals, airports) that received signals directly from VA3CUS are also shown. Other mobile stations are not shown for image clarity. For a complete legend of the symbols shown in Fig. 3.4, please refer to *www.aprs.fi*.

Modern APRS stations involve the same components used for the initial testing: a GNSS receiver such as GPS, a radio modem or terminal node controller (TNC) and a VHF transmitter. Many transceivers (transmitter/receiver) have an integrated TNC and/or GPS receiver and come in various sizes for different applications. Hand-held HAM radios are similar in appearance and size to commercially available UHF walkie-talkies and are portable, but have lower transmit power and consequently range. Mobile transceivers are designed for use in vehicles (primarily ground based although APRS has been used on aircraft, boats, high altitude balloons, satellites and the ISS) and have a wider range in available transmit power and range. Base station



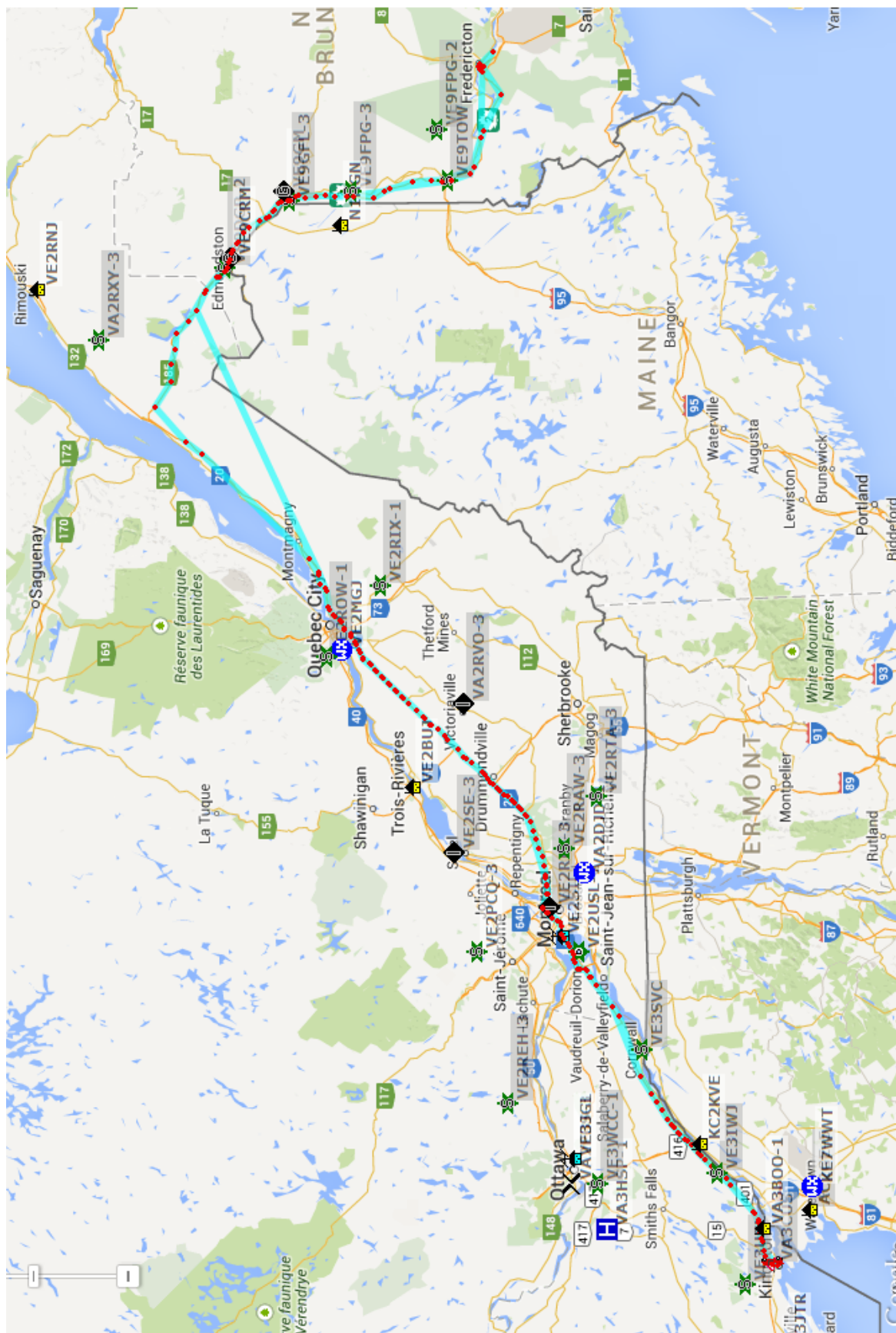


Figure 3.4: APRS-IS tracking the author VA3CUS (red dots) December 2014. Only a subset of other permanent stations that received signals directly from VA3CUS are shown along with VA3CUS. Mobile stations are not shown. For a complete legend, please refer to [www.aprs.fi](http://www.aprs.fi).

transceivers have much higher transmit power and range. Although their position generally does not change, the automatically generated packets can include other information such as weather reports. Most transceivers can be used to repeat the received APRS signals to extend the range of the initial transmission. Some stations function as internet gates; APRS data is ingested into a centralized server called the APRS Internet System (APRS-IS) for immediate public access. The development of APRS and the APRS-IS network itself utilizes the hard work of dedicated HAMs.

Although cellular phones and other subscriber identification module (SIM) tracking and control development have taken over the commercial market, APRS offers the same baseline capability for tracking and is free to use with a HAM licence. APRS can also be a good alternative in regions lacking cellular reception, especially because there are several APRS Satellite Tracking and Reporting System satellites which function as digital relays to the global internet linked system of ground stations to provide 24/7 access [*Bruninga (WB4APR)*, 2006].

There are several satellites (e.g. PCSat and the ISS) that function as APRS repeaters, they do not record the waveform and so they cannot measure FR or time of propagation and are not suitable for the tomographic method described in this thesis. They may be used to measure two-way propagation of the repeated signals using a ground based transceiver with an accurate clock. This data may be considered further in future studies and serve as yet another example of a signal of opportunity for ionospheric sounding. Future satellites should consider measuring FR or signal propagation time for ionospheric studies, which are also beneficial to characterizing propagation conditions for HAM radio.

### 3.3 Ray Tracing

To date, the type of real data required to perform this research has not been available from either ADS-B or AIS. Since polarization measurements of ADS-B and AIS signals are currently not available, an EM-wave ray tracing model developed by [*Gillies et al.*, 2007] has been used generate synthetic data. The ray trace model is capable of determining the wave path and polarization state at the location of the satellite

receiver. The ray trace program, based on the ray formalism developed by *Haselgrove* [1963], uses Eqn. 2.3 to determine the indices of refraction of a radio wave in a magneto-ionic medium used in the ray tracing equations. This model provides the group velocity and rate of change of the wave vector direction. Inputs to the ray trace program include the initial wave-vector direction, the wave frequency, and a set of propagation conditions such as the magnetic field vector, and an electron density profile for the ionosphere. The program computes the path of the wave for a given frequency, that both the O-mode and X-mode takes from the fixed initial position of the transmitter to a specified position of the satellite carrying the receiver.

The initial polarization orientation of the wave leaving the transmitter must be known. For the current purpose of this work all waves will be assumed to be vertically plane polarized for AIS [*The International Telecommunications Union*, 1998; *Kyoutorov et al.*, 2012; *Parsons et al.*, 2013] and ADS-B [*Radio Technical Commission for Aeronautics*, 2003; *Haque et al.*, 2013]. In reality, the initial polarization of the wave may be different for unique transmitters, but would be constant for any given aircraft/ship transmitter. While ship /aircraft orientation (pitch, yaw and roll i.e. banking and climbing) also affects the orientation of the transmitted signal, that information is part of the ADS-B packet and the initial orientation of the polarization can be determined. For the purpose of tomography the initial orientation does not necessarily need to be known since the rate of rotation over consecutive epochs (between transmitter-receiver pairs) rather than the absolute value can be used [*Klobuchar and Liu*, 1989].

A ray-tracing program was obtained from *Gillies et al.* [2007]. The program was used to generate TEC outputs from rays that passed from given locations, at a given elevation angle through the input 2D  $n_e$ -profile to a given satellite location [*Gillies*, 2006; *Gillies et al.*, 2007; *Gillies*, 2010]. The model was used to show that the FR of the signals received by the satellite should be detectable. Previous work by *Yueh* [1999] has shown that FR can be used to obtain the TEC along the paths. The computed TEC and ray path geometry are then used to reconstruct the electron density profile that the EM-waves propagated through. The reconstructed TEC maps

are compared to the input profiles to evaluate the feasibility of ionospheric sounding using ADS-B and AIS signals, particularly applying CIT methods.

For this investigation of CIT, the vertical ionospheric  $n_e$ -profiles were generated using the IRI model [*Bilitza et al.*, 2011]. An ionospheric features altitude (km), height (standard deviation in km), latitude (degrees) and width (standard deviation in degrees) were modified in order to superimpose various ionospheric features. These new maps are then used as input to the ray trace model to simulate rays leaving from an aircraft, passing through the enhancement/depletion and finally being received by the satellite. Measuring (or modelling in this case) the polarization angle of the received wave and knowing the initial polarization of the wave, the FR for the ray path can be calculated.

IDL was used to analyse all ray-files for a single aircraft. The output of the ray-tracing program included various ray parameters that can be printed and/or plotted. They include:  $x$ ,  $y$ ,  $z$ -component of the Earth's magnetic field in nT, geographic latitude and longitude in degrees, altitude in km, aspect angle, electron density (in  $\text{m}^{-3}$ ), the refractive index squared, the elevation angle, great circle distance (km), slant range (km), bending angle, and relative power. Some of these variables were used to calculate parameters along the ray path; like integrating the refractive index and distance along the path to determine phase and Faraday rotation. By dividing the average  $z$ -component of the magnetic field, the TEC was plotted as a function of receiver latitude.

Other pre-processing steps were used to validate output and strip erroneous parameters and their corresponding values. These included elevation cut-off below  $10^\circ$ , correction of elevations to un-flipped tracking, convergence altitude, etc. This simply filtered the rays which did not converge, or were LOS and converged when typically signals at low elevation angles are not robustly received [*Cushley*, 2010].

## 3.4 Reconstruction

### 3.4.1 The Inverse Problems

In mathematical models of physical phenomena, a problem is said to be well posed if it satisfies three conditions: a solution exists, the solution is unique and the behaviour of which does not change dramatically when a small change in the initial conditions is introduced. Otherwise, the problem is said to be ill-posed [*Hadamard*, 1902; *Tikhonov and Arsenin*, 1977]. Examples of ill-posed problems are inversion problems such as the inverse heat problem or CT.

There are several types of sparse linear systems (see Numerical Recipes sect 2.7); a matrix with only a relatively small number of non-zero elements [*Press et al.*, 2007]. When working with very large problems that begin to tax the memory space available, it is wasteful to use general algebraic methods that require memory be wasted on unfruitful zero values. In this case, there are two distinct (and often incompatible) goals for any sparse matrix method; to save time and/or memory. Many practical schemes have been created to deal with sparse matrix problems. They are generally decomposition or elimination schemes that are optimized to reduce the number of *fill-ins*, initially zero elements that must become non-zero during the solution process and for which memory must be reserved. Therefore, direct methods depend on the pattern of sparsity of the matrix. Several different patterns are shown in Fig. 3.5, although are not reviewed further within the scope of this work, which best fits in the “other” category.

One method for matrices that fall under the “other” category because they do not follow a particularly simple pattern of sparsity is to try an *analyze/ factorize/ operate* package in order to automate the procedure of determining how *fill-ins* can be minimized. The *analyze* stage is used only once for each pattern of sparsity, *factorize* is done once for each matrix that fits the pattern and *operate* is performed once for each right-hand side to be used with the particular matrix

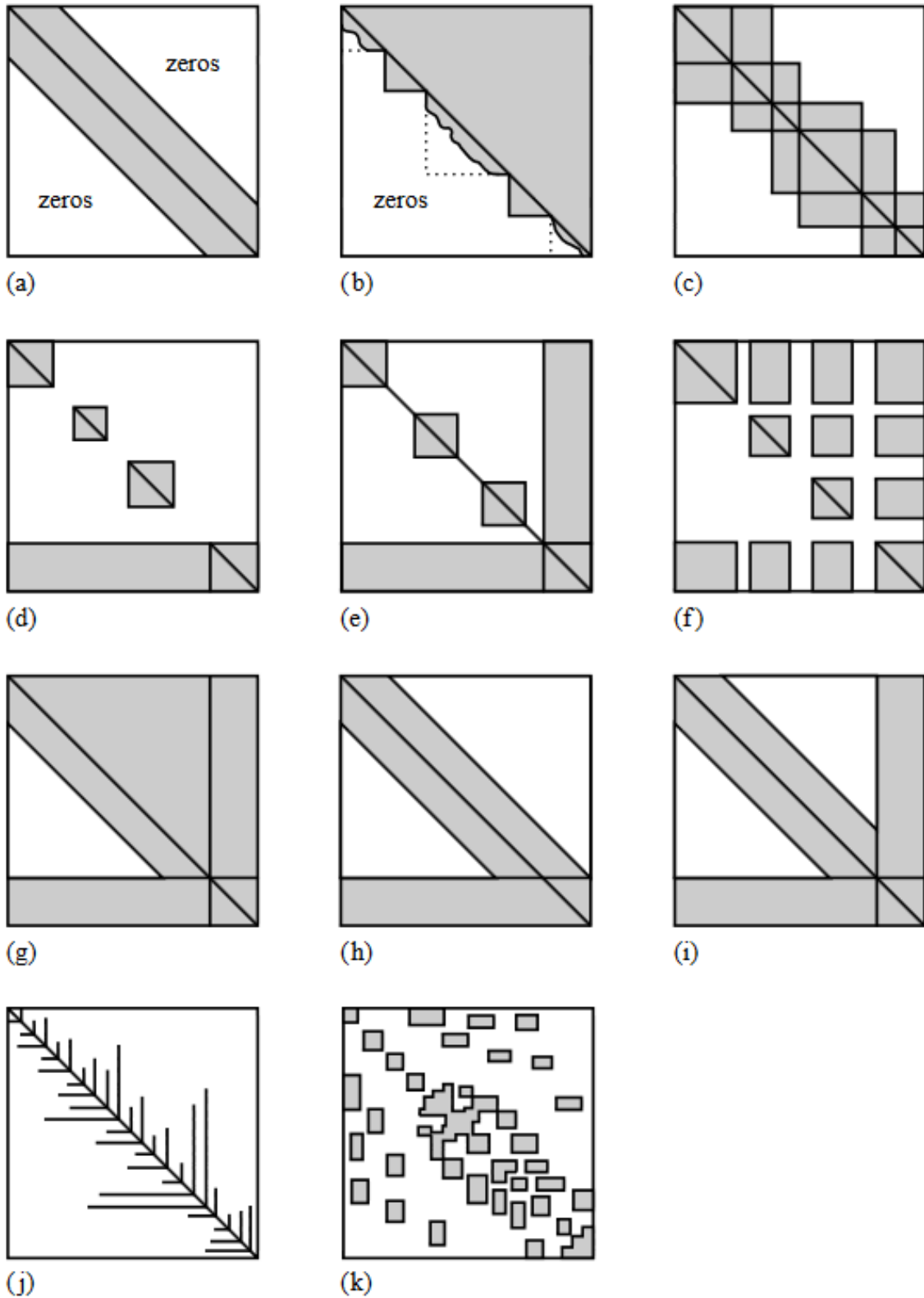


Figure 3.5: Various standard forms of sparse matrices: (a) band diagonal, (b) block triangular, (c) block tridiagonal, (d) singly bordered block diagonal, (e) doubly bordered block diagonal, (f) singly bordered block triangular, (g) bordered band-triangular, (h) singly bordered band diagonal, (i) doubly bordered band diagonal, (j) and (k) other! [Tewarson, 1973; Press et al., 2007]

### 3.4.2 Computer Tomography (CT)

Tomography is part of a family of inverse problems that are often difficult because they are ill-posed. CIT constitutes an under-determined ill-posed inverse problem due to the multi-scale variability of the ionosphere in addition to the biases and errors computing TEC [*IONOLAB Ionospheric Research Laboratory*]. The mathematical problem posed by CT includes projecting radiation through an object at different angles resulting in multiple measurements or estimates of the objects interior; calculating image pixel values from projection values [*Tessa et al., 2007*]. The transmitted radiation passes through an object over many paths to a number of receivers. Over each path, the attenuation, or alternatively the absorption of the transmitted signal varies due to the changes in density of the object.

### 3.4.3 Computerized Ionospheric Tomography (CIT)

In CIT, the integrated measurements of the attenuation coefficient along the ray paths from transmitter to receivers, are due to the variation of the integrated electron density along the paths or TEC as discussed in section 1.3.1.1 and given by Eqn. 1.1.

The sampling geometry from which the projection data is acquired in CIT is shown in Fig. 3.6. The transmit points over the satellite orbit are shown by  $S_n$  with only the parallel rays through the ionospheric layers to ground receivers  $g_n$  forming projections  $P(\theta_n)$ .

The coverage that is required for the purpose of the mission dictates the orbit geometry, and the number of satellites. For example, the satellite that generates the images used to create and update Google Earth and Maps need not be real-time because things like roads, buildings, and cities generally do not change very rapidly. A single Earth remote sensing satellite in a LEO with pointing capability can image the same local region once  $\sim 14$  orbits [*Elachi and van Zyl, 2006*]. For GPS or the proposed ADS-B satellites, the mission requirement is for real-time services therefore a constellation of satellites is required because temporal variations of position occurs on a shorter time-scale than infrastructure development.

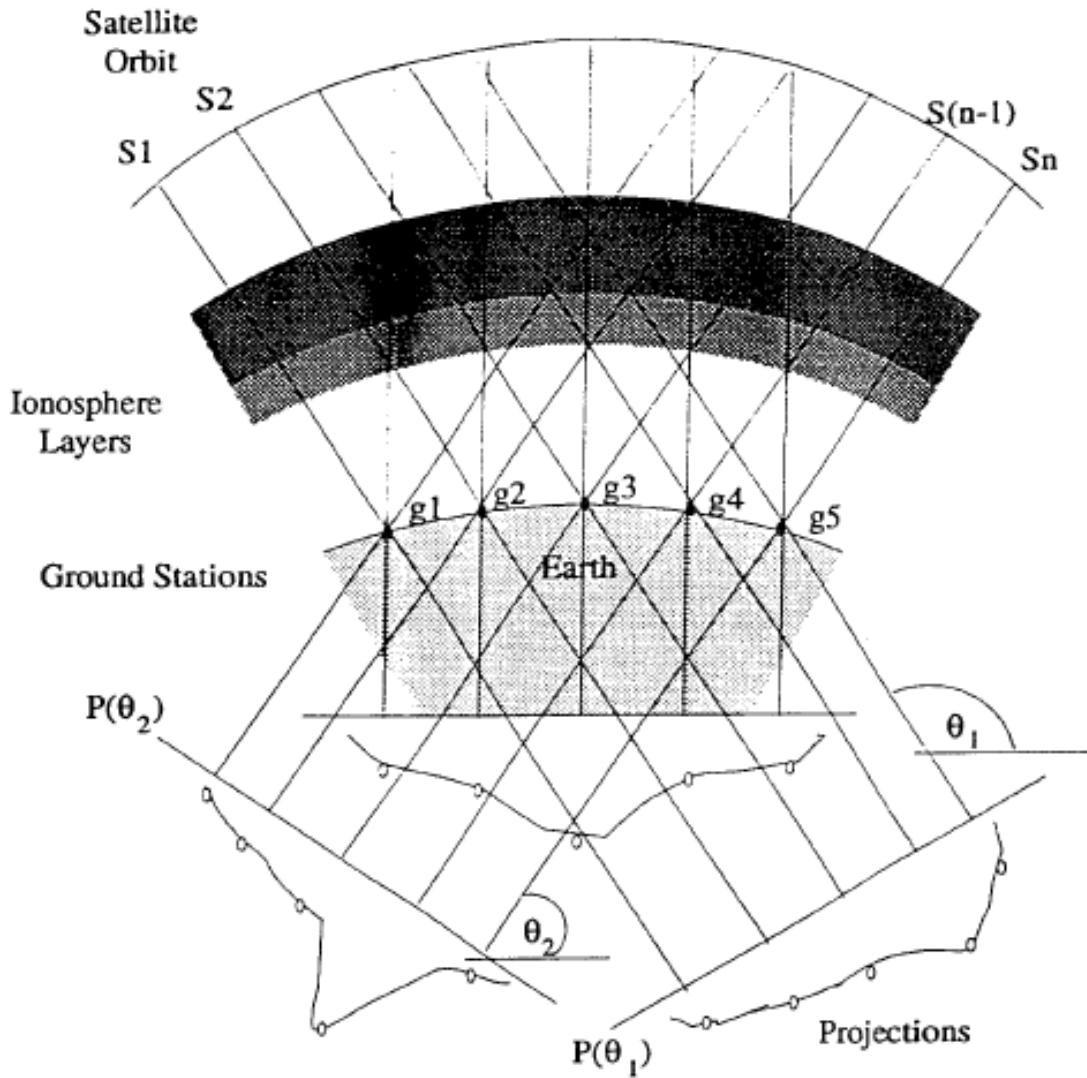


Figure 3.6: CIT imaging geometry. Adapted from *Na* [1996]

Extending this principal to the ionosphere, it can be said that the data collection interval must not exceed the time for which the ionosphere stays relatively inactive. We assume that during the time for which data is collected, the ionosphere is horizontally uniform and does not change significantly in time. This time can vary depending on the number of receiving stations that are used ranging from a few minutes [*Meggs et al.*, 2004; *Max van de Kamp*, 2012] to an hour [*Choi et al.*, 2006] but should be



minimized, whenever possible. For the papers presented in Chapters 4 and 7 the data integration time is 3-4 minutes and  $\sim 7$  minutes respectively.

In conventional CIT using GPS, the differential phase shift encountered by dual-frequency satellite signals for each satellite epoch and receiver pair is proportional to the relative TEC along the corresponding ray path. For the cases studied in this work the TEC was estimated using the FR. There is generally a lack of information pertaining to electron density distribution in the vertical direction since TEC is an integrated value and there are no horizontal ray paths. There are also typically less TEC measurements than unknown pixel values.

Since *Austen et al.* [1986] proposed the possibility of satellite radio tomography, also known as CIT, the study of detailed features of the ionosphere and plasmasphere have become possible by means of tomographic reconstruction. In applications such as CIT, for noisy or incomplete data sets, using pixel-based methods has been shown to have advantages [*Tessa et al.*, 2007]. Each pixel represents a region of space in the ionosphere. The intensity of the pixel is the average value of the measured physical property, generally the amount of attenuation or in the case of this study the FR which is proportional to the electron density.

There are two principle categories of CT reconstruction: pixel based methods and non-pixel based methods. Both methods were considered in numerous literature sources pertaining to medical imaging, geo-physics, GPS CIT, mathematics and computer science by *Cushley* [2013]. It was found that non-pixel based methods could not be applied to CIT. Non-pixel based methods, as first used in medical CT scans, generally apply best to complete datasets. This requires a measure for every sensor position moved in equal increments, whether equiangular or equidistant, and the distance (or height in the case of CIT) is known. This is not the case in CIT therefore pixel-based methods are employed.

#### 3.4.4 Algebraic Reconstruction Technique (ART)

The most commonly used pixel-based method of CIT is the Algebraic Reconstruction Technique (ART). ART forms the basis of most of the other pixel-based methods,

e.g. Simultaneous Algebraic Reconstruction Technique (SART), Simultaneous Iterative Reconstruction Technique (SIRT) [Tessa *et al.*, 2007] or multiplicative algebraic reconstruction technique (MART) [Atkinson and Soria, 2007]. The ART algorithm can be implemented using the following equation [Choi *et al.*, 2006].

$$N_e^{k+1} = N_e^k + \lambda_k \frac{STEC_i - \sum_{j=1}^{\rho} d_{ij} n_{ej}^k}{\sum_{j=1}^{\rho} d_{ij} d_{ij}} D_i \quad (3.1)$$

where  $j$  is the pixel number,  $k$  is the iteration number,  $\lambda_k$  is a relaxation parameter,  $N_e^k$  is a vector of the ionosphere electron densities ( $n_{ej}^k$ ) for the  $k^{th}$  iteration,  $N_e^{k+1}$  is a vector of the modified values of the electron densities ( $n_{ej}^{k+1}$ ) for the next  $k^{th} + 1$  iteration. The vector  $STEC_i$  contains the TEC measurements taken over  $i$  propagation paths with various elevation angles and slant ranges. The matrix  $D$  relates the ray data to the pixels in the reconstruction grid; there is a row for each ray, and column for each pixel in the reconstruction grid (e.g. a  $100 \times 100$  grid has 10000 pixels to solve). The  $STEC_i$  contribution from ray  $i$  to pixel  $j$  in the matrix  $D$  is  $d_{ij}$ . The  $i^{th}$  row of  $D$  is  $D_i$ , and  $\rho = 10000$  is the total number of pixels in the reconstruction grid.

The ART algorithm is used to spread the measured value over the appropriate pixels in the reconstruction grid, analogous to back-projection, and modifies the pixel values in  $N_e^k$  by incremental amounts for each iteration. In the resulting reconstructed image, the brightness of pixels that are intersected by rays change to allow the ray sum to approach the measured projection value in  $STEC$ .

Figure 3.7 shows a flowchart of the implementation of the ART procedure [Choi *et al.*, 2006];

The input data consisted of the modelled TEC measurements obtained in the previous section. It represents a conservative estimate of the air traffic in the AOI, that can be received by a space-borne ADS-B receiver on a LEO satellite during a single pass. Although  $j$  independent equations with  $j$  unknowns can be solved, solving a large system of equations is a challenging and computationally intensive task. Due to the fact that the system is very large, and the unknown offset of

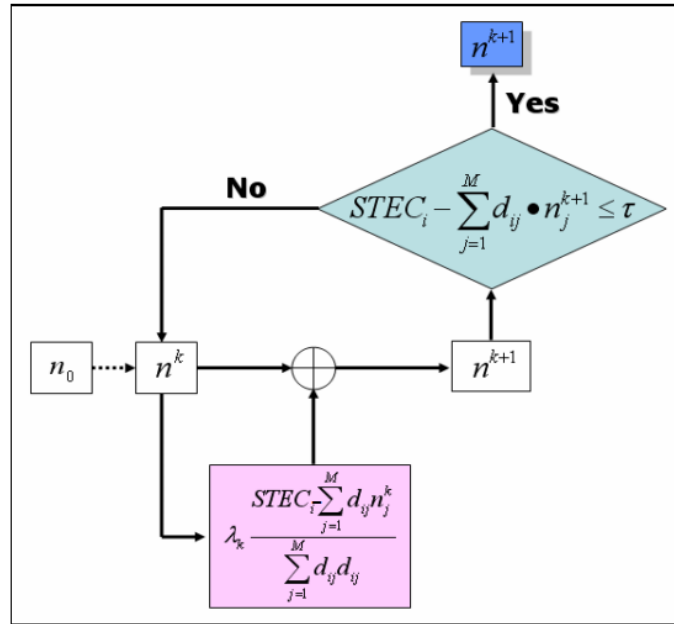


Figure 3.7: Implementation of the ART Algorithm. Note that  $M = \rho$  in Eqn. 3.1 [Choi et al., 2006]

the TEC measurement from absolute TEC discussed in section 3.4.4.3, the program approximated the solution within a given tolerance. Equations were not solved for the electron densities themselves but rather their deviation from the background density for each iteration. This is shown in the blue diamond in Fig. 3.7. The summation of the pixel values along the path, subtracted from the STEC measure is the error ( $E_{i \times 1}$  in Eqn. 3.7), which is compared to the tolerance. If the error is within a given tolerance the algorithm stops and the last iteration is displayed. If the tolerance is not met, the difference is multiplied by a relaxation parameter  $\lambda_k$  and distributed throughout all pixels  $j$  intersected by ray  $i$  as shown in the pink rectangle in Fig. 3.7.

The ART algorithm uses an initial guess (even if that is a blank grid initialized to zero or 1) for the pixel values of the image in the reconstruction image, then after solving Eqn. 3.3 with the initial guess for  $N_e^k$  the direction to proceed to the real value is determined and incrementally adjusted within a tolerance to avoid oscillating about the value indefinitely. The tolerance can be set for convergence that dictates the desired quality of the reconstruction. A smaller value for the tolerance corresponds to lower relative uncertainty, which is correlated with the time needed to

reach convergence [Tessa et al., 2007]. The lower the tolerance, the longer the time required for convergence.

The ART algorithm takes the following form:

$$N_e^{new} = N_e^{old} + \lambda_k[\Delta N] \quad (3.2)$$

The ART method is affected by numerical uncertainties that are introduced by inconsistencies in the system of equations. It is possible to reduce the effect of the uncertainties by using a relaxation parameter  $\lambda_k$ . The parameter  $\lambda_k$  is generally referred to as a relaxation parameter, but is in fact a regularization factor from regularization techniques [Tikhonov and Arsenin, 1977; Tikhonov and Goncharsky, 1987]. The relaxation parameter can be iterative or chosen to be constant for each iteration in order to control the convergence rate of the algorithm and maintains the stability of the numerical method. The value for  $\lambda_k$  is confined between  $0 < \lambda_k < 2$ . An in-depth study of the effect of  $\lambda_k$  on the reconstructions was not performed in previous work by [Cushley, 2013; Cushley and Noël, 2014] and the relaxation parameter was not optimized for this research. After considering the literature sources for GPS CIT using ART a value of  $\lambda_k = 0.005$  was used for all iterations [Choi et al., 2006].

The ART technique converges relatively rapidly compared to other methods [Herman, 1980; Feeman, 2010; Vijayalakshmi and Vindhya, 2014], and can use an initial guess or *a priori* estimate to perform the reconstruction. Although several methods and algorithms exist, ART has been widely used, and is well documented. The source of the initial or *a priori* guess is different for every application, and possibly for each individual reconstruction. For instance, in medical brain scans a Shepp Logan Phantom (see Fig. 3.8) could be used as the *a priori* guess. Possibly the Phantom could be skewed to the measured dimensions of each patients skull. In this case the Phantom is a good representation of what the interior structure of a skull should look like; free-space surrounding skull, and two lobes inside.

In nano-tomography of an unknown mineral structure, the *a priori* guess may simply be a logical index of ones representing the measured dimensions of the unknown

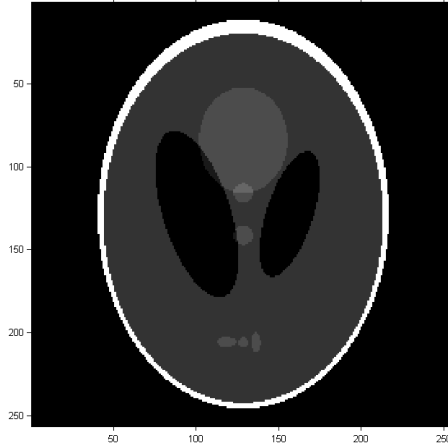


Figure 3.8: Shepp-Logan Phantom image available through MATLAB<sup>®</sup>; a numerical computing environment and programming language, created by Mathworks.

[*Shepp and Logan, 1974*]

object. In seismic CT, the *a priori* guess may be obtained by drilling a bore sample and measuring the density and height of the soil layers, water table, etc. For the ionosphere the *a priori* guess may be determined by empirical models or measurement data from another source. When *a priori* data is otherwise unavailable, the initial guess for ART may simply be the grid, initialized with values of 0 for all pixels. Overall convergence is longer and some reconstructions are not very good representations of the object, dependent especially on the application, method, and density of sampling.

The ART algorithm is a method by which an ill-posed linear algebraic problem can be solved. A system of linear equations may be written as;

$$A\vec{x} = \vec{p}. \quad (3.3)$$

where  $\vec{x}$  is a vector of unknown pixel values,  $\vec{p}$  is a column vector of measured values, and  $A$  is a matrix in which its rows relate the contribution of each measured value  $p$  to the determination of the individual unknown pixel values  $x$ . This is an ill-conditioned system of equations. Generally this will be an under-determined problem with more unknowns than equations, but can also be over-determined with more equations than unknowns.

### 3.4.4.1 A Conceptual Explanation And Simple Numerical Example to Show the Procedure

The mathematics of CT were solved numerous times for different imaging applications such as medical, seismic, micro and nano-imaging. Other derivations were driven by pure mathematics and computer science to enhance the efficiency or accuracy of the solution to this ill-posed problem. John Radon was the first to do so in 1917 in his paper “Über die Bestimmung von Funktionen durch ihre Integralwerte längs gewisser Mannigfaltigkeiten.” (“On the determination of functions by their integral values along certain manifolds”) [*Radon, 1986*]. Radon’s transform for reconstruction of an object is rather involved and non-pixel based methods are not very applicable to CIT, however remains noteworthy in the development of CT applications. A full explanation of the early theory of CT will be set aside for a simple conceptual explanation using a sudoku puzzle as an overly simplified numerical example that can be computed manually without the use of a computer.

Consider a black box that contains a completed Sudoku puzzle. A Sudoku puzzle can have more than one solution. There are in fact several non-unique solutions. This is why there are various sudoku puzzle possibilities. There are in fact  $6.67 \times 10^{21}$  possible solutions, ignoring rotations [*Felgenhauer and Jarvis, 2005*]. The integral of each row and column of the puzzle is 45. There is no variation in the projection data and therefore no information is revealed about the puzzle inside. Additional information, such as the diagonal integrals is required. A well-formed Sudoku puzzle is one that has a unique solution, but even if none of the values for  $x_i$  were given in Fig. 3.9 if a complete set of 34 diagonal projection values were known, at least a non-unique solution to the system may be found using CT by adjusting the pixel values until the difference between the known integrated values along each diagonal and those integrated along the same path in the grid goes to zero. This is an example of an under-determined ill-posed problem.

To demonstrate this procedure further, an overly simplified illustrative example using a square grid containing  $3 \times 3$  pixels to represent an unknown object is used.

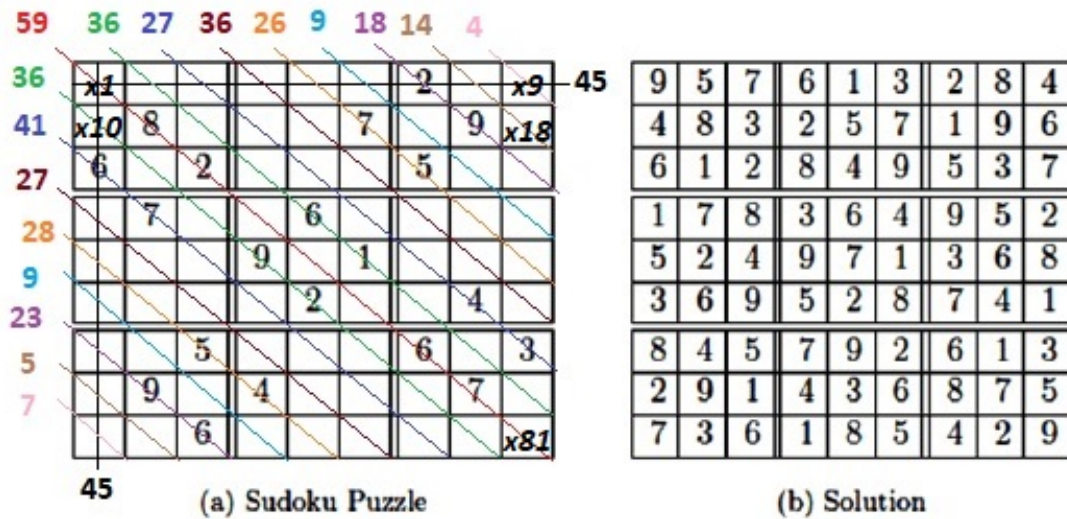


Figure 3.9: Left: a Sudoku puzzle with 20 given values. The integral of each row and column is 45. The integral along each diagonal is shown with a different line and text color for each. Right: The solution to the Sudoku puzzle shown on the left.

The object is sampled in four different directions (horizontally and vertically in the left panel, diagonally in the right panel) shown in Fig. 3.10. This results in a system of 12 equations for 9 unknowns ( $x_1, x_2, \dots, x_9$ ). According to basic algebra in order to solve a system of equations for nine unknown variables  $x_i$ , only nine independent equations are required. The equations are not independent of one another, evident by the summation of the three horizontal and vertical equations forming the same equation ( $x_1 + x_2 + \dots + x_9 = 12$ ). Therefore eleven of the twelve equations must be used to uniquely solve for the values of  $x_i$  in this ill-posed problem.

This simple example is a bit different since it is an over-determined while the above is under-determined. It should be evident that using a computer becomes a necessity when we want to solve larger systems of pixels, simultaneous measurements, and directions for applications in CT. This simple example demonstrates the basic numerical method that is used is inefficient from the surplus of measurements, but represents the basic method of the reconstruction for a single 2D plane in CT.

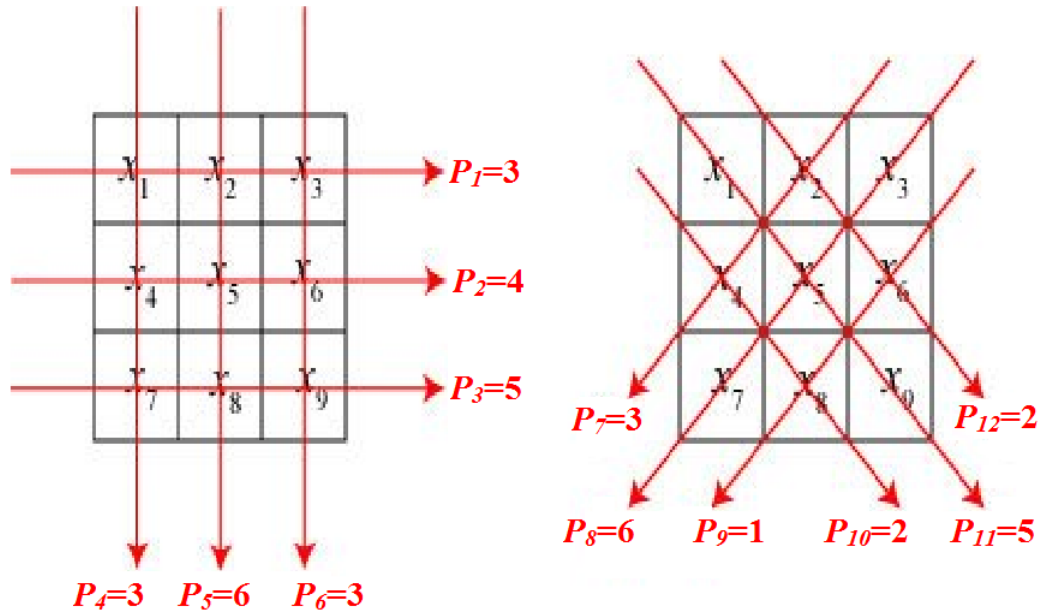


Figure 3.10: Diagram showing the sampling of a square grid containing 3x3 unknown pixels. Red lines show direction sampled and total value attenuated. See Appendix A for the solution to  $x_i$

#### 3.4.4.2 Applying ART to CIT

For this study ART was selected for several reasons:

- it provides a superior reconstruction (for low gradients) [*Kunitsyn and Tereschenko, 2003*];
- it is tolerant of random sampling geometry and sparse dataset, unlike FFT, and;
- it can use *a priori* injection as a first guess then iteratively improve the guess using measurement data.

FR measurements, once they have been converted to STEC constitutes a system of equations of the form of Eq. 3.3 from which the solution of  $x$  may be sought. By examining the electron density in Eqn. 1.1 as a function of pixel  $j$  in the reconstruction grid and neglecting the time-component for all data within the specified collection



period and can be written as follows,

$$STEC_i = \int_0^l N_e(j) dl. \quad (3.4)$$

where  $N_e(j)$  is a vector of  $j$  unknown pixel values, and  $dl$  is an element of the matrix  $D$ , which relates the contribution of the measured value of  $STEC_i$  to pixel  $n_{ej}$  along path  $i$ . Inversion of these relative TEC measurements using the ambient CIT imaging geometry constitutes the tomographic image reconstruction process.

The problem may be written as a system of linear equations for which the unknown pixel values  $n_{e\rho}$  must be solved as follows,

$$\begin{aligned} d_{11}n_{e1} + d_{12}n_{e2} + d_{13}n_{e3} + \dots + d_j n_{ej} &= STEC_1 \\ d_{21}n_{e1} + d_{22}n_{e2} + d_{23}n_{e3} + \dots + d_j n_{ej} &= STEC_2 \\ d_{31}n_{e1} + d_{32}n_{e2} + d_{33}n_{e3} + \dots + d_j n_{ej} &= STEC_3 \\ &\vdots \\ d_{i1}n_{e1} + d_{i2}n_{e2} + d_{i3}n_{e3} + \dots + d_j n_{ej} &= STEC_i \end{aligned} \quad (3.5)$$

Equation 3.5 can be written more compactly as follows,

$$STEC_i = \sum_{j=1}^{\rho} n_{ej} d_{ij} + \Delta_i \quad (3.6)$$

where  $\Delta_i$  is the uncertainty associated with integrated pixels  $j$  (due to discretization errors and measurement noise) for ray path  $i$ . For each and every STEC measurement, there is an equation of the form of Eq. 3.6. The STEC measurement of the ray path can be represented as a series of finite summations of shorter integrals along segments of the ray path length  $d_{ij}$ ; the contribution of ray  $i$  to pixel  $j$ . If the ray does not traverse the pixel,  $d_{ij} = 0$ .

Rather than dealing with such a large system of equations, matrix notation is useful,

$$STEC_{i \times 1} = D_{i \times j} \times N_{e \ j \times 1} + E_{i \times 1} \quad (3.7)$$

where  $STEC_{i \times 1}$ ,  $E_{i \times 1}$ , and  $N_{e \ j \times 1}$  are column vectors of  $i$  measurements of STEC,  $i$  associated error values, and  $j$  unknown pixel values  $n_{ej}$ , respectively.  $D_{i \times j}$  is the

geometry matrix. The *STEC* is the known modelled or measured quantity while  $D$  is computed from the time-tagged aircraft and satellite state vectors. Using a successive iteration approach, the pixel intensities are modified to allow the projection through the pixels ( $DN_e$ ) to approach the measured projection (*STEC*) while minimizing the residuals  $E$ . Each projection provides a different view of the interior.

The matrix  $D$  is often called the geometry matrix or the weight matrix, particularly if the analysis of the ray geometry is made to be more elaborate based on several other factors such as the length segment of the ray for each pixel, or the relationship of a pixel to its neighbouring pixels [Max van de Kamp, 2012]. The simplest form for the geometry matrix is a logical index with a row depicting each ray, and columns for each pixel in the reconstruction grid, assigned 1 if the ray contributes to the pixel and 0 otherwise.

Referring back to the numerical example for the unknown object that was previously shown in Fig. 3.10, the twelve rays can be expressed as follows:

$$\begin{pmatrix} 1 & 1 & 1 & 0 & 0 & 0 & 0 & 0 & 0 \\ 0 & 0 & 0 & 1 & 1 & 1 & 0 & 0 & 0 \\ 0 & 0 & 0 & 0 & 0 & 0 & 1 & 1 & 1 \\ 1 & 0 & 0 & 1 & 0 & 0 & 1 & 0 & 0 \\ 0 & 1 & 0 & 0 & 1 & 0 & 0 & 1 & 0 \\ 0 & 0 & 1 & 0 & 0 & 1 & 0 & 0 & 1 \\ 0 & 1 & 0 & 0 & 0 & 1 & 0 & 0 & 0 \\ 1 & 0 & 0 & 0 & 1 & 0 & 0 & 0 & 1 \\ 0 & 0 & 0 & 1 & 0 & 0 & 0 & 1 & 0 \\ 0 & 1 & 0 & 1 & 0 & 0 & 0 & 0 & 0 \\ 0 & 0 & 1 & 0 & 1 & 0 & 1 & 0 & 0 \\ 0 & 0 & 0 & 0 & 0 & 1 & 0 & 1 & 0 \end{pmatrix} \begin{pmatrix} x_1 \\ x_2 \\ x_3 \\ x_4 \\ x_5 \\ x_6 \\ x_7 \\ x_8 \\ x_9 \end{pmatrix} = \begin{pmatrix} 3 \\ 4 \\ 5 \\ 3 \\ 6 \\ 3 \\ 2 \\ 5 \\ 2 \\ 3 \\ 6 \\ 1 \end{pmatrix} \quad (3.8)$$

A rectangular grid can be used to represent a 2D slice of the ionosphere as shown in Fig. 3.11. To represent the interior structure of the ionosphere, this grid is subdivided using a constant  $\Delta z = 10$  km in altitude from the Earth's surface, and a constant  $\Delta\theta_l = 0.5^\circ$  in terms of the geographic latitude. The end-points for each ray are available from the GPS positions of the time-tagged ADS-B transmissions, and the satellite's on-board GPS receiver, telemetry, or possibly two-line element sets (TLEs) and orbit propagation software for signal time of arrival (TOA) positions. For illustrative purposes, a single ray leaving the transmitter and assuming a straight

line approximation, the pixels in blue would be assigned a value of 1, while those in yellow would be assigned a value of 0.

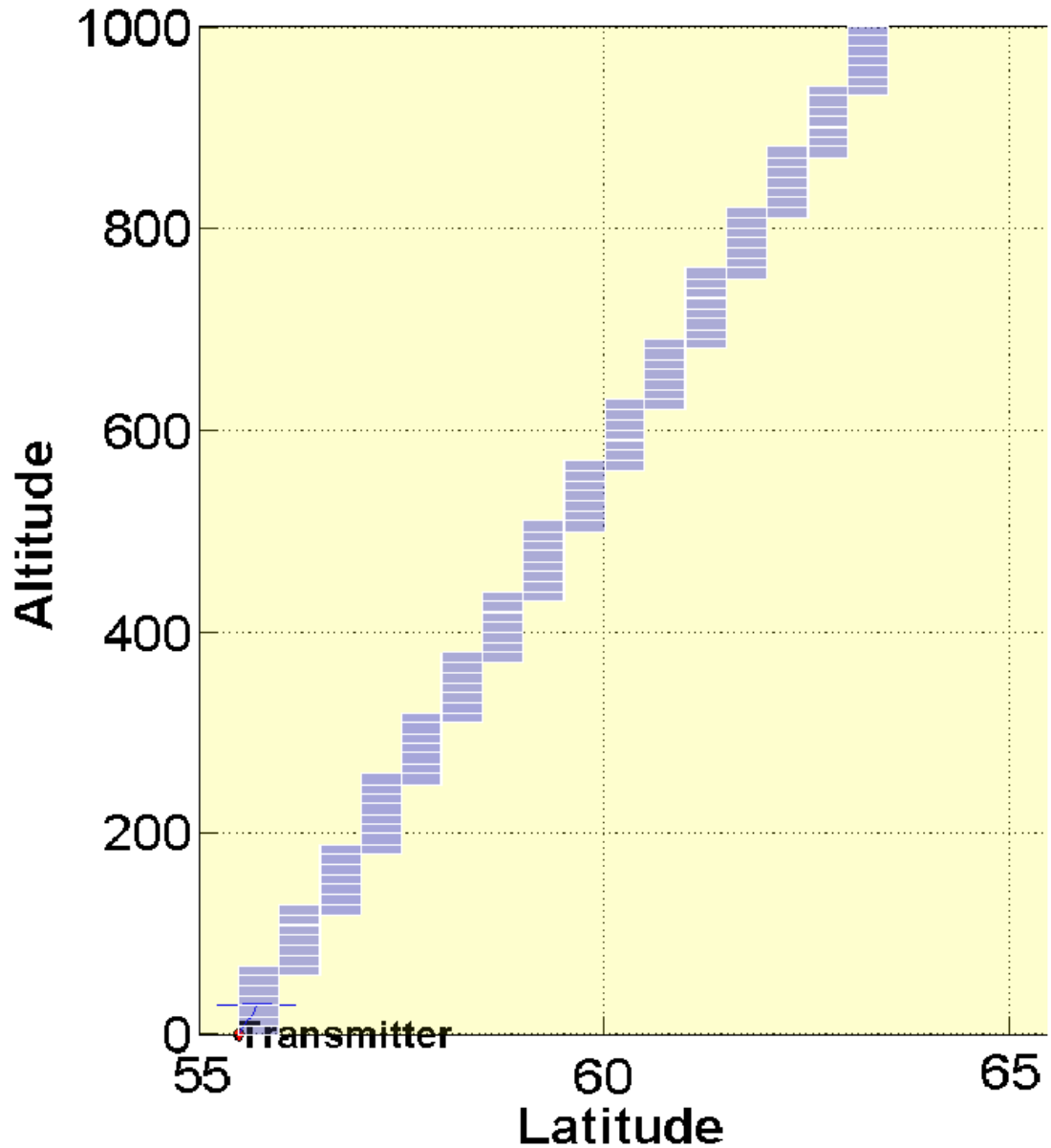


Figure 3.11: An illustration of a signal ray path passing through illuminated pixels (blue) within a portion of the 2D reconstruction grid (yellow).

Each pixel  $j$  has intensity  $n_{ej}$  (an element of  $N_e$ , calculated using Eqn. 3.1), representative of the relative electron density in a volume over which the electron density is assumed to be constant. The index  $j$  is the pixel number used in the reconstruction grid, where  $1 \leq j \leq \rho \sim 10^4$ . It is also the number of terms in Eq.

3.6. The index  $\rho$  is the total number of pixels that are used in the reconstruction grid where  $\rho = g_x \cdot g_y = 10000$ .

For the work conducted by *Cushley* [2013] several different grid sizes ( $g_x \times g_y$ ) were tested. For all the results in *Cushley and Noël* [2014] a grid of  $100 \times 100$  pixels having intervals of 10 km in altitude and  $0.25^\circ$  in latitude was selected. The electron density is also assumed to be uniform over a  $1^\circ$  slice of longitude. Therefore, the depth of the pixels (voxels) in the grid  $g_z$ , or the longitudinal extent over which the 2D reconstruction was representative of the electron density is  $1^\circ$ .

The value of each pixel represents the incremental electron density along the ray path that contributes to the estimated TEC from the total amount of FR at the receiver. Since the electron densities are not measured directly, the projections of the TEC along each path can only determine the electron density relative to the other pixels.

Although the problem can be represented as a system of linear equations, essentially  $i$  equations with  $j$  unknowns, with  $n_{ej}=10000$  values to solve, this is considered to be an under-determined ill-posed problem. When a ray is passed through the grid it intersects a relatively small subset of the total pixels available in the grid. Since the greatest number of pixels a ray can pass through on the reconstruction grid is 141 pixels, at a  $45^\circ$  angle of elevation above the horizon. The resulting  $D$  matrix is very sparse with  $\sim 99\%$  of cells being zero, which results in a non-invertible problem to solve. Non-trivial mathematics requires the use of computers for timely calculations, hence ‘computer’ tomography.

#### 3.4.4.3 Prior Studies of CIT Using TEC

GNSS technology such as the NAVSTAR GPS, Galileo, and Beidou is enabling technology for AIS, APRS and ADS-B. Besides providing autonomous Geo-spatial positioning, GNSS has also been used to provide measurement of the ionosphere TEC [*Hartmann and Leitinger*, 1984; *Austen et al.*, 1986; *Pryse*, 2003; *Choi et al.*, 2006; *Max van de Kamp*, 2012]. The systems use L band transionospheric radio signals for positioning, navigation, and timing (PNT). These signals are susceptible to iono-

spheric propagation effects such as phase advance and group delay, which alter the properties of the received signal. The group path delay of a radio wave is a retardation in the velocity of the information carried by the wave. Group path delay can produce timing errors in radar and navigation systems that use transionospheric signals; signals that propagate through the ionosphere. This group path delay timing error is directly proportional to the TEC. Although the ionosphere can affect PNT services, it may conversely be probed using the variations in these signal properties.

In previous studies, a GPS chain network which consisted of five ground-based GPS receivers was identified in Eastern Australia, with geographical locations from North to South spanning  $23.17^\circ$  [Yizengaw *et al.*, 2004]. As further reference, other investigations with ground stations that were separated by approximately  $9^\circ$  [Choi *et al.*, 2006] and  $30^\circ$  [Andreeva *et al.*, 2001] in latitude, demonstrating the difficulty for using GPS CIT on a large-scale [Choi *et al.*, 2006].

Mitchell *et al.* [1997a] successfully demonstrated CIT was capable of reconstructing signals from polar LEO satellites by receiving dual-frequency beacons at five ground stations in Scandinavia thereby achieving a spatial resolution for features as small as 50 km. Although this experiment demonstrated the utility of the CIT method for LEO satellites, the results were limited to a single meridian in latitude and time giving only a small snapshot for each satellite pass.

Mitchell *et al.* [1997b] observed that for a LEO satellite, the measurements were not evenly distributed, and for GPS measurements taken in a relatively small area, particularly at high altitude, the situation was worse; very dense in some directions and very sparse in others. Due to this, his work suffered from poor vertical resolution at altitudes above 200 km. Both studies by Mitchell, as well as others used *a priori* information of the vertical distribution of the electron density profile obtained from models such as the IRI, or modified Chapman.

The use of GNSS signals has followed as an input source for CIT, and over time more GPS ground receiving stations have been installed to receive signals from many directions (different satellites) continuously over long integration times enabling reconstruction of the electron density profile in 4D (3 spatial dimensions, and time)

[*Bust et al., 2007; Max van de Kamp, 2012*]. Additional GPS CIT campaigns have successfully shown the importance of CIT demonstrating methods for different input data: LEO and GNSS applied from equatorial to polar regions [*Austen et al., 1986; Andreeva et al., 2001; Bust et al., 2007; Marcio T.A.H. Muella et al., 2011*].

While there are many variations in the methods for which the TEC can be obtained for CIT, it is principally derived from dual-frequency differential phase measurements. In GPS nomenclature, the phase difference of the GPS dual-frequency receiver bands L1 and L2 respectively, travelling through the same medium at a different frequency results in differential phase and time delay [*Lanyi and Roth, 1998; Choi et al., 2006*]. Due to ambiguities, the absolute ionospheric delay of the carrier phase  $\phi_1$  and  $\phi_2$  cannot be determined. Despite this ambiguity, the differential ionospheric delay over two consecutive epochs can be determined [*Cannon, 1997; Choi et al., 2006*].

Referring back to Eqn. 2.2 and recall that the refractive index depends on the frequency of an EM wave, the travel time will be different for the two frequencies (see Eqn. 1.2). By measuring the phase difference between the two signals at two different frequencies, the difference in travel time can be determined and is directly proportional to TEC. Although TEC can be measured by other methods, the TEC is related to the phase difference by the following equation [*Max van de Kamp, 2012*];

$$TEC = \frac{f_1}{R_e c (f_1^2 / f_2^2 - 1)} \Delta\phi. \quad (3.9)$$

where  $TEC$  is measured in electrons per square meter,  $f_1$  and  $f_2$  are the two carrier frequencies (MHz),  $R_e$  is the radius of an electron ( $2.81794 \times 10^{-15} \text{m}$ ),  $c$  is the velocity of light in a vacuum ( $299792458 \text{ m} \cdot \text{s}^{-1}$ ), and  $\Delta\phi$  phase difference in radians defined as [*Max van de Kamp, 2012*]:

$$\Delta\phi = \frac{f_1}{f_2} (\phi_2 - \phi_1) \quad (3.10)$$

Using the GPS L1 and L2 bands, where  $f_1 = 1575.42 \text{ MHz}$  and  $f_2 = 1227.6 \text{ MHz}$ , Eq 3.9 may be written as:

$$TEC = 2.88255 \times 10^{15} \Delta\phi \quad (3.11)$$

The measurement of the differential phase  $\Delta\phi$  is ambiguous when it is larger than  $\pi$ , because a phase of  $\pi$  is equal to a phase of zero. Consequently, the absolute phase

difference between the two signals cannot be measured. Each measurement of phase difference may be greater than  $\pi$  as variation is primarily time dependent. Not only does the ionosphere vary in time, but the satellites are moving at a high velocity and as a result, the measured path changes dramatically.

The change between consecutive measurements of phase difference from the same transmitter and receiver pair is much smaller than the phase difference itself and is therefore considered unambiguous as long as it is less than  $\pi$  radians in absolute value. This assumption can be justified for high enough frequencies such as those used for GPS or ADS-B [Kunitsyn and Tereschenko, 2003]. Generally, the frequency must be greater than the plasma frequency (as discussed in Chapter 2). Because of this, the useful data obtained from GPS dual-frequency receivers must be preprocessed and analysed to derive measurements of TEC over increments of  $\Delta\phi$ , or what is referred to as  $dTEC$ . From the  $dTEC$ , the TEC can be reconstructed apart from an unknown offset from the absolute TEC using the following equation [Max van de Kamp, 2012];

$$TEC = TEC(t) - TEC(t - dt). \quad (3.12)$$

where  $t$  is time and  $dt$  is the time between consecutive epochs.

In other studies, the offset was determined using the time-stamp codes that are transmitted by the GPS satellites. This allows for the calculation of the absolute time delay. Range determination by this means is known as *pseudo-range*. Although it is too noisy for the calculation of TEC, it is sometimes used to refine the aforementioned offset from the absolute TEC in the reconstructed TEC [Zhen et al., 2004].

A great deal of work has been undertaken using GPS CIT methods. Other studies of interest in terms of future comparison are studies performed over the Northern polar cap during a period of increased disturbance by *Spencer and Mitchell* [2007], *Yin et al.* [2008] and *Pokhotelov et al.* [2011]. Those studies used *a priori* knowledge of the plasma motion in the inversion procedure, which gave good results for the motion of large-scale structures, but failed to reveal structures that were smaller than 500 km in horizontal extent. For events such as these, ionospheric structures were moving and changing at a high rate, making the detection of small-scale structures

very difficult.

Another GPS CIT campaign of interest was an investigation using a dense network of GPS receivers over Finland which identified structures with horizontal resolution of approximately 100 km [*Max van de Kamp*, 2012]. As the investigation was dependent on the location of ground based GPS receivers that were connected by a local area network (LAN), the reconstruction region was limited to 2000 km around Scandinavia in 4D.

An important result from these studies was the challenge in detecting ionospheric features in these regions due to the reported low density of GNSS receivers. Although successful, the GPS approach to CIT requires a meridional chain of ground-based GPS receivers, constraining the coverage regions for imaging. Additionally, GNSS receivers are typically sparsely and unevenly distributed, thus the resolution is generally worse for 3D and 4D reconstruction than using the 2D method, depending on the region.

Like ADS-B, GPS ground stations are difficult to install and maintain in high latitudes, and near-impossible in polar, and mid-ocean regions. For this reason among others, when considering the problem of global coverage in general, whether for ATC or space weather, it is logical to investigate a space-based solution, or one which is not constrained by ground assets.

### 3.4.5 Ambiguity of FR Measurements

The ambiguity of the phase may be dealt with in one of three manners. The first would be to use the change in TEC (dTEC) measurements between consecutive measurements rather than the individual TEC measurements. This essentially uses two RM to give the dTEC from one epoch to the other and not the absolute value [*Max van de Kamp*, 2012]. Another similar method would be to use the rotation rate rather than the rotation measurements to derive the TEC measurements, shown in Fig. 3.12 [*Klobuchar and Liu*, 1989]. Once again the dTEC rather than absolute value is used. The third method is to use dual-frequency measurements similar to GPS by adding a reference beacon frequency for the next generation satellite or when considering using the methods discussed for other satellite missions.



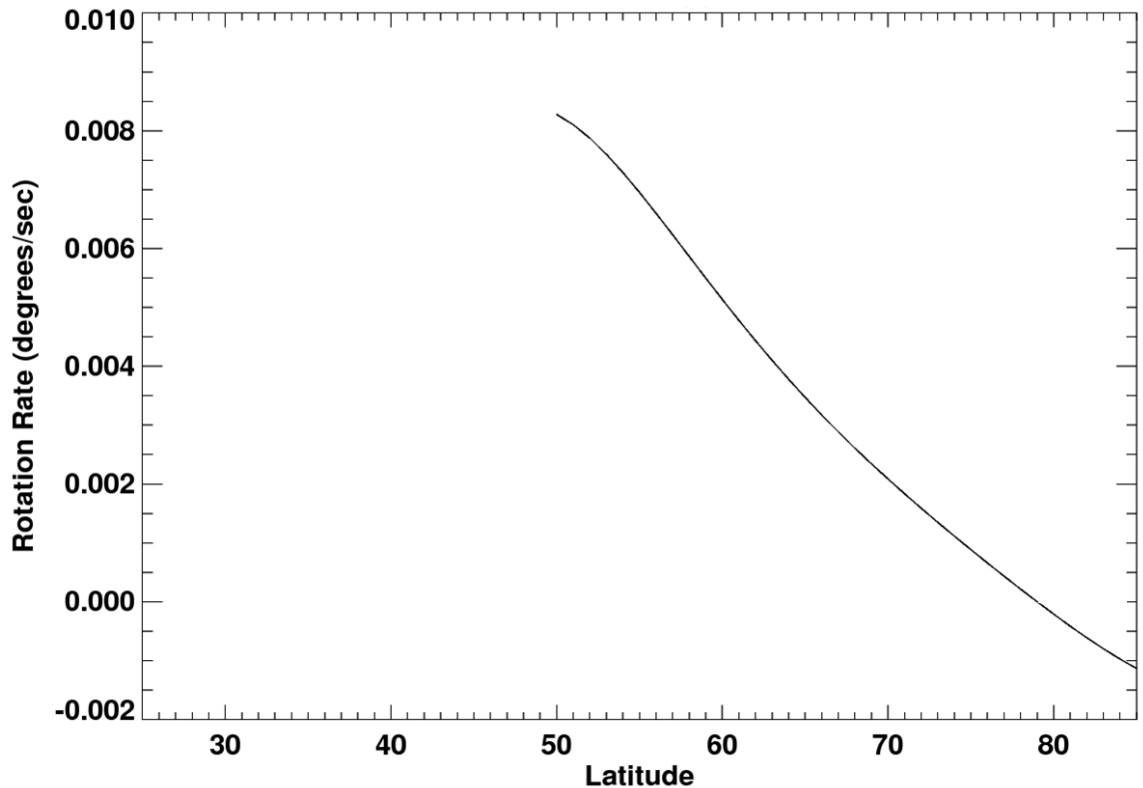


Figure 3.12: Faraday rotation rate

In the worst case scenario (iteration of the existing aircraft and satellite hardware) a reference beacon may be considered to use the dual-frequency method previously discussed with respect to GPS CIT in order to obtain the TEC [Leitinger, 1994; Choi *et al.*, 2006; Selcher, 2007; Max van de Kamp, 2012]. Adding a reference signal may not be practical for ADS-B and AIS, but is a consideration for the design of new satellite missions that could either benefit from using two channels (to avoid signal collisions for example) or wish to pursue the option of producing ionospheric data as a secondary purpose of the satellite mission (e.g. future generations of amateur radio and university satellites).

The rotation for UHF is low enough for effective robust satellite communications, and to avoid the  $n\pi$  ambiguity as the signal will not have multiples of  $\pi$  measured. Higher frequencies such as C-band (4 GHz) would undergo even less rotation, making these frequencies feasible for robust communications however there is not enough

variation to measure FR and subsequently to infer TEC.

In the past, differential GPS measurements have been used to determine the TEC and produce vertical electron density profiles using tomography, among other uses. A comparison of the FR estimates for ADS-B (row 1), GPS L1 (2) and L2 (3) bands, AIS marine channels 87 (4) and 88 (5), and APRS (6) and is presented in Table 3.1. Note that for the GPS carriers, the frequency was applied to a linearly polarized signal because the GPS carrier is in practice circularly polarized and FR does not take place. After consulting the literature, the TEC values were selected to represent a wide range of typical values (and beyond). For example global ionosphere TEC maps can be obtained from *NASA Jet Propulsion Laboratory California Institute of Technology* [2014] NRCan, etc.

Table 3.1: FR as a TEC observable; a comparison of the expected FR from Eqn. 2.11 for ADS-B, GPS L1 and L2, AIS ( 161.975 MHz (ch 87) and 162.025 MHz (ch 88)) and APRS.

Carrier	TEC ( $1 \text{ TEC}_u = 10^{16} m^{-2}$ )			
	1	10	100	1000
	FR (degrees)			
<b>ADS-B</b> 1090 MHz	0.07	0.72	7.19	71.87
<b>GPS L1</b> 1575.42 MHz	0.02	0.22	2.17	21.72
<b>GPS L2</b> 1227.60 MHz	0.03	0.34	3.47	34.66
<b>ch 87 AIS</b> 161.975 MHz	3.38	33.77	<i>337.74</i>	<i>3377.36</i>
<b>ch 88 AIS</b> 162.025 MHz	3.38	33.75	<i>337.52</i>	<i>3375.1</i>
<b>APRS</b> 144.390 MHz	4.62	46.20	<i>461.96</i>	<i>4619.59</i>

The average radial magnetic field was calculated using the IGRF model to be 6542 nT for both AIS and ADS-B at an altitude of 781 km, 3993 nT for GPS at 20200 km , and 7111 nT for APRS at 408 km. AIS satellites orbit between 650–850 km altitude, while APRS satellites are at lower altitudes, such as the ISS at approximately 400 km and HAMSAT (VO-52) at 595–621 km. A value of 55619.13 nT was used for the magnetic field at AIS altitudes and 55625.51 nT for APRS altitudes as a an approximation. The wavelengths used were 0.27 m for ADS-B and 0.19 m and 0.24 m for GPS L1 and L2 respectively. The wavelengths for the VHF band are 1.8509 m,

1.8503 , and 2.0763 m for AIS1, AIS2 and APRS respectively. These characteristic values were selected and used to calculate and to compare the degree of rotation that could be expected for each type of signal using Eqn 2.12, given their respective frequencies and the average radial component of the magnetic field using values from IGRF (5:25 UTC on 19 Oct 2012 at 12.87° latitude and 130°) and the altitude of each satellite system respectively.

The VHF carriers all suffer ambiguous measurements above a certain level of TEC and the values are shown in italics in the table. For APRS, measurements do not suffer  $n\pi$  ambiguity for less than 9 TECu, while both AIS carriers are unambiguous up to approximately 12 TECu. This does not necessarily mean that these data sources can only be used for relatively quiet conditions. Rather than consider the TEC calculated from FR as input to CIT, the change in TEC ( $dTEC$ ) between consecutive epochs can be computed from the change in FR or rotation rate.

## Ionospheric tomography using ADS-B signals

### 4.1 Overview

The scientific results presented in this chapter are based on the following publication:

- Cushley, A. C., and J.-M. Noël, Ionospheric tomography using ADS-B signals, *Radio Sci.*, 49, 2014.

This study examined the potential feasibility of using ADS-B signals transmitted by aircraft, which propagate through the ionosphere to a receiver carried by a LEO satellite, as input to CIT techniques in order to reconstruct 2D maps of the ionospheric electron content. Numerical simulations using synthetic data were performed, which used a single electron density enhancement and five electron density enhancements for the same aircraft distribution.

### 4.2 The Study

It was proposed by *Francis et al.* [2011] that a satellite could act as a receiver for the ADS-B signals and this would improve air traffic surveillance and navigation. In the paper presented in Chapter 4 it was proposed that in addition to tracking aircraft, ADS-B could also be used to map the electron density of the ionosphere. Other researchers have investigated the navigation and operational aspects (improved safety, wide-area surveillance, etc.), while this research is strictly focussed on science. In anticipation of a demonstration satellite, originally scheduled to be launched in 2014, but eventually launched in 2016, this paper simulates an ionosphere and ADS-B signals and applies CIT techniques to recover the ionosphere electron density profiles. It uses the proposed orbital parameters for an ADS-B demonstration satellite that was yet to be launched at the time of the paper's publication.

ADS-B was conceived for ground-based and inter-aircraft monitoring [*ADS-B Technologies*, 2011]. Recent studies have suggested that ADS-B can also be used

to construct 2D electron density maps of the ionosphere. This research sets out to demonstrate that in addition to the benefits for air traffic safety, ADS-B signals can be used for the scientific purpose of CIT. The initial dedicated use of ADS-B is expected to be by air traffic control and for surveillance purposes to enhance pilot situational awareness (and as a surveillance tool in maintaining the sovereignty of Canadian airspace). In addition to the operational purpose, this would create a unique opportunity to obtain scientific data, enabling use as a dual-purpose payload for ionospheric sounding. Specifically, the opportunity may exist to use the FR of these signals for LOS estimates of the relative TEC, which could be used as input to reconstruct images of the ionospheric electron content using CIT techniques.

The topic of ionospheric sounding using ADS-B has not been explored prior to the work by *Cushley* [2013]. In fact, prior to *Francis et al.* [2011] ADS-B receivers had only been used as part of ground based networks for monitoring aircraft regionally and space-based ADS-B aircraft monitoring had not yet been proposed. All previous work involving ADS-B technologies by *Tremblay et al.* [2009]; *Francis* [2009]; *Francis et al.* [2011]; *Castillo et al.* [2012]; *Van Der Pryt* [2014]; *Van Der Pryt and Vincent* [2015a,b, 2016]; *Vincent and Van Der Pryt* [2017]; *Freitag* [2017] focussed on the feasibility of the signal for operational communications and not on their potential scientific uses. At the time that the research for the paper by *Cushley and Noël* [2014] was undertaken, a satellite carrying an ADS-B receiver had not yet been launched. This research sets out to demonstrate the potential of a single payload to not only improve air traffic management, but also to provide scientific observations of the space environment.

A space-borne ADS-B receiver was in its infancy with only concept demonstration satellites such as CanX-7 (launched Sept 2016) to demonstrate that ADS-B signals would be received at orbital altitudes. Considerations for how these signals could be used for other purposes such as ionospheric sounding were not taken into consideration in the satellite design. It was also assumed that since the intended purpose of ADS-B is to track aircraft, the raw data from the payload may not be available publicly for some time. In fact, real-time raw data may never be made publicly available due to

the sensitivity of such information and the risk of signal spoofing.

In the context of information security and network security, a spoofing attack is a situation in which a person or program successfully impersonates another by falsifying data, generally to gain an illegitimate advantage [*Office of Information Technology*, 2013]. In theory, any signal can be spoofed although some may be more difficult than others. The consequences for air traffic control receiving spoofed ADS-B signals may be devastating [*Thurber*, 2012; *Zetter*, 2012].

This research was intended to demonstrate that this data may be used and processed as a data product, or archival data would be useful if it were to be released in the future for longer duration climatological study of the Earth's ionosphere. Ground testing the instrument cannot be used to image the ionosphere due to the aircraft and receiver being co-located; they are both below the ionosphere. In this geometry, measurements of the signal attenuation cannot be taken, let alone the reconstruction of the IEDs for comparison to other methodologies.

The ADS-B signal/frequency was selected for four main reasons:

- it allows for robust communications for it's intended purpose of tracking aircraft yet undergoes measurable perturbation due to the ionosphere;
- the ray spatial sampling density of the ionosphere estimated between multiple aircraft transmitters and (a single) passive satellite receiver throughout its pass;
- the high transmission rate and global coverage available in order to fill the gaps in coverage from ground-based instrumentation such as GNSS receivers.
- In addition, the secondary use of ADS-B for scientific studies of the ionosphere as well as its intended purpose was pursued to support and expedite the launch of an operational ADS-B equipped satellite constellation.

As it was previously described, as electromagnetic waves propagate from the transmitting aircraft through the ionosphere to passive satellite receiver(s) they are modified and present an opportunity to characterize and study the ionospheric medium through which the rays have passed and potentially provide a better understanding

of magneto-ionic wave propagation. The scientific purpose of this study was to investigate the potential exploitation of ADS-B operational data and to contribute to current methods of ionospheric electron density mapping, mainly at high latitudes and in oceanic regions. While the utility of CIT has been shown using differential GPS received at ground stations for ionospheric mapping, there exist the same ground station constraints as ADS-B leaving coverage gaps.

The manuscript describes the ionosphere tomography results using the STEC simulated data for an ADS-B system. Various features of the signal were analysed and ray path modelling was performed. The CIT technique presented in the following manuscript is based on well established techniques, but considering the data source from ADS-B is new, it is an interesting work that will complement the existing ground-based GPS and LEO satellite-based GPS ionosphere TEC data.

One of the main differences in the ADS-B scenario is that the transmitters and receivers positions are inverted. Rather than having a fixed number of satellites being employed as transmitters and receivers that are constrained to land masses or by terrain and infrastructure requirements, the mobile aircraft transmitters are deployable anywhere while it is assumed that the constellation of ADS-B equipped satellites provides full global coverage in order to satisfy the operational requirement of tracking aircraft globally with seamless coverage. These were coined ‘signals of opportunity’ for the purpose of ionospheric sounding since they serve other operational purposes such as tracking aircraft. This is believed to be the first proposed inverted model for CIT, aircraft transmitters (below the ionosphere) and LEO satellite forming a synthetic detector.

While the GPS model requires ground stations, the ADS-B model is governed by the operational requirement; the transmitters are installed on aircraft. The significant difference is that in the ADS-B scenario considerably more aircraft transmitters can be used than the relatively fixed number of GPS transmitting satellites. In many regions, air traffic densities in the FOV exceed the total number of GPS satellites. The constant fast-moving LEO satellite forms a synthetic row of receivers similar to a synthetic aperture radar (SAR), which creates a more dynamic sampling geometry

for projections and a more spatially dense basis for CIT.

This work shows that ADS-B signals can potentially alleviate gaps in coverage for GIMs and air traffic monitoring concurrently. Although these problems may seem unrelated, even at 9100 m (30 000 feet) ASL, and despite the protection afforded by the magnetosphere, harmful effects of energetic particle radiation from the Sun are still a serious concern for aircrew and passengers on trans-polar flights. Airlines often alter flight plans to longer, less efficient and more costly routes away from the magnetic pole, sometimes when an aircraft is already in flight [*CSEW6 steering committee*, 2009]. In both instances, the solution is to use a space-based rather than a ground-based array of sensors because they are less constrained in terms of achieving global coverage.

Using aircraft, the models extend easily to all regions of the globe including polar and mid-oceanic regions where ground stations are difficult to install, and where data is otherwise unavailable. This model will reduce the ground dependence and data collection is essentially redundant from the operational purpose of flight safety, for CIT. The elimination of ground stations yields a more economically feasible model for CIT, also permitting output to be produced over dynamic geometry, with a particular potential of complementing measurements by other techniques.

As described in subsection 3.4.3, in addition to supplementing GIMs of the VTEC, the raw STEC data collected by ADS-B can be used the same way GNSS station STEC data is also used to produce 2D electron density maps of the ionosphere using CIT. The STEC measurements, or the sum of the electron content along the ray paths from transmitting aircraft to the passive satellite receivers, were inverted and reconstructed to acquire a 2D  $n_e$ -profile along a slice of longitude.

The FR was modelled using a modified version of the University of Saskatchewan's enhanced Polar Outflow Probe (ePOP) satellite's HF (3-30MHz) Radio Receiver Instrument (RRI) detection model that was originally developed for the SuperDARN radars. The ray tracing program was used to determine the characteristics of the EM-wave, including the wave path and the full polarization state at the satellite receiver [*Gillies*, 2006]. This methodology was extended for characterization of UHF



(1090 MHz) radio waves.

The paper shows that ADS-B data can be used to reconstruct two-dimensional electron density maps of the ionosphere using techniques from computerized tomography. The modelled Faraday rotation is determined and converted to TEC along the ray-paths. The resulting TEC is input for CIT algorithm ART based on using Eqn. 3.1. This study concentrated on mesoscale structures 100–1000 km in horizontal extent.

This chapter outlines the study that was undertaken, and describes the experimental procedures that were used to obtain the solution to the CIT problem, using ADS-B data for global TEC measurement, and  $n_e$ -profile reconstruction from the first air-space system. Although this method can extend to other regions, current work was guided by a demonstrator satellite design, and mission of data collection only over the Hudson Bay AOI. The required input parameters for reconstruction, method, procedures of the ADS-B CIT reconstruction experiment are discussed.

The minimum number of aircraft, which spanned the reconstruction expanse ( $\sim 25^\circ$ ) for the Hudson bay AOI was chosen to be 5 in *Cushley* [2013]. Additional correspondence with Nav Canada confirmed that the air-traffic density in the Hudson Bay AOI is 25 aircraft on average at a given time [*Burridge*, 2009].

To facilitate the investigation into the feasibility of using ADS-B signals for CIT, the following assumptions were made:

- A proper antenna can be carried by a satellite in an appropriate orbit. In other words, it was assumed the ADS-B receiver is already in space, and the satellite orbit is LOS to the transmitting aircraft.
- Quasi-static ionospheric structures of dimensions ranging from tens to thousands of kilometres will not vary significantly over the time over which data is collected by GPS radio tomography stations [*Yizengaw et al.*, 2004; *Andreeva et al.*, 2001]. For a single LEO satellite LOS time to observers on the ground is much less than GPS so the structures are relatively stationary.
- Characteristic air traffic density was assumed to be that for the Hudson Bay

AOI.

- The number of transmitters can be increased. Although GPS ground stations are low cost, aircraft can be deployed in formation flight much easier than ground stations set-up due to terrestrial obstacles, lack of infrastructure, or lack of a stable platform (oceanic regions).
- Feasibility of ADS-B CIT in 2D should be indicative of whether feasibility in 3D should be investigated further.

### 4.3 Published Paper

The analysis and modelling of synthetic ADS-B data using 25 aircraft as ADS-B transmitters and one satellite at the altitude of 1000 km as ADS-B receiver discussed in this chapter was published in *Radio Science* in 2014. Presented immediately below is the paper in the journal format reproduced by permission of American Geophysical Union:

- Cushley, A. C., and J.-M. Noël, Ionospheric tomography using ADS-B signals, *Radio Sci.*, 49, doi:10.1002/2013RS005354, 2014. Copyright 2014 American Geophysical Union.



## RESEARCH ARTICLE

10.1002/2013RS005354

## Key Points:

- The modeled ionospheric electron densities were reconstructed using CIT
- Mesoscale ionospheric features can be detected without a priori knowledge

## Correspondence to:

A. C. Cushley,  
alex.cushley@rmc.ca

## Citation:

Cushley, A. C., and J.-M. Noël (2014), Ionospheric tomography using ADS-B signals, *Radio Sci.*, 49, doi:10.1002/2013RS005354.

Received 4 DEC 2013

Accepted 7 JUL 2014

Accepted article online 12 JUL 2014

## Ionospheric tomography using ADS-B signals

A. C. Cushley<sup>1</sup> and J.-M. Noël<sup>1</sup>

<sup>1</sup>Department of Physics, Royal Military College of Canada, Kingston, Ontario, Canada

**Abstract** Numerical modeling has demonstrated that Automatic Dependent Surveillance Broadcast (ADS-B) signals can be used to reconstruct two-dimensional (2-D) electron density maps of the ionosphere using techniques for computerized tomography. Ray tracing techniques were used to determine the characteristics of individual waves, including the wave path and the state of polarization at the satellite receiver. The modeled Faraday rotation was computed and converted to total electron content (TEC) along the raypaths. The resulting TEC was used as input for computerized ionospheric tomography (CIT) using algebraic reconstruction technique. This study concentrated on reconstructing mesoscale structures 25–100 km in horizontal extent. The primary scientific interest of this study was to show that ADS-B signals can be used as a new source of data for CIT to image the ionosphere and to obtain a better understanding of magneto-ionic wave propagation.

## 1. Introduction

Automatic Dependent Surveillance Broadcast (ADS-B) is a technology developed to track the position and movement of aircraft through intermittent broadcasts of their identity, itinerary, and position state vectors to ground-based receivers and other aircraft within range. The system is intended to replace radar as the standard for air traffic control by providing an enhanced ranging and separation distinction capability with a reduced footprint for ground support infrastructure [Marsh, 2006; Brown and Hendricks, 2011; ADS-B-Technologies, 2011].

ADS-B networks that monitor air traffic have already been deployed around the world in high-volume air traffic areas; however, ground stations cannot be installed mid-ocean and are difficult to maintain in the Arctic. The lack of coverage over oceanic and high-latitude airspace has hampered further development. Francis *et al.* [2011] have suggested that ADS-B receivers could be deployed on a constellation of satellites to allow for worldwide tracking of aircraft, alleviating this problem.

CanX-7 [University of Toronto Institute for Aerospace Studies Space Flight Laboratory, 2014], an ADS-B capable nanosatellite has been assembled, integrated, and tested to validate this idea, but a launch has yet to be brokered. CanX-7 is a demonstration mission that will use a lightweight, deployable drag sail to achieve the deorbit requirements of the Inter-Agency Space Debris Coordination Committee. Prior to deploying its four drag sails, CanX-7 will be among the first satellites in the world to evaluate the use of an ADS-B receiver in space [Shmuel *et al.*, 2012; University of Toronto Institute for Aerospace Studies Space Flight Laboratory, 2014].

The launch of an ADS-B receiver on a satellite will create a unique opportunity to study the propagation of 1090 MHz radio waves through the ionosphere from the transmitting aircraft to the passive satellite receiver(s).

The 1090 MHz ADS-B signal was selected for research conducted in space mission analysis and design at the Royal Military College of Canada (RMCC) due to its global adoption as the standard mode of ADS-B, especially for larger aircraft [Tremblay *et al.*, 2009]. Moreover, for this study, the ADS-B signal was selected for several other reasons: the ADS-B frequency allows for robust operational communications and measurable perturbation due to ionospheric effects, the spatially dense data set estimated by the geometry between multiple transmitting aircraft and the passive satellite receiver(s), and to support and expedite the launch of an operational ADS-B constellation.

When electromagnetic (EM) waves propagate through the electrically charged ionosphere in the near-Earth space environment, they are modulated and can provide an exceptional opportunity to model the medium through which they have passed. Modeling the electron density of Earth's ionosphere (and plasmasphere), in general, is essential in determining the state of ionospheric activity. This information can be used to

correct for propagation delays in satellite communications, predicting space weather, as well as ionospheric disturbances due to geomagnetic storms and solar flares [Jin *et al.*, 2006].

This work sets out to demonstrate the potential dual purpose of a single payload for improving air traffic management as well as scientific observation of the ionosphere. The topic of ionospheric modeling using ADS-B has not been explored prior to this work [Cushley, 2013]. All previous work surrounding ADS-B technologies by Tremblay *et al.* [2009], Francis [2011], Francis *et al.* [2011], Castillo *et al.* [2012], and VanDerPryt [2014] have focussed on the feasibility of the signal for operational communications and not on their potential scientific benefits. The scientific purpose of this study is to investigate the potential exploitation of ADS-B operational data and to contribute to current methods of ionospheric electron density mapping, mainly at high latitudes and in oceanic regions.

The primary benefit of using ADS-B is to improve flight safety and efficiency by providing timely, cost-effective wide-area surveillance. Since the full potential of the scientific model presented in this study cannot be realized until a constellation of ADS-B receivers are in orbit, an impending objective is to support the immediate use of ADS-B air traffic control from space.

In order to characterize the ionospheric electron content under different aircraft placement scenarios, ray-path geometries, geomagnetic, and solar conditions, the current study combines knowledge that can be extracted from EM wave propagation theory and ionospheric electron density and geomagnetic models to produce independent static data of the wave path and polarization state that will be received at the satellite receiver.

## 2. Theory

### 2.1. Faraday Rotation

The ionosphere is assumed to be a circular birefringent medium due to the Earth's magnetic field [Hartmann and Leitinger, 1984; Orfanidis, 2008]. Any EM wave propagating through a magnetized plasma decomposes into two propagation modes which have different indices of refraction and polarizations due to the terrestrial magnetic field. Two modes of propagation, called the ordinary and extraordinary modes or *O* mode and *X* mode, respectively, exist in the ionosphere [Chen, 1984]. When collisions between neutral and charged particles are neglected, the refractive indices of the two modes are given by the Appleton-Hartree equation [Hartree, 1929; Appleton and Builder, 1933]:

$$n^2 = 1 - \frac{X}{1 - \frac{Y^2 \sin^2 \theta}{2(1-X)} \pm \sqrt{\frac{Y^4 \sin^4 \theta}{4(1-X)^2} + Y^2 \cos^2 \theta}} \quad (1)$$

where  $\theta$  is the aspect angle of the wave,  $X$  and  $Y$  are the ratios of the plasma frequency  $\omega_p$ , and gyrofrequency  $\omega_c$  to the radio wave frequency  $\omega$  respectively [Schunk and Nagy, 2000], namely,

$$X = \left(\frac{\omega_p}{\omega}\right)^2, \quad Y = \frac{\omega_c}{\omega} \quad (2)$$

The plasma frequency describes the oscillation of the electron density for a cold neutral plasma. If thermal motion is neglected and electrons are displaced with respect to the relatively heavy ions, the Coulomb force acts as a restoring force.

The refractive index for the two modes is determined by the positive (*O* mode) and negative (*X* mode) sign of the denominator in equation (1). Since the two modes have different refractive indices, the phase velocities ( $v_\phi$ ) are different for each mode of propagation [Budden, 1961; Chen, 1984]. The resulting imbalance between the phase velocities produces a change in the orientation angle of the polarization ellipse [Budden, 1961; Canada Centre for Remote Sensing, 2007], which is known as Faraday rotation.

Examining the cases when propagation of the wave is parallel or antiparallel to the external magnetic field (i.e., the aspect angle  $\theta = 0^\circ$  or  $\theta = 180^\circ$ ), the index of refraction for each mode is given by [Chen, 1984]

$$n^2 = \frac{c^2}{v_{\phi(O)}^2} = 1 - \frac{\omega_p^2/\omega^2}{1 + \omega_c/\omega} \text{ (O mode)} \quad (3)$$

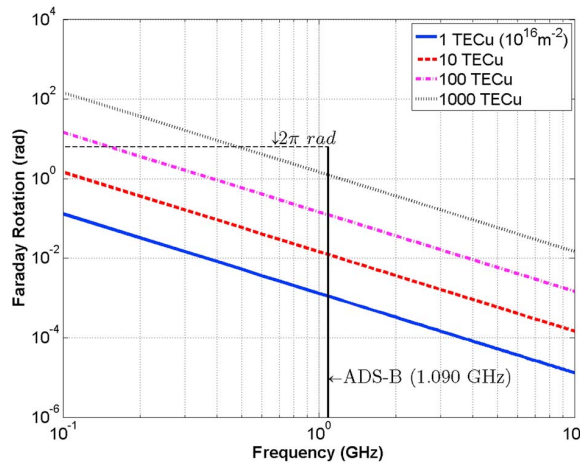


**Figure 1.** Faraday rotation increases as a function of TEC and decreases as a function of frequency. The solid vertical black line indicates the 1.090 GHz ADS-B frequency. The dashed horizontal black line denotes a full  $2\pi$  rotation of the Faraday rotation. This is the point at which there is a  $2\pi$  ambiguity in the measurement of the Faraday rotation.

$$n^2 = \frac{c^2}{v_{\phi(X)}^2} = 1 - \frac{\omega_p^2/\omega^2}{1 - \omega_c/\omega} \quad (X \text{ mode}) \quad (4)$$

where  $c$  is the speed of light in a vacuum.

The magnitude of the rotation is proportional to the integrated product of the electron density,  $n_e(l)$ , along the raypath or plasma column and the strength of the parallel component of the magnetic field  $b_z(l)$  and inversely proportional to the square of the frequency as follows [Gurnett and Bhattacharjee, 2005]

$$\Omega \simeq \frac{1}{2c} \frac{e^3}{\epsilon_0 m_e^2} \frac{1}{\omega^2} \int_0^l n_e b_z dl \quad (5)$$

where the Faraday rotation,  $\Omega$  is in radians,  $c = 3 \times 10^8$  m/s is the speed of light,  $e = 1.602 \times 10^{-19}$  C is the elementary charge,  $m_e = 9.109 \times 10^{-31}$  kg is the mass of an electron, and  $\epsilon_0 = 8.854 \times 10^{-12}$  C<sup>2</sup>/N m<sup>2</sup> is the vacuum permittivity. The magnetic field  $b_z$  is in nanotesla.

In the absence of a magnetic field,  $\omega_c = 0$  and there is only one refractive index. As a result, there is no separation of the modes and there is no difference in the rate of change in the polarization angle, and hence, Faraday rotation does not occur Chen [1984].

The total electron content (TEC) along the path or within the plasma column of unit cross section is defined by

$$\text{TEC} = \int_0^l n_e dl \quad (6)$$

where TEC is the integrated electron density  $n_e$  along the path length  $l$ .

Using the ADS-B wavelength in equation (5), the Faraday rotation can be written as,

$$\Omega = 1.974 \times 10^{14} \int_0^l n_e b_z dl. \quad (7)$$

$$\Omega = 1.974 \times 10^{14} B_{\text{avg}} \text{TEC}. \quad (8)$$

where  $B_{\text{avg}}$  is the average  $z$  component of the magnetic field of the satellite. In equation (7) the vertical component  $b_z$  was assumed to be a constant value  $B_{\text{avg}}$ . The TEC values are computed using equation (8) for the modeled Faraday rotation. The average magnetic field  $B_{\text{avg}}$  was computed using the International Geomagnetic Reference Field model data [International Association of Geomagnetism and Aeronomy, Working Group V-MOD et al., 2010]. The TEC values and ray endpoints are used as the input to computerized ionospheric tomography (CIT) in order to reconstruct the resulting electron density maps.

In Figure 1 we show plots of equation (5) for given values of TEC ranging from 1 TEC unit (1 TECU =  $10^{16}$  el m<sup>-2</sup>) to 1000 TECU as a function of frequency. Although TEC is highly variable, typically, the daily global maximum TEC is found to range between 80 and 200 TECU over equatorial regions at solar maximum conditions [Wahi et al., 2005; Zhao et al., 2009; NASA Jet Propulsion Laboratory California Institute of Technology, 2014] and generally decreases with latitude [Soicher and Gorman, 2012]. We remind the reader that if the intended use of ADS-B is robust operational communications in support of air traffic safety and that if signal modulation and degradation are generally undesirable, the ADS-B frequency is a very unique selection. A signal having a lower frequency would undergo a greater amount of Faraday rotation yielding better data for CIT but could become unusable or infeasible due to volume, power, and mass considerations for communications between aircraft and satellites due to the requirement of higher-gain transmitters

**Table 1.** Faraday Rotation as a TEC Observable; a Comparison of the Expected Faraday Rotation From Equation (5) for ADS-B and GPS L1 and L2

TEC (1 TECU = $10^{16}$ m <sup>-2</sup> )	Faraday Rotation (deg)		
	ADS-B	GPS L1	GPS L2
1	0.6	0.3	0.5
5	3.1	1.5	2.4
10	6.1	3.0	4.8
20	12.2	6.0	9.6
40	24.4	12.0	19.1
100	61.1	30.0	47.8
200	122.2	59.9	95.6

and/or larger antennas. A signal with a much higher frequency would propagate through the medium relatively unaffected and therefore would be suitable for communications, but the Faraday rotation may not be detectable and could not be amenable for this type of study. It is evident from Figure 1 that the amount of Faraday rotation expected for the ADS-B transmission even for unrealistically high values of TEC is clearly less than  $2\pi$  radians. Therefore, we would not expect a  $2\pi$  ambiguity for the ADS-B operating frequency.

Table 1 shows a comparison of the Faraday rotation estimates for ADS-B and GPS L1 and L2 bands. From a variety of literature sources, for example, global ionosphere TEC maps can be obtained

from NASA Jet Propulsion Laboratory California Institute of Technology [2014], characteristic TEC values were selected and a calculation performed to compare the degree of rotation expected for each. Using equation (5) and the TEC values shown in Table 1, the Faraday rotation was determined for both GPS L1 and L2 bands as well as ADS-B. The magnetic field used was 55,639.51 nT for ADS-B at 1000 km altitude and 55555.55 nT for GPS at 20,200 km respectively. The wavelengths used were 0.27 m for ADS-B and 0.19 m and 0.24 m for GPS L1 and L2 respectively. The first column of Table 1 shows the TEC values used in equation (8). The second column shows the amount of Faraday rotation computed for the ADS-B frequency for each of the TEC values. The second and third columns show the amount of Faraday rotation computed for the GPS L1 and L2 bands, respectively.

Most notable in Table 1 is the comparison of the Faraday rotation between ADS-B and GPS. For a given TEC value the Faraday rotation will be greatest or have more variation as a TEC observable for the ADS-B carrier frequency than for either GPS carrier.

### 2.2. Ray Tracing

An EM wave ray tracing model developed by Gillies *et al.* [2007] was used to generate simulated ADS-B data to determine the wave path and the polarization state received at the satellite. The ray trace program, based on the ray formalism developed by Haselgrove [1963], uses equation (5) to determine the indices of refraction of a radio wave in a magneto-ionic medium used in the ray tracing equations. This model provides the group velocity and rate of change of the wave vector direction. Inputs to the ray trace program include the initial wave vector direction, the wave frequency, and a set of propagation conditions such as the magnetic field vector and an electron density profile for the ionosphere. The program computes the path of the wave for a given frequency that both the *O* mode and *X* mode takes from the fixed initial position of the transmitter to a specified position of the satellite carrying the receiver.

The initial polarization orientation of the wave leaving the aircraft must be known. For the current purpose of this work all waves were assumed to be vertically plane polarized [*Radio Technical Commission for Aeronautics*, 2003; *Haque et al.*, 2013]. In reality, the initial polarization of the wave may be different but would be constant for any given aircraft. While aircraft orientation (banking and climbing) also affects the orientation of the transmitted signal, that information is part of the ADS-B packet, and the initial orientation of the polarization can be determined. For the purpose of tomography the initial orientation does not necessarily need to be known since the rate of rotation over consecutive epochs (between aircraft-satellite pairs) rather than the absolute value can be used [*Klobuchar and Liu*, 1989]. In the worst case scenario (iteration of the existing aircraft and satellite hardware) a reference beacon may be considered to use the dual frequency method used often in GPS CIT to obtain the TEC [*Choi et al.*, 2006; *Max van de Kamp*, 2012].

The ray trace program was used to generate TEC outputs from rays that passed from given locations, at a given elevation angle through a 2-D electron density profile to a specified satellite location [*Gillies*, 2006, 2010; *Gillies et al.*, 2007]. An example of the raypath density for a subset of the modeled raypaths is shown in Figure 2. This example shows one tenth of the possible raypaths transmitted from three aircraft transmitters to a single-satellite receiver throughout its pass. The aircraft are located at 70°, 73°, and 81° of geographic latitude and 11 km altitude while the satellite orbit is at 1000 km altitude. The rays

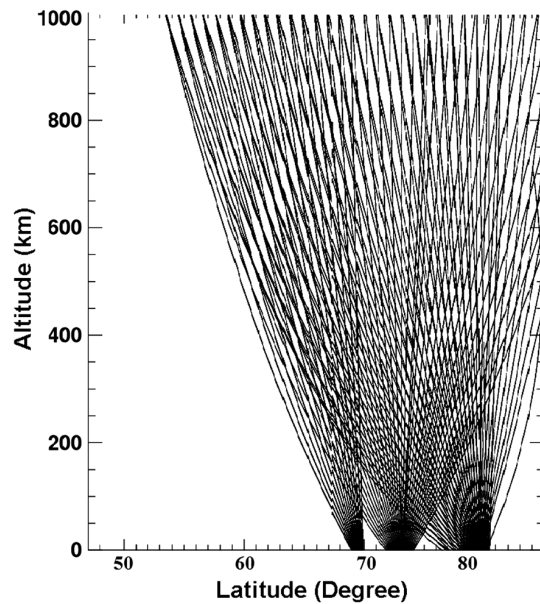


**Figure 2.** Plot of the raypath density for a subset of the modeled ray data. We present this example to show the apparatus with one tenth of the possible raypaths for 3 min duration using three aircraft transmitters to a single satellite throughout its pass.

originate from sea level (0 km), but the electron densities below 60 km were zero and did not contribute to the modeled values of Faraday rotation.

The model was used to show that the Faraday rotation of the signals received by the satellite should be detectable. Previous work by Yueh [1999] has shown that Faraday rotation can be used to obtain the TEC along the paths. The computed TEC and raypath geometry are then used to reconstruct the electron density profile that the EM waves propagated through.

In Figure 3 (left) we show an electron density profile generated using the International Reference Ionosphere (IRI) [Bilitza, 2007; Bilitza et al., 2011] that was used to produce the uniform standard quiet background electron density map shown in Figure 3 (right). This uniform electron density map was used to superimpose all the modeled density enhancements to create 2-D electron density maps to pass rays. These new maps were used as

input to the model to simulate a ray leaving from an aircraft, passing through the enhancement, and finally, being received by the satellite. Measuring (or modeling in this case) the polarization angle of the received wave and knowing the initial polarization of the wave, the Faraday rotation for the raypath can be calculated.

### 2.3. Reconstruction

In mathematical models of physical phenomena, a problem is said to be well posed if it satisfies three conditions: the solution exists, the solution is unique, and the behavior of the solution does not change dramatically when a small change in the initial conditions is introduced. Otherwise, the problem is said to be

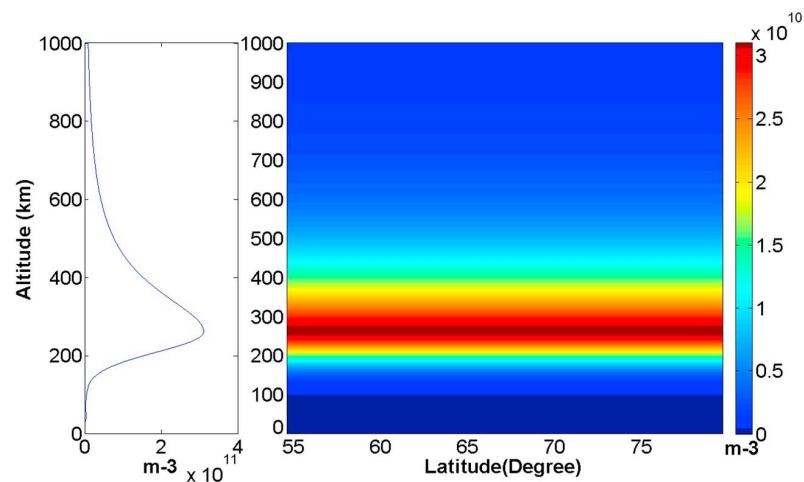


**Figure 3.** (left) Initial electron density profile for geomagnetically quiet conditions. (right) A contour plot of the initial electron number densities prior to the addition of the enhancement.

ill posed [Hadamard, 1902]. Examples of ill-posed problems are inversion problems such as the inverse heat problem or computerized tomography.

Since Austen et al. [1986] proposed the possibility of satellite radio tomography, also known as CIT, the study of detailed features of the ionosphere and plasmasphere have become possible by means of tomographic reconstruction. In applications such as CIT, for noisy, or incomplete data sets, using pixel-based methods has been shown to have advantages [Tessa et al., 2007]. Each pixel represents a region of space in the ionosphere. The intensity of the pixel is the average value of the measured physical property, generally, the amount of attenuation, or in the case of this study the Faraday rotation which is proportional to the electron density. The most commonly used pixel-based method of CIT is the algebraic reconstruction technique (ART). ART forms the basis of most of the other pixel-based methods, e.g., Simultaneous Algebraic Reconstruction Technique and Simultaneous Iterative Reconstruction Technique [Tessa et al., 2007]. The ART algorithm can be implemented using the following equation [Choi et al., 2006].

$$N_e^{k+1} = N_e^k + \lambda_k \frac{\text{STEC}_i - \sum_{j=1}^{\rho} d_{ij} n_{ej}^k}{\sum_{j=1}^{\rho} d_{ij} d_{ij}} D_i \quad (9)$$

where  $j$  is the pixel number,  $k$  is the iteration number,  $\lambda_k$  is a relaxation parameter,  $N_e^k$  is a vector of the ionosphere electron densities  $(n_{ej}^k)$  for the  $k$ th iteration,  $N_e^{k+1}$  is a vector of the modified values of the electron densities  $(n_{ej}^{k+1})$  for the next  $k$ th + 1 iteration. The vector  $\text{STEC}_i$  contains the TEC measurements taken over various elevation angles and slant ranges. The  $\text{STEC}_i$  contribution to pixel  $j$  from ray  $i$  in the matrix  $D$  is  $d_{ij}$ . The  $i$ th row of  $D$  is  $D_i$ , and  $\rho$  is the total number of pixels in the reconstruction grid. The matrix  $D$  relates the ray data to the pixels in the reconstruction grid; there is a row for each ray, and column for each pixel in the reconstruction grid (100 × 100). We will discuss the logical matrix  $D$  in more detail below.

The ART method is affected by numerical uncertainties that are introduced by inconsistencies in the system of equations. It is possible to reduce the effect of the uncertainties by using a relaxation parameter  $\lambda_k$ . The relaxation parameter maintains the stability of the numerical method and was chosen to be constant for each iteration. The value for  $\lambda_k$  is confined between  $0 < \lambda_k < 2$ . An in-depth study of the effect of  $\lambda_k$  on the reconstructions was not performed in this work, and the relaxation parameter was not optimized. After considering the literature sources for GPS CIT using ART, a value of  $\lambda_k = 0.005$  was used for all iterations [Choi et al., 2006].

The ART technique converges relatively rapidly and can use an initial guess or a priori estimate to perform the reconstruction. Although many other methods and algorithms exist ART has been widely used and is well documented. For this particular investigation on the feasibility of using ADS-B occultation data as an input to CIT, ART was considered to be a good method for a first-order evaluation.

The ART algorithm is a method by which an ill-posed linear algebraic problem can be solved. The system of linear equations may be written as

$$A\vec{x} = \vec{p}. \quad (10)$$

where  $\vec{x}$  is a vector of unknown pixel values,  $\vec{p}$  is a column vector of measured values, and  $A$  is a matrix in which its rows relate the contribution of each measured value  $p$  to the determination of the individual unknown pixel values  $x$ . We note that the Faraday rotation measurements from ADS-B signals, once they have been converted to slant TEC (STEC), is a system of equations of the same form as equation (10) and can be written as follows:

$$\text{STEC}_i = \int_0^l N_e(j) dl. \quad (11)$$

where  $N_e(j)$  is a vector of  $j$  unknown pixel values and  $dl$  is an element of the matrix  $D$ , which relates the contribution of the measured value of  $\text{STEC}_i$  to pixel  $n_{ej}$ .



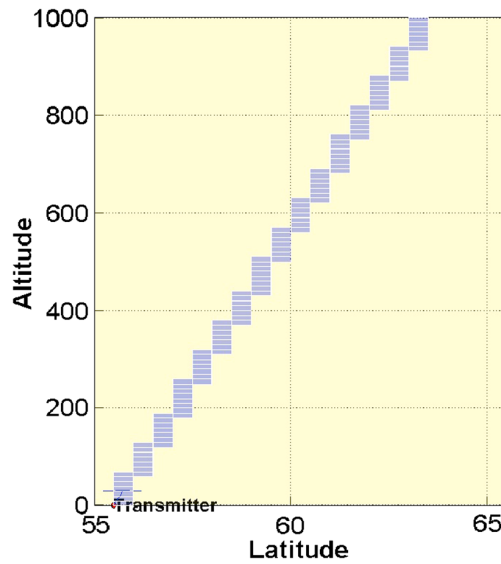


**Figure 4.** ADS-B signal passing through illuminated pixels (blue) within a portion of the 2-D reconstruction grid (yellow).

We can write the problem in mathematical form as a system of linear equations for which the unknown pixel value  $n_{ej}$  must be solved as follows:

$$\begin{aligned} d_{11}n_{e1} + d_{12}n_{e2} + d_{13}n_{e3} + \dots + d_{1j}n_{ej} &= \text{STEC}_1 \\ d_{21}n_{e1} + d_{22}n_{e2} + d_{23}n_{e3} + \dots + d_{2j}n_{ej} &= \text{STEC}_2 \\ d_{31}n_{e1} + d_{32}n_{e2} + d_{33}n_{e3} + \dots + d_{3j}n_{ej} &= \text{STEC}_3 \\ &\vdots \\ d_{i1}n_{e1} + d_{i2}n_{e2} + d_{i3}n_{e3} + \dots + d_{ij}n_{ej} &= \text{STEC}_i \end{aligned} \quad (12)$$

Equation (12) can be written more compactly as follows:

$$\text{STEC}_i = \sum_{j=1}^{\rho} n_{ej}d_{ij} + \Delta_i \quad (13)$$

where  $\Delta_i$  is the uncertainty associated with pixel  $j$  (due to discretization errors and measurement noise). The STEC measurement of the raypath can be represented as a series of finite summations of shorter integrals along segments of the raypath

length  $d_{ij}$ ; it is the contribution of ray  $i$  to pixel  $j$ . For each and every STEC measurement, there is an equation of the form of equation (13).

The matrix  $D$  is often called the geometry matrix or the weight matrix. The simplest form for the geometry matrix is a logical index with a row depicting each ray and columns for each pixel value in the reconstruction grid. Each element in  $D$  has a value of 1 if the ray contributes to the pixel value and 0 otherwise. Stated another way, if the ray passes through the pixel, it is assigned a value of 1; otherwise, it is assigned a value of 0. The geometry matrix can be made to be more elaborate based on several other factors such as the length segment of the ray for each pixel or the relationship of a pixel to its neighboring pixels [Max van de Kamp, 2012], but these elaborations were not considered in this study.

A rectangular grid was selected to represent a 2-D slice of the ionosphere as shown in Figure 4. To represent the interior structure of the ionosphere, the grid was created by subdividing using a constant  $\Delta z = 10$  km in altitude from the Earth's surface and a constant  $\Delta\theta_l = 0.25^\circ$  in terms of the geographic latitude.

The end points for each ray are available from the GPS positions of the time-tagged ADS-B transmissions, and the satellite's onboard GPS receiver. For illustrative purposes, a single ray leaving the transmitter and assuming a straight line approximation, the pixels in blue would be assigned a value of 1, while those in yellow would be assigned a value of 0. For this experiment several different grid sizes ( $g_x \times g_y$ ) were tested. For all the results in this paper a grid of  $100 \times 100$  pixels having intervals of 10 km in altitude and  $0.25^\circ$  in latitude was selected. When a ray is passed through the grid, it intersects a relatively small subset of the total pixels available in the grid. The resulting  $D$  matrix is very sparse with  $\sim 99\%$  of cells being zero. The result is that we have a noninvertible problem to solve. The depth of the pixels in the grid  $g_z$  or the longitudinal extent over which data were simulated and for which the 2-D reconstruction was representative of the electron density was chosen to be  $1^\circ$  (i.e., the electron density was assumed to be uniform over a  $1^\circ$  slice of longitude).

Each pixel  $j$  has intensity  $n_{ej}$  (an element of  $N_e$ , calculated using equation (9)), representative of the relative electron density in a volume over which the electron density is assumed to be constant. The value of each pixel represents the incremental electron density along the raypath which contributes to the total amount of Faraday rotation at the receiver. Since the electron densities are not measured directly, the projections of the total Faraday rotation along each path can only determine the electron density relative to the other pixels. The index  $j$  is the pixel number used in the reconstruction grid, where  $1 \leq j \leq \rho \sim 10^4$ . It is also the number of terms in equation (13). The index  $\rho$  is the total number of pixels that are used in the reconstruction grid where  $\rho = g_x \cdot g_y = 10,000$ .

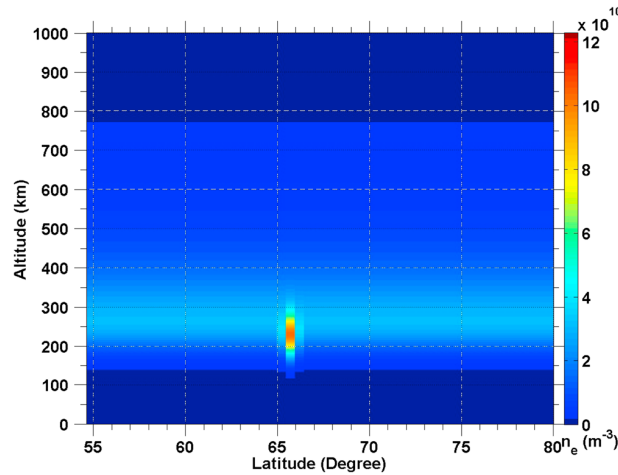


**Figure 5.** Single feature electron density profile; scaling factor = 5.0, full width (in latitudinal extent) at half maximum = 0.25°, vertical extent = 50 km, latitude = 65.5°, and altitude = 225 km.

Rather than working with a large system of equations, the matrix notation is used where we define

$$STEC_{i \times 1} = D_{i \times j} \times N_{e \ j \times 1} + E_{i \times 1} \quad (14)$$

where STEC,  $E$ , and  $N_e$  are column vectors of  $i$  measurements of STEC,  $i$  associated error values, and  $j$  unknown pixel values  $n_{ej}$ , respectively.  $D_{i \times j}$  is the geometry matrix, with  $d_{ij}$  equal to 1 if ray  $i$  passes through pixel  $j$  and 0 otherwise as shown in Figure 4.

Although the region can be represented as a system of linear equations, essentially,  $i$  equations with  $j$  unknowns, with  $n_{ej}=10,000$  values to solve, this is considered to be an under-determined ill-posed problem. The

STECh is the known modeled or mea-

sured quantity while  $D$  is computed from the time-tagged aircraft and satellite state vectors. Both can be obtained from a GPS receiver on board the ADS-B equipped satellite.

The ART inversion algorithm was used to determine the unknown pixel intensity  $n_{ej}$ . Using a successive iteration approach, the pixel intensities are modified to allow the projection through the pixels ( $DN_e$ ) to approach the measured projection (STECh).

The effect of the curvature of the Earth was taken into account in the ray tracing program by calculating the elevation as a function of range-to-target height integrated through the input electron density and geomagnetic model. This was shown to be computationally intensive; so for the purposes of our reconstructions of the rays, a line-of-sight approximation was used. This means that we neglected diffraction, bending, or refraction due to the Earth's atmosphere, as well as attenuation or absorption of energy by the gases in the atmosphere. In general, only the aircraft and satellite positions and Faraday rotation measurements, from which the STECh values are computed, will be available.

### 3. Results

The satellite (nominally at an altitude of 1000 km and in a Sun-synchronous circular orbit) was simulated using a commercial software called Systems Tool Kit (STK). STK was used to calculate the line-of-sight access time, which determines the CIT data integration time and temporal resolution of the reconstructions. The temporal resolution was determined to be between 3 and 4 min for different satellite passes. The worst case scenario of 3.005 min (182.3 s) was used in all of the reconstructions in this paper.

We assumed that the ionosphere remained constant for the 3–4 min duration of the satellite pass with mutual coverage to all aircraft used. This time of mutual visibility and the average interval between ADS-B signal transmissions (which are randomly broadcast between 0.4 and 0.6 ms for an average interval of 0.5 ms) determined that the maximum number of rays for each aircraft-satellite pair was 118, with satellite receiver positions spaced by no less than 0.087° in latitude, thereby limiting the number of rays per aircraft during mutual line-of-sight access. This is analogous to fixing the number of detectors in a computed tomography (CT) machine to 118 and representing the maximum number of detectors that form the projections during the satellite pass.

To simulate a realistic scenario, 25 aircraft were distributed over the latitude between 54.63° and 79.80°, unequally spaced resulting in 2950 rays (i.e., 25 aircraft, 118 rays per aircraft-satellite pair) for a single-satellite pass that was visible to all aircraft from 61.96° to 72.14° in latitudinal extent. The aircraft were separated by no less than 50 mi (~80 km or 0.7°) to represent the best case along-track interaircraft spacing that is permitted by far-field radar regulations for a single flight level [TransportCanada, 2012].

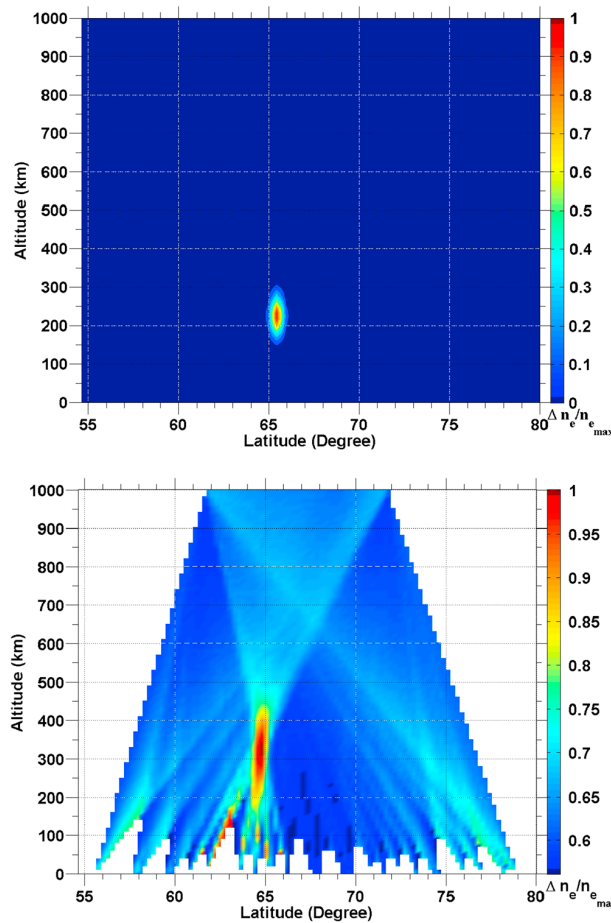


**Figure 6.** (top) Single feature electron density profile shown as relative weight; scaling factor = 5.0, full width at half maximum =  $0.25^\circ$ , vertical extent = 50 km, latitude =  $65.5^\circ$ , and altitude = 225 km. The profile was normalized relative to the peak density. (bottom) Raw reconstructed relative electron density profile of ray trace input above using TEC measurements and line-of-sight path. Regions where no data for reconstruction were available are shown in white.

Using these modified maps as input to the ray trace program is analogous to using the Shepp-Logan head Phantom as the input for medical imaging [Shepp and Logan, 1974]. The known input profile was also used to verify the relative agreement between the final CIT reconstruction and the initial input electron density map.

Figure 6 (top) shows the relative enhancement of the feature in Figure 5 that was used as input for the ray trace program. This figure was created by dividing the electron density map shown in Figure 5 by the background density in Figure 3. We normalized the map in order to get the relative amplitude of the enhancement and its position.

The reconstruction grid was initialized to zero-value pixels for the background. The normalized relative densities were reconstructed using only the modeled STEC measurements and the line-of-sight path. The reconstruction produced by passing rays through the electron density profile in Figure 5 is presented in Figure 6 (bottom). In this figure we clearly see an enhancement in the reconstructed electron density map near  $65^\circ$  latitude and  $\sim 300$  km altitude.

The reconstructed enhancement in Figure 6 (bottom) is located at a higher altitude than the initial enhancement shown in Figure 6 (top). This shift in altitude is due to the constraints in orbital geometry consideration

In order to generate the ray data it took days to weeks. To analyze the ray data in order to obtain the Faraday rotation and corresponding STEC values required an additional 5–10 min. To perform the reconstructions in this study on a standard workstation, the elapsed time was generally between 18.5 and 18.8 s. The time-limiting task in this paper was producing the ray data, but with satellite measurements the reconstructions will be limited by the data throughput rate of the ADS-B equipped satellite.

### 3.1. Scenario I—A Single Ionospheric Electron Density Enhancement

In Figure 5 we present the electron density map that was used as an input for the ray tracing model to simulate the expected Faraday rotation measurements and their associated TEC values for each raypath. This map was created by superimposing a 2-D normal Gaussian distribution with a specified scaling factor (the unit scale height of the peak density of the symmetric stable distribution), which determined the statistical dispersion of the quiet background profile. The maximum of the density enhancement was located at a latitude of  $65.5^\circ$  and altitude of 250 km, with horizontal and vertical extent of  $0.25^\circ$  and 50 km respectively (see Figure 5). An altitude of 250 km was selected for the modeled enhancements since the F region (above 150 km) is present during the day and night [Hunsucker and Hargreaves, 2003].

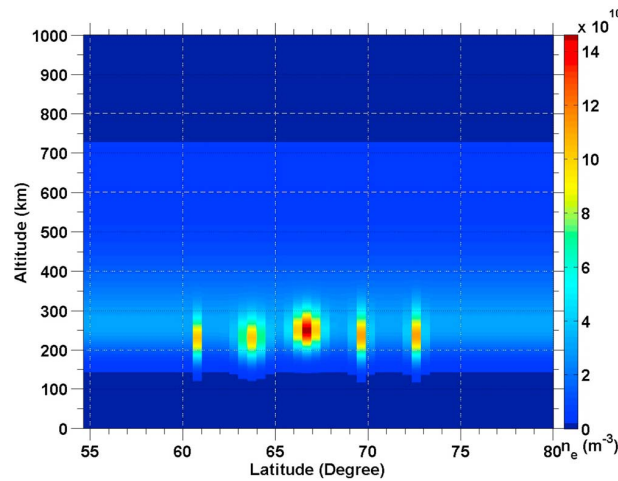


**Figure 7.** Five-feature electron density profile (left to right); latitude = 60.5°, 63.5°, 66.4°, 69.5°, and 72.5°; scaling factor = 3.0, 3.0, 5.0, 3.0, and 3.0; full width at half maximum = 0.25°, 1.0°, 1.0°, 0.25°, and 0.25°; vertical extent = 90 km; and altitude = 225 km, 225 km, 250 km, 225 km, and 225 km.

for a satellite and line-of-sight conditions throughout a satellite pass. It is not possible to acquire data from all viewing angles since horizontal path measurements are not possible (the satellites are always situated above the aircraft). As a result, there exists a predominantly vertical ray geometry between aircraft within the field of view of the satellite, which may have biased the reconstruction in terms of the altitude distribution of the reconstruction.

In addition, the number of paths and number of intersecting paths, especially at lower altitudes, are quite limited when compared to medical CT imaging machines. The white regions on either side of Figure 6 (bottom) and the triangles that are formed between aircraft at low altitudes are

zero-value pixels. These are regions where no rays have passed and as a result; no data are available for the reconstruction to be performed. It is important to note that the electron density is not actually zero in these regions.

The horizontal position of the reconstructed enhancement is much better. Although the reconstructed map shown in Figure 6 (bottom) is not a perfect representation of the input electron density map used as input (Figure 6, top), a feature is clearly discernible near the region where the enhancement was located in the initial profile. This shows that there is good relative agreement between the input and the reconstruction considering the relatively few number of rays that were used in the reconstruction. As a reference, the number of rays that are used in GPS CIT is typically much larger. For GPS CIT there are on the order of  $\sim 4000$  to  $\sim 2 \times 10^5$  rays [Choi *et al.*, 2006]. For this study, using ADS-B ray geometry a maximum of 2950 rays were used for 25 aircraft. At a minimum, this result demonstrates that ADS-B data could be a useful tool to highlight areas of interest where enhancements in the electron density above the nominal background is most probable to occur.

### 3.2. Scenario II—Multiple Ionospheric Electron Density Enhancements

In reality, for an active ionosphere, electron density enhancements may not occur as single features orders of magnitude greater than the entire background. Enhancements are complex structures of different scale sizes and magnitudes (peak density). In fact, a particular layer or the entire background may be enhanced uniformly in which case many small-scale features (smaller than the resolution of current measurement techniques) may appear as a large single enhancement. To evaluate the capability of CIT from ADS-B signals to differentiate multiple features within the same reconstruction space, an input electron density map was created containing five small-scale enhancements.

In Figure 7 we show the input electron density profile that was used for a five-feature enhancement. It was created using the same quiet background electron density profile shown in Figure 3 and clearly shows five different enhancements of the same vertical extent, varying in peak densities, horizontal extent, and latitude. Figure 8 (top) shows the relative enhancement of the feature in Figure 7 that was used as input for the ray trace program in this scenario.

As we did in the previous scenario we used 25 aircraft with 2950 rays and modeled TEC measurements. The objective of analyzing such a data set was to determine the extent of *tailing* and whether multiple features merge and appear as one larger feature in the reconstruction, indicating that the enhancements that are in close proximity to one another cannot be resolved using this technique.

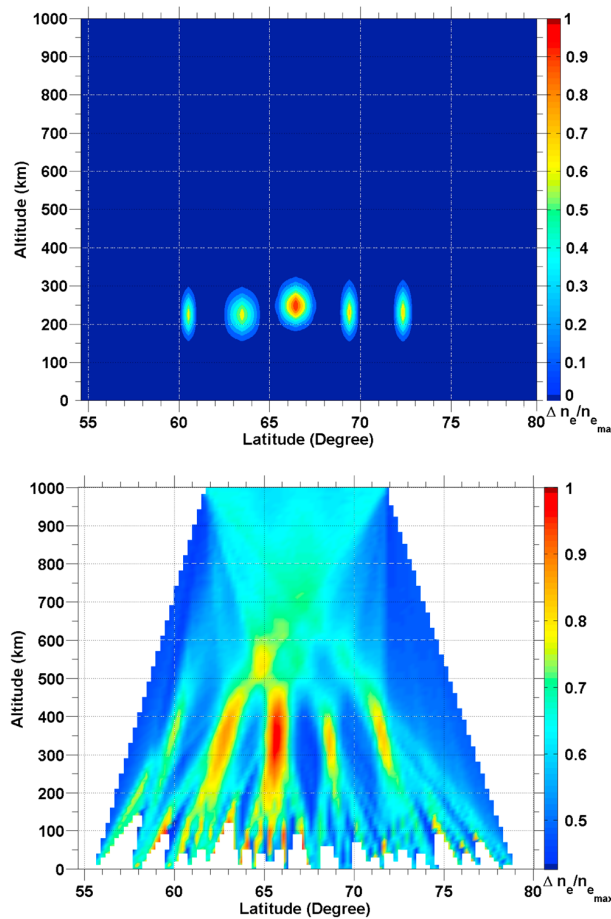


**Figure 8.** (top) Multiple feature electron density profile (see Figure 7) shown as relative weight. (bottom) Reconstructed relative electron density profiles of ray trace input (Figure 7, top) using TEC measurements and line-of-sight path.

We proceeded as in the first scenario where the reconstruction was performed using only the raypath end points and the integrated TEC measurements. The reconstructed relative density map is presented in Figure 8 (bottom). The time required to perform this reconstruction was 18.733669 s. The reconstruction was not a perfect representation of the input electron density map (see Figure 7), but it did agree reasonably well in terms of the relative densities as well as their locations.

Five features are clearly evident in the reconstruction. However, the enhancement at 60.5° and 63.5° latitude appear to be elongated in altitude. Additionally, the enhancement at 60.5° appears to be double peaked with one peak at ~ 57.5°, 150 km and the other at ~ 59.0°, 350 km. The differences in enhancement positions, as well as the double peak feature may be explained by the fact that the sampling geometry is asymmetrical. The twin peak arises from the rays that are associated with the two planes at the lowest latitudes, namely, 55.5° and 58.0°, respectively. The only rays which passed through the enhancement at 60.5° came from the three aircraft at ~ 55.5°, ~ 58°, and ~ 59.5°. These three aircraft transmitted all rays to receiver positions that were at a greater geographic latitude

than their respective positions. The problem occurs because there are not any aircraft which transmit rays through the enhancement vertically or toward lower latitudes. As a result, the feature appears to be stretched across the reconstruction region toward lower latitudes and the location was heavily weighed toward the latitude where the rays originated from.

### 3.3. Discussion

In this work, the structures detected were localized boundary blobs of different magnitudes (3 to 5 times the background density). The accuracy of the CIT technique deteriorated above regions where there was an absence of receivers. This occurred due to a lack of vertical rays to provide information about the pixels below the lowest ray intersection from neighboring receivers. The reconstruction can be improved by increasing the aircraft density since the number of rays and intersections in a reconstruction having a specified grid size also increases proportional to the number of transmitting aircraft.

Another parameter that can be modified to improve the reconstruction is the grid size. The grid size selection was based on trial and error. In order to perform a reasonable reconstruction, the grid size has to be large enough so that it does not require days for the ray tracing program to complete its simulations or that the computer does not run out of access memory. A grid size that maximizes the number of intersections and that reduces the sparsity of the geometry matrix gave the best result for the reconstructions [Cushley, 2013]. It was found that a grid size of 100 by 100 gave a good resolution and was used in our two scenarios.

For this paper, we assumed that the air traffic density was constant. In other words, the number of aircraft in the field of view of the satellite was held constant. In reality, in situ data will have a large variation in how aircraft are distributed in the airspace that might require sophisticated algorithms that would bin the global data in time and into slices of longitude with sufficient ray sampling density to perform the inversion.

The algorithm may also involve adaptive grid selection with the associated data binning. As the numbers of aircraft change so will the number of raypaths and STEC values that will be measured. As a result of the increase in raypaths and STEC measurements, the number of algebraic equation that must be solved for, simultaneously, also increases. The grid size or, equivalently, the total number of pixels should be selected in such a way as to control the extent to which the ill-posed problem is either overdetermined or underdetermined.

In this study, we fixed the latitudinal expanse. It was found that reconstructions were improved with an increase in the expanse of the reconstruction region where sufficient data existed. This was particularly the case when the density enhancement was only partially located within the region of the reconstruction. When a fixed grid size is used and the latitudinal expanse changes, the grid resolution must change as a result. It was found that in order for a structure to be resolved in the reconstruction, the scale size of the initial structure must be larger than the grid resolution but smaller than the total size of the reconstruction region. If the horizontal size of the enhancement was larger than the reconstruction region, there would be little to no gradient to discriminate features from the measurements. Features that result in steep gradients and variations in STEC measurements produced the best results [Muella *et al.*, 2011]. Gradients are of utmost importance in images of any kind [Elachi and van Zyl, 2006].

Other aspects that can affect the reconstruction include the following: the frequency of the EM wave selected, adverse propagation effects (e.g., refraction at low elevations and velocity bunching), the geometry of satellite relative to both the ionospheric feature and aircraft, the enhancement scale size, the satellite pointing accuracy, additional measurement interference (e.g., phase, Faraday rotation, and TEC) introduced to reconstruction caused by the relative motion between the aircraft and the satellite as well as, measurement noise from the receiver to name a few. By using several satellite receivers, the time interval required to collect a given number of raypaths can be reduced. Alternatively, if the time interval remains constant, using more receivers would imply a greater number of raypaths could be collected to be used in the reconstruction.

#### 4. Summary and Conclusions

The main objective of this work was to investigate the capability of reconstructing 2-D ionospheric electron density structures using the Faraday rotation of modeled ADS-B signals. The work concentrated on modeling the effects of the ionosphere on ADS-B signals traveling through electron density enhancements that were localized in space.

To this end, using a ray tracing program, we modeled vertically polarized waves that originated from ADS-B transmitters on aircraft and computed the expected Faraday rotation that an orbiting satellite would observe. The Faraday rotation was used to infer the STEC along the raypath. Using only the raypath and the inferred STEC values as input, the ART algorithm was used to reconstruct the 2-D ionospheric electron density map.

In order to simulate a realistic situation we used 25 ADS-B equipped aircraft as our transmitters and a single satellite acting as our receiver. Each aircraft produced 118 rays for a total of 2950 rays crossing the ionosphere from  $54.63^\circ$  to  $79.80^\circ$  in latitude. To test the feasibility of using ADS-B for CIT, we modeled two different scenarios.

The first scenario involved using a uniform electron density map containing a single localized electron density enhancement as the input for the ray tracing program. We showed that a localized enhancement in electron density can be reconstructed using the raypaths and their associated STEC. We observed that the reconstructed feature was elongated in vertical extent but that its latitudinal position agreed quite well with the original input structure.

Although it may not be apparent from the reconstruction, rays from the right side do not intersect the enhancement due to the curvature of the Earth. We noted that the reconstructed feature was shifted slightly

to the left (i.e., lower latitude) which we argued is due to the fact that there are fewer raypaths traversing the enhancement from the right side (fewer aircraft situated at higher latitudes) compared to those traversing from the left (more aircraft at lower latitudes). The imbalance in the number of raypaths may have caused a slight shift in the reconstructed structures toward the direction of greater aircraft.

Having shown that a single density enhancement could be resolved, we set out to investigate if multiple enhancements could be resolved using the same technique. Our second scenario involved starting with a uniform ionosphere and superimposing five density enhancements of varying peak density, altitude, latitude and horizontal extent, and fixed vertical extent. Similar to the first scenario, we showed that the reconstructed electron density map agreed reasonably well with the initial map. Once more, the enhancements were slightly shifted to the left. This indicates that a further investigation into the reason for the systematic shifts needs to be undertaken.

It is apparent that the position and horizontal extent of the enhancement could be determined with a reasonable degree of accuracy from the raw data. However, the predominantly vertical nature of the rays and the relatively few intersections of rays requires an accurate a priori estimate of the vertical distribution of the electron density to refine the enhancement in terms of the peak altitude and its vertical extent. In addition, rays cannot be horizontal or at very low elevation angles due to the assumed satellite orbital geometry and the line-of-sight conditions that must exist in order to obtain the measurements. This highlights the additional challenges that are imposed using CT to image the ionosphere when compared to other applications of CT (where a precise apparatus is used or constructed to satisfy the requirement of generating equally spaced data and obtaining a complete data set at the spatial interval or correlation length required).

A sparse data set such as this could reduce the satellite downlink budget in terms of the required size of the data set especially for an initial concept demonstrator, while providing a useful and more economical method for prioritizing further observations using other ground-based assets. The reconstructions illustrate the feasibility for CIT using ADS-B data to analyze qualitative phenomena over time. This showed that at a minimum, ADS-B may be a useful tool for indicating the approximate location of features. Generally, a ground-based campaign can only deploy to a specific location. Therefore, observations are confined, and many regions such as oceanic and polar regions have been neglected. Reconstructions from an orbital platform over time can be made for various regions and may indicate areas of interest of most probable occurrence to prioritize other ground-based instrument campaigns (e.g., incoherent scatter radar).

From this study and a literature review of GPS CIT applications and experimental campaigns, it was determined that a relevant, accurate vertical profile a priori estimate should be considered for further refinement of magnitude and altitude distribution of the structures in the reconstruction [Austen *et al.*, 1986; Andreeva *et al.*, 2001; Liu and Gao, 2001; Bust *et al.*, 2007; Muella *et al.*, 2011; Max van de Kamp, 2012]. As a result, it is not unreasonable to expect that ADS-B CIT should incorporate data injection from other sources to be used as a refinement for the reconstruction as well as for comparison.

Although IRI is questionable at 60°N [Schunk *et al.*, 1994; Rawer, 1995], it could be used to provide some estimate of the electron density profile as a priori guess or initialization of the reconstruction grid rather than setting the values to zero for all pixels. If this background were obtained from another instrument in real time rather than empirical models the reconstruction would be a more realistic representation of the current state of the ionospheric electron density.

Once more, we remind the reader that reasonable agreement between the input and the reconstructions were obtained from the raw ADS-B data, without an a priori guess. These results clearly demonstrate the feasibility of using CIT from ADS-B data, especially considering the relatively few number of rays that were used to perform the reconstruction. For this study, using ADS-B ray geometry a maximum of 2950 rays were used for 25 aircraft. For GPS CIT there are on the order of ~4000 to  $\sim 2 \times 10^5$  rays used to perform the reconstructions [Choi *et al.*, 2006].

In conclusion, the modeled ionospheric electron densities within a given reconstruction region was successfully imaged using CIT techniques. The data used for image reconstruction were simulated using theoretical modeling under different geometric, geomagnetic, and density conditions using ray tracing. The ray trace output was reconstructed using the ART pixel-based method of CT and compared to the corresponding input electron density profile to the ray trace.

From the results of this study, we conclude that CIT with ADS-B data is feasible. Important ionospheric features of latitudinal scales 25–100 km can be detected in the raw reconstruction. For a meaningful comparison of ADS-B with another method such as GPS in situ a priori data from another source would be required to improve the vertical distribution and to calibrate units.

### Acknowledgments

The authors acknowledge the significant contributions of R. Gillies (University of Saskatchewan) for providing the ray tracing program used to model Faraday rotation and TEC measurement data used as input for this investigation. The authors would like to thank the Natural Sciences and Engineering Research Council (NSERC) for supporting this research, in addition to contributions and interesting discussions with A. Russell (RMCC).

### References

- ADS-B-Technologies (2011), Welcome, ADS-B Technologies LLC, Anchorage, Alaska. [Available at <http://www.ads-b.com/>.]
- Andreeva, E. S., S. J. Franke, K. C. Yeh, V. E. Kunitsyn, and I. A. Nesterov (2001), On generation of an assembly of image in ionospheric tomography, *Radio Sci.*, *36* Issue 2, 299–309.
- Appleton, E. V., and G. Builder (1933), The ionosphere as a doubly refracting medium, *Proc. Phys. Soc.*, *45*, 208–220.
- Austen, J. R., S. J. Franke, C. H. Liu, and K. C. Yeh (1986), Application of computerized tomography techniques to ionospheric research, in *URSI and COSPAR International Beacon Satellite Symposium on Radio Beacon Contribution to the Study of Ionization and Dynamics of the Ionosphere and to Corrections to Geodesy and Technical Workshop*, vol. 1, edited by A. Tauriainen, pp. 25–35, Univ. of Oulu, Oulu, Finland.
- Bilitza, D. (2007), *IRI-2007: Online Computation and Plotting Through IRI-2007web*, NASA/Goddard Space Flight Center, Heliospheric Physics Lab., Greenbelt, Md. [Available at [http://omniweb.gsfc.nasa.gov/vitmo/iri\\_vitmo.html](http://omniweb.gsfc.nasa.gov/vitmo/iri_vitmo.html).]
- Bilitza, D., L.-A. McKinnell, B. Reinisch, and T. Fuller-Rowell (2011), The international reference ionosphere today and in the future, *J. Geod.*, *85*, 909–920, doi:10.1007/s00190-010-0427-x.
- Brown, S. J., and T. L. Hendricks (2011), *Automatic Dependent Surveillance–Broadcast (ADS–B) In Aviation Rulemaking Committee (ARC)—Recommendations to Define a Strategy for Incorporating ADS–B in Technologies Into the National Airspace System (NAS)*, A Report from the ADS–B In ARC to the FAA, ADS–B In ARC, Washington, D. C. [Available at <http://www.faa.gov/nextgen/implementation/programs/adbsb/media/ADSB>.]
- Budden, K. G. (1961), *Radio Waves in the Ionosphere: The Mathematical Theory of the Reflection of Radio Waves From Stratified Ionized Layers*, Cambridge Univ. Press, Cambridge, U. K.
- Bust, G. S., G. Crowley, T. W. Garner, T. L. Gaussiran II, R. W. Meggs, C. N. Mitchell, P. S. J. Spencer, P. Yin, and B. Zapfe (2007), Four-dimensional GPS imaging of space weather storms, *Space Weather*, *5*, S02003, doi:10.1029/2006SW000237.
- Canada Centre for Remote Sensing (2007), *Advanced Radar Polarimetry Tutorial: Radar Polarimetry*, National Resources Canada, Ottawa, Ontario, Canada.
- Castillo, J., M. Earl, M. Baskey, D. Stolzman, M. Grieve, R. Vincent, R. Van Der Pryt, and A. Cushley (2012), Canadian Satellite Design Competition Proposal: SABRE, The deployment of a space based sensor for the collection of Automatic Dependent Signal-Broadcast transponder transmissions from commercial aircraft operating over Hudson Bay, *Tech. Rep.*, Royal Military College of Canada, Kingston, Ontario, Canada.
- Chen, F. F. (1984), *Introduction to Plasma Physics and Controlled Fusion, Volume 1: Plasma Physics*, 2nd ed., Plenum Press, New York.
- Choi, B.-K., J.-U. Park, and J.-K. Chung (2006), Ionospheric tomography using a regional GPS network over South Korea, *J. Global Positioning Syst.*, *5*(1–2), 47–51.
- Cushley, A. (2013), Ionospheric tomography using Faraday rotation of Automatic Dependent Surveillance Broadcast (UHF) signals, MS thesis, Royal Military College of Canada, Kingston, Ontario, Canada.
- Elachi, C., and J. van Zyl (2006), *Introduction to the Physics and Techniques of Remote Sensing*, 2nd ed., edited by J. A. Kong, John Wiley, Hoboken, N. J.
- Francis, R. (2011), Detection of Automatic Dependent Surveillance - Broadcast signals using stratospheric and orbital platforms, MS thesis, Royal Military College of Canada, Kingston, Ontario, Canada.
- Francis, R., R. Vincent, J. M. Noël, P. Tremblay, D. Desjardins, A. Cushley, and M. Wallace (2011), The flying laboratory for the observation of ADS-B signals, *Int. J. Navig. Observ.*, *2011*(A2), 973656.
- Gillies, R. G. (2006), Modelling of transionospheric HF radio wave propagation for the ISIS II and ePOP satellites, MS thesis, Department of Physics and Engineering Physics, University of Saskatchewan.
- Gillies, R. G. (2010), Transionospheric signal modelling for ePOP and SuperDARN, PhD thesis, Physics and Engineering Physics, University of Saskatchewan.
- Gillies, R. G., G. C. Hussey, H. G. James, G. J. Sofko, and D. André (2007), Modelling and observation of transionospheric propagation results from ISIS II in preparation for ePOP, *Ann. Geophys.*, *25*, 87–97.
- Gurnett, D. A., and A. Bhattacharjee (2005), *Introduction to Plasma Physics With Space and Laboratory Applications*, Cambridge Univ. Press, Cambridge, U. K.
- Hadamard, J. (1902), Sur les problèmes aux dérivées partielles et leur signification physique, *Princeton Univ. Bull.*, *13*, 49–52.
- Haque, J., H. N. Altan, A. Malaga, D. I. Parmet, and D. R. Tabor (2013), *Systems and Methods for Receiving Aircraft Position Reports*, US Patent App. 13/316,052.
- Hartmann, G. K., and R. Leitinger (1984), Range errors due to ionospheric and tropospheric effects for signal frequencies above 100 MHz, *Bull. Geod.*, *58*, 109–136.
- Hartree, D. R. (1929), The propagation of electromagnetic waves in a stratified medium, *Proc. Cambridge Philos. Soc.*, *25*, 97–120, Clearwater, Fla.
- Haselgrove, J. (1963), The Hamiltonian ray path equations, *J. Atmos. Terr. Phys.*, *25*, 397–399.
- Hunsucker, R. D., and J. K. Hargreaves (2003), *The High-Latitude Ionospheres and its Effects on Radio Propagation*, Cambridge Univ. Press, Cambridge, U. K.
- International Association of Geomagnetism and Aeronomy, Working Group V-MOD, et al. (2010), International geomagnetic reference field: The eleventh generation, *Geophys. J. Int.*, *183*(3), 1216–1230.
- Jin, S., J. U. Park, J. L. Wang, B. K. Choi, and P. H. Park (2006), Electron density profiles derived from ground-based GPS observations, *J. Navigation*, *59*(3), 395–401.
- Klobuchar, J. A., and C. H. Liu (1989), *World Ionosphere Modern Total Electron Content Measurement Ionosphere/Thermosphere Study*, SCOSTEP Secretariat, Urbana, Ill.
- Liu, Z., and Y. Gao (2001), Ionospheric tomography using GPS measurements, paper presented at KIS-2001, Banff, Alberta, Canada.
- Muella, M., E. R. de Paula, C. N. Mitchell, P. M. Kintner, R. R. Paes, and I. S. Batista (2011), Tomographic imaging of the equatorial and low-latitude ionosphere over central-eastern Brazil, *Earth Planets Space*, *63*, 129–138.
- Marsh, G. (2006), *European Air Traffic Surveillance*, Avionics Today, Danbury, Conn.



- Max van de Kamp, M. J. L. (2012), Medium-scale 4D ionospheric tomography using a dense GPS network, *Ann. Geophys.*, 31, 75–89.
- NASA Jet Propulsion Laboratory California Institute of Technology (2014), *Real-Time Ionospheric Maps*, NASA JPL Caltech, Pasadena, Calif. [Available at [http://iono.jpl.nasa.gov/latest\\_rti\\_global.html](http://iono.jpl.nasa.gov/latest_rti_global.html).]
- Orfanidis, S. J. (2008), *Electromagnetic Waves and Antennas*, Rutgers Univ., 94 Brett Road Piscataway, N. J.
- Radio Technical Commission for Aeronautics (2003), *(DO-260) Minimum Operational Performance Standards for 1090 MHz Extended Squitter Automatic Dependent Surveillance- Broadcast (ADS-B) and Traffic Information Services -Broadcast (TIS-B)*, RTCA.
- Rawer, K. (1995), *The High Latitudes in the International Reference Ionosphere*, *Adv. in Space Res.*, Pergamon Press, Greenbelt, Md.
- Schunk, R., D. Anderson, D. Rees, B. Reinisch, and D. McEwen (1994), *The High Latitudes in the International Reference Ionosphere (IRI)*, Cospar Scientific Assembly Meeting Report, Hamburg, Germany.
- Schunk, R. W., and A. F. Nagy (2000), *Ionospheres: Physics, Plasma Physics, and Chemistry*, *Cambridge Atmos. and Space Sci. Ser.*, edited by A. J. Dressler, J. T. Houghton, and M. J. Rycroft, Cambridge Univ. Press, Cambridge, U. K.
- Shepp, L. A., and B. F. Logan (1974), *The Fourier Reconstruction of a Head Section*, vol. 21, 21–43.
- Shmuel, B., J. Hiemstra, V. Tarantini, F. Singarayar, G. Bonin, and R. E. Zee (2012), The Canadian Advanced Nanospace eXperiment 7 (CanX-7) demonstration mission: De-orbiting nano- and microspacecraft, paper presented at 26th Annual AIAA/USU Conference on Small Satellites, UTIAS Space Flight Laboratory, Toronto, Canada.
- Soicher, H., and F. J. Gorman (2012), Seasonal and day-to-day variability of total electron content and mid-latitudes near solar maximum, *Radio Sci.*, 20(3), 383–387, doi:10.1029/RS020i003p00383.
- Tessa, V. H., W. Sarah, G. Maggie, B. K. Joost, and S. Jan (2007), The implementation of iterative reconstruction algorithms in MATLAB, iterative reconstruction algorithms, MS, Department of Industrial Sciences and Technology, University of Antwerp, Belgium.
- TransportCanada (2012), *RAC 2.0 Airspace Requirements and Procedures*, Transport Canada Aeronautical Information Manual (TC AIM), Canada. [Available at <http://archive.today/kWz7#selection-1283.11-1283.68>.]
- Tremblay, P., R. Francis, A. Cushley, D. Desjardins, and M. Wallace (2009), FLOAT: Flying Laboratory for Observation of ADS-B Transmissions, *Tech. Rep. FLOAT-RP-RMC-0001 Issue 1.0*, Royal Military College of Canada, Kingston, Ontario, Canada.
- University of Toronto Institute for Aerospace Studies Space Flight Laboratory (2014), *Nanosatellites: Canx-7*, UTIAS SFL News, Toronto, Ontario, Canada. [Available at [http://utias-sfl.net/?page\\_id=210](http://utias-sfl.net/?page_id=210).]
- VanDerPryt, R. (2014), Modelling aircraft Automatic Dependent Surveillance- Broadcast (ADS-B) signals received by a low-Earth-orbiting satellite: Examining the North Atlantic oceanic airspace control areas, MS thesis, Royal Military College of Canada, Kingston, Ontario, Canada.
- Wahi, R., S. Dubey, and A. K. Gwal (2005), Ionospheric total electron content measurement in Malaysian region during high solar activity using GPS receiver, *Indian J. Radio Space Phys.*, 34, 399–401.
- Yueh, S. H. (1999), *Estimates of Faraday Rotation With Passive Microwave Polarimetry for Micro-Wave Remote Sensing of Earth Surfaces*, *IEEE Trans. Geosci. and Remote Sensing*, Jet Propulsion Laboratory, Calif. Inst. of Technol., Pasadena, Calif.
- Zhao, B., W. Wan, L. Liu, and Z. Ren (2009), Characteristics of the ionospheric total electron content of the equatorial ionization anomaly in the Asian-Australian region during 1996–2004, *Ann. Geophys.*, 27, 3861–3873.

## Faraday rotation of Automatic Dependent Surveillance-Broadcast (ADS-B) signals as a method of ionospheric characterization

### 5.1 Overview

The scientific results presented in this chapter are based on the following publication:

- Cushley, A. C., Kabin, K., & Noël, J.-M.. Faraday rotation of Automatic Dependent Surveillance-Broadcast (ADS-B) signals as a method of ionospheric characterization. *Radio Sci.*, 52, 2017.

This study examined the use of linearly polarized signals from transmitting aircraft to receiving spacecraft to measure FR and TEC, thereby creating a wide data base upon which the distribution of IED can be modelled. Using as a first approximation vertical propagation at frequencies of 1090 MHz from a transmitter in the ADS-B system, candidate orbital receivers in LEO spacecraft that are capable of polarization measurement, and using a 3-parameter Epstein ionospheric density model, FR values under various circumstances are computed. With the cited existing infrastructure, this demonstrates encouraging accuracy or precision of the study at mid latitudes.

### 5.2 The Study

*Cushley* [2013] and *Cushley and Noël* [2014] have shown that ADS-B data is useful for a secondary scientific purpose, other than the intended use for ATC. Not only can the ADS-B receiver be used to monitor air traffic improving efficiency and safety, it also is feasible as a dual-purpose payload. The theoretical modelling in *Cushley* [2013]; *Cushley and Noël* [2014] has clearly shown the practicality for additional investigation.

The reconstruction results from *Cushley and Noël* [2014] showed that using only the TEC output and without *a priori* estimate, the presence of electron density

enhancements or depletions were reproduced, and were approximately in the proper locations in terms of latitude. They were used to demonstrate the viability of ADS-B CIT to highlight localized regions of electron density structures. It was found that by using a quiet *a priori* guess for initialization of the reconstructed image, the features became clearly defined. Overall, the reconstructions showed that the structures were better localized in terms of latitude than in terms of altitude.

This was attributed to the predominantly vertical ray geometry between aircraft within the FOV of the LEO satellite, and the short data collection duration which caused a small, sparse dataset when compared to other applications of CT. The horizontal resolution was found to depend primarily on the air-traffic density, while the vertical resolution depended primarily on the resolution of the *a priori* data. The *a priori* guess provided an adequate basis for vertical distribution, which localized the feature, with sharp contrast between data and the background.

The paper by *Cushley et al.* [2017] is directly related to the research by *Cushley* [2013] and the work that was presented in the previous chapter by *Cushley and Noël* [2014]. It can be considered as a method to form an *a priori* estimate for the first iteration of the CIT reconstruction in order to provide information about the vertical distribution of the electron content. Work from GPS CIT by *Liu and Gao* [2001]; *Max van de Kamp* [2012] has shown that in-situ data used for the creation of the *a priori* guess, as opposed to built-in profiles, yielded better results. Although data injection from other sources is preferable to empirical models, data from other instruments may not always be available. The problem of mapping the IEDs is an ill-posed problem and therefore relies heavily on the accuracy of the *a priori* estimate. This research outlines a method to generate IED profiles based on available parameters from other sources (e.g. ionosondes). For vertical propagation paths, this method yields one or more electron density profiles for a single FR measurements and TEC measurement (or assuming the value for the VTEC can be provided accurately enough from a GIM).

The paper presented in this chapter is not only relevant for CIT, but also related to other applications that require information about the ionospheric electron content.

The method and results presented in the following paper describes how, given independent FR and TEC measurements, ionospheric profiles can be created to describe the vertical distribution of electrons along the path and provide more information about the ionosphere than using only TEC measurements.

VTEC maps are regularly produced by GNSS and used to assess the state of the ionosphere and propagation conditions. They are available from a variety of sources such as DLR, NRCan, *NASA Jet Propulsion Laboratory California Institute of Technology* [2014]. However, they do not provide any information about how the electron content is distributed vertically. Although this manuscript is applied to ADS-B signals as the candidate carrier, the technique can also be applied to other linearly polarized signals.

### 5.3 Published Paper

The technique using independent FR and TEC measurements to obtain ionospheric profiles discussed in this chapter was published in *Radio Science* in 2017. Presented immediately below is the paper in the journal format reproduced by permission of American Geophysical Union:

- Cushley, A. C., Kabin, K., & Noël, J.-M.. Faraday rotation of Automatic Dependent Surveillance-Broadcast (ADS-B) signals as a method of ionospheric characterization. *Radio Sci.*, 52, doi:10.1002/2017RS006319, 2017. Copyright 2017 American Geophysical Union.



## RESEARCH ARTICLE

10.1002/2017RS006319

## Key Points:

- By using two measurements (Faraday rotation and TEC), rather than only the TEC, we can improve the characterization of the ionosphere
- This technique will be most effective at midlatitudes, where the maximum amount of Faraday rotation occurs
- ADS-B can be used for ionospheric sounding in addition to its operational purpose of monitoring air traffic

## Correspondence to:

A. C. Cushley,  
alex.cushley@rmc.ca

## Citation:

Cushley, A. C., Kabin, K., & Noël, J.-M. (2017). Faraday rotation of Automatic Dependent Surveillance-Broadcast (ADS-B) signals as a method of ionospheric characterization. *Radio Science*, 52, 1293–1300. <https://doi.org/10.1002/2017RS006319>

Received 30 MAR 2017

Accepted 22 SEP 2017

Accepted article online 9 OCT 2017

Published online 19 OCT 2017

©2017. American Geophysical Union.  
All Rights Reserved.

## Faraday Rotation of Automatic Dependent Surveillance-Broadcast (ADS-B) Signals as a Method of Ionospheric Characterization

A. C. Cushley<sup>1</sup> , K. Kabin<sup>1</sup> , and J.-M. Noël<sup>1</sup> 

<sup>1</sup>Department of Physics, Royal Military College of Canada, Kingston, Ontario, Canada

**Abstract** Radio waves propagating through plasma in the Earth's ambient magnetic field experience Faraday rotation; the plane of the electric field of a linearly polarized wave changes as a function of the distance travelled through a plasma. Linearly polarized radio waves at 1090 MHz frequency are emitted by Automatic Dependent Surveillance Broadcast (ADS-B) devices that are installed on most commercial aircraft. These radio waves can be detected by satellites in low Earth orbits, and the change of the polarization angle caused by propagation through the terrestrial ionosphere can be measured. In this manuscript we discuss how these measurements can be used to characterize the ionospheric conditions. In the present study, we compute the amount of Faraday rotation from a prescribed total electron content value and two of the profile parameters of the NeQuick ionospheric model.

### 1. Introduction

The Earth's ionosphere is a region of Earth's upper atmosphere between approximately 60 and 1,000 km altitude, composed of free electrons, different atomic and molecular ions, and neutral particles, where the extreme solar ultraviolet (EUV) and X-ray radiation causes ionization. The practical importance of studying the ionosphere is that it has a sufficient electron density to affect electromagnetic wave propagation for satellite communications and distant Earth communications (Rawer, 1993).

The ionospheric electron number density changes with altitude above the Earth's surface. Total electron content (TEC) is defined as the integrated electron density within a column of ionospheric plasma of one square meter in cross-sectional area. The TEC parameter is studied extensively, because it is very useful and relatively simple to measure. TEC can be used for many applications and routine tasks, such as prediction of propagation delays for Global Navigation Satellite Systems (GNSS) and other systems, as a proxy for GNSS position error, to validate ionospheric models and even as a potential precursor in earthquake forecasting tools (Hammerstrom & Cornely, 2016; Hoque & Jakowski, 2012; Klobuchar et al., 1973; Wen et al., 2010). For these reasons, global maps of the vertical TEC (VTEC) are routinely produced from GNSS and used to assess the state of the ionosphere and propagation conditions. Such maps are made available at [http://iono.jpl.nasa.gov/latest\\_rti\\_global.html](http://iono.jpl.nasa.gov/latest_rti_global.html), among other sources.

One of the earliest ground-based observations of ionospheric phenomena that is consequential to the TEC was made by DeWitt and Stodola (1949) by using signals bounced off the Moon. They observed systematic amplitude fading in their signals, but they did not fully understand that this fading was in fact a signature of Faraday rotation (FR), which is proportional to the TEC (Budden, 1961). The first estimates of the TEC were also made using echoes from the Moon by Browne et al. (1956). Soon thereafter, the opportunity for extended TEC observations was provided by amplitude versus time records of the signals received from Sputnik 3 (Garriott, 1960). These early TEC measurements in the late 1950s showed diurnal and seasonal variations for the topside and bottomside ionosphere (Lawrence et al., 1963).

Even during magnetically disturbed periods, TEC measurements provide continuous information about the electron content in the *F* region (>160 km), where the highest concentration of electrons tend to occur. The electron density peak altitude is typically seen at ~300 km, in the *F* region, but with a high degree of variation (Anderson & Fuller-Rowell, 1999; Wahi et al., 2005; Zhao et al., 2009). For example, Chuo (2014) observed

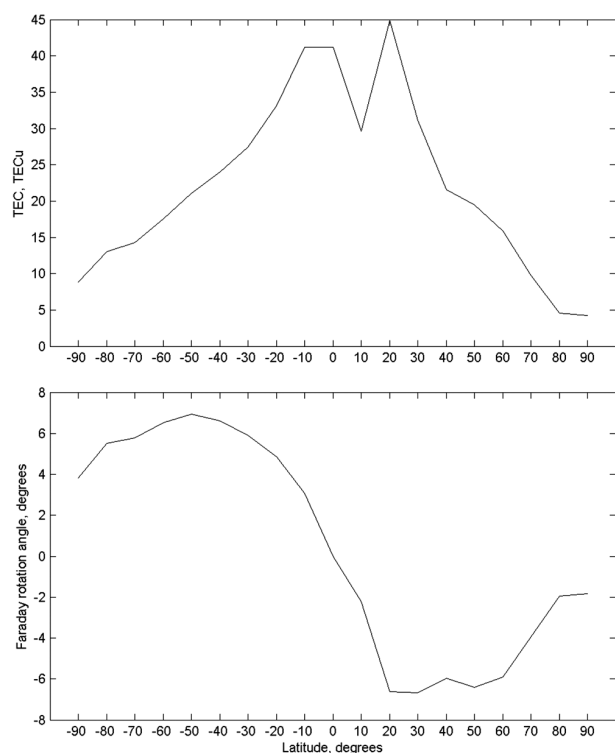


**Figure 1.** (top) The VTEC as a function of geographic latitude for 15 January 2015 along the Greenwich Meridian 0° longitude at 12 UTC. Although TEC is highly variable, the daily global maximum is typically found over equatorial regions at solar maximum conditions and generally decreases with latitude. The peak occurs between 15 and 20° on either side of the equator with an ionization trough at the geomagnetic equator. (bottom) A plot of the Faraday rotation (FR) as a function of latitude. The maximum FR occurs in the midlatitude region, making this the region most amenable to this type of procedure because the amount of FR is above the detectable threshold.

the altitude of the ionospheric peak to range from 250 to 380 km from 0600 to 1000 LT, while the scale height changed from 38 to 65 km over the same 4 h period.

Radio waves propagate at a slower velocity through the Earth’s ionosphere than through free space due to the group path delay caused by the ionosphere (Hoque & Jakowski, 2012; Klobuchar et al., 1973). The most important layer from a navigation and communications perspective is the F2 layer, where the electron content reaches a peak density. The propagation time delay due to the ionosphere is directly proportional to the ionospheric TEC along the path. TEC therefore is one of the most important quantitative measurements to characterize the Earth’s ionosphere. The exact value of TEC is a function of many variables, for example, the geographic location, the local time, the season, the amount of solar EUV flux, and magnetic activity.

The VTEC is defined as the integral of the electron density along a radial path from the Earth’s surface up to the transmitting satellite or a higher altitude which we can assume to be infinity (Leitinger, 1994; Stankov et al., 2003). Figure 1 (top) shows the VTEC as a function of geographic latitude, obtained by integrating electron density profiles using the semi-empirical NeQuick2 Web Model (Nava et al., 2008) from the surface of the Earth up to 22,250 km for 15 January 2015 along the Greenwich Meridian 0° longitude at 12 UTC. We note that the VTEC is maximum between 15 and 20° on either side of the equator with an ionization trough at the geomagnetic equator. This is known as the equatorial anomaly (Appleton, 1946; Eccles & King, 1969; MacDougall, 1969). The VTEC decreases as we move toward higher latitudes (Soicher & Gorman, 2012). There is also a hemispherical asymmetry that is produced due to seasonal effects and the magnetic axis tilt angle of the Earth with respect to the rotational axis (Fuller-Rowell et al., 2016).

FR depends on both electron density profile and magnetic field, and for vertical propagation, the FR increases for more vertical magnetic field lines. Since TEC depends on latitude, it would be reasonable to assume that FR would also depend on latitude. Using the value for VTEC shown in Figure 1 (top) and the dipole magnetic field, the FR angle as a function of latitude is shown in Figure 1 (bottom). We assume that there is negligible density above the satellite so that the full VTEC is used to calculate FR. An equatorial observer,

receiving the signal from a satellite passing directly overhead, would encounter a relatively high value of TEC; however, due to the geometry, only a small radial component of the magnetic field would exist as a consequence and very little to no FR would occur as shown in Figure 1 (bottom). At the poles, an observer would encounter a stronger radial component of the magnetic field compared to an equatorial observer, but the TEC at high latitudes is much lower than equatorial latitudes. The maximum amount of FR occurs at midlatitudes, which shows that the technique that we will present in section 2 of this manuscript would work best in the midlatitude region.

Automatic Dependent Surveillance-Broadcast (ADS-B) is a technology developed to track the position and movement of aircraft through intermittent broadcasts of linearly polarized 1,090 MHz radio waves containing information about their identity, itinerary, and position state vectors to ground-based receivers and other aircraft within range. The system is intended to augment radar for air traffic control by providing an enhanced ranging and separation distinction capability with a reduced footprint for ground support infrastructure (ADS-B-Technologies, 2011; Brown & Hendricks, 2011; Marsh, 2006). ADS-B coverage will be particularly useful for oceanic and polar regions, where coverage from another source is otherwise unavailable. These regions also correspond to the largest errors for TEC maps (Jakowski et al., 2011). Therefore, using ADS-B measurements in those areas can improve the accuracy of the TEC maps.

The required transmitter power for the ADS-B signal varies as a function of aircraft category with a maximum output power for all classes of 500 W. Smaller aircraft use a minimum transmission power of 75 W, but any aircraft that is capable of operating at altitudes greater than 15,000 ft (4,570 m) above sea level (ASL), or with

cruising speeds above 175 kts (324 km/h), are required to transmit at a minimum power of 125 W. Aircraft use quarter-wave monopole antennas for ADS-B transmissions that transmit vertically polarized signals (Francis et al., 2011; NavCanada, 2008).

ADS-B signals were first detected at 35 km, well above commercial flight level (~10 km) by a high-altitude balloon mission, which successfully demonstrated the reception of ADS-B signals from near space, paving the way to the development of a space-based ADS-B system (Francis et al., 2011). CanX-7 (University of Toronto Institute for Aerospace Studies Space Flight Laboratory, 2014) is a nanosatellite equipped with an ADS-B receiver that was recently launched into a 690 km Sun-synchronous orbit on 26 September 2016 to validate this idea. While the primary mission of CanX-7 is to demonstrate deorbiting technology, it is also used to evaluate an ADS-B receiver in space (Shmuel et al., 2012; University of Toronto Institute for Aerospace Studies Space Flight Laboratory, 2014). CanX-7 has received ADS-B signals from various aircraft distributions and geometries with slant ranges in excess of 2,000 km and up to 3,300 km at look angles (off-nadir) of ~64° (Vincent & Van Der Pryt, 2017; K. Freitag, personal communication, 2017). For the purpose of this manuscript we assume that ADS-B signals are detectable over vertical paths, which will be shorter than off-nadir slant ranges.

Other organizations interested in space-based air traffic monitoring using ADS-B include the European Space Agency Proba-V mission (European Space Agency, 2013a, 2013b; Francois et al., 2014) and GomSpace GomX-1 (Alminde et al., 2012, 2014; GomSpace, 2013). ADS-B receivers have also been assembled, integrated, and tested as hosted secondary payloads on the Iridium Next constellation, Iridium's second generation 75 satellite LEO constellation that has commenced deployment in early January 2017, with full service expected to be available by 2018 (Aireon, 2015; Gupta, 2011; Van Der Pryt & Vincent, 2016). The first ever global aircraft tracking capability will play a key role in the modernization of global air traffic management infrastructure (Harris Corporation, 2012, 2014).

One of the main benefits of considering ADS-B signals and of the method proposed in this manuscript is that ADS-B receivers are able to distinguish and identify signals from different aircraft, which results in potentially hundreds or even up to a couple of thousand independent FR measurements along different propagation paths. The ADS-B signals, currently produced by aircraft, offer a unique opportunity to be used for ionospheric sounding in addition to their main operational purposes. This is similar to how GNSS systems have been used for ionospheric science in addition to their intended purpose of geospatial positioning. In the next section, a relatively simple method is presented that can be used to characterize the ionosphere using two parameters that can be adjusted in order to produce an electron density profile that agrees with FR and TEC observations. In the present study, we compute the amount of Faraday rotation from a prescribed ionospheric electron density profile, specified by NeQuick. We study the sensitivity of FR angle to ionospheric parameters such as layer thickness and the altitude of the peak density. By considering the FR in addition to the TEC, we show that the ionospheric characterization can be improved.

## 2. Theory and Methodology

The TEC along a propagation path or within a column of ionospheric plasma of unit cross section is defined as

$$TEC = \int_0^{z_{max}} n_e(z) dz \tag{1}$$

where  $n_e$  is the electron density and  $z$  is the path length. TEC is usually expressed in TEC units (TECU) equal to  $10^{16}$  electrons  $m^{-2}$ , with typical values ranging from 1 to 100 TECU (Klobuchar et al., 1973). The upper limit of integration,  $z_{max}$  in this definition is somewhat arbitrary, as long as it is well above the altitude of the peak ionospheric density, usually values of at least 1,000 km are used (Klobuchar et al., 1973). In practice, the upper limit typically coincides with the altitude of the Global Positioning System (GPS) satellites at 20,180 km (~3.1  $R_E$ ), which are regularly used to calculate TEC.

In addition to experiencing time delays, linearly polarized plasma waves propagating through the ionosphere undergo FR of the polarization plane. The angle of this rotation is given by Kraus (1966) among others

$$\beta = \frac{e^3}{8\pi^2 \epsilon_0 m_e^2 c f^2} \int n_e(z) B_{||}(z) dz \tag{2}$$

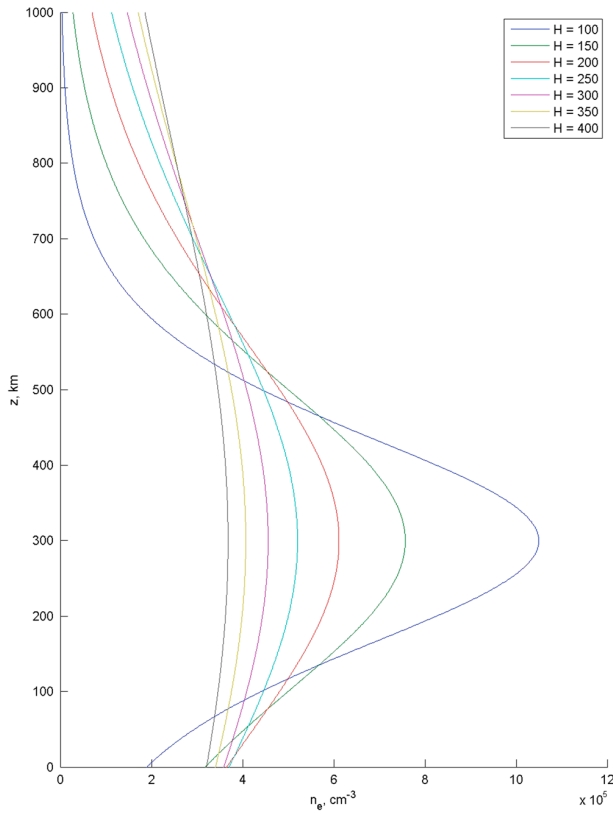


**Figure 2.** Electron number density,  $n_e$ , profile for  $z_0 = 300$  km,  $TEC = 40$  TECu, and different values for the layer thickness.

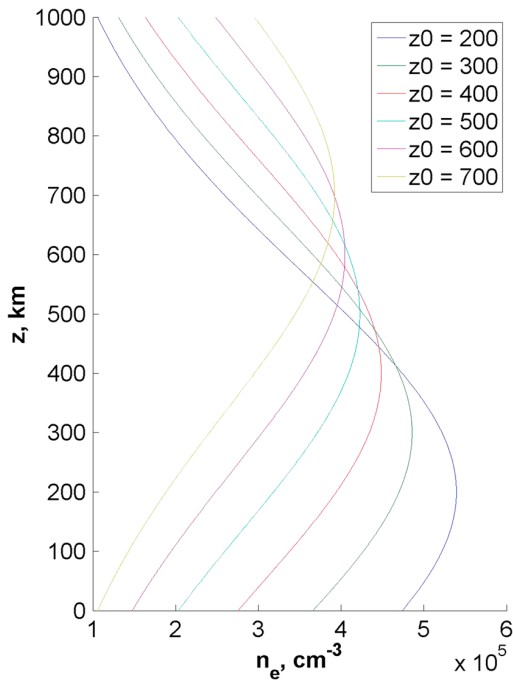


**Figure 3.** Electron number density,  $n_e$ , profile for  $H = 275$  km,  $TEC = 40$  TECu, and different altitudes for the peak ionospheric density.

where the FR,  $\beta$  is measured in radians,  $c = 3 \times 10^8$  m/s is the speed of light in a vacuum,  $e = 1.602 \times 10^{-19}$  C is the elementary charge,  $m_e = 9.109 \times 10^{-31}$  kg is the mass of an electron,  $f$  is the frequency of the radio wave,  $\epsilon_0 = 8.854 \times 10^{-12}$  C<sup>2</sup>/N m<sup>2</sup> is the permittivity of free space, and  $B_{||}$  is the component of the magnetic field parallel to the direction of the wave propagation in tesla. The magnitude of the rotation is directly proportional to the integrated product of the electron density,  $n_e(z)$ , along the ray path or plasma column and the strength of the parallel component of the magnetic field  $B_{||}(z)$ .

Using equations (1) and (2) together provide more information about the electron density than simply using equation (1). By assuming that  $B_{||} = B$ , we restrict our analysis to the cases when the satellite is directly overhead. This describes the simplest and the most ideal observational geometry. Only this geometry will be considered in this proof of concept study. In what follows, we further assume that the magnitude of the parallel component of the magnetic field can be described by the dipole approximation; then the component parallel to the propagation of the radio wave can be written as

$$B_{||} = B_r = B_{eq} \frac{2R_E^3 \sin \lambda}{(z + R_E)^3} \quad (3)$$

where  $B_{eq} = -31,000$  nT is the equatorial dipole strength at the surface of the Earth and  $\lambda$  is the latitude of the point in consideration.

As a suitable model for the ionospheric electron density, we use the NeQuick model (Leitinger et al., 2005; Radicella & Zhang, 1995), which only has a few adjustable parameters. The altitude dependence of  $n_e$  in the NeQuick model is based on the Epstein layer (Rawer, 1963), given by

$$n_e(z) = \frac{4n_m \alpha}{(1 + \alpha)^2} \quad (4)$$

where

$$\alpha = \exp\left(\frac{z - z_0}{H}\right).$$

Here  $n_m$  is the maximum density of electrons in the ionosphere,  $z_0$  is the altitude of the density peak, and  $H$  is the layer thickness parameter. In this manuscript, the layer thickness rather than the scale height is used. Wright (1960) shows that for a Chapman profile, slab thickness is  $\sim 4$  times larger than scale height. Typical values for scale height are found to range  $\sim 30$ – $100$  km (Chuo, 2014; D. R. Themens, personal communication, 2017). Also, we are using an Epstein layer, so the relation is likely different. The NeQuick model has three adjustable parameters, namely,  $n_m$ ,  $z_0$ , and  $H$ . TEC can be computed analytically for the profile (4) as

$$TEC = 4n_m \int_0^\infty \frac{\exp\left(\frac{z - z_0}{H}\right)}{\left(1 + \exp\left(\frac{z - z_0}{H}\right)\right)^2} dz = \frac{4n_m H}{1 + \exp\left(\frac{-z_0}{H}\right)} \quad (5)$$

We assume that the TEC of the ionosphere is a known quantity; thus, equation (5) can be used to provide one relationship that can be used to evaluate  $n_m$  for given  $z_0$  and  $H$ . The profile is a function of three parameters:  $n_m$ ,  $z_0$ , and  $H$ . We can choose two of the parameters independently and calculate the third. Then, equation (2) is used to compute the FR angle  $\beta$  as a function of  $H$  and  $z_0$  for fixed values of TEC.



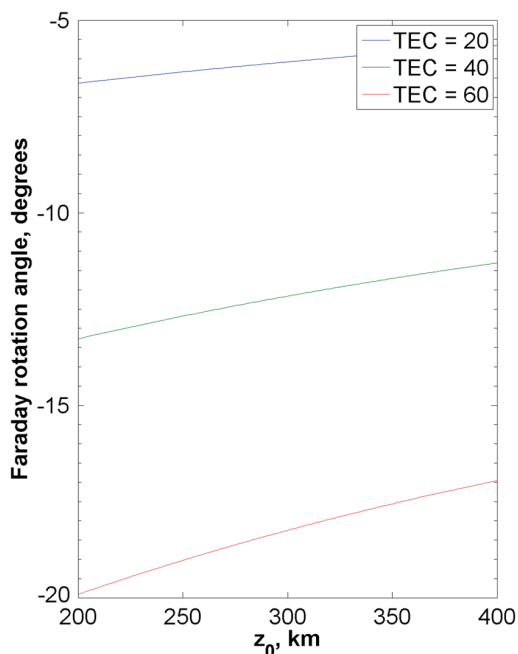


**Figure 4.** The FR angle as a function of  $z_0$  for  $H = 275$  km for constant TEC (20 TECu blue line, 40 TECu green line, and 60 TECu red line).

range of values beyond what is normally observed; however, a value of  $H=275$  km is used in Figure 3, which is considered to be a fairly typical value.

Figures (4) and (5) show the FR angle computed as a function of the parameters of the NeQuick ionospheric model, assuming that the TEC value is constant (at 20 TECu blue line, 40 TECu green line, and 60 TECu

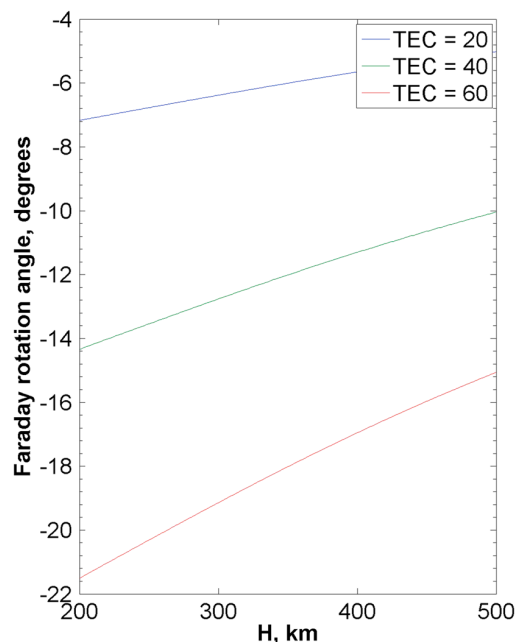


**Figure 5.** The FR angle as a function of  $H$  for  $z_0 = 300$  km for constant TEC (20 TECu blue line, 40 TECu green line, and 60 TECu red line).

The present study determines the amount of Faraday rotation from a chosen TEC value and two of the profile parameters (in this case  $z_0$  and  $H$ ). By specifying TEC, we assume the peak density is inferred from the TEC and is not an independent variable. The actual experiment/application of this technique will be somewhat the opposite, that is, measuring FR and TEC and attempting to determine the profile parameters from those two quantities. This problem is, however, underdetermined—we have only two constraints and three parameters. Thus, the ambiguous determination of the ionospheric parameters will require additional measurements, for example,  $z_0$  from ionosonde data (Kersley et al., 1993; Stankov et al., 2003). At present, however, we focus on the feasibility of using ADS-B for ionospheric research and study the sensitivity of FR to the ionospheric parameters such as  $H$  and  $z_0$ .

### 3. Results

We set the TEC at 40 TECu, which is a typical value during quiet ionospheric conditions for  $\lambda = 45^\circ$  (see Figure 1, top) given that TEC typically ranges from 5 to 50 TECu for diurnal midlatitude TEC and 10 to 50 TECu through the day, over the solar cycle (Anderson & Fuller-Rowell, 1999). We select  $\lambda = 45^\circ$  because the midlatitude region is where the FR angle is largest (see Figure 1, bottom). Figures 2 and 3 show plots of electron density profiles as a function of  $H$  (Figure 2) and  $z_0$  (Figure 3) for TEC = 40 TECu. Figure 2 shows the electron density profiles obtained for fixed  $z_0 = 300$  km as a function of varying  $H$ . Similarly, Figure 3 shows the electron density profiles for fixed  $H = 275$  km and for different altitudes of the peak ionospheric density. Slab thickness values can range 100–500 km with a typical range between 200 and 350 km for the midlatitude ionosphere (Jayachandran et al., 2004; Stankov & Warnant, 2009). We deliberately explore a

range of values beyond what is normally observed; however, a value of  $H=275$  km is used in Figure 3, which is considered to be a fairly typical value. Figures (4) and (5) show the FR angle computed as a function of the parameters of the NeQuick ionospheric model, assuming that the TEC value is constant (at 20 TECu blue line, 40 TECu green line, and 60 TECu red line). In this calculation, we set the lower limit of the integration in equation (2) to 10 km (a typical cruising altitude of commercial aircraft) and upper limit to 1,000 km (close to the actual satellite(s) that will receive ADS-B signals; the CanX-7 and the Iridium NEXT satellites orbit at  $\sim 800$  km and  $\sim 780$  km, respectively).

Figure 4 shows the dependence of the FR angle,  $\beta$ , as a function of the altitude of the ionospheric peak  $z_0$ . The other model parameter, namely, the layer thickness parameter  $H$ , is kept constant at 275 km. Figure 4 shows that the FR angle  $\beta$  changes by more than  $1^\circ$  (from  $\sim -6.6^\circ$  to  $\sim -7.9^\circ$ ) for 20 TECu, more than  $2^\circ$  (from  $\sim -13.1^\circ$  to  $\sim -15.8^\circ$ ) for 40 TECu, and by  $\sim 4^\circ$  (from  $\sim -19.7^\circ$  to  $\sim -23.7^\circ$ ) for 60 TECu as the altitude of the ionospheric peak increases from 200 to 400 km. The change in FR is near the  $1^\circ$  threshold that can be detected by instruments on board an orbiting satellite (Anderson et al., 2011; Dhar et al., 1977; Rogers & Quegan, 2014). The FR is consistent with equation (2); as the altitude of the ionospheric peak increases, the angle of the FR decreases, since the electron density is multiplied by the parallel component of the magnetic field in equation (2), which decreases as a function of altitude. The lower the altitude of the peak density, the stronger the radial component of the magnetic field at its location.

Figure 5 shows the variation of the FR angle as a function of the model parameter  $H$  for fixed  $z_0 = 300$  km. As the layer thickness parameter of the model  $H$  increases from 200 to 500 km,  $\beta$  changes by more than  $2^\circ$  (from  $\sim -7.2^\circ$  to  $\sim -5.0^\circ$ ) for 20 TECu, more than  $4^\circ$  (from  $\sim -14.3^\circ$  to  $\sim -10.0^\circ$ ) for 40 TECu, and more than  $6^\circ$  (from  $\sim -21.5^\circ$  to  $\sim -15.0^\circ$ ) for 60 TECu. These changes in magnitude of the rotation angle should be detectable. It is evident from Figures 4 and 5 that the amount of FR expected for the ADS-B transmission even for elevated values of TEC is clearly less than  $180^\circ$ , so we do not need to be concerned with phase ambiguity.

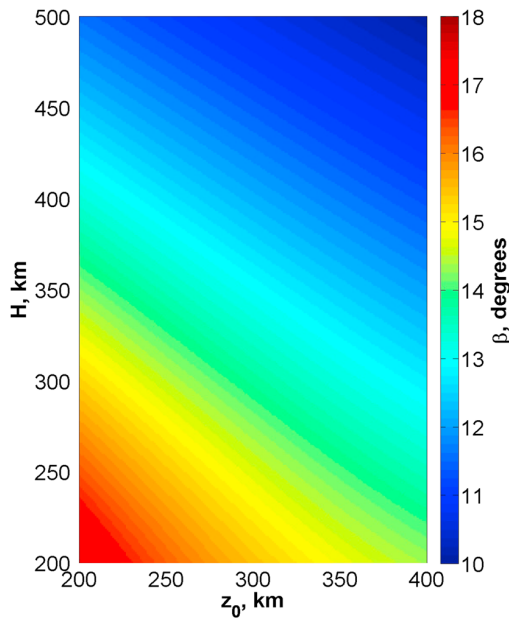


**Figure 6.** The FR angle as a function of  $z_0$  and  $H$  for  $TEC = 40$  TECu.

Figure 6 shows, with a color contour plot, the FR angle as a function of  $z_0$  and  $H$  for  $TEC = 40$  TECu. From this figure we see that as  $H$  increases from 200 km to 500 km and  $z_0$  increases from 200 km to 400 km, the angle  $\beta$  decreases from  $\sim 17^\circ$  to  $\sim 10^\circ$ . The maximum FR corresponds to small values of  $H$  and  $z_0$ . All values of the FR angle are shown to be above the detectable threshold (Anderson et al., 2011; Dhar et al., 1977; Rogers & Quegan, 2014).

#### 4. Summary and Conclusions

Modern TEC measuring systems rely on either the observation of signal phase differences or on differences in the pulse travel time and pulse shape measurements based on geostationary and other orbiting satellites. A standard way of measuring TEC is to use ground-based receiver processing signals from the following: GNSS satellites, satellites in geostationary orbits such as ATS-6 and SIRIO and polar orbiting satellites like the U.S. Navy Navigation Satellite System (NNSS). These techniques using GNSS have created new opportunities to investigate the ionosphere and plasmasphere on a global scale (Davies & Hartmann, 1997; Stankov et al., 2003). Similarly, ADS-B can be used for ionospheric sounding as an added secondary scientific benefit in addition to its main operational purpose of monitoring air traffic.

We have discussed how a relatively simple model can be used to characterize the ionosphere using three parameters that can be adjusted in order to produce an electron density profile that agrees with FR and TEC observations. By using two measurements (FR and TEC), rather than only the TEC, we can improve the characterization of the ionosphere although the problem, however, even for the simplest NeQuick version with

three independent parameters, remains underdetermined. Additional independent measurements, such as CADI, can reduce this ambiguity. A potential source for the type of data considered as input to this model are conjunctions between satellites that receive linearly polarized beacon signals, such as the constellation of ADS-B receivers that will be hosted by the Iridium NEXT constellation. ADS-B signals can be used to measure the FR over various propagation paths. These observations can be used as input to the model discussed in this manuscript, which allows adjustable parameters to be calculated.

In this manuscript, the FR angle was determined from a prescribed TEC value. The peak density  $n_m$  was inferred from the TEC using equation (5). In reality, application of this technique will likely be the inverse problem to that presented in the present study, that is, FR and TEC observations will be used to determine profile parameters  $H$  and  $z_0$ .

Although the technique presented is feasible, with a receiver polarization angle uncertainty of  $1^\circ$  and changes in the FR of only  $2^\circ$  for lower values of TEC (see the cases for 20 TECu in Figures 4 and 5), the results are likely to be noisy. These results are still useful for distributing the electron density vertically and may be improved with data ingestion from another source. For example, the peak density and corresponding altitude from a nearby ionosonde may be used to constrain the problem further, leaving only the layer thickness to be calculated using equation (5). If both  $n_m$  and  $z_0$  are measured, then the problem becomes overdetermined and will probably require some version of a least squares computation.

By varying the parameters  $z_0$  or  $H$ , the FR angle changes by more than  $1$  to  $3^\circ$  for a fixed value of TEC. This should be detectable and will work best at midlatitudes, where the effect is largest (see Figure 1, bottom). Variations in the FR smaller than  $1^\circ$  may not be detectable using current instruments but could present an engineering problem to be solved for future application. We presented the simulation results using a relatively simple three-parameter model for midlatitudes with  $\lambda = 45^\circ$ . The profile(s) resulting from the two parameters that have been adjusted to agree with TEC and FR observations may be useful for applications such as computerized ionospheric tomography (CIT) as an a priori estimate for reconstruction of the ionospheric electron content over regions where a priori information from other instrumentation is otherwise unavailable (Cushley, 2013; Cushley & Noël, 2014; Siefring et al., 2015). Our study shows that it is possible to improve ionospheric characterization by obtaining electron density profiles using FR and TEC. This technique will be applied to real ADS-B data, when they are available. However, more detailed studies are needed in the future, particularly, to investigate other more general propagation geometries between the transmitting aircraft and passive satellite receiver(s) as well as multiple ionospheric layers.

## Acknowledgments

All values and equations used to perform the simulations presented are given in the manuscript. The authors would like to thank the Government of Canada | Natural Sciences and Engineering Research Council of Canada (NSERC) [10.13039/501100000038] (249806), for supporting this research.

## References

- ADS-B-Technologies (2011). Welcome, Website. Anchorage: AL.
- Aireon (2015). Aireon<sup>SM</sup> ADS-B payloads installed on first Iridium NEXT satellites, News and Updates. McLean, VA.
- Alminde, L. K., Midtgaard, A., Brisgard, M., Jensen, M., Gosvig, B., Birklykke, A., ... Moullec, Y. L. (2012). GomX-1: A nano-satellite mission to demonstrate improved situational awareness for air traffic control. In *26th Annual AIAA/USU Conference on Small Satellites, SSC12-I-6* (pp. 1–7). Aalborg, Denmark.
- Alminde, L. K., Kaas, K., Brisgard, M., Brisgard, M., Chistiansen, J., & Gerhardt, D. (2014). GomX-1 flight experience and air traffic monitoring results. In *Proceedings of the AIAA/USU Conference on Small Satellites, SSC14-XII-7* (pp. 1–7). Logan, Utah, USA.
- Anderson, D., & Fuller-Rowell, T. (1999). The ionosphere. In *NOAA Space Environment Topics* (pp. 14). Boulder, CO.
- Appleton, E. V. (1946). Two anomalies in the ionosphere. *Nature (London)*, *157*(3995), 691–691.
- Anderson, J. P., Phelps, E. B., Erickson, P. J., Lind, F. D., Coster, A. J., & Langston, G. I. (2011). Characterization of system calibration parameters for high gain dual polarization satellite beacon diagnostics of ionospheric variations. *Radio Science*, *46*(RS5017), 1–13.
- Brown, S. J., & Hendricks, T. L. (2011). Automatic Dependent Surveillance Broadcast (ADS-B) in Aviation Rulemaking Committee (ARC) recommendations to define a strategy for incorporating ADS-B in technologies into the National Airspace System (NAS). *A Report from the ADS-B In ARC to the FAA*. Washington, DC: ADS-B In ARC.
- Browne, I., Evans, J. V., Hargreaves, J. K., & Murray, W. A. S. (1956). Radio echoes from the Moon. *Proceedings of the Physical Society of London*, *69*, 901–920.
- Budden, K. G. (1961). *Radio Waves in the Ionosphere: The Mathematical Theory of the Reflection of Radio Waves from Stratified Ionised Layers*. Cambridge, UK: Cambridge University Press.
- Chuo, Y.-J. (2014). Variations of scale height at F-region peak based on ionosonde measurements during solar maximum over the crest of equatorial ionization anomaly region. *Scientific World Journal*, *2014*, 397402. <https://doi.org/10.1155/2014/397402>
- Cushley, A. (2013). Ionospheric tomography using Faraday rotation of Automatic Dependent Surveillance Broadcast (UHF) signals (Master's thesis), Royal Military College of Canada, Kingston, On.
- Cushley, A., & Noël, J.-M. A. (2014). Ionospheric tomography using Automatic Dependent Surveillance Broadcast (ADS-B) signals. *Radio Science*, *49*, 549–563. <https://doi.org/10.1002/2013RS005354>
- Davies, K., & Hartmann, G. K. (1997). Studying the ionosphere with the global positioning system. *Radio Science*, *84*, 1695–703.
- DeWitt, J. H., & Stodola, E. K. (1949). Detections of radio signals reflected from the Moon. *Proceedings IRE*, *37*, 229–42.
- Dhar, B., Vadher, N. M., & Deshpande, M. R. (1977). An equipment to measure Faraday rotation angle of VHF waves received from a geostationary satellite. *IEEE Journal of Research*, *23*(12), 708–711. <https://doi.org/10.1080/03772063.1977.11451514>
- Eccles, D., & King, J. W. (1969). A review of topside sounder studies of the equatorial ionosphere. *Proceedings of the IEEE*, *57*(6), 1012–18.
- European Space Agency (2013a). Tracking aircraft from orbit. Paris, France.
- European Space Agency (2013b). Hitching a ride. Paris, France.
- Francis, R., Vincent, R., Noël, J., Tremblay, P., Desjardins, D., Cushley, A., & Wallace, M. (2011). The flying laboratory for the observation of ADS-B signals. *International Journal of Navigation and Observation*, *2011*(A2), 5. <https://doi.org/10.1155/2011/973656>
- Francois, M., Santandrea, S., Mellab, K., Vrancken, D., & Versluys, J. (2014). The PROBA-V mission: The space segment. *International Journal of Remote Sensing*, *35*(7), 2548–2564. <https://doi.org/10.1080/01431161.2014.883098>
- Fuller-Rowell, T., Yizengaw, E., Doherty, P., & Basu, S. (2016). *Ionospheric Space Weather: Longitude Dependences and Lower Atmosphere Forcing, Geophysical Monograph Series*. Washington, DC: Wiley.
- Garriott, O. (1960). The determination of ionospheric electron content and distribution from satellite observations 1 and 2. *Journal of Geophysical Research*, *65*, 1139–1157.
- GomSpace (2013). GomSpace GOMX-1. Aalborg, Denmark.
- Gupta, O. (2011). Global augmentation of ADS-B using iridium NEXT hosted payloads. In *Proceedings of the Integrated Communications, Navigation and Surveillance Conference (ICNS)* (pp. 1–15). Herndon, VA, USA.
- Hammerstrom, J. A., & Cornely, P.-R. J. (2016). Total electron content (TEC) variations and correlation with seismic activity over Japan. *Journal of Young Investigators*, *31*(4), 13–6.
- Harris Corporation (2012). Aireon awards Harris Corporation contract for largest implementation of hosted satellite payloads; will provide global satellite-based aircraft tracking, Harris Press Release. Washington, DC and Melbourne, FL.
- Harris Corporation (2014). Harris Corporation completes space qualification testing of hosted payload for satellite-based global aircraft tracking system, Harris Press Release. Washington, DC and Melbourne, FL.
- Hoque, M. M., & Jakowski, N. (2012). *Ionospheric Propagation Effects on GNSS Signals and New Correction Approaches, Global Navigation Satellite Systems: Signal theory and applications*. Rijeka: InTech.
- Jakowski, N., Mayer, C., Hoque, M. M., & Wilken, V. (2011). Total electron content models and their use in ionosphere monitoring. *Radio Science*, *46*, RS0D18. <https://doi.org/10.1029/2010RS004620>
- Jayachandran, B., Krishnankutty, T. N., & Gulyaeva, T. L. (2004). Climatology of ionospheric slab thickness. *Annales Geophysicae*, *22*, 25–33.
- Kersley, I., Heatyon, J., Pryse, S., & Raymond, T. (1993). Experimental ionospheric tomography with ionosonde input and EISCAT verification. *Annals of Geophysics*, *11*, 1064–1074.
- Klobuchar, J. A., Arons, J., Mendillo, M., Allen, R. S., John, P., Seeman, D. R., & Basu, S. (1973). Total electron content studies of the ionosphere (*Tech. rep.*) Bedford, Massachusetts: Ionospheric Physics Laboratory-Air Force Cambridge Research Laboratories-L. G. Hanscom Field.
- Kraus, J. (1966). *Radio Astronomy*. New York: McGraw Hill.
- Lawrence, R. S., Posakony, D. J., Garriott, O. K., & Hall, S. C. (1963). The total electron content of the ionosphere at middle latitudes near the peak of the solar cycle. *Journal of Geophysical Research*, *68*(7), 1889–1898. <https://doi.org/10.1029/JZ068i007p01889>
- Leitinger, R. (1994). Data from orbiting navigation satellites for tomographic reconstructions. *International Journal of Imaging Systems and Technology*, *5*, 86–96.
- Leitinger, R., Zhang, M.-L., & Radicella, S. M. (2005). An improved bottomside for the ionospheric electron density model NeQuick. *Annals of Geophysics*, *48*(3), 525–34.
- MacDougall, J. W. (1969). The equatorial ionospheric anomaly and the equatorial electrojet. *Radio Science*, *4*(9), 805–810. <https://doi.org/10.1029/RS004i009p0805>
- Marsh, G. (2006). European air traffic surveillance. Danbury, CT.
- Nava, B., Coisson, P., & Radicella, S. (2008). A new version of the NeQuick ionosphere electron density model. *Journal of Atmospheric and Solar-Terrestrial Physics*, *70*(15), 1856–1862. <https://doi.org/10.1016/j.jastp.2008.01.015>
- NavCanada (2008). Hudson bay implementation, Brochure. Ottawa, ON.
- Radicella, S. M., & Zhang, M. L. (1995). The improved DGR analytical model of electron density height profile and total electron content in the ionosphere. *Annals of Geophysics*, *38*(1), 35–41.

- Rawer, K. (1963). *Propagation of Decameter Waves (HF band)*, in *Meteorological and Astronomical In Uences on Radio Wave Propagation* (pp. 221–250). New York: Academic Press.
- Rawer, K. (1993). *Wave Propagation in the Ionosphere*. Dordrecht: Kluwer Acad. Publ.
- Rogers, N. C., & Quegan, S. (2014). The accuracy of Faraday rotation estimation in satellite synthetic aperture radar images. *IEEE Transactions on Geoscience and Remote Sensing*, 52(8), 4799–807.
- Shmuel, B., Hiemstra, J., Tarantini, V., Singarayar, F., Bonin, G., & Zee, R. E. (2012). Canadian Advanced Nanospace eXperiment 7 (CanX-7) demonstration mission: De-orbiting nano- and microspacecraft. In *26th Annual AIAA/USU Conference on Small Satellites*, UTIAS Space Flight Laboratory, Toronto, ON, Canada.
- Siefring, C. L., Bernhardt, P. A., James, H. G., & Parris, R. T. (2015). The CERTO beacon on CASSIOPE/e-POP and experiments using high-power HF ionospheric heaters. *Space Science Reviewssr*, 189(1–4), 107–122. <https://doi.org/10.1007/s11214-014-0110-2>
- Soicher, H., & Gorman, F. (2012). Seasonal and day-to-day variability of total electron content and mid-latitudes near solar maximum. *Radio Science*, 20, 383–387. <https://doi.org/10.1029/RS020i003p00383>
- Stankov, S. M., Jakowski, N., Heise, S., Muhtarov, P., Kutiev, I., & Warnant, R. (2003). A new method for reconstruction of the vertical electron density distribution in the upper ionosphere and plasmasphere. *Journal of Geophysical Research*, 108(A5), 1164. <https://doi.org/10.1029/2002JA009570>
- Stankov, S., & Warnant, R. (2009). Ionospheric slab thickness—Analysis, modelling and monitoring. *Advances in Space Research*, 44(11), 1295–1303.
- University of Toronto Institute for Aerospace Studies Space Flight Laboratory (2014). Nanosatellites: CanX-7, UTIAS SFL News. Toronto, ON.
- Van Der Pryt, R., & Vincent, R. (2016). A simulation of reflected ADS-B signals over the North Atlantic for a spaceborne receiver. *Positioning*, 7, 51–62.
- Vincent, R., & Van Der Pryt, R. (2017). The CanX-7 nanosatellite ADS-B mission: A preliminary assessment. *Positioning*, 8, 1–11.
- Wahi, R., Dubey, S., & Gwal, A. K. (2005). Ionospheric total electron content measurement in Malaysian region during high solar activity using GPS receiver. *Indian Journal of Radio and Space Physics*, 34, 399–401.
- Wen, D., Yuan, Y., Ou, J., & Zhang, K. (2010). Ionospheric response to the geomagnetic storm on August 21, 2003 over China using GNSS-based tomographic technique. *IEEE Transactions on Geoscience and Remote Sensing*, 48(8), 3212–3217.
- Wright, J. W. (1960). A model of the F-region above hmaxF2. *Journal of Geophysical Research*, 65, 185.
- Zhao, B., Wan, W., Liu, L., & Ren, Z. (2009). Characteristics of the ionospheric total electron content of the equatorial ionization anomaly in the Asian-Australian region during 1996–2004. *Annals of Geophysics*, 27, 3861–3873.

## Faraday Rotation, total electron content, and their sensitivity to the average parallel component of the magnetic field

### 6.1 Overview

The scientific results presented in this chapter are based on the following publication:

- Cushley, A. C., Noël, J.-M., & Kabin, K., Faraday rotation, total electron content, and their sensitivity to the average parallel component of the magnetic field. *Radio Sci.*, 53., 2018.

This study examined the relationship between FR, TEC, and the parallel component of the Earth's magnetic field. A sensitivity analysis was performed using synthetic ADS-B signals over vertical propagation paths for different characteristic values of the average parallel component magnetic field in Eqn. 2.15. The results from different methods were compared to a benchmark solution, using IRI for  $n_e(z)$  and IGRF for  $B_{\parallel}(z)$  in Eqn. 2.11.

It is found that the best solutions are obtained when a weighted average of the magnetic field measured at both the satellite and on the ground are used with a slight bias towards the satellite measurement. The relative weight  $w = 0.451$  was found for the specific case presented in this manuscript.

### 6.2 The Study

Qualitatively, the FR is given by Eqn. 2.11, and largely depends on the integral  $\int n_e(z)B_{\parallel}(z)dz$ , where  $n_e$  is the electron density, and  $B_{\parallel}$  is the Earth's magnetic field projection in the radio wave propagation direction. The integral is taken along the radio wave propagation direction. The (anti-) parallel component of Earth's magnetic field plays a critical role in the occurrence of FR. Therefore, accurate knowledge or a correct model for both  $n_e$  and  $B_{\parallel}$  as well as the propagation trajectory is required for the proper interpretation of FR measurements.

In the presence of different local disturbances (eigen waves, terminator effects, etc. that disturb the  $n_e$ ), which are not taken into account by  $n_e$  models, correct calculation of the integral adds to the complexity of the task. Consequently, the average value (over 1-2 hours) is all that is generally used to estimate the FR experienced or expected in TEC data [*Berngardt and Themens, personal communication*].

At best, only ground-based and space-based measurements are available for an arithmetic average of the magnetic field. Information about the magnetic field between the ground and satellite are obtained from magnetic field models or neglected in place of an average value. *Wright et al.* [2003]; *Sheriff and Hu* [2003]; *Ippolito* [2008]; *Jehle et al.* [2009] all assume a constant value  $B_{avg}$  for the vertical component of the magnetic field in order to obtain Eqn. 2.15, from which the TEC values are computed as input to CIT in *Cushley* [2013]; *Cushley and Noël* [2014]. IGRF is a widely used model for the component magnetic field data used to compute  $B_{avg}$  [*International association of geomagnetism and aeronomy, Working Group V-MOD, 2010*]. However, the magnetic field strength is not linear as a function of altitude. Due to the inverse cubic relationship between the magnetic field strength and distance, the average value for the magnetic field will systematically underestimate the FR, which is particularly important for the determination of TEC from FR measurements. This relationship also has direct implications for the more common estimation of FR from TEC.

Further investigation into the accuracy of  $B_{avg}$  as a representation of the magnetic field along a ray path is presented in order to better understand the effect on the interpretation of TEC from FR measurements using Eqn. 2.15. The IRI and IGRF models were used to generate IED profiles and the corresponding parallel component of the magnetic field along vertical ray paths in order to compare the value of the integral with a characteristic value for the parallel component of the magnetic field along the path such as an average or from a specified altitude (i.e. thin shell altitude).

Another method for the determination of a characteristic value for the parallel component of the magnetic field that is an improvement over  $B_{avg}$  was established by comparing different methods. For example, the field from different fixed altitudes as well as the varying altitude of the peak electron density were considered. The

exact solution for the average value of  $B_{\parallel}$ , assuming FR and TEC measurements are both available. Furthermore, a comparison of the (normalized) magnetic field and electron density profiles as a function of altitude was made to clearly show how each parameter contributes to the FR at different altitudes and the total FR measured.

The following manuscript is related to the previous research by *Cushley* [2013]; *Cushley and Noël* [2014] since it investigates the validity of using an average value for the magnetic field along a propagation path in order to remove it from inside the integral to reduce Eqn. 2.11 to Eqn. 2.15. It also prescribes a method that is more accurate than by using a simple linear average for the magnetic field. This information may be used to improve the accuracy of TEC estimation from FR measurements, for input to CIT in Chapters 4 and 7. Improved TEC estimations consequently reduces the errors that will inevitably propagate throughout the reconstruction region. This method also applies to estimating FR from TEC more accurately. This technique may also prove useful for computing ionospheric parameters from independent FR and TEC measurements more accurately by using the technique described in Chapter 5.

For most of the comparisons, normalized data was used. For input to CIT, ultimately the absolute TEC does not matter as much as the relative variation or shape of the projection data since the pixels values are not absolute. The pixel values are established relative to one another. It is planned that such maps could be constrained by other data sources, for example the peak density inferred from an ionosonde within the reconstruction region could be used to multiply by the normalized densities in the map in order to scale the entire IED profile accordingly. Ionosonde peak density altitude could also be used prior to the reconstruction in order to constrain the vertical distribution of the electron density.

### 6.3 Published Paper

The sensitivity analysis to different methods of obtaining characteristic values for the parallel component of the magnetic field to improve the estimation of TEC from FR (and vice-versa) that were discussed in this chapter was published in *Radio Science*

in 2018. Presented immediately below is the paper in the journal format reproduced by permission of American Geophysical Union:

- Cushley, A. C., Noël, J.-M., & Kabin, K., Faraday rotation, total electron content, and their sensitivity to the average parallel component of the magnetic field. *Radio Sci.*, 53. doi:10.1029/2018RS006667, 2018. Copyright 2017 American Geophysical Union.





# Radio Science

## RESEARCH ARTICLE

10.1029/2018RS006667

# Faraday Rotation, Total Electron Content, and Their Sensitivity to the Average Parallel Component of the Magnetic Field

### Special Section:

URSI General Assembly and Scientific Symposium (2017)

A. C. Cushley<sup>1</sup> , J.-M. Noël<sup>1</sup> , and K. Kabin<sup>1</sup> 

<sup>1</sup>Department of Physics, Royal Military College of Canada, Kingston, Ontario, Canada

### Key Points:

- Although commonly used, a reference height or mean value for the magnetic field may not always be appropriate to calculate FR from TEC
- FR estimation from TEC measurements and TEC mapping from FR measurements are limited by the accuracy of the magnetic field
- The results were shown to bias the result toward the magnetic field value measured on the ground

### Correspondence to:

A. C. Cushley,  
alex.cushley@rmc.ca

### Citation:

Cushley, A. C., Noël, J.-M., & Kabin, K. (2018), Faraday rotation, total electron content, and their sensitivity to the average parallel component of the magnetic field. *Radio Science*, 53. <https://doi.org/10.1029/2018RS006667>

Received 8 JUN 2018

Accepted 2 AUG 2018

Accepted article online 23 AUG 2018

**Abstract** A plane-polarized electromagnetic wave that propagates through a plasma, (anti)parallel to a magnetic field, experiences a gradual rotation of its plane of polarization called Faraday rotation (FR). The FR angle depends on the integrated product of the electron density and the strength of the parallel magnetic field projection to the radio wave propagation direction. The integral is taken along the radio wave propagation direction over the entire path length. Therefore, accurate measurements or a suitable model for both the electron density and the magnetic field as well as the propagation trajectory are required for the interpretation of FR measurements. Many authors use the average value of the parallel magnetic field for estimation of FR from ionospheric total electron content measurements. Although it is known that the strength of Earth's geomagnetic field varies slowly at ionospheric altitudes, a reference height characteristic value or mean value may not always be appropriate. This work considers alternative methods to establish a characteristic value for the average parallel component of the magnetic field, particularly when independent FR and total electron content measurements are available.

## 1. Introduction

When electromagnetic waves propagate through and interact with the ionosphere, they are modified and can be used to describe the medium through which they have passed. A plane-polarized wave propagating parallel to a magnetic field in a plasma experiences a rotation of its plane of polarization called Faraday rotation (FR; e.g., Budden, 1961; Kraus, 1966). The angle of rotation is dependent on the integrated product of the electron density along the path of unit cross-section, with the strength of the magnetic field projection to the radio wave propagation direction. It is also inversely proportional to the square of the wave frequency.

Total electron content (TEC) is defined as the integrated electron density within a column of ionospheric plasma of 1 m<sup>2</sup> in cross-sectional area. The ionospheric TEC along the path can be used to estimate the FR or propagation time delay due to the ionosphere. Although TEC is highly variable, typically the daily global maximum TEC is found to range between 80 and 200 TEC units (1 TECu = 10<sup>16</sup> electrons per square meter) over equatorial regions at solar maximum conditions (NASA Jet Propulsion Laboratory California Institute of Technology, 2014; Wahi et al., 2005; Zhao et al., 2009) and generally decreases with latitude (Soicher & Gorman, 2012). Many authors, for example, Brunner and Gu (1991); Ippolito (2008); Jehle et al. (2009); Lawrence et al. (1963); Sheriff and Hu (2003); and Wright et al. (2003), use an average value for the parallel component of the magnetic field in order to simplify the estimation of FR. By removing the parallel component of the magnetic field from the integral, the FR can be estimated using the TEC.

To estimate FR the magnetic field can be obtained using data when available or models while the TEC spatial distribution is measured and mapped by the Global Navigation Satellite System (GNSS) network. Empirical models of TEC and the geomagnetic field represent long-term averaged data, neglecting specific events. While models can be useful for general behavior and even show diurnal variation quite well, they cannot be used for the analysis of sporadic short time scale (minutes to hours) events such as auroral patches, terminator effects, and other processes that disturb the electron density  $n_e$ . The presence of these different local disturbances are not taken into account by average ionospheric electron density models, therefore these models do not accurately predict the FR. Consequently, the average TEC value over 1–2 hr is generally used to estimate the FR that would result when a radio wave propagates through the ionosphere [Berngardt and Themens, *personal communication*]. This may be sufficient for some applications such as the estimation of FR from TEC to predict or forecast the amount of FR in satellite systems, but may not be adequate for the inverse

problem namely the estimation of TEC from FR measurements and magnetic field models as input for computerized ionospheric tomography (CIT) (Cushley & Noël, 2014), or in applications that require greater precision such as synthetic aperture radar (SAR) imagery correction (Jehle et al., 2009; Rogers & Quegan, 2014) and radio astronomy [*Tony Willis - personal communication*]. Measuring FR in the interstellar media is a widely used astronomical technique (Sotomayor-Beltran et al., 2013). However, it requires separation of the time-variable ionospheric FR contribution from that caused by the interstellar media. This becomes particularly important for nearby sources, where the ionospheric contribution to these measurements can be a significant fraction of the observed rotation, and therefore must be accounted for accurately. Thus, what we do here is very important for the astronomers as well.

Generally, only ground-based and/or space-based measurement of the Earth's magnetic field using magnetometers are available for FR calculations, not a complete knowledge of the magnetic field profile. However, the magnetic field strength is not exactly a linear function of altitude and can be disturbed during high geomagnetic activity (Kivelson & Russell, 1995; Treumann & Baumjohann, 1996). As a result, a simple averaging of the ground- and space-based measurements, when they are available, is not an accurate representation of the magnetic field.

The scientific objective of the present work is to investigate the relationship between FR and TEC for different characteristic values of the Earth's magnetic field. We attempt to address the main question: what is the best expression for the effective parallel component of the magnetic field to be used for FR calculations? Given that Earth's magnetic field is dipole-like and that the strength varies as a function of geocentric distance as an inverse cubic, would it be appropriate to use the magnetic field value measured at the satellite as opposed to an average value, or would it be more appropriate to use the magnetic field value at the altitude of the peak density since the majority of the contribution to the TEC is in the F-region? Ultimately, what is the best averaging procedure for the parallel component of the geomagnetic field?

Many methods to determine a characteristic value for the parallel component of the magnetic field that is an improvement over an arithmetic average were investigated by comparing several different methods to one another with respect to a benchmark solution. The work demonstrates the potential of using independent FR and TEC measurements to determine the average parallel component over vertical paths, which can then be used to predict FR in other systems, including correction of SAR imagery, and/or to estimate the TEC from FR measurements as input for CIT. Although there are several potential applications, the main motivation for this work came from our study of CIT using the FR of Automatic Dependent Surveillance Broadcast (ADS-B) signals as input (Cushley & Noël, 2014). Typically, CIT uses TEC measurements made by ground-based receivers processing dual frequency signal phase differences or differences in the pulse travel time and pulse shape measurements from GNSS satellites as input (Davies & Hartmann, 1997; Stankov et al., 2003). Ground stations cannot be installed mid-ocean and are difficult to maintain in the Arctic, which has hampered further development. These high latitude and oceanic regions correspond to the largest errors for TEC maps (Jakowski et al., 2011). Therefore, using ADS-B measurements in those areas can improve the accuracy of the TEC maps and be used for CIT; however, ADS-B is only single frequency so the TEC cannot be measured using the differential method that is used for GNSS signals. The TEC can be estimated using FR measurements and magnetic field models, which requires accurate models or measurements of the parallel component of the magnetic field so that unknown magnetic field uncertainties do not propagate to the TEC estimation and CIT reconstruction. This method could support the potential exploitation of preexisting networks and operational data to contribute to current methods of ionospheric sounding.

## 2. Theory and Methodology

### 2.1. Faraday Rotation

The FR angle,  $\Omega$ , is measured in radians (Budden, 1961; Kraus, 1966) viz.,

$$\Omega = \frac{1}{8\pi^2 c} \frac{e^3}{\epsilon_0 m_e^2} \frac{1}{f^2} \int_0^l n_e(z) B_z(z) dz, \quad (1)$$

where  $n_e(z)$  is the electron density at altitude  $z$  and varies over propagation path of length  $l$ ,  $c = 3 \times 10^8$  m/s is the speed of light in free space,  $e = 1.602 \times 10^{-19}$  C is the elementary charge,  $m_e = 9.109 \times 10^{-31}$  kg is the mass of an electron,  $f$  is the frequency (Hz) of the incident radio wave,  $\epsilon_0 = 8.854 \times 10^{-12}$  C<sup>2</sup>/N · m<sup>2</sup> is the permittivity of free space and  $B_z(z)$  is the component of the magnetic field parallel to the direction of the wave propagation measured in T.

The FR angle is directly proportional to the integrated electron density and often approximated (e.g., Lawrence et al., 1963) as

$$\Omega \simeq \frac{2.36 \times 10^4}{f^2} B_{avg} \cos \theta \sec \chi \int_0^l n_e dl, \quad (2)$$

where  $B_{avg}$  is the average magnetic field intensity in T,  $\theta$  is the angle between the wave vector  $\vec{k}$  and the magnetic field vector  $\vec{B}$ , and  $\chi$  is the zenith angle (between the wave vector and the vertical). The geometrical factor,  $B_{avg} \cos \theta \sec \chi$ , varies slowly along the ray path and should in fact be within the integral, but it is sometimes taken outside the integral by assuming that it has an average value, suitably weighted over the part of the ray path that lies within the ionosphere (Lawrence et al., 1963).

The TEC along the ray path of unit cross-section is given by

$$TEC = \int_0^l n_e dl, \quad (3)$$

where  $TEC$  is the integrated electron density  $n_e$  along the path length  $l$  and is usually expressed in TECu.  $TEC$  can either be measured using signal time delay or obtained from vertical TEC (VTEC) maps that are regularly produced using GNSS differential phase measurements. Such maps are made available at [http://iono.jpl.nasa.gov/latest\\_rti\\_global.html](http://iono.jpl.nasa.gov/latest_rti_global.html) among other sources.

Among others, Brunner and Gu (1991), Ippolito (2008), Lawrence et al. (1963), Jehle et al. (2009), Sheriff and Hu (2003), The International Telecommunications Union (2003), and Wright et al. (2003) all assume an average value for the parallel component of the magnetic field  $B_{||avg} = B_{avg} \cos \theta \sec \chi$  in order to simplify equation (2).

The inverse problem of estimating  $TEC$  from FR measurements and magnetic field models can be expressed by rearranging equation (2) for a particular fixed frequency.

To properly calculate the average parallel component of the magnetic field  $\langle B \rangle$  in order to extract it from the integral, it should be determined using

$$\langle B \rangle = \frac{8\pi^2 c \epsilon_0 m_e^2 f^2}{e^3} \cdot \frac{\Omega}{TEC} = \frac{1}{TEC} \int_0^l n_e(z) B_z(z) dz, \quad (4)$$

where  $\langle B \rangle$  is the average magnetic field. However, applying equation (4) may not always be practical. The only way to obtain  $\langle B \rangle$  exactly is to measure both the FR and  $TEC$  and then there is no need to compute FR from  $TEC$  or vice versa. However, both measurements are not usually available from the same satellite. If independent FR and  $TEC$  measurements were available from either a single satellite or conjunctions between two satellites, they would be useful for mapping the parallel component of the magnetic field, which then could be used for other applications.

There are different ways to compute the average magnetic field that can be considered: for example, arithmetic, geometric, and mean value theorem for integrals to name a few. In this paper, we compare different methods of calculating the effective parallel component of the magnetic field in order to find a simple method that works best for a satellite in a circular orbit at 1,000-km orbital altitude.

Figure 1 shows the electron density profile (left panel) from the International Reference Ionosphere (IRI) version IRI2012web (Bilitza, 2007; Bilitza et al., 2011) and magnetic field profile (center panel) from the International Geomagnetic Reference Field (IGRF) version 11 (International association of geomagnetism and aeronomy, 2010; Maus et al., 2005) as a function of altitude. These profiles were used to create the benchmark solution; the cumulative FR (right panel) at the altitude of the satellite given by equation (1). For this figure,  $n_e(z)$  in equation (1), we arbitrarily selected 1 January 2000 at 0130 UTC at 50°N latitude, 40°E longitude as the location for the comparisons, which is the default location for the IRI model. While IRI is not very accurate above the F2 peak, where it is hard to constrain it with measurements, it is an obvious choice for this initial study. The  $TEC$  for the electron density profile is 3.3 TECu and the total FR angle at the 1,000-km orbital altitude of the satellite is 1.43°.

The percent difference (%diff) in the cumulative FR for a given method ( $\Omega_{method}$ ) from the benchmark solution ( $\Omega_{IGRF}$ ) is computed as follows:

$$\%diff = \frac{\Omega_{IGRF} - \Omega_{method}}{\Omega_{IGRF}} \times 100. \quad (5)$$

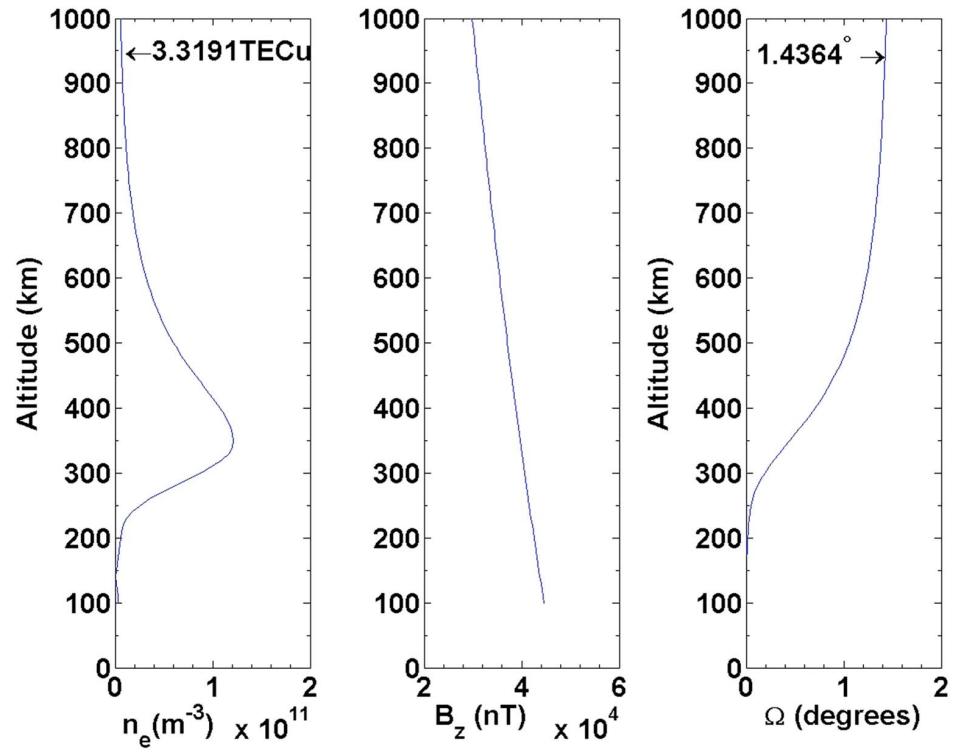


**Figure 1.** Profiles of the electron density (left) from International Reference Ionosphere and the corresponding radial magnetic field (center) from International Geomagnetic Reference Field as a function of altitude calculated by International Reference Ionosphere and International Geomagnetic Reference Field for 1 January 2000 at 0130 UTC at 50° geographic latitude, 40° longitude that were used to create the benchmark solution for the cumulative Faraday rotation (right) given by equation (1). TECu = total electron content unit.

It can be seen from equation (5) that when a particular method overestimates the amount of rotation than the benchmark solution, the percent difference is a negative value.

Figure 2 shows a comparison of the percent difference in the cumulative FR as a function of altitude using four different methods to calculate the average magnetic field. This figure illustrates the uncertainty that results in the FR when a characteristic value for  $B_{\parallel avg}$  is used in order to extract it from the integral (see equation (2)). The dashed blue curve shows the percent difference of the FR computed for an electron density profile from IRI and the corresponding magnetic field profile from the IGRF evaluated every 10 km, is labeled  $B_{IGRF}$ , and will be considered as the benchmark solution to which all others will be compared. The value of the cumulative FR at 1,000 km is the same as using the exact value  $\langle B \rangle$  from equation (4). The red curve shows that using a value of the magnetic field corresponding to the value of  $B_{\parallel avg}$  at the Earth's surface (e.g., ground-based magnetometers—shown by the red curve labeled  $B_{Gnd} = B_{IGRF}(0) = 4.6750 \times 10^{-5} \text{T}$ ) tends to overestimate the FR by  $\sim 17.4\%$ , while a value for  $B_{\parallel avg}$  from a higher altitude (e.g., satellite-based magnetometer shown by the green curve labeled  $B_{Sat} = B_{IGRF}(1000) = 2.9901 \times 10^{-5} \text{T}$ ) tends to underestimate the FR by  $\sim 21.2\%$ . The arithmetic average of  $B_{Gnd}$  and  $B_{Sat}$  shown as the blue curve, labeled  $B_{Avg}^A$ , is much better than either  $B_{Gnd}$  or  $B_{Sat}$ , but it still tends to underestimate the FR by  $\sim 1.9\%$  when compared to the value for the cumulative FR at 1,000 km. The geometric average of  $B_{Gnd}$  and  $B_{Sat}$  labeled  $B_{Avg}^G$  shown as the cyan curve is also much better than either  $B_{Gnd}$  or  $B_{Sat}$ , but it underestimates the FR by slightly more than 3.8%.

We note that the largest deviations are found to be at 100-km altitude in Figure 2. A back-of-envelope calculation is used to explain this. At 100-km altitude, the FR for the benchmark solution is only  $1.6 \times 10^{-3}^\circ$ , whereas it reaches a maximum value of  $1.43^\circ$  at 1,000 km. For the arithmetic average the FR at 100 km is  $1.3 \times 10^{-3}^\circ$  at 100 km and  $1.40^\circ$  at 1,000 km. Using equation (5), we find that this corresponds to a deviation of 18.8% at 100 km and 1.9% at 1,000 km.

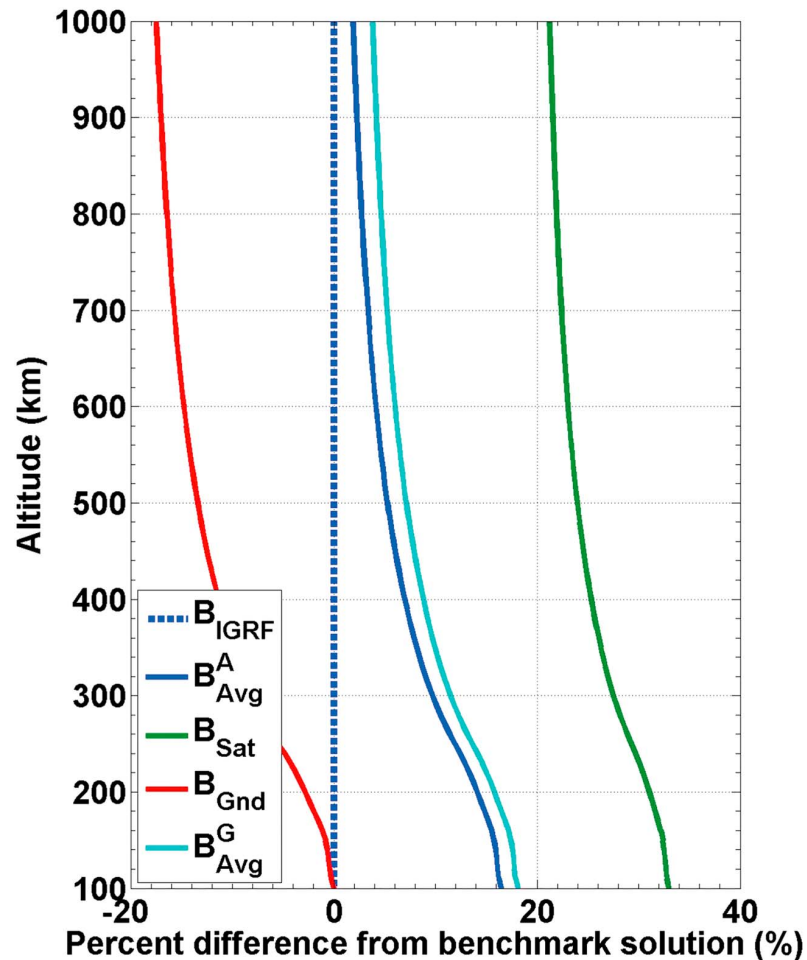


**Figure 2.** A comparison of the percent difference from benchmark solution using different methods to obtain the characteristic magnetic field from various altitudes. All methods have been normalized as a cumulative percentage as a function of altitude with respect to the total Faraday rotation (received by a satellite) at 1,000 km for the benchmark solution. IGRF = International Geomagnetic Reference Field.

The underestimation shown by the blue curve in Figure 2 is due to the fact that the geomagnetic field does not vary linearly with altitude. This fact is not taken into account when using the arithmetic average of two measurements is taken at each end of the propagation path. If  $B$  was a linear function of altitude then an arithmetic average would give the exact value  $\langle B \rangle$ . In reality, the Earth's magnetic field is dipole-like and decreases with geocentric distance as an inverse cubic (neglecting higher order moments which fall off more rapidly than  $1/r^3$ ; de Pater & Lissauer, 2010). Due to the inverse cubic relationship, an average value for the magnetic field will systematically overestimate the FR in the scenario we considered, which causes particular concerns for the accurate determination of FR using TEC measurements if a simple arithmetic average is used to compute  $B_{\parallel avg}$ . Although it is more common to estimate FR from TEC, the  $1/r^3$  relationship also has direct implications for the inverse problem of computing TEC from FR. Once the FR angle is known, the relationship between FR and TEC can be used for the generation of TEC maps from SAR data (Lavalle, 2009). In order to use models for an average of  $B_{\parallel avg}$  from incremental values along the entire path, the exact path the waves takes must be known. Lower frequencies undergo more refraction, making the determination of the wave path more difficult to determine (Balsler & Smith, 1962).

## 2.2. Numerical Modeling

We restrict our analysis to the case when the satellite is directly overhead (i.e.,  $\theta = \chi = 0$  in equation (2) by assuming that  $B_{\parallel} = B_r$  (Cushley et al., 2017). Then the component parallel to the propagation of the radio

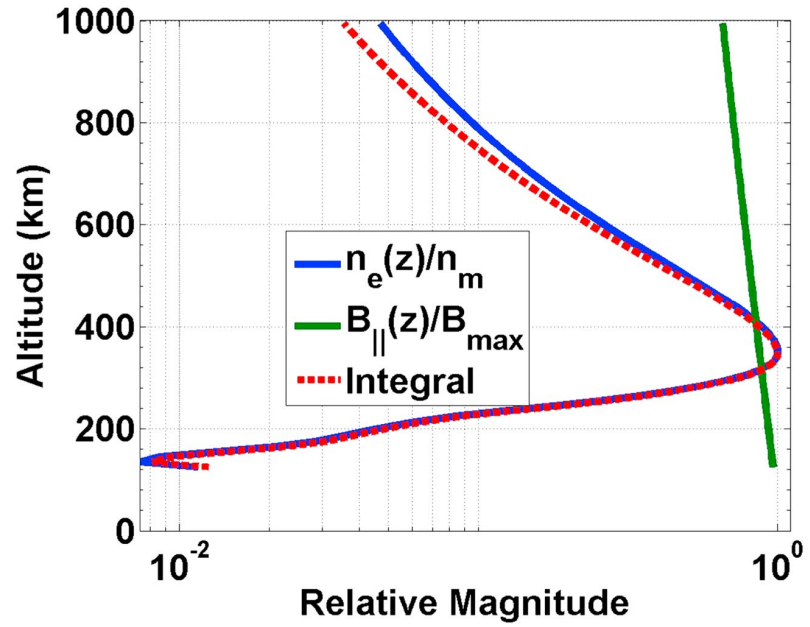


**Figure 3.** A semilogarithmic comparison of the normalized magnetic field (green trace) and electron density (blue trace) profiles as a function of altitude shows how each parameter contributes to the Faraday rotation. The integral (red-dashed trace) has been normalized with respect to  $n_m B_z(n_m)$ . Note that the electron density is more variable than the magnetic field.

wave can be described using a dipole approximation, written as

$$B_{||} = B_r = B_{eq} \frac{2R_E^3 \sin \lambda}{(z + R_E)^3}, \quad (6)$$

where  $B_{eq} = -3.1 \times 10^4$  nT is the equatorial dipole strength on the surface of the Earth and  $\lambda$  is the geomagnetic colatitude, which was set to  $45.1^\circ$  to coincide with the default values of geographic latitude of IRI. This choice of geometry describes the simplest and the most ideal observational geometry due to the availability of routinely produced global VTEC maps. For the sake of simplicity, in this study we will only consider this geometry.

For the benchmark solution, values for the electron density were computed from 100 to 1,000 km in 10-km intervals using the IRI model. The corresponding values for the parallel component of the magnetic field were computed using IGRF in the same altitude range. A sensitivity analysis was undertaken using different methods of obtaining the characteristic values of the average parallel component of the magnetic field  $B_{||avg}$  used in equation (2).

Figure 3 shows a comparison of the normalized magnetic field ( $B_z(z)/B_{max}$  green trace) and electron density profiles ( $n_e(z)/n_m$  blue trace) as functions of altitude and how each parameter contributes to the cumulative FR shown as the red-dashed trace. The maximum value of the parallel component of the magnetic field  $B_{max}$  is achieved at the Earth's surface. The electron density profile is the relative density with respect to the peak density  $n_m$ . The benchmark solution (shown as the dashed red line) follows the general shape of the electron density profile, which suggests that the electron number density  $n_e$  is the dominant parameter in the integral and contributes more to the total FR calculation. This is consistent with the results shown in Figure 3 where we observe that the normalized magnetic field varies relatively little as a function of altitude, therefore the variability of the cumulative FR would necessarily originate from variability in  $n_e(z)$ . The relative variation of  $n_e$  is much larger than that of  $B$ .

For cases that follow, the TEC was computed by integrating the electron densities obtained from IRI using equation (3). The effect on the FR using the different methods of computing the effective parallel component of the magnetic field was compared to the benchmark solution.

Specifically, the cases that were studied in this paper are as follows:

1.  $B_{IGRF} \equiv$  the benchmark solution;
2.  $B_{Gnd} \equiv$  the magnetic field value from IGRF at sea level;
3.  $B_{Sat} \equiv$  the value from IGRF at the 1,000-km orbital altitude of the satellite;
4.  $B_{Avg}^A \equiv$  the arithmetic average of the transmitter and orbital (receiver) altitude,

$$B_{Avg}^A = \frac{B_{Gnd} + B_{Sat}}{2}; \quad (7)$$

5.  $B_{Avg}^G \equiv$  the geometric mean of the IGRF radial component profile from the transmitter and orbital (receiver) altitude,

$$B_{Avg}^G = \sqrt{B_{Gnd} \cdot B_{Sat}}; \quad (8)$$

6.  $B_{Dip}^i \equiv$  three dipole extrapolations where  $B_r^m$  is measured at  $z^m$  ( $B_r^m = B_{Gnd}$  at  $z^m = 0$  km to obtain  $B_{Dip}^{Gnd}$ , and  $B_r^m = B_{Sat}$  at  $z^m = 1000$  km to obtain  $B_{Dip}^{Sat}$ ) and determined at other altitudes using

$$B_r = B_r^m \left( \frac{z^m + R_E}{z + R_E} \right)^3. \quad (9)$$

- The average  $B_{Dip}^{avg}$  of the previous two dipoles ( $B_{Dip}^{Gnd}$  and  $B_{Dip}^{Sat}$ ) will also be used for comparison;
7. the magnetic field at different altitudes of  $B_{IGRF}$  from 350 to 500 km in 50-km intervals;
  8. the altitude of the peak electron density (i.e.,  $h_m n_m$ ) computed from IRI;
  9.  $B_w \equiv$  weighted average  $B_w$  to favor either the ground-based or orbital altitude value. The weight  $w$  was varied from 0 to 1 in increments of 0.001 to find the weight that minimizes the difference with the benchmark solution for  $\Omega$  at 1,000 km.

$$B_w = w B_{Sat} + (1 - w) B_{Gnd}. \quad (10)$$

Early satellite missions (e.g., Sputnik3, ATS-6) used linear polarization, which allowed FR to be calculated in addition to the time delay and TEC. More recently, satellite systems normally use circular polarization in order to mitigate the FR effect and signal fading associated with the satellite changing its orientation combined with changing polarization as the signal encounters any anomalies in the ionosphere (Orfanidis, 2008). Circular polarization can be used to make communications more robust and avoid the negative consequences of FR. For a satellite using linear polarization, the FR and TEC data could be independently measured by the same satellite. For example, FR can be measured from phase difference and the TEC from the time delay as described by Davies et al. (1979) for the ATS-6 satellite. Alternatively, the change in received amplitude as a function of time can be used to calculate the FR as was done by Aitchison and Weekes (1959), de Mendonto and Garriott (1962), and Ross (1960) for Sputnik3. The FR and TEC can also be obtained for conjunctions using two different satellites; for example, the FR can be measured using ADS-B at vertical incidence in conjunction with the VTEC maps obtained from GNSS.

### 3. Results

In Figure 2, the arithmetic average (solid blue line) clearly shows that it overestimates the integral since it is to the right of the benchmark solution (blue-dashed line). It would seem reasonable to assume that  $B_{||}$  should be selected slightly closer to the value of  $B_{Sat}$ . It might also seem reasonable from Figure 3 to assume that since the electron density is the parameter that seems to dominate the shape of the integral, that selecting  $B_{||}$  near the altitude of the peak density, we might approach the benchmark solution (Bassiri & Hajj, 1993).

To this end, a comparison with the benchmark solution, the arithmetic average, and the radial component of the magnetic field from IGRF at various intermediate reference altitudes in 50-km intervals from 400 to 500 km, as well as from the altitude of the peak electron density (i.e.,  $h_m n_m$ ), was made.

The percent difference from the benchmark solution (dashed blue line) is shown in Figure 4. In this case,  $h_m n_m = 350$  km (black dotted curve) and the cumulative FR as would be measured by a satellite at 1,000-km altitude overestimates the benchmark solution by 4.57%, while the solution using  $B$  from 450 km (red curve) overestimates the FR angle by only 0.06%.

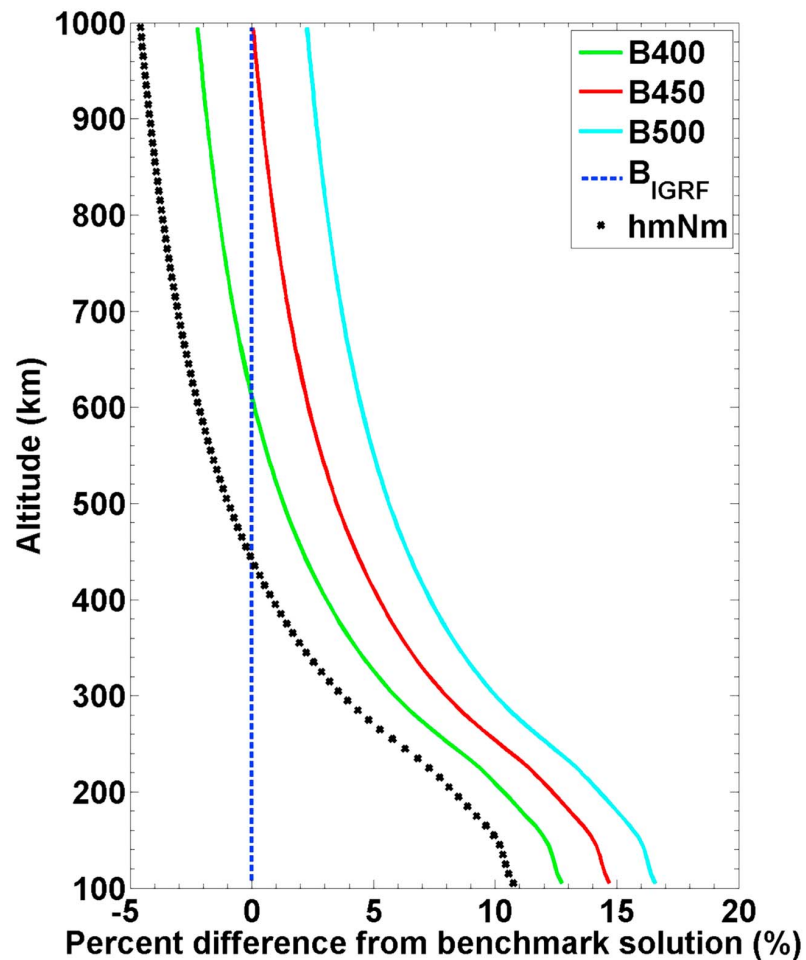


**Figure 4.** A comparison of the percent difference from benchmark solution using different methods to obtain the characteristic magnetic field from different altitudes. IGRF = International Geomagnetic Reference Field.

The cases above 500 km and below 350 km are not shown here; however, the results indicate that the errors in these cases are larger than 2.36%. Using a magnetic field from altitudes greater than 500 km resulted in curves moving toward the right of the cyan 500-km curve in Figure 4 underestimating the total FR. Using values for the magnetic field from altitudes lower than 350 km resulted in curves that moved toward the left of the trace denoted by the black ( $h_m n_m = 350$  km) curve overestimating the total FR using this method. This suggests that in this particular case study, the radial magnetic field from an altitude of 450 km approximates the benchmark solution with the smallest percentage difference.

Usually, simultaneous ground- and space-based measurements are not available at the locations of the transmitter and receiver. Therefore, the arithmetic average is not normally available, and as a result methods using only a single measurement should be considered. Let us consider a method which can map either a ground-based measurement up to the altitude of the satellite or vice versa. Equation (9) allows us to extrapolate a measurement  $B_r(z^m)$  using the dipole approximation.

A comparison of the profiles derived from single values along with the IGRF profile that was used as the benchmark solution is shown in Figure 5. The space- and ground-based magnetic field values  $B_r$  are where the radial field is at either the maximum or minimum altitude from the IGRF profile, respectively. These exact values from the benchmark profile simulated perfectly accurate magnetometers that are either on the surface of the Earth or onboard the satellite.



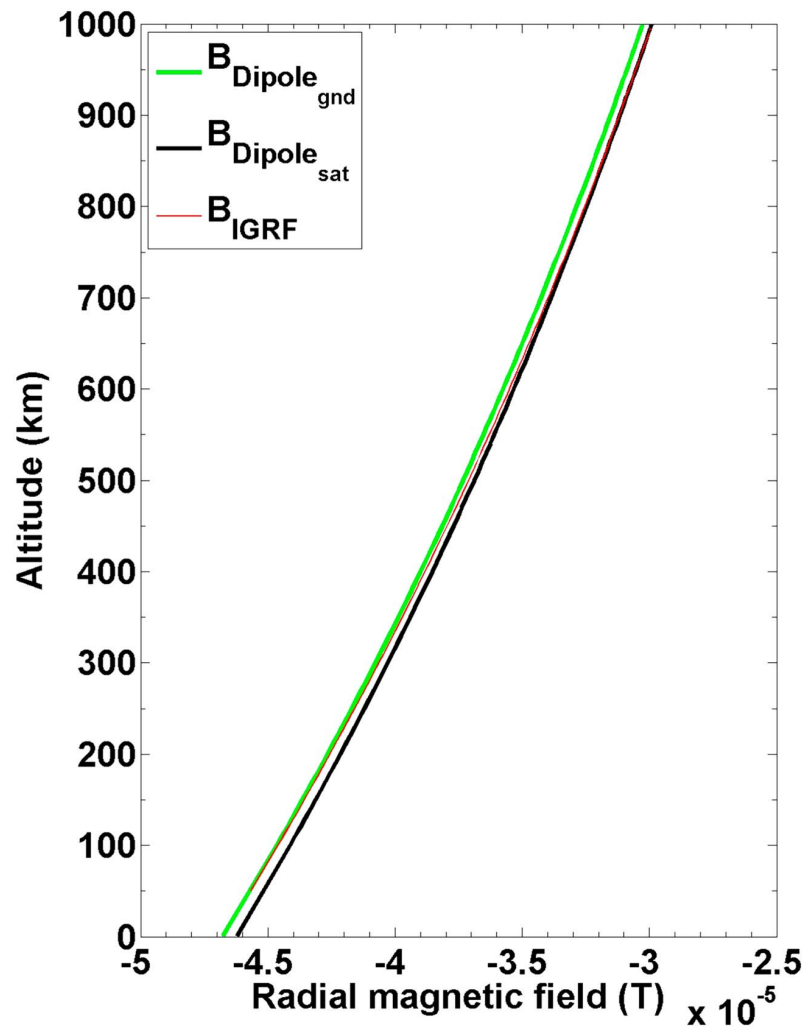


**Figure 5.** For a single measurement, the parallel component of the magnetic field can be fitted to from either a ground-based measurement  $B_{gnd}$  up to the satellite altitude or fitted using a space-based measurement  $B_{sat}$  to the ground using the dipole approximation. IGRF = International Geomagnetic Reference Field.

The red curve in Figure 5 shows the benchmark solution from IGRF. The green curve uses the value from the IGRF profile at the surface (0 km) as the measured value for the radial component of the geomagnetic field to calculate the radial profile as a function of altitude using equation (9), and thus obtain a magnetic field profile based on a single measurement. Similarly, the black curve shows the profile obtained by using the value of the radial component of the magnetic field at 1,000 km.

Figure 6 is similar to Figure 2 and shows a comparison of three dipole approximations to the IGRF benchmark. The green curve and black curve are determined by solving equation (9) using the values  $B_{Gnd}$  and  $B_{Sat}$  at  $z = 0$  and  $z = 1000$ , respectively. Once more, the dipole method using  $B_{dip}^{Gnd}$  tends to overestimate the FR, while a value from  $B_{dip}^{Sat}$  tends to underestimate the FR. These curves do not provide any improvement compared to using  $B_{Avg}^A$ , however they provide a way to map a single ground- or space-based measurement of the magnetic field to other altitudes when two simultaneous measurements are not available to calculate the average. The solid blue line is the arithmetic average  $B_{Dip}^{avg}$  of the two results and it shows improvements in the results. Figure 6 shows that  $B_{avg}^A$  overestimates the benchmark solution by  $\sim 1.9\%$ , while  $B_{Dip}^{avg}$  overestimates by roughly the same amount.

In Figure 7, we present a comparison of the cumulative FR as a function of altitude for different methods of averaging the parallel component of the magnetic field. The same traces that were presented in Figure 2,

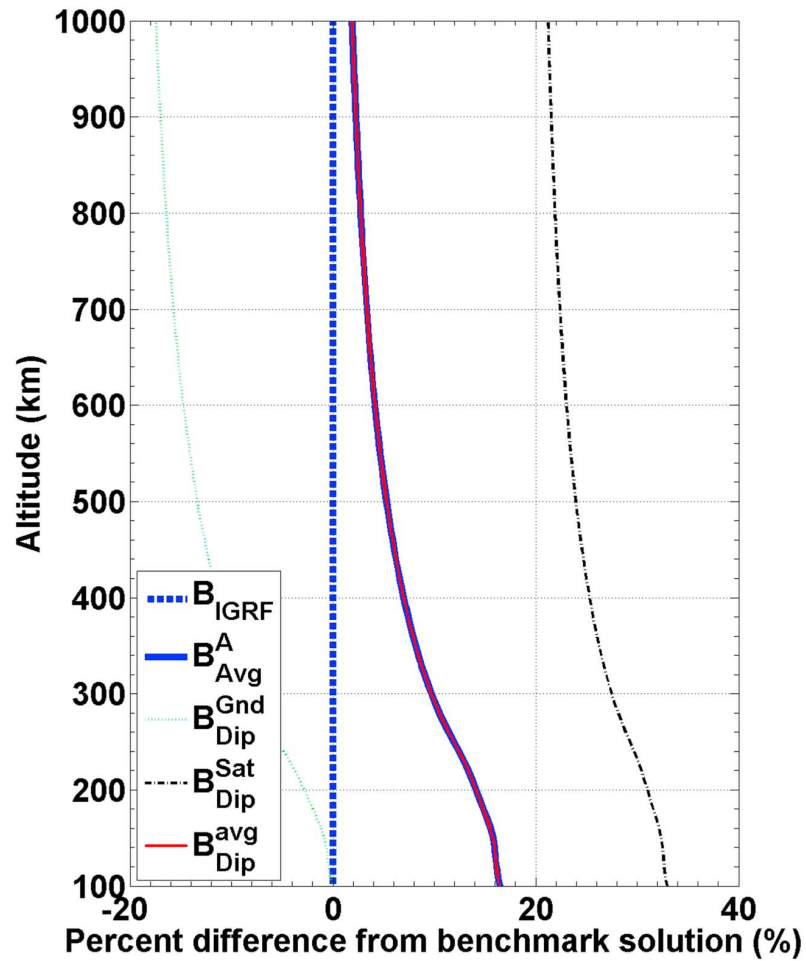


**Figure 6.** A comparison of the percent difference from benchmark solution using different methods to obtain the characteristic magnetic field from various altitudes. IGRF = International Geomagnetic Reference Field.

representing the arithmetic average of the ground- and space-based measurements ( $B_{avg}^A$ , green curve where  $w = 0.5$ ), and the benchmark solution (blue-dashed line) are repeated here along with the weighted average  $B_w$  (red curve) and the average dipole method ( $B_{Dip}^{avg}$ , dotted-black curve) that was shown in Figure 6. The red curve coincides with the solution for  $\langle B \rangle$  from equation (4).

The inset plot shows the difference from the benchmark solution  $\Delta B = B_w - B_{calc}$  in nT as a function of weight. The point where the line intersects  $\Delta B = 0$  nT is the weight that corresponds to the benchmark solution where the FR calculated using  $B_w$  outside the integral using equation (2) coincides with the FR computed with  $B_{IGRF}$  inside the integral using equation (1). The appropriate weight for this scenario was computed numerically by varying the value of  $w$  in equation (10) from 0 to 1 in increments of 0.0001. It was found that  $w = 0.451$ , which corresponds to a value that slightly favors the ground-based measurement of the magnetic field. The weighted method was calculated with respect to the exact solution  $\langle B \rangle$  by minimizing the difference between the two (see inset plot in the middle-right of Figure 7). When  $w = 0.451$  is plugged back into equation (10), we get a value of  $B_w = 3.7973 \times 10^4$  nT. The altitude that this value for the radial component of the magnetic field corresponded to from the IGRF profile in 10-km intervals, that was used to create the benchmark solution, was  $\approx 450$  km. The difference from the benchmark solution for the weighted solution was found to be  $1.8 \times 10^{-3}\%$ . We note that from Figure 2, the weight should be in favor of the ground value because the average is to the right of the benchmark solution. This could imply that even a value slightly less than  $w = 0.5$  would be an improvement over the arithmetic average in this case. For satellite orbits at different altitudes, especially eccentric orbits, it can be expected that the weight will be different.

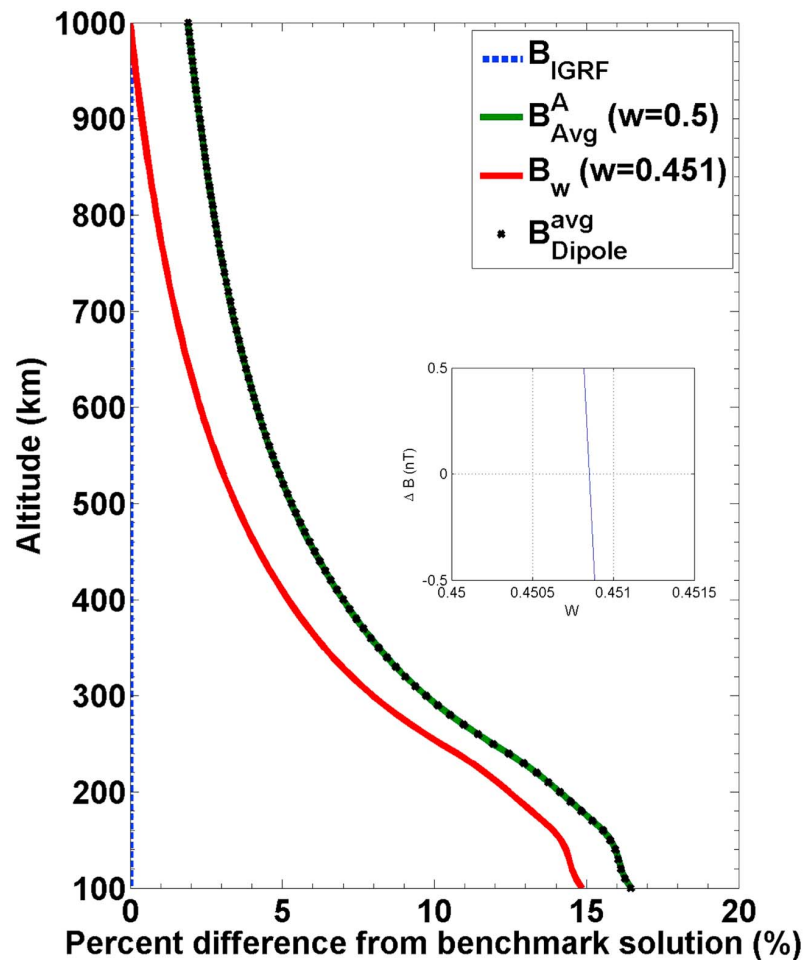


**Figure 7.** Comparison of the integration of the electron density with different methods to obtain a characteristic value for the magnetic field. All methods have been normalized as a cumulative percentage as a function of altitude with respect to the total Faraday rotation (received by a satellite) at 1,000 km for the benchmark solution. The inset shows the difference from the benchmark solution (nT) as a function of weight. IGRF = International Geomagnetic Reference Field.

#### 4. Conclusion

The FR effect can seriously affect 30 to 300 MHz VHF space communications systems that use linear polarization. The accuracy of FR estimation from TEC measurements and TEC mapping from FR measurements is limited by the accuracy of magnetic field measurements and models that are being used. Although it is known that the strength of Earth’s geomagnetic field varies slowly at ionospheric altitudes, a characteristic value from a reference altitude or mean value, although they are commonly used, may not always be appropriate. Empirical magnetic field models such as IGRF are useful for general behavior, but are based on long-term averaged data and neglect short time scale events. Likewise, electron density models such as IRI do not account for isolated events, and the electron density is far more variable than the magnetic field. The arithmetic (or some other) average from empirical models is not always reliable and measurements should be used, whenever they are available. This is particularly important during high solar and geomagnetic activity, since magnetic field models may not be capable to account for sporadic space weather events. Our numerical analysis has demonstrated that FR for 1,000-km orbit can be calculated more accurately by applying a weighted average that favors the ground-based measurements rather than using a simple arithmetic average value for the magnetic field based on satellite and ground measurements.

This manuscript has described the relationship between FR and TEC, reviewed past and current treatments of the average magnetic field with respect to the relationship between FR and TEC, and presented results that

show that some of these approximations may be inappropriate for certain applications requiring high precision (e.g., SAR imagery and CIT using FR as direct input or to obtain TEC values). The ADS-B signals, currently produced by aircraft, offer a unique opportunity to be used for ionospheric sounding in addition to their main operational purposes. This is similar to how GNSS systems have been used for ionospheric science in addition to their intended purpose of geospatial positioning. One of the main benefits of considering ADS-B signals and of the method proposed in this manuscript is that ADS-B receivers are able to distinguish and identify linearly polarized 1,090 MHz signals from different aircraft, which results in potentially hundreds or even up to a couple of thousand independent FR measurements along different propagation paths (Cushley et al., 2017). Another benefit is that aircraft fly in regions (e.g., over oceans) that are not amenable to using other instruments to map the electron density or TEC, specifically oceanic regions and high/polar latitudes (Cushley & Noël, 2014; Francis et al., 2011). In order to consider applying CIT using FR of ADS-B signals as input in order to map these regions electron content, the parallel component of the magnetic field must be accounted for accurately so that uncertainties rising from assumptions made about the magnetic field do not propagate to the TEC estimation and CIT reconstruction.

A sensitivity analysis was performed to determine the resulting uncertainty for each method that was used to obtain a characteristic value for the average parallel component of the magnetic field by comparing them to a benchmark solution based on the IGRF. Nine methods were described in the paper that resulted in moderate improvements in the calculated cumulative FR compared to the most common method based on a simple arithmetic average. The first two methods assumed that both ground- and space-based measurements were available to calculate the dipole average, as well as the weighted average. The results were shown to bias the result toward the magnetic field value measured on the ground.

The exact solution for the characteristic parallel magnetic field value along the path may be calculated using conjunctions between FR and TEC observations, which were assumed to be independently obtained. FR and TEC measurements were assumed to be available from either the same satellite (e.g., ATS-6) or measured in conjunction between two different satellite systems (e.g., TEC from GNSS and FR from ADS-B). Conjunctions between two different satellite systems may be particularly useful for creating a map of  $B$  that could then be applied to other systems and have possible uses for other applications. This would be different than maps of the magnetic field at the surface or for a shell at a particular altitude. It would be a map of the altitude of the effective parallel component of the magnetic field for FR calculations. By using measured FR and TEC using vertical paths, the exact value for the effective parallel component of the magnetic field along the path can be calculated using equation (4), and estimates of the cumulative FR over a propagation path can be improved. More general geometries between the transmitting aircraft and passive satellite receiver(s) will be considered in future studies.

Numerical results were presented in which the unmodified and modified formulas (equations (1) and (2), respectively) for FR were compared with  $B$  evaluated inside and outside the integral. This method can be applied to other satellite systems to determine the best method for other applications, such as satellites at different altitudes, inclination angles (different latitudinal extents), and carrier frequencies.

The following are the specific conclusions based on information gathered during this study. An average value for the magnetic field tends to overestimate the amount of FR because the magnetic field decreases as an inverse cubic with respect geocentric distance. Although it was not presented here, in Figure 2 the curves diverge at 1,000 km and continue to diverge as the altitude increases which shows that the uncertainty also increases when satellites at higher altitudes are considered. For example, for a satellite at a much higher altitude (e.g., geostationary) would measure a lower value for  $B_{Sat}$ , and the electron density would be integrated over a much longer path. For a satellite in an orbit with a high eccentricity (e.g., Molniya), the preferred method for estimating the effective parallel component of the magnetic field may be different at apogee and perigee. This would be worthy of further investigation.

A weighted average in favor of the magnetic field values from lower altitudes was shown to improve the results, even when the exact weight is not known (i.e.,  $w = 0.49$  gives better results than the arithmetic average, where  $w = 0.5$ ). The weight is not 0.5, which would be the arithmetic average, but was found to be  $w = 0.451$  for this example. The study of  $B_{w}$  and the statistics used to arrive at this value will be the subject of a forthcoming paper. The method using FR and TEC observation conjunctions provided the exact value for  $B$  and can be used for satellites at any orbital altitude. The calculated magnetic field  $B_{calc}$  from the FR measurements and TEC estimates from measurements and/or maps is the best method in terms of minimizing the

difference in the estimated value of the integral at 1,000 km. In this particular case, the altitude from the IGRF profile that gives the closest value to  $\langle B \rangle$  was 450 km.

Future work may include the following: considering elevation angles below 88°, using existing satellite data if it were made available (e.g., ATS-6, ADS-B), or Earth-moon-Earth propagation testing to obtain independent FR and TEC observations over the same propagation path. These types of measurements could also be crowd-sourced globally by the amateur radio community (Frissell et al., 2014; Silver, 2016) if a relatively simple nano-satellite was launched that transmitted linearly polarized signals (e.g., signals with a time stamp and possibly other parameters such as health status, attitude, and telemetry).

### Acknowledgments

All values and equations used to perform the simulations presented are given in the manuscript. The authors would like to thank the Government of Canada | Natural Sciences and Engineering Research Council of Canada (NSERC) [https://doi.org/10.13039/501100000038] (249806) for supporting this research. The electron density values were determined using the IRI model available at [http://omniweb.gsfc.nasa.gov/vitmo/iri\\_vitmo.html](http://omniweb.gsfc.nasa.gov/vitmo/iri_vitmo.html), and the values for the geomagnetic field were computed using the IGRF model available from <https://www.ngdc.noaa.gov/IAGA/vmod/igrf.html>

### References

- Aitchison, G., & Weekes, K. (1959). Some deductions of ionosphere information from observations in emissions from 1958. *Journal of Atmospheric and Terrestrial Physics*, 14(3-4), 236.
- Balsler, M., & Smith, W. B. (1962). Some statistical properties of pulsed oblique HF ionospheric transmissions. *Journal of Research of the National Bureau of Standards-D. Radio Propagation*, 66D(6), 721–30.
- Bassiri, S., & Hajj, G. (1993). High-order ionospheric effects of the global positioning system observables and means of modeling them. *Manuscripta Geodetica*, 18, 280–289.
- Bilitza, D. (2007). IRI-2007: Online computation and plotting through IRI-2007.web.
- Bilitza, D., McKinnell, L.-A., Reinisch, B., & Fuller-Rowell, T. (2011). The international reference ionosphere today and in the future. *Journal of Geodesy*, 85, 909–920.
- Brunner, F. K., & Gu, M. (1991). An improved model for the dual frequency ionospheric correction of GPS observations. *Manuscripta Geodetica*, 16(3), 205–214.
- Budden, K. G. (1961). *Radio waves in the ionosphere: The mathematical theory of the reflection of radio waves from stratified ionized layers*. London, UK: Cambridge University Press.
- Cushley, A., Kabin, K., & Noël, J.-M. A. (2017). Faraday rotation of Automatic Dependent Surveillance Broadcast(ADS-B) signals as a method of ionospheric characterization. *Radio Science*, 52, 1293–1300. <https://doi.org/10.1002/2017RS006319>
- Cushley, A., & Noël, J.-M. A. (2014). Ionospheric tomography using ADS-B signals. *Radio Science*, 49(7), 549–563. <https://doi.org/10.1002/2013RS005354>
- Davies, K., Donnelly, R. F., Grubb, R. N., Rao, P. V. S. R., Rastogi, R. G., Deshpande, M. R., et al. (1979). ATS-6 satellite radio beacon measurements at Ootacamund, India. *Radio Science*, 14(1), 85–95.
- Davies, K., & Hartmann, G. K. (1997). Studying the ionosphere with the global Positioning System. *Radio Science*, 84, 1695–703.
- de Mendonto, F., & Garriott, O. (1962). Ionospheric electron content calculated by a hybrid Faraday-Doppler technique. *Journal of Atmospheric and Terrestrial Physics*, 24, 317–21.
- de Pater, I., & Lissauer, J. (2010). *Planetary Sciences*. Cambridge, UK: Cambridge University Press.
- Francis, R., Vincent, R., Noël, J., Tremblay, P., Desjardins, D., Cushley, A., & Wallace, M. (2011). The flying laboratory for the observation of ADS-B signals. *International Journal of Navigation and Observation*, 2011(A2), 973656. <https://doi.org/10.1155/2011/973656>
- Frissell, N. A., Miller, E. S., Kaeppler, S. R., Ceglia, F., Pascoe, D., Sinanis, N., et al. (2014). Ionospheric sounding using real-time amateur radio reporting networks. *Space Weather*, 12, 651–656. <https://doi.org/10.1002/2014SW001132>
- International association of geomagnetism and aeronomy, Working Group V-MOD (2010). International geomagnetic reference field: The eleventh generation. *Geophysical Journal International*, 183(3), 1216–1230. <https://doi.org/10.1111/j.1365-246X.2010.04804.x>
- Ippolito, L. (2008). *Satellite communications systems engineering: Atmospheric effects, satellite link design and system performance, wireless communications and mobile computing*. West Sussex, UK: Wiley.
- Jakowski, N., Mayer, C., Hoque, M. M., & Wilken, V. (2011). Total electron content models and their use in ionosphere monitoring. *Radio Science*, 46, RS0D18. <https://doi.org/10.1029/2010RS004620>
- Jehle, M., Rüegg, M., Zuberbühler, L., Small, D., & Meier, E. (2009). Measurement of ionospheric Faraday rotation in simulated and real spaceborne SAR data. *IEEE Transactions on Geoscience and Remote Sensing*, 47(5), 1512–23.
- Kivelson, M. G., & Russell, C. T. (1995). Introduction to space physics, (1st ed.). *Cambridge Atmospheric and Space Science* (pp. 588). Cambridge: Cambridge University Press.
- Kraus, J. (1966). *Radio astronomy*. New York: McGraw Hill.
- Lavalle, M. (2009). Full and compact polarimetric radar interferometry for vegetation remote sensing. Signal and image processing (PhD. Thesis), Université Rennes.
- Lawrence, R. S., Posakony, D. J., Garriott, O. K., & Hall, S. C. (1963). The total electron content of the ionosphere at middle latitudes near the peak of the solar cycle. *Journal of Geophysical Research*, 68(7), 1889–1898. <https://doi.org/10.1029/JZ068i007p01889>
- Maus, S., Macmillan, S., Chernova, T., Choi, S., Dater, D., Golovkov, V., et al. (2005). The 10th generation international geomagnetic reference field. *Physics of the Earth and Planetary Interiors*, 151, 320–322.
- NASA Jet Propulsion Laboratory California Institute of Technology (2014). Real-time ionospheric maps (Website).
- Orfanidis, S. J. (2008). *Electromagnetic waves and antennas*. NJ: Rutgers University.
- Rogers, N. C., & Quegan, S. (2014). The accuracy of Faraday rotation estimation in satellite synthetic aperture radar images. *IEEE Transactions on geoscience and remote sensing*, 52(8), 4799–807.
- Ross, W. (1960). The determination of ionospheric electron content from satellite doppler measures 1 and 2. *Journal of Geophysical Research*, 65(9), 2601–15.
- Sheriff, R., & Hu, Y. (2003). *Mobile satellite communication networks*. New York: Wiley.
- Silver, H. W. (2016). Hamsci: Ham radio science citizen investigation, *QST* (Vol. 100, pp. 68–71). San Francisco: American Geophysical Union.
- Soicher, H., & Gorman, F. (2012). Seasonal and day-to-day variability of total electron content and mid-latitudes near solar maximum, pp. 383–387. <https://doi.org/10.1029/RS020i003p00383>
- Sotomayor-Beltran, C., Sobey, C., Hessels, J. W. T., de Bruyn, G., Noutsos, A., Alexov, A., et al. (2013). Calibrating high-precision Faraday rotation measurements for LOFAR and the next generation of low-frequency radio telescopes. <https://doi.org/10.1051/0004-6361/201220728>
- Stankov, S. M., Jakowski, N., Heise, S., Muhtarov, P., Kutiev, I., & Warnant, R. (2003). A new method for reconstruction of the vertical electron density distribution in the upper ionosphere and plasmasphere. *Journal of Geophysical Research*, 108(A5), 1164. <https://doi.org/10.1029/2002JA009570>

- The International Telecommunications Union (2003). Ionospheric propagation data and prediction method required for the design of satellite services and systems (*Recommendation ITU-R P.531-7*): The ITU Radiocommunication Assembly.
- Treumann, R. A., & Baumjohann, W. (1996). *Basic space plasma physics*. London: Imperial College Press.
- Wahi, R., Dubey, S., & Gwal, A. K. (2005). Ionospheric total electron content measurement in Malaysian region during high solar activity using GPS receiver. *Indian Journal of Radio and Space Physics*, *34*, 399–401.
- Wright, P. A., Quegan, S., Wheadon, N. S., & Hall, C. D. (2003). Faraday rotation effects on L-band spaceborne SAR data. *IEEE Transactions on Geoscience and Remote Sensing*, *41*(12), 2735–2744.
- Zhao, B., Wan, W., Liu, L., & Ren, Z. (2009). Characteristics of the ionospheric total electron content of the equatorial ionization anomaly in the Asian-Australian region during 1996–2004. *Annales Geophysicae*, *27*, 3861–3873.

## Ionospheric sounding and tomography using Automatic Identification System (AIS) and other signals of opportunity

### 7.1 Overview

The scientific results presented in this chapter are based on the following publication:

- Cushley, A. C. & Noël, J.-M., Ionospheric sounding and tomography using Automatic Identification System (AIS) and other signals of opportunity. Submitted to *Radio Sci.*, Accepted 11 December 2019.

This study examined the potential feasibility of using AIS signals transmitted by ships, as they propagate through the ionosphere to a receiver carried by the Iridium NEXT satellite(s), as input to CIT techniques to reconstruct 2D maps of the ionospheric electron content. In the first portion of the attached manuscript, a comparison was made with the results of ADS-B reconstructions presented in Chapter 4 to investigate how the change in carrier frequency affects the CIT reconstructions. This was followed by a case study using a realistic distribution of AIS equipped ships in the Philippine Sea. The final study was using a combination of AIS and ADS-B synthetic data to perform the reconstruction.

### 7.2 The Study

A number of assumptions were made pertaining to the satellite design and proposed orbit in *Cushley* [2013]; *Cushley and Noël* [2014] which required further investigation. Many factors that are dependent on iterations to SMAD and space mission geometry such as orbit determination, antenna type, and pointing accuracy were difficult to characterize beyond a reasonable envelope for the demonstrator satellite. The unknown orbit as a secondary dependant launch contractor, or secondary payload, along with the probability that the orbit would likely be much different for a future satellite

constellation implied iteration to these design considerations and implications thereof. Recently, the Iridium NEXT constellation has been launched and the constellation has been operational since Feb 2019. Design parameters were re-evaluated using the Iridium NEXT constellation as the basis for this investigation into the feasibility of AIS signals for VTEC mapping and CIT.

The ultimate goal of the research presented in the attached paper was to show that AIS could also be used as an independent source for TEC measurements to supplement GIMs of VTEC in oceanic regions, where few if any measurements currently exist. Due to the lower transmit cadence, it was originally hypothesized that there would not be a sufficient number of signals to be used as input to CIT for a single satellite pass. This is especially true in regions with lower ship traffic densities. The ability to do CIT was a bonus! The ray-trace program also provided the opportunity to compare the exact same distribution for two different frequencies (ADS-B and AIS) to see how the reconstructions were affected. This information is useful since we could use different types of signals of opportunity to perform a single CIT reconstruction.

Although the research in the paper as well as that presented in Chapter 4 is mainly focussed on the reconstruction of the 2D electron content from the STEC derived from FR observations, the STEC can also be used on its own particularly when sufficient data is not available from one source to perform a reconstruction of a particular region. For example, there may only be a single ship in the Antarctic Ocean resulting in an insufficient number of signals for CIT, however the STEC can be easily mapped to VTEC. The STEC is measured or inferred from other observables along the ionospheric path from the transmitter to the receiver, making the measurements dependent on the satellite orbital geometry, specifically the elevation angle. To correctly map the VTEC as an estimation of the TEC above a certain coordinate on the Earth's surface, the STEC must be correctly converted into VTEC. In order to accomplish this, a single thin layer model is often used, which assumes that the electrons are concentrated in a layer of infinitesimal thickness located at altitude  $h$  as shown in Fig. 7.1.

The VTEC can be estimated at each Ionospheric Pierce Point (IPP) using a



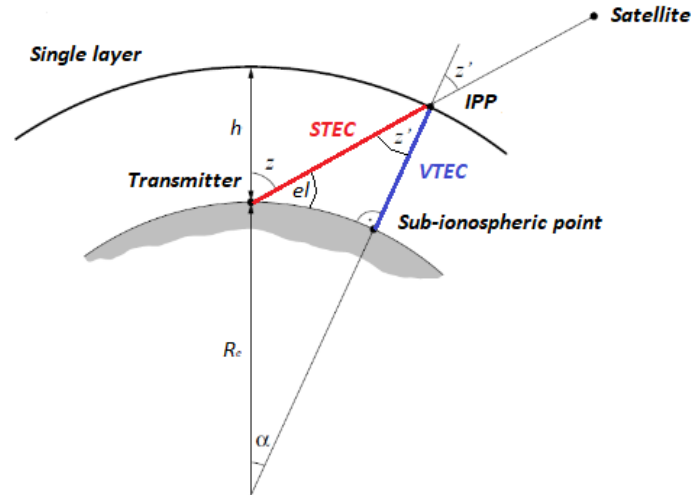


Figure 7.1: Geometry of single layer ionosphere model for mapping STEC to VTEC [Musa, 2007; Royal Observatory of Belgium, 2014].

mapping function  $MF_I(el)$  which is a function of the elevation angle  $el$ , given by

$$MF_I(el) = \frac{STEC}{VTEC} = \frac{1}{\cos(z')} \quad (7.1)$$

where

$$\sin(z') = \frac{R_E}{R_E + h} \cos(el) \quad (7.2)$$

In Eqn. 7.1  $R_E = 6371$  km is the radius of Earth and  $h$  is the altitude of the thin shell, usually 300–400 km, and  $z'$  is the ionospheric zenith angle.

Figure 7.2 shows a comparison of the multiplication factor used to convert STEC to VTEC for a selected range of mean ionospheric heights from 300 to 400 km. Differences occur depending on the multiplication factor can also be used to determine STEC and consequent time delay at another elevation angle. This conversion does not account for temporal or geographic TEC gradients, which produce additional differences between VTEC and STEC.

### 7.3 Accepted Paper

The manuscript describing the analysis and modelling of synthetic AIS data for CIT and VTEC mapping was accepted by the Journal of *Radio Sci.* in Dec 2019. Im-

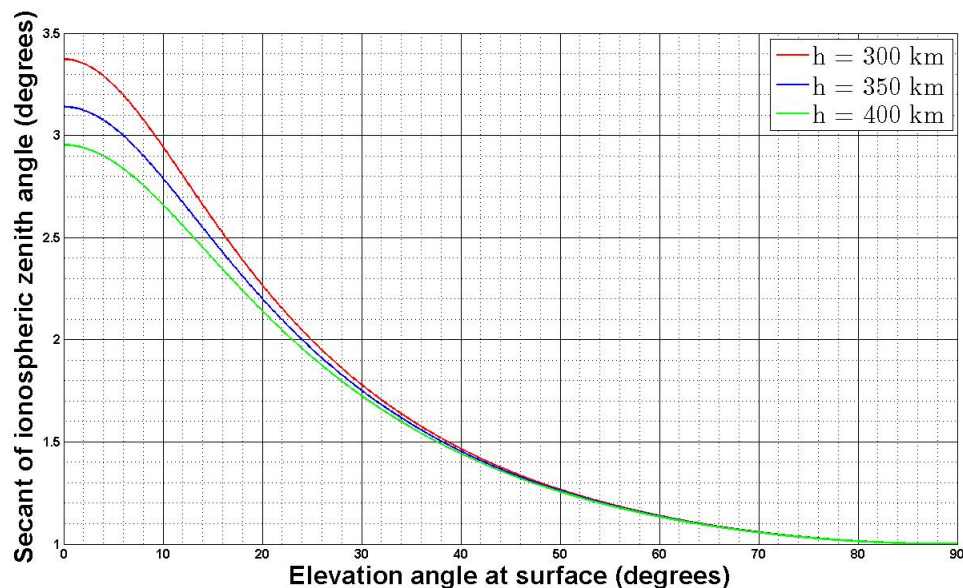


Figure 7.2: The multiplication factor used to convert STEC to VTEC for a selected range of mean ionospheric heights from 300 to 400 km. At 25 degrees elevation, the time delay calculated for zenith would be approximately doubled due to the greater TEC encountered along an oblique path. Adapted from *Klobuchar et al.* [1973].

mediately following is the paper in manuscript format (figures appear at the end of manuscript as per AGU requirements) reproduced by permission of American Geophysical Union:

- Cushley, A. C. & Noël, J.-M. (2019), Ionospheric sounding and tomography using Automatic Identification System (AIS) and other signals of opportunity. Submitted to *Radio Sci.*, Accepted 11 December 2019.

# Radio Science

## RESEARCH ARTICLE

10.1029/2019RS006872

### Key Points:

- AIS signals undergo Faraday rotation, which can provide information about the ionospheric TEC
- The modeled ionospheric electron densities were reconstructed using CIT
- Mesoscale ionospheric features can be detected without a priori knowledge

### Correspondence to:

A. C. Cushley,  
alex.cushley@rmc.ca

### Citation:

Cushley, A. C., & Noel, J.-M. (2020). Ionospheric sounding and tomography using Automatic Identification System (AIS) and other signals of opportunity. *Radio Science*, 55, e2019RS006872. <https://doi.org/10.1029/2019RS006872>

Received 30 APR 2019

Accepted 11 DEC 2019

Accepted article online 21 DEC 2019

## Ionospheric Sounding and Tomography Using Automatic Identification System (AIS) and Other Signals of Opportunity

A. C. Cushley<sup>1</sup> and J.-M. Noël<sup>1</sup>

<sup>1</sup>Department of Physics, Royal Military College of Canada, Kingston, Ontario, Canada

**Abstract** Numerical modeling has demonstrated that Automatic Identification System (AIS) signals can be used not only to estimate vertical total electron content (TEC) to supplement current TEC maps and data assimilation models but also to reconstruct two-dimensional (2-D) electron density maps of the ionosphere using computerized tomography. A ray tracing model was used to determine the characteristics of individual linearly polarized waves transmitted by ships to satellites in circular orbits at 780- and 1,000-km altitude, including the wave path and the state of polarization at the satellite receiver. The modeled Faraday rotation was computed and used to calculate the TEC along the ray paths. The resulting TEC was used as input for computerized ionospheric tomography using the algebraic reconstruction technique. This study concentrated on reconstructing mesoscale structures 25–100 km in horizontal extent. The primary scientific interest of this study was to show that AIS signals can be used as a new source of input data for computerized ionospheric tomography to image the ionosphere and to obtain a better understanding of magneto-ionic wave propagation.

## 1. Introduction

### 1.1. TEC Mapping

Total electron content (TEC) is defined as the integrated electron density within a column of ionospheric plasma having a cross-sectional area of one square meter. Among a variety of other applications, TEC measurements are used as the input to computerized ionospheric tomography (CIT) in order to reconstruct electron density maps.

There are two different types of TEC to consider: slant TEC (STEC) and vertical TEC (VTEC). The STEC is the integrated electron density along a propagation path of any elevation angle and length. For modeling purposes, the VTEC value is usually given for a zenith path with unit cross section. Typical values for this VTEC column can vary from  $10^{16}$  to  $10^{18}$  el/m<sup>2</sup>, with the peak occurring on the dayside near (but not exactly at) the equator (The International Telecommunications Union, 2003). VTEC models and maps are used to improve satellite communications and navigation and in particular for positioning accuracy of GPS. TEC maps can also be used to estimate time delay and Faraday rotation (FR) of satellite signals (Jehle et al., 2009). VTEC maps are also of interest to radio astronomers and ionospheric physicists because ground-based astronomical observations must account for the ionospheric effects and be corrected (Campbell, 1999; Erickson et al., 2001; Ruzmaikin & Sokoloff, 1979; Ros et al., 2000; Sotomayor-Beltran et al., 2013).

Maps are regularly produced by using the differential phase between two Global Navigation Satellite Systems (GNSS) frequencies (Choi et al., 2006; Max van de Kamp, 2012). For example, a TEC map and its associated TEC errors are shown in Figure 1. These maps are readily available from the Ionosphere Monitoring and Prediction Center, operated by the German Aerospace Center (DLR) at the Neustrelitz location. The top panel shows a global TEC map for a shell height of 400 km. The locations of GNSS receivers are depicted as the white dots in the bottom panel. Note that these ground-based receivers are constrained to land mass, with few at high latitudes due to significant requirements for infrastructure (power, networks, access, etc.) and a hospitable climate. The bottom panel shows a map of the errors associated with the VTEC map in the top panel. Note that the largest errors occur over oceanic, mountainous, and high-latitude regions (denoted by the light blue color). The errors are derived from uncertainty in the GNSS measurements and error propagation based on the modeling and data assimilation process. The errors are reduced in the dark blue regions

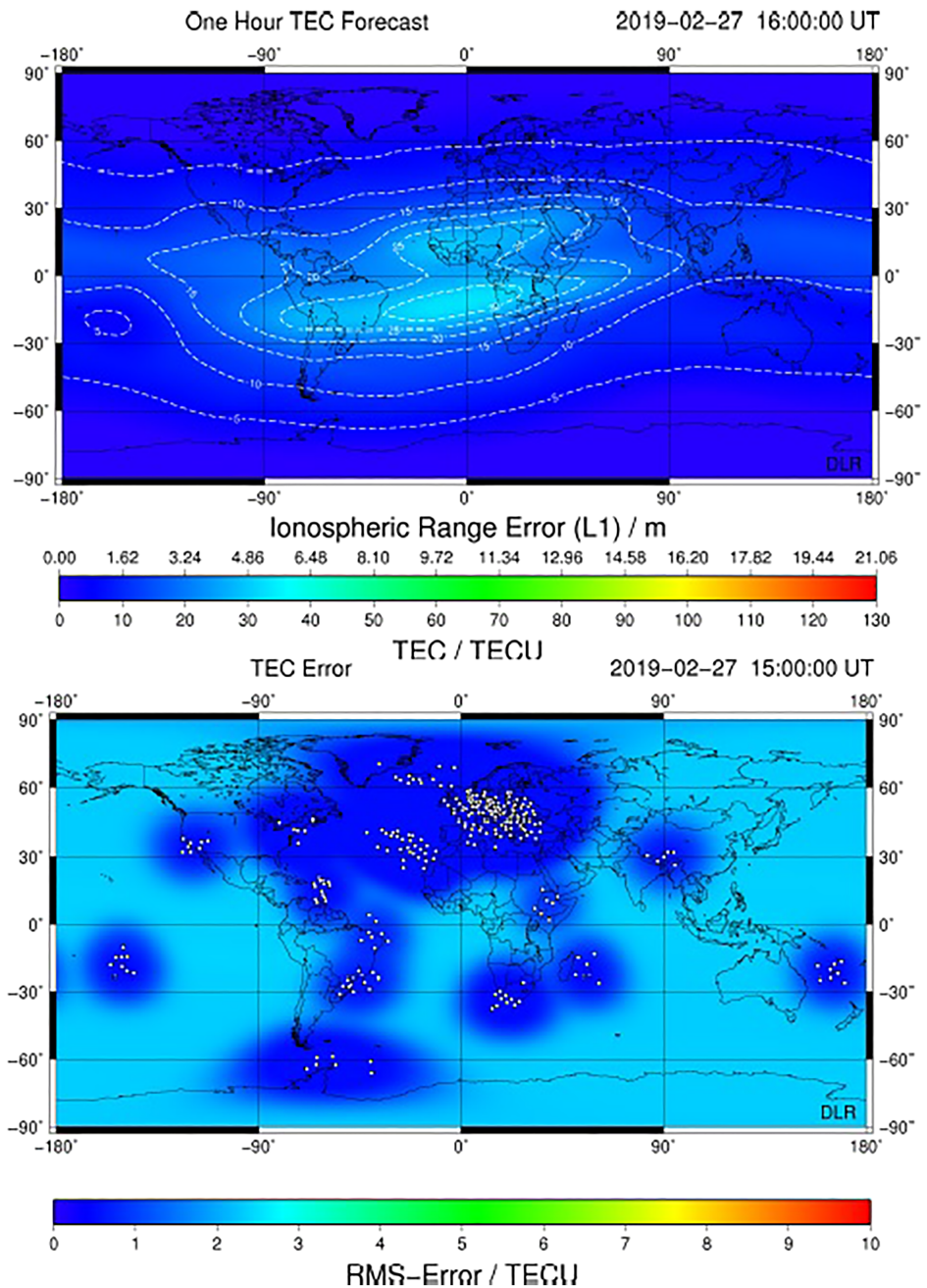


**Figure 1.** (top) Global VTEC map derived from ground-based GNSS measurements. (bottom) Error of the VTEC map shown in the top panel derived from errors and uncertainties of the GNSS measurements and propagation based on the modeling and data assimilation process. These maps are available from the Ionosphere Monitoring and Prediction Center (IMPC), operated by the German Aerospace Center (DLR) at the Neustrelitz location.

where there is a high density of observations available while it is greater in regions where fewer observations are available and where the TEC values are based solely on a model.

In order to address the gaps in coverage and to supplement current VTEC maps as well as consideration of new sources for tomographic imaging of the ionospheric electron content, we consider signals of opportunity originating from aircraft and ships. These sources of signals have the advantage of not being constrained

to land masses. These are so-called “free” transmitters for the purpose of ionospheric sounding since they serve other operational purposes (e.g., the tracking of ships and aircraft).

### 1.2. AIS

Ship detection has been made possible by a combination of remote sensing data as well as from other sources such as Automatic Identification System (AIS) (Greidanus, 2005). AIS is a marine vessel tracking and maritime situational awareness technology that is used to monitor and control marine traffic, particularly in high traffic areas such as ports and harbors.

AIS is a technology developed to track the position and movement of ships through intermittent broadcasts of their identity, itinerary, and position state vectors to ground- and satellite-based receivers and to other nautical traffic within range. AIS was initially conceived as a safety augmentation system so that vessels could be tracked in coastal waters by maritime agencies and ship operators. Before AIS, ships had to communicate with local receiving stations, which placed two main restrictions on the ability to track these vessels. First, communications were restricted to line-of-sight (LOS) meaning that once vessels were over the horizon in the open ocean there was no way to monitor their activities using voice communications or radar. Second, marine agencies had to rely on the accuracy of the information that they were being provided from the ships themselves. The accuracy of the information could be affected by issues with the navigational instruments and/or human error, or even deliberately corrupted because of potential illegal activities that the vessel may be engaged in. “The reality was that there were 60 000 ships carrying 9 trillion dollars in cargo, and when the captain went over the horizon, unless he sent a signal, no one knew where he went”—John Allan ExactEarth (Amos, 2012).

AIS addressed this shortcoming as well as provided other benefits including enhanced ranging and separation distinction capability with a reduced footprint for ground support infrastructure among others. To briefly summarize the benefits of AIS, equipping larger vessels with this system has led to improved capabilities in maritime traffic monitoring, control, and as a consequence improves maritime safety, security, and efficiency by providing timely, cost-effective wide-area surveillance in high-traffic regions such as ports. By equipping smaller vessels like fishing fleets with inexpensive AIS transceivers, the system is used as an important tool for fisheries management as well as to combat piracy. Ships transmit 161.975-MHz (Marine ch 87) or 162.025-MHz (ch 88) beacons that include state vectors derived from on-board GPS receivers and other instrumentation.

AIS networks that monitor marine traffic have already been deployed around the world in high-volume marine traffic areas such as ports, harbors, and canals, but as we all know, ground stations cannot be installed mid-ocean and are difficult to maintain in the Arctic. These limitations are similar to many other ground-based technologies (Cushley & Noël, 2014). The lack of coverage over mid-oceanic and high-latitude waters has been alleviated by using a constellation of satellites to allow for worldwide tracking of vessels. As a result, AIS data are collected from space using a constellation of nine satellites that provides total global coverage.

The exactEarth is a publicly traded Canadian data services company that has pioneered global maritime vessel data monitoring by using spaceborne AIS receivers for ship tracking and maritime situational awareness. Since its establishment in 2009, exactEarth has provided a powerful maritime surveillance tool called Satellite-AIS (S-AIS), producing regional and global maritime pictures of the world’s oceans, unrestricted by the terrestrial limitations that would be encountered using ground-based technologies. In 2015, exactEarth announced the successful launch of its ninth AIS satellite, exactView-9 (EV9) to expand and compliment the constellation that was currently being used for global vessel monitoring (exactEarth, 2016). EV9 employs a next generation AIS payload that would support exactEarth’s patented ground-based AIS spectrum processing technology in order to deliver superior detection performance.

The AIS satellites have orbital periods of 97 min, making the constellation of polar orbiting satellites capable of providing adequate coverage, particularly for busy tropical shipping regions of the world with high maritime traffic density (exactEarth, 2015). More recently, the constellation has been expanded with 58 additional hosted payloads on-board the Iridium NEXT satellites (de Selding, 2105).

There are two classes of AIS transponders called Class A and Class B. AIS Class A transponders are required on larger self-propelled vessels, including commercial vessels carrying dangerous cargo or more 150 passengers. AIS Class B was designed to give smaller vessels like fishing industry vessels comparable but reduced

tracking capabilities. Class A transponders are prioritized and displayed to other ships in the area. Class B are transmitted at lower power (2 W as opposed to 12.5 W for Class A) and will not be displayed to Class A ships until there is room on the AIS channel. EV9 also provides high-performance detection of low power Class B AIS transceivers, for the small vessel market (exactEarth, 2015).

AIS signals are transmitted at different intervals for different classes of AIS. Class A transponders broadcast every 2 to 10 s while underway, and every 3 min while moored. Position updates for Class B transponders are broadcast less often than Class A transponders. Vessels traveling slower than 2 knots ( $\sim 1$  m/s) transmit position updates every 3 min while vessels traveling faster than 2 knots transmit position information every 30 s (Marine, 2018). Therefore, for this study, the ships with Class A transponders that are underway in high ship traffic density regions are of more interest than those that are moored because there will be a greater number of signals that are transmitted during a single satellite pass in this type of scenario.

The AIS infrastructure is composed of an operational data processing supply chain employing a constellation of satellites, receiving ground stations, patented decoding algorithms and advanced “big data” processing and distribution facilities. exactEarth utilizes a network of high data rate ground stations to enable rapid distribution of the data to global customers. This system provides the most comprehensive picture of the locations of AIS-equipped maritime vessels in the world and allows exactEarth to deliver data and information services characterized by high performance, reliability, security, and simplicity to large international markets (exactEarth, 2015).

AIS signals transmitted by ships are received by a satellite constellation and relayed to a ground network in near real time. The AIS constellation provides updated information on identified vessels, including their respective locations and a wide range of other relevant maritime geospatial information at least once per hour. This same space mission analysis and design architecture was the inspiration for a proposed deployment of space-borne Automatic Dependent Surveillance Broadcast (ADS-B) transceivers to monitor air traffic (Francis et al., 2011).

GNSS technology such as the NAVSTAR GPS is an enabling technology for AIS, Automatic Packet Reporting System (APRS), and ADS-B. APRS is a radio-based digital communication protocol developed and utilized by the amateur radio community to report and track the position and status of APRS-equipped stations. Besides providing autonomous geospatial positioning, GNSS has also been used to provide measurement of the ionospheric TEC (Austen et al., 1986; Choi et al., 2006; Hartmann & Leitingner, 1984; Max van de Kamp, 2012).

These additional transmitters and ray paths would improve the spatial sampling suitability for the CT methods proposed by Cushley and Noël (2014) for ADS-B. An example of the global distribution of maritime traffic, showing the potential number, density and distribution of AIS-equipped vessels is presented in Figure 2.

### 1.3. ADS-B

ADS-B is a technology similar to AIS that was developed to track the position and movement of aircraft through intermittent broadcasts containing information about their identity, itinerary, and position state vectors to ground-based receivers and other aircraft within range. In fact, the potential for ADS-B monitoring from a space-based platform was inspired by the AIS architecture (Francis et al., 2011). ADS-B coverage is particularly useful for oceanic and polar regions, where coverage from another source is otherwise unavailable. These regions also correspond to the largest errors for TEC maps (see Figure 1; Jakowski et al., 2011). Therefore, using ADS-B measurements in those particular areas could improve the accuracy of the TEC maps.

One of the main benefits of considering ADS-B signals as a source of electromagnetic (EM) soundings signals is that ADS-B receivers are able to distinguish and identify signals from different aircraft, resulting in potentially hundreds or even thousands of independent FR measurements along different propagation paths. The ADS-B signals, currently originating from aircraft, offers a unique opportunity to be used for ionospheric sounding in addition to their operational purpose. This was already discussed in Cushley and Noël (2014) and is similar to how GNSS systems have been used for ionospheric science in addition to their original intended purpose of geospatial positioning. An in-depth study using ADS-B signals as input for CIT

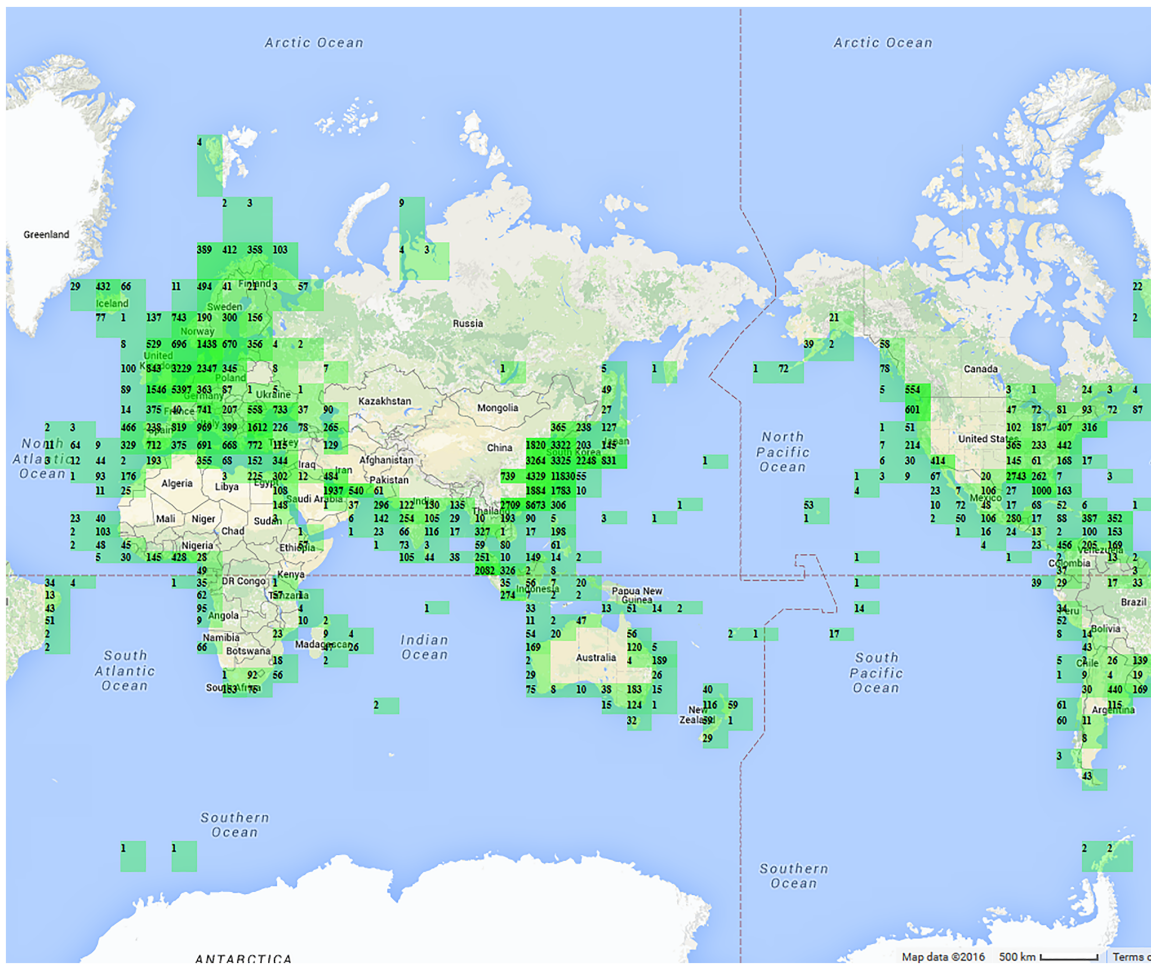


**Figure 2.** A map taken from MarineTraffic ([www.marinetraffic.com](http://www.marinetraffic.com)) showing the last known positions from 84 449 vessels for 11 Oct 2018 at ~1pm EST.

was undertaken in Cushley (2013, 2014). Those results will be compared directly with the AIS results presented in this manuscript in order to evaluate AIS as a potential independent source of CIT data. In addition, ADS-B synthetic data will be merged with modeled data from AIS.

## 2. Theory

### 2.1. Ionospheric Sounding

When EM waves propagate through the electrically charged ionosphere in the near-Earth space environment they are modulated and can provide an exceptional opportunity to model the medium through, which they have passed. Modeling the electron density of Earth's ionosphere (and plasmasphere) in general is essential in determining the state of ionospheric activity. This information can be used to correct for propagation delays in satellite communications, predicting space weather, and ionospheric disturbances due to geomagnetic storms, solar flares (Jin et al., 2006), and the neutral atmosphere (Frissell et al., 2016).

Using AIS data for ionospheric sounding creates a novel opportunity to study the propagation characteristics of VHF radio waves through the ionosphere originating from the transmitting ships to passive satellite receivers.

For this study, AIS signals were selected because the AIS frequency allows for robust operational communications and measurable perturbation due to ionospheric effects and due to the spatially dense data set estimated by the geometry between multiple transmitting ships and the passive satellite receivers (see Figure 2).

This work sets out to demonstrate the potential use of a single payload for improving marine traffic management as well as scientific observation of the ionosphere. To the knowledge of the authors, the topic of ionospheric sounding using AIS signals has not been reported prior to this work. However, it was proposed in Cushley (2015). The main scientific purpose of this study is to investigate the potential exploitation of AIS operational data and to contribute to current methods of ionospheric electron density mapping in oceanic regions where ground-based sensors cannot be located and to compare these results with those obtained using ADS-B.

A secondary benefit of this research is to communicate that linearly polarized single frequency signals that are used for operational purposes may also be used to contribute to ionospheric sounding if the frequency, antenna configurations, and signal timing accuracy are taken into account during the mission design process. This can all be achieved with very little to no alteration and/or additional expenses to the primary mission and may offer a data product or funding opportunities to lower the cost of the original primary mission.

In order to characterize the ionospheric electron content under different transmitter placement scenarios, ray path geometries, and geomagnetic and solar conditions, the current study combines knowledge that can be extracted from EM wave propagation theory and ionospheric electron density and geomagnetic models to produce independent static data of the wave path and polarization state that will be received at the satellite receiver.

## 2.2. FR

The ionosphere can be considered a birefringent medium due to the geomagnetic field (Hartmann & Leitinger, 1984; Orfanidis, 2008). An EM wave propagating through a magnetized plasma decomposes into two propagation modes called the ordinary and extraordinary modes (or O mode and X mode, respectively), having different indices of refraction and polarization due to the external terrestrial magnetic field (Chen, 1984). When collisions between neutral and charged particles are neglected, the refractive indices of the two modes are given by the Altar-Appleton-Hartree dispersion relation (Appleton & Builder, 1933; Gillmor, 1982; Hartree, 1929):

$$n^2 = 1 - \frac{X}{1 - \frac{Y^2 \sin^2 \theta}{2(1-X)} \pm \sqrt{\frac{Y^4 \sin^4 \theta}{4(1-X)^2} + Y^2 \cos^2 \theta}} \quad (1)$$

where  $\theta$  is the aspect angle of the wave,  $X$  and  $Y$  are the ratios of the plasma frequency  $\omega_p$ , and gyrofrequency  $\omega_c$  to the angular radio wave frequency  $\omega$ , respectively (Schunk & Nagy, 2000) namely,

$$X = \left(\frac{\omega_p}{\omega}\right)^2, \quad Y = \frac{\omega_c}{\omega} \quad (2)$$

The plasma frequency describes the oscillation of the electron density for a cold neutral plasma. If thermal motion is neglected, and electrons are displaced with respect to the relatively heavy ions, the Coulomb force acts as a restoring force.

The refractive index for the two modes is determined by the positive (O mode) and negative (X mode) sign of the denominator in equation (1). Examining the cases when propagation of the wave is parallel or antiparallel to the external magnetic field (i.e., the aspect angle  $\theta = 0^\circ$  or  $\theta = 180^\circ$ ) the index of refraction for each mode is given by (Chen, 1984),

$$n^2 = \frac{c^2}{v_{\phi(O)}^2} = 1 - \frac{\omega_p^2/\omega^2}{1 + \omega_c/\omega} \quad (O - mode) \quad (3)$$

$$n^2 = \frac{c^2}{v_{\phi(X)}^2} = 1 - \frac{\omega_p^2/\omega^2}{1 - \omega_c/\omega} \quad (X - mode) \quad (4)$$

where  $c = 3 \times 10^8$  m/s is the speed of light in a vacuum.

The refractive indices, and consequentially the phase velocities ( $v_\phi$ ), are different for each mode of propagation (Budden, 1961; Chen, 1984). The imbalance between the phase velocities induces a change in the orientation angle of the polarization ellipse (Budden, 1961; Canada Centre For Remote Sensing, 2007). This



is known as FR. The magnitude of the rotation is proportional to the integrated product of the electron density,  $n_e(l)$ , along the ray path or plasma column and the strength of the parallel component of the magnetic field  $b_z(l)$ , and inversely proportional to the square of the frequency as follows, (Kraus, 1966)

$$\Omega = \frac{e^3}{8\pi^2\epsilon_0 m_e^2 c f^2} \int_0^l n_e(z) b_{\parallel}(z) dz \quad (5)$$

where the FR is denoted by  $\Omega$  and is measured in radians,  $e = 1.602 \times 10^{-19}$  C is the elementary charge,  $m_e = 9.109 \times 10^{-31}$  kg is the mass of an electron,  $\epsilon_0 = 8.854 \times 10^{-12}$  C<sup>2</sup>/N f<sup>2</sup>m<sup>2</sup> is the vacuum permittivity, and  $f$  is the frequency of the radio wave. The electron density  $n_e$  is in electrons per cubic meter while the parallel magnetic field  $b_{\parallel}(z)$  is in teslas.

The TEC along the path or within the plasma column of unit cross section is defined by

$$TEC = \int_0^{z_{max}} n_e(z) dz \quad (6)$$

where  $TEC$  is the integrated electron density along the path length  $l$  from  $z = 0$  to  $z_{max}$ .

Although  $TEC$  is highly variable, typically, the daily global maximum  $TEC$  is found to range between 80 and 200 TECu (1 TECu =  $10^{16}$  electrons m<sup>-2</sup>) over equatorial regions at solar maximum conditions (NASA Jet Propulsion Laboratory California Institute of Technology, 2014; Wahi et al., 2005; Zhao et al., 2009) and generally decreases with latitude (Soicher & Gorman, 2012).

Using the AIS wavelength ( $\lambda = 1.85085$  m for 161.975-MHz AIS) in equation (5), the FR can be written as

$$\Omega = 9.007 \times 10^{-13} \int n_e(z) b_{\parallel}(z) dz. \quad (7)$$

$$\Omega = 9.007 \times 10^{-13} B_{avg} TEC. \quad (8)$$

where  $B_{avg}$  is the average  $z$  component of the magnetic field along the path. In equation (7) the parallel component  $b_z$  was assumed to be a constant value  $B_{avg}$  and taken out of the integral. The  $TEC$  values are computed by rearranging equation (8) for the modeled FR. The average magnetic field  $B_{avg}$  is computed using the International Geomagnetic Reference Field (IGRF) model data (International association of geomagnetism and aeronomy, Working Group V-MOD, 2010). Although the magnetic field can be treated more accurately using the method described in Cushley, Noël, et al. (2017), IGRF can be considered sufficient for this concept demonstration and can be compared directly to the results obtained by Cushley and Noël (2014) in their study for ADS-B signals.

The  $TEC$  values and ray endpoints are used as the input to CIT in order to reconstruct the resulting electron density maps. Alternatively, reconstruction using FR directly as input rather than  $TEC$  could be used and will be considered in a future paper.

In Figure 3 we show plots of equation (5) for given values of  $TEC$  ranging from 1 TEC unit to 1,000 TECu as a function of frequency. We remind the reader that the intended use of AIS and ADS-B is robust operational communications in support of marine and air traffic safety, and that signal modulation and degradation are generally undesirable. Therefore, these frequencies are favorable selections. A signal having a lower frequency would undergo a greater amount of FR yielding better data for CIT but could become unusable or infeasible due to volume, power, and mass considerations aboard the satellites due to the requirement of higher gain transmitters and/or larger antennas. A signal with a much higher frequency would propagate through the medium relatively unaffected and therefore would be suitable for communications, but the FR may not be detectable and would not be amenable for this type of study. Changes in the FR angle that are less than 1° are considered to be below the current detectable threshold of instruments on board an orbiting satellite (Anderson et al., 2011; Dhar et al., 1977; Rogers & Quegan, 2014).

In fact, most satellite communications systems utilize circular polarization in order to mitigate the FR effect and signal fading associated with the satellite changing its orientation combined with changing polarization as the signal encounters any anomalies traveling through the ionosphere (Orfanidis, 2008). The rotation of a linearly polarized signal can result in polarization mismatch between the transmitting and receiving antennas. Circular polarization can be used to make communications more robust and avoid the negative

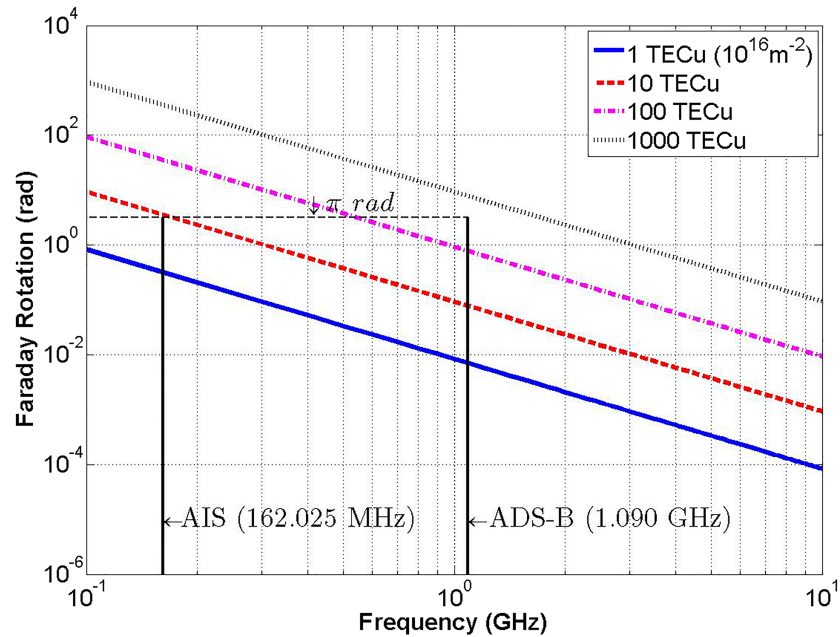


**Figure 3.** FR increases as a function of TEC and decreases as a function of frequency. The solid vertical black lines indicate the 162.025-MHz AIS and 1.090-GHz ADS-B frequencies. The dashed horizontal black line denotes a half turn  $\pi$  of the FR. This is the point at which there is an  $n\pi$  ambiguity in the measurement of the FR.

consequences of FR. For example, GNSS systems use circular polarization so that the orientation of the ground-based receiver does not necessarily matter and the receivers can be used to receive multiple GNSS signals from different satellites in dynamic geometries simultaneously. Similarly, a circularly polarized signal transmitted from a stationary terrestrial transmitter can be received by a satellite that is moving at a relatively high velocity, and potentially even when it is tumbling. Without robust and precise attitude control, as well as knowledge of the initial polarization and pointing direction of the transmitted signal, a linear signal may not be received, not because the signal strength is not strong enough, but because the transmitting and receiving antennas are orthogonal to one another.

It is evident from Figure 3 that the amount of FR expected for the ADS-B transmission even for unrealistically high values of TEC is clearly less than  $\pi$  radians. Therefore, we would not expect a  $n\pi$  ambiguity for the ADS-B operating frequency. Even if ambiguity was an issue, it could be dealt with by using the rate of rotation rather than the absolute rotation angle to determine the change in TEC (i.e., we could use  $dTEC$ ) over consecutive epochs as input to CIT, rather than TEC estimated from the FR.

Another signal that could potentially be used for CIT is the APRS signals. APRS is a linearly polarized beacon signal that could also be considered in addition to ADS-B and AIS, but it was not explored in any great detail in this paper other than to examine the FR due to APRS to compare it with AIS and ADS-B. For illustrative purposes the FR expected from APRS is compared as a TEC observable in Figure 4. APRS is primarily used over land and operates at the lowest frequency of the systems considered making the FR  $\pi$  ambiguity potentially an issue to be considered.

A comparison of the FR estimates for ADS-B (solid black line), GPS L1 (green) and L2 (blue) bands, AIS marine channels 87 (cyan) and 88 (dashed black), and APRS (red) and is presented in Figure 4. The TEC values were selected to represent a range of typical values (and beyond) after consulting the literature, for example, global ionosphere TEC maps can be obtained from NASA Jet Propulsion Laboratory California Institute of Technology (2014) NRCan. These characteristic values were selected and used to calculate and to compare the degree of rotation expected for each type of signal using equation (8), given their respective frequencies and the average radial component of the magnetic field using values from IGRF (for 5:25 UTC on 19 October 2012 at 12.87° latitude and 130°) and the altitude of each satellite system, respectively.

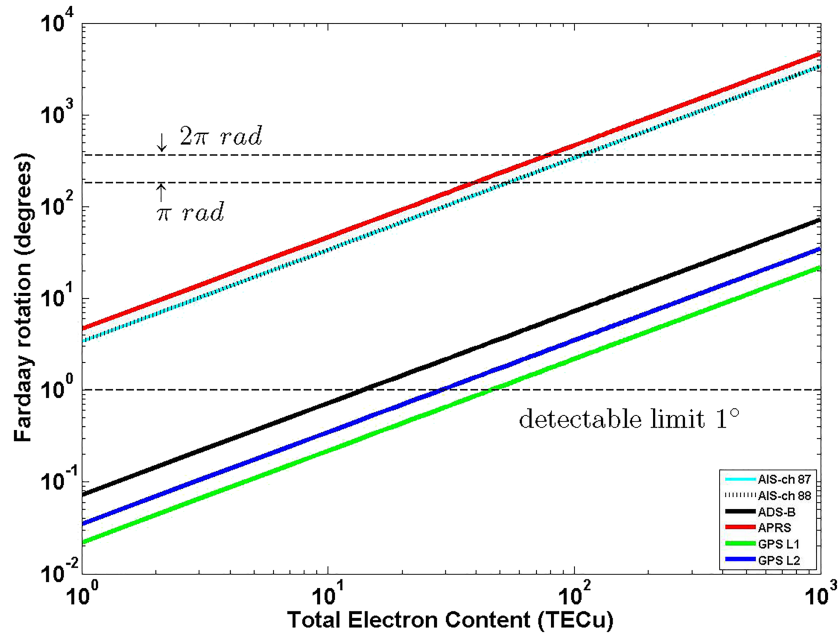


**Figure 4.** FR as a TEC observable; a comparison of the expected FR from equation (5) for ADS-B, GPS L1 and L2, AIS (161.975 MHz (ch 87) and 162.025 MHz (ch 88)), and APRS.

AIS receivers have been flown on the exactView (EV1-9) constellation of satellites operated by exactEarth Inc at orbital altitudes of 810 km; however, the next generation of receivers are hosted payloads on the Iridium NEXT constellation at 781 km (exactEarth, 2016). In this paper we chose an altitude of 781 km to compare the results obtained from AIS and ADS-B. Although Cushley and Noël (2014) used 1,000-km altitude in their study for ADS-B, since it is now a hosted payload on the Iridium NEXT constellation we choose 781 km as the orbital altitude of ADS-B to allow direct comparison and potential conjunctions between data sets.

For Figure 4, the average radial magnetic field is 6,542 nT for both AIS and ADS-B at an altitude of 781 km, 3,993 nT for GPS at 20,200 km, and 7,111 nT for APRS at 408 km. The wavelengths are 1.85 m for AIS (1.8509 for ch 87 and 1.8503 for ch 88), 0.27 m for ADS-B, 2.07 m for APRS, and 0.19 and 0.24 m for GPS L1 and L2, respectively. The amount of FR expected for the ADS-B frequency for each of the TEC values is shown as the black trace. The FR for the GPS L1 and L2 bands are shown by the green and blue traces, respectively. The amount of FR computed for the two AIS frequencies are shown by the cyan and dashed black traces while the red trace shows the FR computed for APRS. The horizontal dashed lines show the limits where the FR measurements would be undetectable (below 1°) or be ambiguous (above 180°).

Most notable in Figure 4 is that for a given TEC value the FR will be least, or have less variation as a TEC observable for the GPS carrier frequencies (blue and green traces) compared to the AIS (cyan and dashed black traces), ADS-B (black) or APRS (red) signals. We note that GPS signals are transmitted with circular polarization, but the same cannot be said about the received signal. The fact that GPS receivers are not designed to infer the polarization of the received wave is a limitation of the current receiver design; however, it is possible to measure polarization of GPS signals as was shown by Benton and Mitchell (2014).

Also notable in Figure 4 is that the FR for both the APRS and AIS measurements may have ambiguity due to phase wrapping, which occurs at ~39 and ~53 TECu, respectively. Although a value of 1,000 TECu may not be realistic, it is used to show the extreme conditions under which the FR measurements may become ambiguous ( $\geq 180^\circ$ ) for certain carriers. Any polarization measurement has an ambiguity associated with it of any integer number ( $n = 0, 1, 2, \dots$ ) of half turns  $\pi$ , which makes it difficult to distinguish between polarization angle measurements  $\chi$  and  $\chi \pm n\pi$  (Ruzmaikin & Sokoloff, 1979). Methods to interpret or mitigate phase wrapping were previously discussed in section 1.2, although a sanity check could also be applied, particularly if AIS and ADS-B data are both available on the same satellite. The potential may also exist to use one data set during quiet conditions and the other during active conditions, using AIS, which

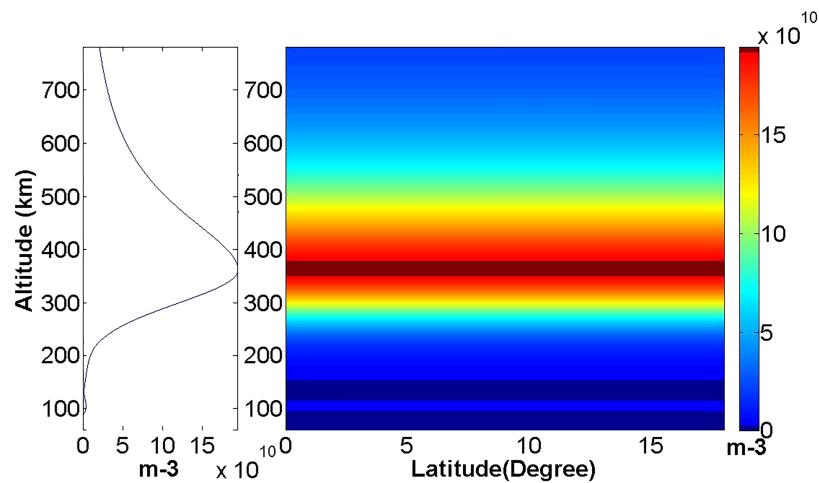


**Figure 5.** (left) Initial electron density profile for geomagnetically quiet conditions generated using the IRI model. (right) A contour plot of the initial electron number densities prior to the addition of the enhancement.

is more sensitive to lower TEC values when TEC is below a given threshold (e.g., 13 TECu corresponding to the detectable limit of current FR measurements of 1° for ADS-B) and ADS-B when it is above another threshold (e.g., 53 TECu when AIS is ambiguous), and amalgamated data sets between 13 and 53 TECu. The best signals are those which remain unambiguous under normal ionospheric conditions while providing the most measurable change in  $\Omega$  as the TEC varies, making AIS and ADS-B the best signals to consider in this technique.

### 2.3. Ray Tracing

An EM wave ray tracing model developed by Gillies et al. (2007) was used to generate synthetic ADS-B and AIS data to compute the wave path and the polarization state of the transmitted signal received at the satellite. The ray trace program, based on the ray formalism developed by Haselgrove (1963), uses equation (1) to determine the indices of refraction of a radio wave in a magneto-ionic medium. This model provides the group velocity and rate of change of the wave vector direction. Inputs to the ray trace program include the initial wave vector direction, the wave frequency, and a set of propagation conditions such as the magnetic field vector and an electron density profile for the ionosphere. The program computes the path of the waves of a given frequency that both the O mode and X mode take from the initial position of the transmitter to the satellite receiver.

The initial polarization orientation of the wave leaving the ship must be known. For the purpose of this work all waves were assumed to be vertically plane polarized for AIS (Kyovtorov et al., 2012; The International Telecommunications Union, 1998; Parsons et al., 2013) and ADS-B (Radio Technical Commission for Aeronautics, 2003; Haque et al., 2013). In reality, the initial polarization of the wave may be significantly different but would be constant for any given ship. While ships offer a relatively stable platform, aircraft orientation (banking and climbing) may affect the orientation of the transmitted signal. That information is part of the ADS-B packet and the initial orientation of the polarization can be determined. For the purpose of tomography the initial orientation does not necessarily need to be known since the rate of rotation over consecutive epochs (between aircraft-satellite pairs) rather than the absolute value can be used (Klobuchar & Liu, 1989) to provide  $dTEC$  rather than absolute  $TEC$ .

The ray trace program was used to generate TEC outputs from rays that passed from given locations, at a given elevation angle through a 2-D electron density profile to a specified satellite location (Gillies, 2006, 2010; Gillies et al., 2007). The model was used to show that the FR of the signals received by the satellite should be detectable. Previous work by Yueh (1999) has shown that FR can be used to obtain the TEC along the paths. The computed TEC and ray path geometry are then used to reconstruct the electron density profile that the EM waves propagated through.

In the left panel of Figure 5 we show an electron density profile generated using the International Reference Ionosphere (IRI) (Bilitza, 2007; Bilitza et al., 2011) that was used to produce the uniform standard quiet

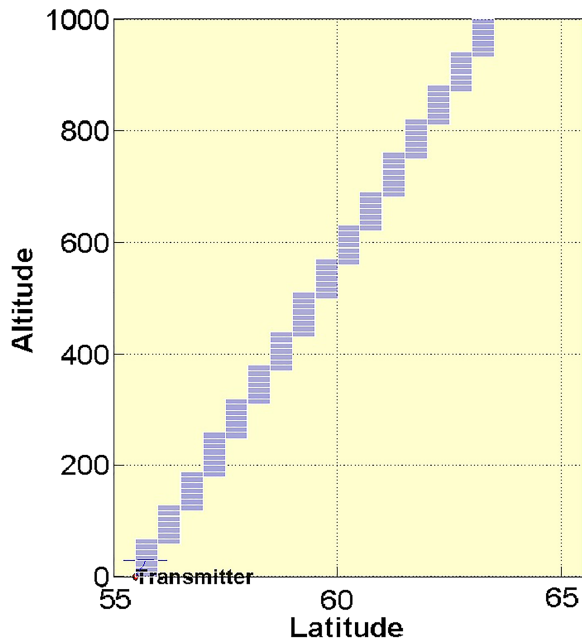


**Figure 6.** An illustration of a signal ray path passing through illuminated pixels (blue) within a portion of the 2-D reconstruction grid (yellow). Each blue pixel is  $\Delta z = 10$  km in altitude  $\Delta\theta_l = 0.25^\circ$  in terms of the geographic latitude.

background electron density map shown in the right panel of Figure 5. This uniform electron density map was used to superimpose all the modeled density enhancements to create 2-D electron density maps through which to pass rays. The new maps were used as input to the ray tracing model to simulate a ray leaving from a ship, passing through the ionospheric enhancement and received by the satellite. Measuring (or modeling in this case) the polarization angle of the received wave and knowing the initial polarization of the wave, the FR for the ray path can be computed.

#### 2.4. Reconstruction

A complete description of the standard reconstruction techniques used in our case studies can be found in Cushley and Noel 2014 (section 2.3) and the references within. We only briefly review the procedure here.

For each and every STEC measurement, there is an equation of the form of equation (9). The STEC measurement of the ray path can be represented as a series of finite summations of shorter integrals along segments of the ray path length  $d_{ij}$  (the contribution of ray  $i$  to pixel  $j$ ).

$$STEC_i = \sum_{j=1}^{\rho} n_{ej} d_{ij} + \Delta_i \quad (9)$$

where  $\Delta_i$  is the uncertainty associated with the integrated pixels  $j$  for a given ray path  $i$  due to discretization errors and measurement noise.

Rather than working with such a large system of equations, matrix notation is useful

$$STEC_{i \times 1} = D_{i \times j} \times N_{e \ j \times 1} + E_{i \times 1} \quad (10)$$

where  $STEC_{i \times 1}$ ,  $E_{i \times 1}$ , and  $N_{e \ j \times 1}$  are column vectors of  $i$  measurements of STEC,  $i$  associated error values, and  $j$  unknown pixel values  $n_{ej}$ , respectively. The matrix  $D_{i \times j}$  is the geometry matrix, with element  $d_{ij}$  equal to 1 if ray  $i$  traverses pixel  $j$ , and 0 otherwise (see Figure 6). The STEC is the known modeled or measured quantity while the matrix  $D$  is computed from the time-tagged transmitter and satellite receiver state vectors.

The matrix  $D$  is often called the weight matrix when the analysis of the ray geometry is made to be more elaborate based on several other factors such as the length segment of the ray for each pixel, or the relationship of a pixel to its neighboring pixels (Max van de Kamp, 2012). The simplest form for  $D$  is a logical index with a row depicting each ray, and columns for each pixel value in the reconstruction grid.

A rectangular grid can be used to represent a 2-D slice of the ionosphere as shown in Figure 6. To represent the interior structure of the ionosphere, the grid is subdivided using a constant  $\Delta z = 10$  km in altitude from the Earth's surface, and a constant  $\Delta\theta_l = 0.25^\circ$  in terms of the geographic latitude. The endpoints for each ray are available from the GPS positions of the time-tagged AIS transmissions, and the satellite's on-board GPS receiver, telemetry, or possibly two-line element sets and orbit propagation software for signal time of arrival positions.

For illustrative purposes, a single ray leaving the transmitter and assuming a straight line approximation, the pixels in blue would be assigned a value of 1, while those in yellow would be assigned a value of 0. In Cushley (2013) several different grid sizes ( $g_x \times g_y$ ) were tested. For all the results in Cushley and Noël (2014) a grid of  $100 \times 100$  pixels having intervals of 10 km in altitude and  $0.25^\circ$  in latitude was selected. The depth of the pixels (or voxels) in the grid  $g_z$ , or the longitudinal extent over which data were simulated and for which the 2-D reconstruction was representative of the electron density was chosen to be  $1^\circ$  (i.e., the electron density was assumed to be uniform over a  $1^\circ$  slice of longitude).

The TEC measurements, or the sum of the electron content along the ray paths from transmitting ships to the passive satellite receivers, may be inverted and reconstructed to acquire a 2-D  $n_e$  map along a slice of longitude. The relative TEC along each ray path  $i$  can be expressed as a line integral of the electron densities ( $N_e(j)$ ) along path  $i$  and is similar to the Radon transform of conventional tomography (Kak & Slaney, 1988).

FR measurements, once they have been converted to STEC constitutes a system of linear equations from which the solution may be sought. If the time component for all data within the specified collection period is neglected, the STEC can be written in terms of the electron density  $N_e$  in equation (11) as a function of pixel  $x$  in the reconstruction grid as follows

$$STEC_i = \int_0^l N_e(j) dl. \quad (11)$$

where  $N_e(j)$  is a vector of  $j$  unknown pixel values and  $dl$  is an element of the matrix  $D$ , which relates the contribution of the measured value of  $STEC_i$  to pixel  $n_{ej}$ . Inversion of these relative TEC measurements using the ambient CIT imaging geometry constitutes the tomographic image reconstruction process.

The Algebraic Reconstruction Technique (ART) inversion algorithm was used to determine the unknown pixel intensity  $n_{ej}$ . Using a successive iteration approach, the pixel intensities are modified to allow the projection through the pixels ( $DN_e$ ) to approach the measured projection (STEC).

The ART algorithm can be implemented using the following equation (Choi et al., 2006).

$$N_e^{k+1} = N_e^k + \lambda_k \frac{STEC_i - \sum_{j=1}^{\rho} d_{ij} n_{ej}^k}{\sum_{j=1}^{\rho} d_{ij} d_{ij}} D_i \quad (12)$$

where  $j$  is the pixel number,  $k$  is the iteration number,  $\lambda_k$  is a relaxation parameter,  $N_e^k$  is a vector of the ionosphere electron densities ( $n_{ej}^k$ ) for the  $k^{th}$  iteration, and  $N_e^{k+1}$  is a vector of the modified values of the electron densities ( $n_{ej}^{k+1}$ ) for the  $k^{th} + 1$  iteration. The vector  $STEC_i$  contains the TEC measurements taken over various elevation angles and slant ranges. The matrix  $D$  relates the ray data to the pixels in the reconstruction grid; there is a row for each ray, and column for each pixel in the reconstruction grid ( $100 \times 100$ ). The  $STEC_i$  contribution to pixel  $j$  from ray  $i$  in the matrix  $D$  is  $d_{ij}$ . The  $i$ th row of  $D$  is  $D_i$ , and  $\rho$  is the total number of pixels in the reconstruction grid, in this case  $10^4$  pixels.

ART forms the basis of most of the other pixel-based methods, for example, Simultaneous ART and Simultaneous Iterative Reconstruction Technique (Tessa et al., 2007), multiplicative algebraic reconstruction technique (MART) (Atkinson & Soria, 2007), and decomposed algebraic reconstruction technique (Kunitsyn et al., 1994, 1995). Although many other methods and algorithms exist ART has been widely used and is well documented.

The ART method is affected by numerical uncertainties that are introduced by inconsistencies in the system of equations. It is possible to reduce the negative effect of the uncertainties by using a relaxation parameter  $\lambda_k$ . The parameter  $\lambda_k$  is generally referred to as a relaxation parameter, but it is in fact a regularization factor from regularization techniques (Tikhonov & Arsenin, 1977; Tikhonov & Goncharsky, 1987). The relaxation parameter can be iterative or chosen to be constant for each iteration in order to control the convergence rate of the algorithm and maintains the stability of the numerical method. The value for  $\lambda_k$  is confined between  $0 < \lambda_k < 2$  (Hackbusch, 1994). After considering the literature sources for GPS CIT using ART a conservative value of  $\lambda_k = 0.005$  was used for all iterations (Choi et al., 2006).

The ART technique can use an initial guess or a priori estimate to perform the reconstruction, which converges in an iterative manner. For this particular investigation on the feasibility of using AIS radio occultation data as an input to CIT, ART was considered to be a reasonable method as a first-order evaluation. Any benefits from more complex algorithms would only add to the computational expense of the task. If reconstruction of the ionospheric electron density was possible using ART, it would certainly be possible and probably refined using more complex algorithms.

The effect of the curvature of the Earth was taken into account in the ray tracing program by computing the elevation as a function of range-to-target height integrated through the input electron density and geomagnetic model. This was shown to be computationally intensive so for the purposes of the reconstructions of the rays a LOS approximation was used. This means that we neglected diffraction, bending or refraction due to the Earth's atmosphere, as well as attenuation or absorption of energy by the gases in the atmosphere.

In general, only the aircraft/ship and satellite positions and FR measurements, from which the STEC values are computed, will be available.

### 3. Results and Discussions

The Iridium NEXT satellite(s) are in polar orbits at 781-km altitude with an inclination of  $86.4^\circ$  and a 101-min orbital period. The satellites were simulated using a commercial software called Systems Tool Kit (STK). STK was used to calculate the LOS access times, which determines the data integration time and temporal resolution of the CIT reconstructions. In this case study, the temporal resolution was determined to be between 7 and 8 min, which is consistent with the coverage expected from a space-borne AIS receiver; Miller (2016) reports that each satellite pass from horizon to horizon takes about 10 min with a revisit time of about 100 min. Based on STK access reports, a more conservative data integration time of 7 min and 4 s (424 s) was used in all of the reconstructions in this paper.

In this investigation we assumed that the ionosphere remained constant for the 7-min duration of the satellite pass. The pass length and the average interval between AIS signal transmissions determined that the maximum number of rays for each ship-satellite pair was 40, with satellite receiver positions spaced  $\sim 0.260^\circ$  ( $\sim 28.9$  km) in latitude, thereby limiting the number of rays that could be observed per ship for a single satellite pass. This is analogous to having the number of detectors in a medical CT machine fixed to 40. It also represents the number of detectors that form the projections during a satellite pass. For CIT using GPS, the number of transmitters cannot be increased, although the number of ground-based receivers can, but their locations are constrained to land masses and supporting infrastructure. In the inverted apparatus presented here, the number of transmitters can be increased by simply adding more sources from ships and/or aircraft, neither of which are generally constrained geographically. The only exception is that ships are constrained to water.

To simulate a realistic scenario, a single satellite pass over a reconstruction region of  $18.1^\circ$  latitudinal extent between  $0.7^\circ$  and  $18.8^\circ$  was considered, with 15–45 ships distributed between  $1.96^\circ$  and  $12.14^\circ$  ( $10.18^\circ$ ) latitude resulting in 600–1,800 rays to be used in the reconstruction (i.e., 15–45 aircraft with 40 rays per ship-satellite pair).

#### 3.1. Comparing Results From ADS-B And AIS

Cushley and Noël (2014) examined case studies using the method described in this manuscript to evaluate ADS-B signals as a potential source of TEC data to complement the existing ground-based GPS ionospheric TEC data as well as an independent source for determining electron density maps of the ionosphere. In their work they described the ionosphere tomography results using the slant TEC data simulated from an ADS-B system—25 aircraft as ADS-B transmitters and one satellite at the altitude of 1,000 km as ADS-B receiver. At the time, the ADS-B demonstration satellite had yet to be launched and was planned for an orbital altitude of 1,000 km. Since that time, other ADS-B receivers have been payloads on a number of satellites in other orbits, including the Iridium NEXT constellation. Since this paper is primarily interested in AIS signals, we use the altitude of the Iridium NEXT constellation satellites at 781-km orbital altitude. The results in the next section will be shown to be consistent with those published by Cushley and Noël (2014). In order to compare the results from ADS-B and AIS, we assume the AIS orbit to be the same orbit that originally was studied for ADS-B.

##### 3.1.1. Scenario I—A Single Localized Electron Density Enhancement

The first scenario we consider is the same electron density enhancement (Figure 7 in this manuscript) that was presented in Cushley and Noël (2014) (their Figure 5). In this scenario 25 ships were used and spaced between  $54.63$ – $79.80^\circ$  latitude for AIS. This is the same distribution that was used where they simulated 25 aircraft by Cushley and Noël (2014). To facilitate the comparison between the results using ADS-B and AIS the satellite altitude for both was chosen to be at an orbital altitude of 1,000 km and the pass length was 3–4 min. The parameters of this scenario are the same as those presented in Cushley and Noël (2014) with the exception of the AIS frequency, which is lower than for ADS-B.

In the top panel of Figure 7 we present the input electron density map used in Cushley and Noël (2014) (their Figure 5) as the input to the ray tracing model to simulate the expected FR measurements and their associated TEC values. This map was created by superimposing a single 2-D normal Gaussian distribution with a specified scaling factor (the unit scale height of the peak density of the symmetric stable distribution), which determined the statistical dispersion of the quiet background profile. The maximum of the density

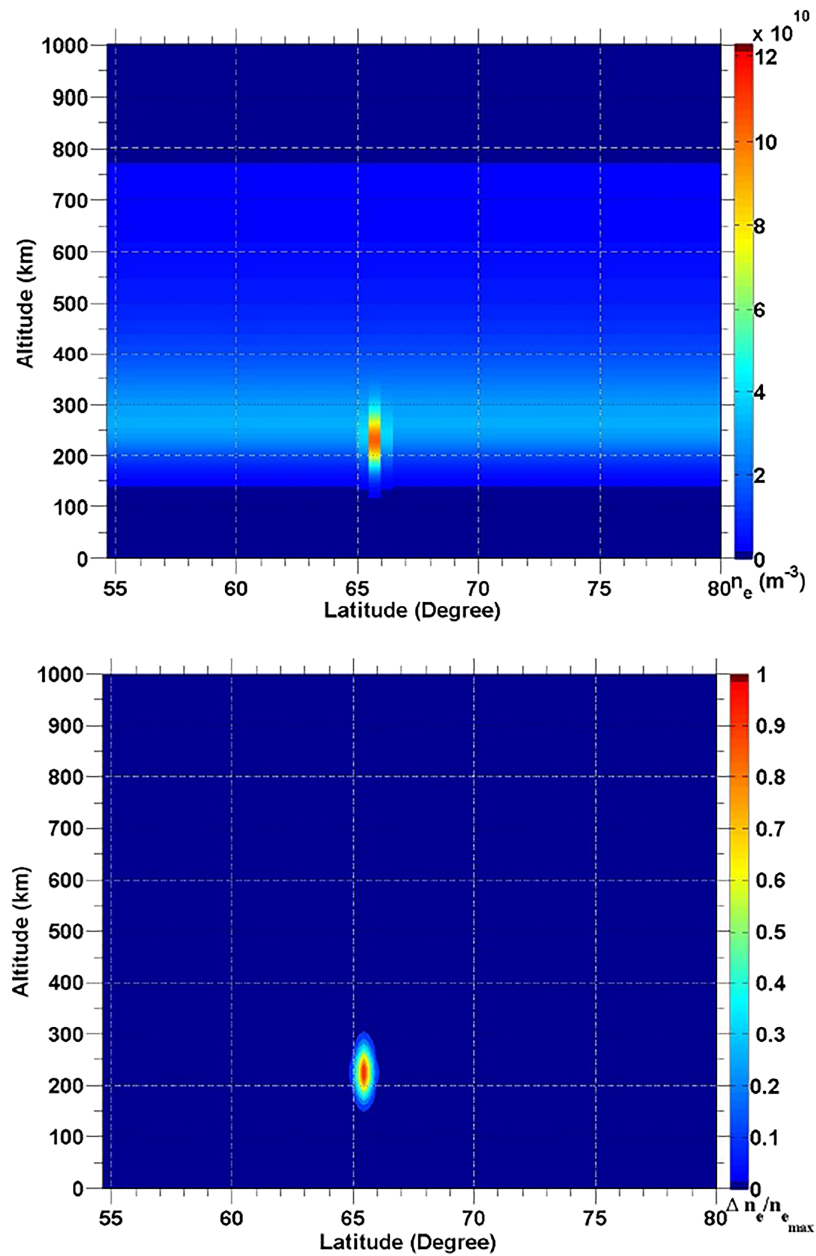


**Figure 7.** (top) Single feature electron density profile; scaling factor = 5.0, full width (latitudinal extent) at half maximum =  $0.25^\circ$ , vertical extent = 50 km, latitude =  $65.5^\circ$ , altitude = 225 km. (bottom) Single feature electron density profile from top panel shown as relative weight. The profile was normalized relative to the peak density.

enhancement was located at a latitude of  $65.5^\circ$ , and altitude of 250 km, with latitudinal width of  $0.25^\circ$  and vertical thickness of 50 km. An altitude of 250 km was selected for the modeled enhancements because the *F* region (above 150 km) is present during the day and night (Hunsucker & Hargreaves, 2003).

The initial electron density maps were used to evaluate the relative agreement between the initial input electron density map and the final result of the CIT reconstruction. The bottom panel shows the normalized enhancement of the feature of the top panel. The normalized map is used for comparison with the reconstruction because the latter will only give the relative value for the electron density within a particular pixel with respect to other pixels within the reconstruction.



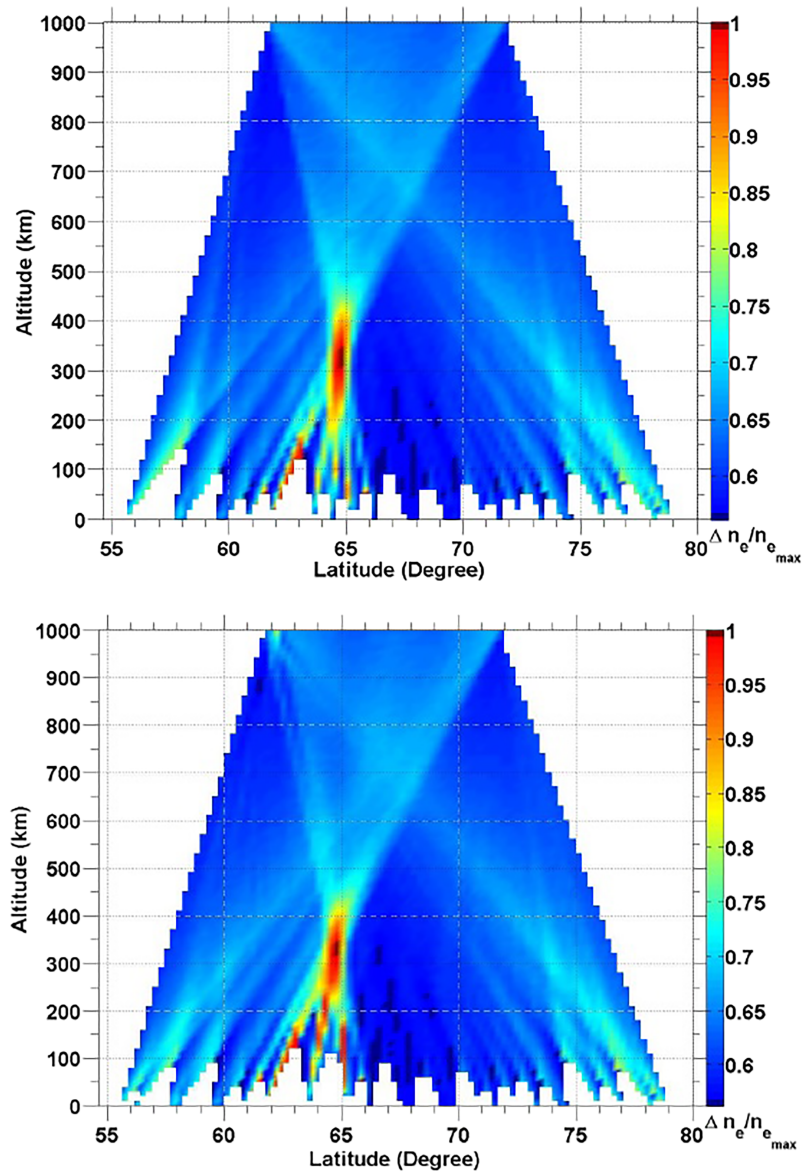


**Figure 8.** (top) Raw reconstructed relative electron density profile of ray trace input above using TEC measurements and LOS path from 25 ADS-B transmitters (Cushley & Noël, 2014). (bottom) Raw reconstructed relative electron density profile of ray trace input above using TEC measurements and LOS path for 25 AIS transmitters. Regions where there is an absence of data for reconstruction are shown in white.

To obtain absolute values for the densities, additional steps would be required such as an a priori guess for the reconstruction, or using data from another independent source (e.g., ionosonde or radar) that gives the peak density at some location within the reconstruction region in order to scale the remainder of the reconstruction region accordingly.

The reconstruction grid was initialized to zero value pixels for the background. It is typical to use a model such as IRI to provide an a priori guess for the first iteration of the reconstruction, but in order to evaluate the benefits and shortcomings of using the ADS-B/AIS data distributions alone a priori estimate was not used for this scenario. The simulated 2-D ionosphere also does not correspond to a specific date or time so the model would not necessarily be a relevant guess or may bias the results, if one were used. Admittedly, using a value of 0 (or 1) for every pixel is not a very good initial guess, but the advantage is that it does not provide any additional information to the reconstruction other than the data itself, thereby preserving the

integrity of the reconstruction and not bias the results toward a preferred electron density map. Besides a negative value for the electron density, which has no physical meaning, 0 is about the worst possible guess possible for the initial electron density. The normalized relative densities were reconstructed using only the modeled STEC measurements, and the LOS path between the known transmitter and receiver positions.

The reconstruction for the ADS-B distribution presented in Cushley and Noël (2014) using the STEC values and ray endpoints for the input electron density map is shown in the top panel of Figure 8. For comparison, the reconstruction using the AIS signals is shown in the bottom panel of Figure 8. From these figures we can clearly identify the enhancement in the reconstructed electron density map relative to the background density near 65° latitude and between 200- and 400-km altitude with a maximum ~350 km for both the AIS and ADS-B signals. From this figure we can see that either ADS-B or AIS can be used to reconstruct a single enhancement. The results show that ADS-B and AIS are consistent with one another and that these reconstructions are faithful to the original input ionosphere.

The horizontal position of the reconstructed enhancement is shown to be roughly in the same location in both panels of Figure 8; however, the peak is located at a slightly higher altitude than the original input enhancement (see Figure 7). The spread in altitude is attributed to constraints in orbital geometry for a low Earth orbit (LEO) satellite and the LOS conditions during an overhead pass of a single satellite. There is a predominantly vertical ray geometry between the transmitters in the field of view of the satellite, which provides information about the electron distribution as a function of latitude, however does not give much information pertaining to the vertical distribution of the TEC, which is integrated over the entire path length. This may have biased the reconstruction in terms of the altitude distribution of the reconstruction. It is not possible to acquire data from all viewing angles since horizontal path measurements are not possible (the satellites is always situated overhead the ships/aircraft).

In this work the data were limited to transmitters located within the reconstruction region. This limits the radio ray paths to be more vertical due to the constraint, while more horizontal ray paths would be available if rays that passed through only a portion of the reconstruction region were included in the reconstruction. In Future work all data available will be used, which should serve to further improve the reconstruction.

The lack of horizontal ray paths results in difficulties with altitude discrimination and introduces artifacts to the reconstruction. By using all data available (including signals originating from transmitters beyond the reconstruction region), an a priori estimate, and a different reconstruction algorithm the number of artifacts and altitude distribution of the electron density should improve. For example, MART has been shown in other applications to be preferable to that of additive ART which leaves artifacts or tracer in the reconstructed field (Atkinson & Soria, 2007; Elsinga et al., 2006).

There are techniques such as limb sounding that could be used when more than one satellite can be used. Signals from low-elevation angles originating from transmitters that are located beyond the reconstruction region are also a possibility, but these have not been considered due to the constraints that were imposed by using a single satellite and mutual LOS visibility to transmitters within the reconstruction space throughout a satellite pass. We simply wanted to use AIS signals to assess its benefits and its shortcomings as an independent source of TEC measurements for CIT.

Other instruments that give the peak height and density such as ionosondes could provide this information along with a 2-D profile that can be used to scale the vertical distribution. We can also use ionospheric/thermospheric models such as those discussed by Cushley, Kabin, et al. (2017) for distributing the TEC as a function of altitude in the future but those elaborations were not considered here.

The white regions on either side of the reconstructions in Figure 8 as well as the white triangular shapes below ~150-km altitude between the transmitters are pixels with zero value. It is important to note that the actual electron density is not 0 in these regions. These are regions where no rays have passed and as a result, no data are available for the reconstruction to be performed in those areas. Recall that the grid was initialized to zero from the outset.

We also note regions within the reconstruction that appear to be enhanced. These are shown in red, yellow, and green at lower (below 200 km) altitudes. These are artifacts and generally occur where only a single ray has passed through the ionosphere to the receiver. When a single ray has traversed a pixel and the STEC value of the ray is distributed among the other pixels along the path the possibility exists to have

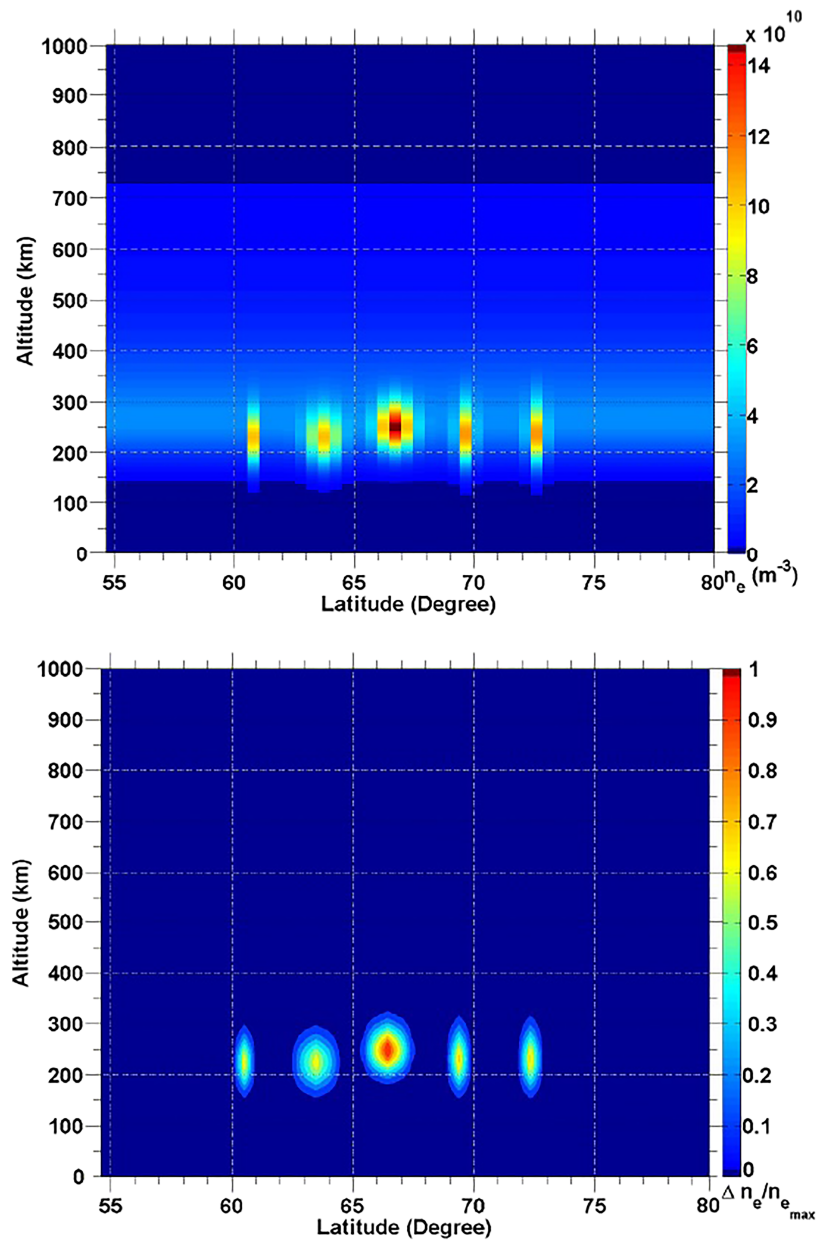


**Figure 9.** (top) Five feature electron density profiles (left to right): latitude = 60.5°, 63.5°, 66.4°, 69.5°, 72.5°; scaling factor = 3.0, 3.0, 5.0, 3.0, 3.0; full width at half maximum = 0.25°, 1.0°, 1.0°, 0.25°, 0.25°; vertical extent = 90 km; altitude = 225, 225, 250, 225, 225 km. (bottom) Five feature electron density profiles from top panel shown as relative weight. The profile was normalized relative to the peak density.

a disproportionate amount of the STEC from the total path being distributed to other pixels along the path that have several rays intersecting in order to maintain the STEC along each individual path. This is particularly true at high and low altitudes where the number of total paths and the number of intersecting paths are quite limited. This is in contrast to medical and/or material CT imaging machines which are specifically designed to sample at a higher resolution using all possible viewing angles. Although there are methods to interpolate the regions with zero-value pixels and smooth the reconstruction and minimize the effect of artifacts, for this comparison, we are only interested in examining the raw reconstructions to determine which signal is better.

Although the reconstructed map in Figure 8 is not a perfect representation of the input electron density map (Figure 7), a feature can clearly be discerned within the same general area where the original enhancement was located in the input profile. This suggests that there is good relative agreement between the input reconstruction and the original input profile. The agreement demonstrates that AIS could be a useful tool to highlight areas where enhancements in the electron density occur, for example, it could be potentially used to detect and observe evolution of polar cap plasma patches (Dahlgren et al., 2012; Gondarenko & Guzdar, 1999, 2001).

### 3.1.2. Scenario II—Multiple Ionospheric Electron Density Structures

In the next scenario we evaluate the suitability of using AIS data to resolve more complex ionospheric structures. In reality, electron density enhancements will not necessarily occur as single features orders of magnitude greater than the entire background. This is particularly true when the ionosphere is active. Enhancements may occur as complex structures of different scale sizes and densities. In fact, if a particular layer is enhanced with numerous small-scale features smaller than the resolution of current measurement techniques, they may appear as a large single enhancement and may not individually resolved.

In the top panel of Figure 9 we present the same input electron density profile that was used by Cushley and Noël (2014) for a five-feature enhancement. It was created using the same initial horizontally stratified quiet electron density profile from Figure 5 and clearly shows five different enhancements of the same vertical extent, but differing only in peak densities, horizontal width, and latitude. The enhancements are located at 60.5°, 63.5°, 66.4°, 69.5°, and 72.5° latitude with relative amplitudes to the background of 3, 3, 5, 3, and 3 and latitudinal widths of 0.25°, 1°, 1°, 0.25°, and 0.25° in latitude with a vertical spread of 90 km, at a peak altitude of 225, 225, 250, 225, and 225 km.

This scenario is not intended to represent a realistic ionospheric structure; it is only meant to be representative of an ionosphere having complex structures that includes multiple features. The objective of this scenario was to determine the extent to which the structures could be reconstructed using the technique described herein. The fundamental question to be addressed is whether the individual features can be resolved.

This scenario proceeded in the same manner as the first. The reconstructed relative density map is presented in Figure 10 for ADS-B (top panel) and AIS (bottom panel) using Figure 9 as input for the ray trace program.

We note from both reconstructions that they are not perfect reconstructions of the input electron density map (Figure 9), but it did agree reasonably well in terms of the relative densities as well as their locations. Five features are clearly evident in the reconstructions. As in Scenario I, the enhancement at 60.5° and 63.5° latitude appear to be elongated in altitude. In addition, the enhancement at 60.5° in the top panel of Figure 9 seems to have a double peak with one peak located ~57.5° at 150 km while the other is located ~59.0° at 350 km. This feature appears prominently in the ADS-B reconstruction while it is not as evident in the AIS case. Cushley and Noël (2014) explained the differences in enhancement positions, as well as the double peak feature due to the fact that the sampling geometry is asymmetrical, especially on the edges of the reconstruction region. The asymmetry cannot be avoided since the positions of the receivers for GNSS are constrained by infrastructure, terrain, and air/ship traffic distributions. Asymmetry in the technique may be unavoidable if we want to consider signals of opportunity for CIT.

### 3.2. Scenario III—AIS Phillipine Sea

Having presented the comparison of using the AIS frequency and ADS-B frequency and showing their relative agreement using the input electron distribution from Cushley and Noël (2014) we now focus on AIS signals for a realistic distribution of ships. There are very few ships in the Hudson Bay region which was chosen for the ADS-B reconstructions in the work of Cushley and Noël (2014). In this scenario we consider areas where higher marine traffic density/volume can be found since these regions will be more amenable for CIT techniques.

To get a realistic distribution for AIS, equipped ships a variety of sources were considered. In Figure 11 we present a maps from MarineTraffic ([www.marinetraffic.com](http://www.marinetraffic.com)). The top panel of Figure 11 shows the annual global marine traffic density distribution. The regions of the map that are shown in red indicate the areas where the greatest number of ships pass. They are the regular shipping routes. The regions in blue may have as few as a single ship using these routes in one year. As a result, regions in red would be deemed to be the most appropriate to consider for CIT since they would provide opportunity for the most data. Several of the

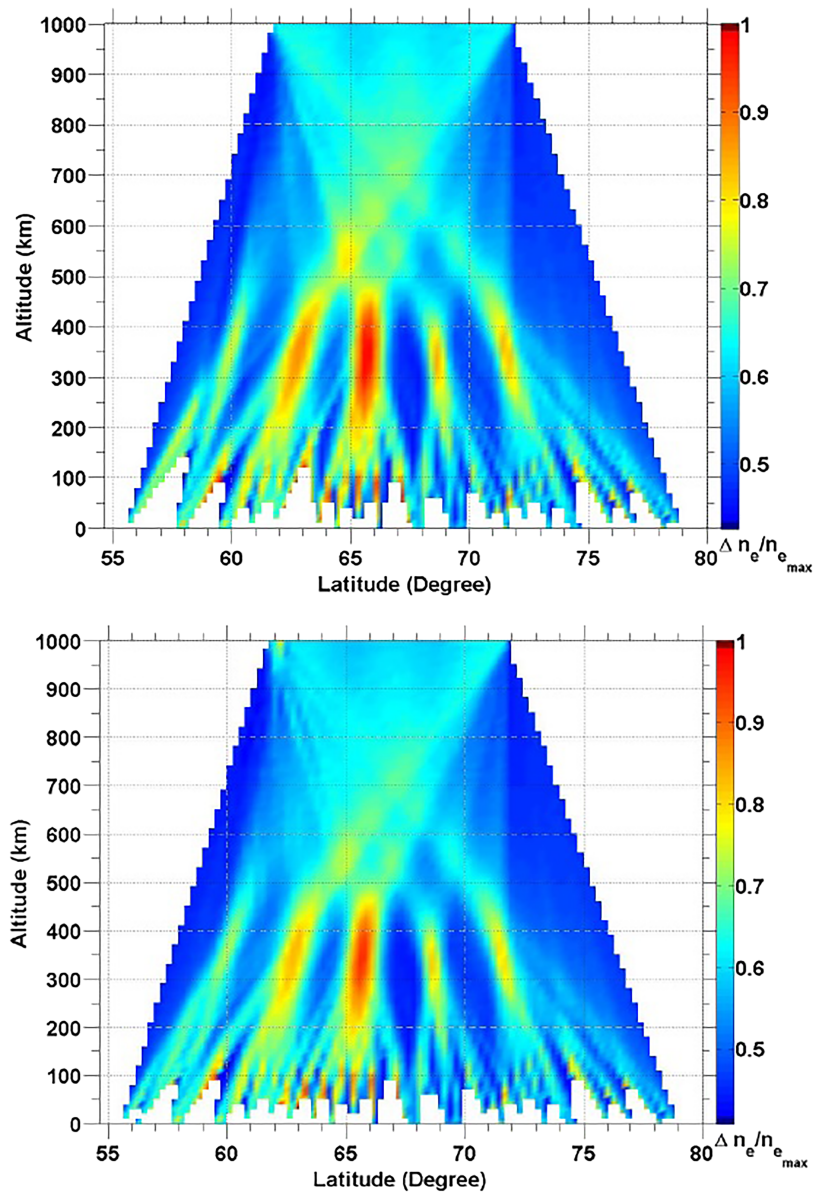


**Figure 10.** (top) Relative electron density profiles of ray trace input, the top panel of Figure 9 using TEC measurements and LOS path from ADS-B (Cushley & Noël, 2014). (bottom) Raw reconstructed relative electron density profile of ray trace input above using TEC measurements and LOS path for AIS. Regions where there is an absence of data for reconstruction is shown in white.

regions with the highest ship density occur near land, for example, harbors. The Port of Hong Kong can have up to a few thousand ships at any given time. In these areas, coverage from GNSS networks already exist. It is important to note that ships that are moored while in port do not transmit as frequently as ships that are underway. These regions were not considered in this study even though these areas would be very useful for future calibrations using existing GNSS networks (e.g., GeoNet), radar, ionosondes, or any other appropriate instruments.

The Hong Kong Harbour (roughly 22.3°N, 114.2°E), the South China Sea (12.5°N, 115.0°E) and the Philippine Sea (12.5°N, 130.0°E) were considered due to the greater number of ships present in these regions as well as their relevance, their importance, and their connection to the tracking of both air and ship traffic. One region of particular interest for both AIS and ADS-B is the oceanic area between China and Australia.

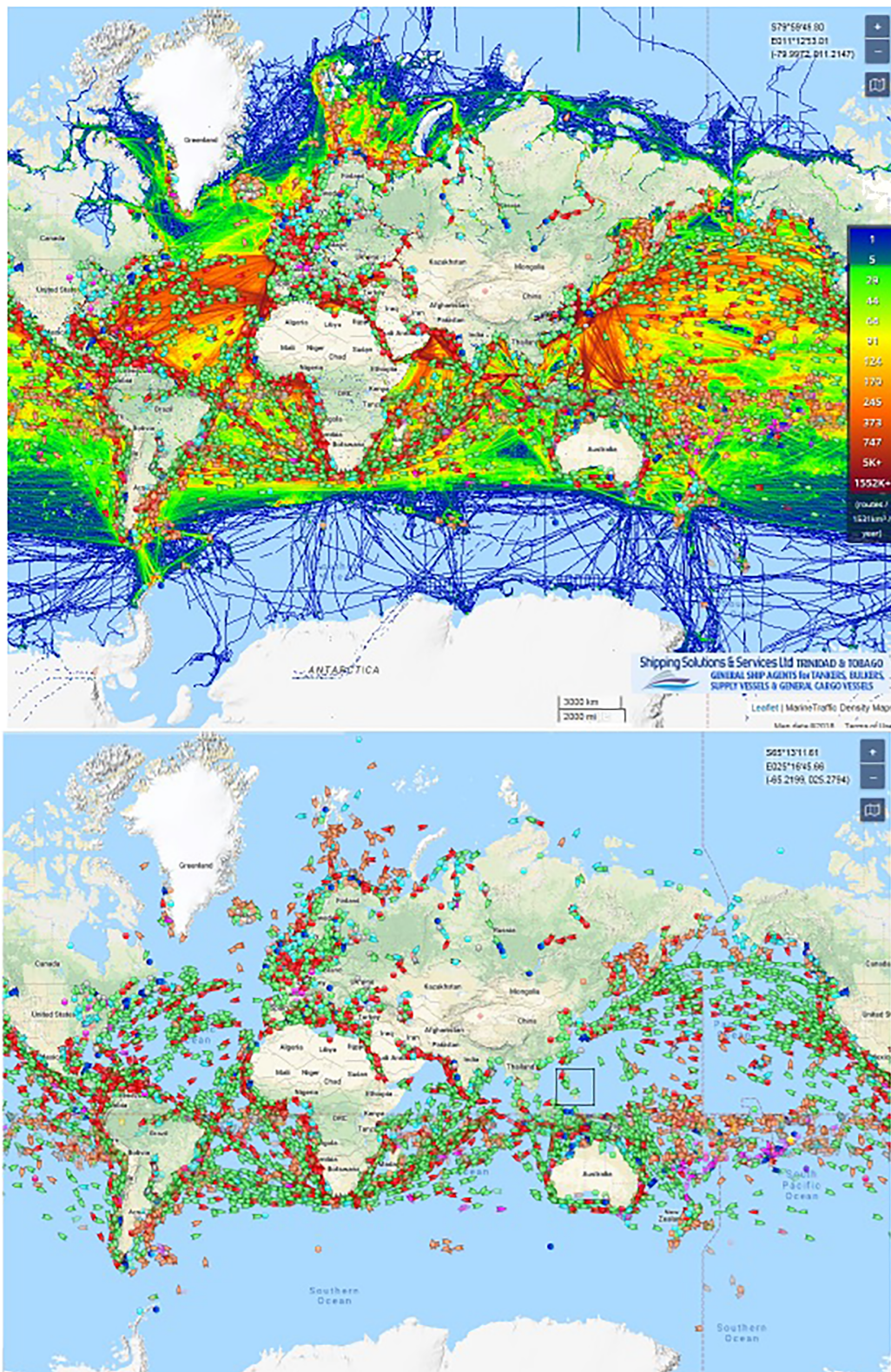


**Figure 11.** (top) Annual global density map of AIS-equipped marine traffic for 2017. (bottom) A live marine traffic map from 20 September 2018 at 11:09 EST of the active AIS ships. The black box shows the Philippine Sea region used later. These maps taken from MarineTraffic ([www.marinetraffic.com](http://www.marinetraffic.com)).

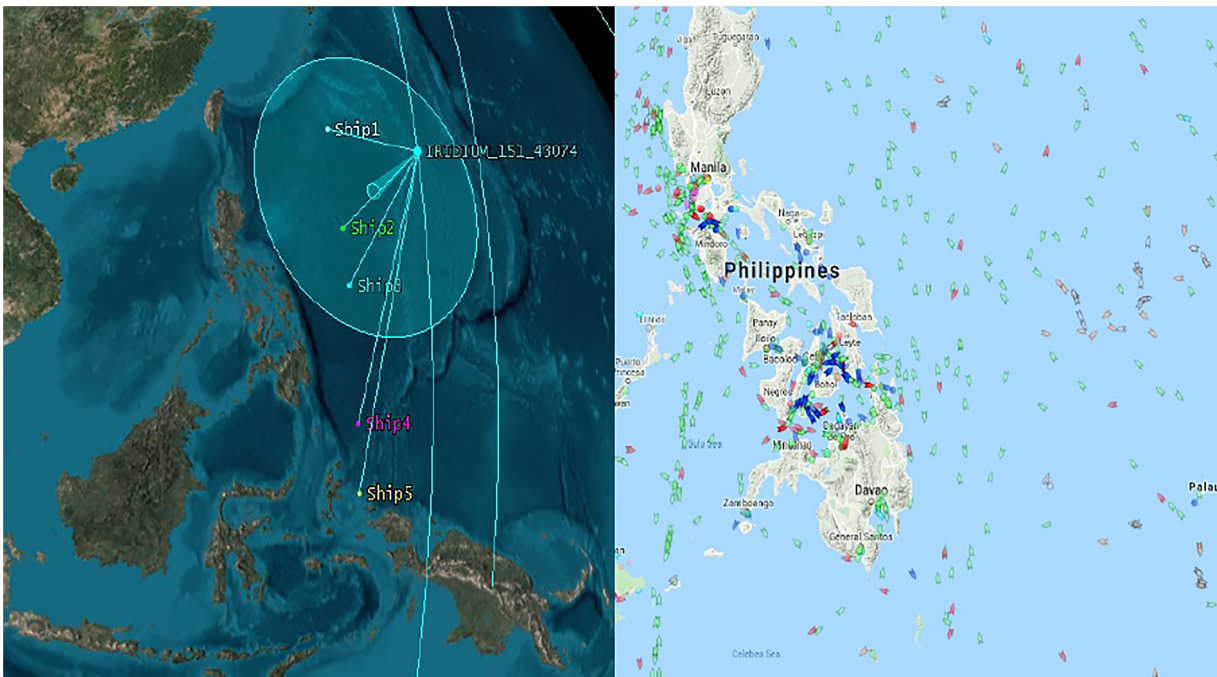


**Figure 12.** (left) The STK scenario for this case study; five ships with coverage from Iridium 151. (right) A map taken from Marine Traffic showing the distribution of ships in the Philippine Sea 20 September 2018 at 11:09 EST.

The shipping route between Australia and Hong Kong Harbour shows an excess of 1.5 million ships per year and is one of the busiest shipping lanes in the world. For these reasons, the Philippine Sea was chosen for this case study.

In the left panel of Figure 12 we show the location of five ships that were used to calculate the access conditions for coverage during the pass of a single Iridium satellite using STK. The right panel of Figure 12 shows the ship traffic in this region for 20 September 2018. When this figure is separated into one degree slices in longitude between Ship 1 at  $0.7^\circ$  and 5 at  $18.8^\circ$ , there are generally between 13 to 53 ships within a reconstruction region of this size.

The number of ships used for the scenarios were varied from 15 to 45, but the positions of ships 1 and 5 (endpoints) remains fixed. This scenario was designed in a similar manner to the scenarios for ADS-B, using STK to compute access geometries and times between the ships and a single satellite from the Iridium NEXT constellation (Iridium 151) for 19 October 2012 from 05:17:49.000 UTCG to 05:34:19.997 UTCG for a pass with mutual coverage of all ships for a duration of  $\sim 7$  min. The small null cone directly under the satellite is a region where signals cannot be received from the ships due to the antenna gain pattern.

In Cushley and Noël (2014) they determined that a minimum of five planes were required to resolve the structures in Figures 7 and 9. With 118 rays per pass for ADS-B and only 40 from AIS, the number of transmitters must be greater for AIS than for ADS-B. In order to have the same number of rays ( $5 \times 118 = 590$ ) for AIS we require at least 15 AIS transmitters to provide similar coverage as ADS-B.

After consulting a number of sources such as Marine Traffic (Figure 12) and assessing the access conditions for ships that are distributed between Ships 1 and 5 (left panel of Figure 12), we simulated 15 ships using the preexisting ray trace model. The cadence for AIS signal transmissions is lower than the cadence for ADS-B so there will be fewer ray paths and as a result fewer STEC measurements available for the reconstruction.

Ships equipped with AIS transmit at a lower cadence (once every minute for AIS compared to  $\sim 0.5$  s for ADS-B) due to the slower speed of ships and other considerations such as less flexible routes since ships are confined to the surface of the Earth. Due to the fact that transmission cadence can vary widely between Class A and Class B ships that are underway and because Class B AIS transponders have lower transmit power and cadence, it was assumed that all ships in this scenario were Class A underway and a value of 10 s

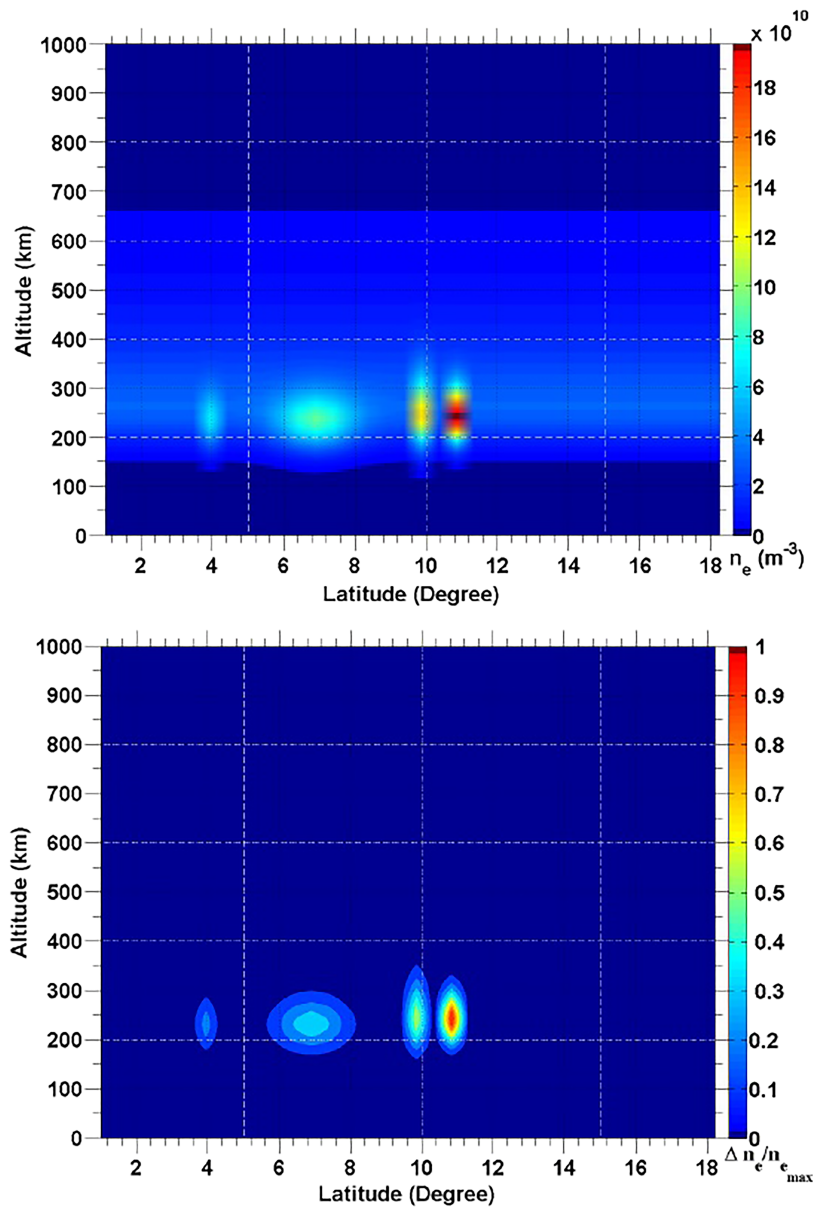
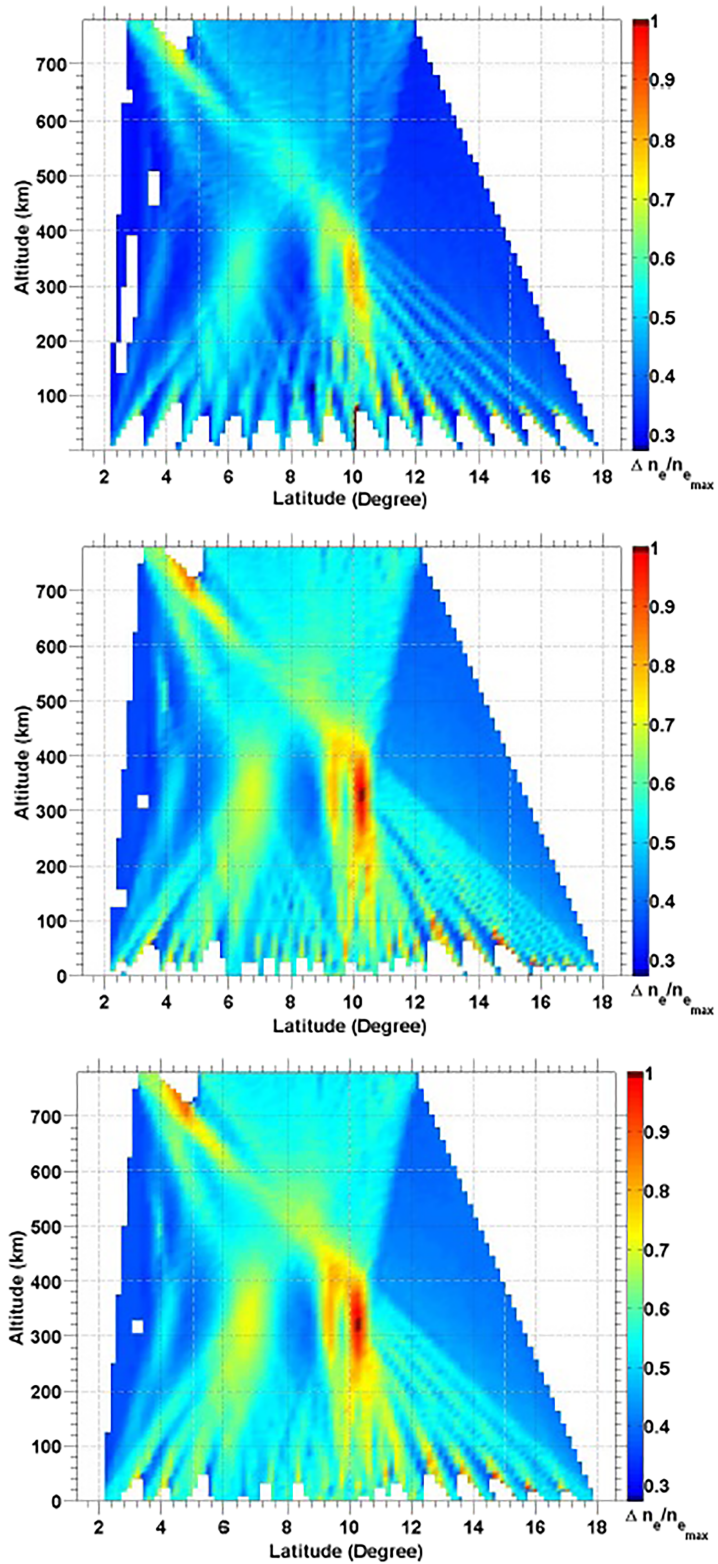


**Figure 13.** (top) Four feature electron density profiles (left to right); latitude = 4°, 7°, 9.75°, 11°; scaling factor = 2.0, 3.0, 4.0, 5.0; full width at half maximum = 0.25°, 1.25°, 0.25°, 0.25°; vertical extent = 60, 60, 90, 60 km; altitude = 250 km. (bottom) Multiple feature electron density profile shown as relative weight. The profile was normalized relative to the peak density.

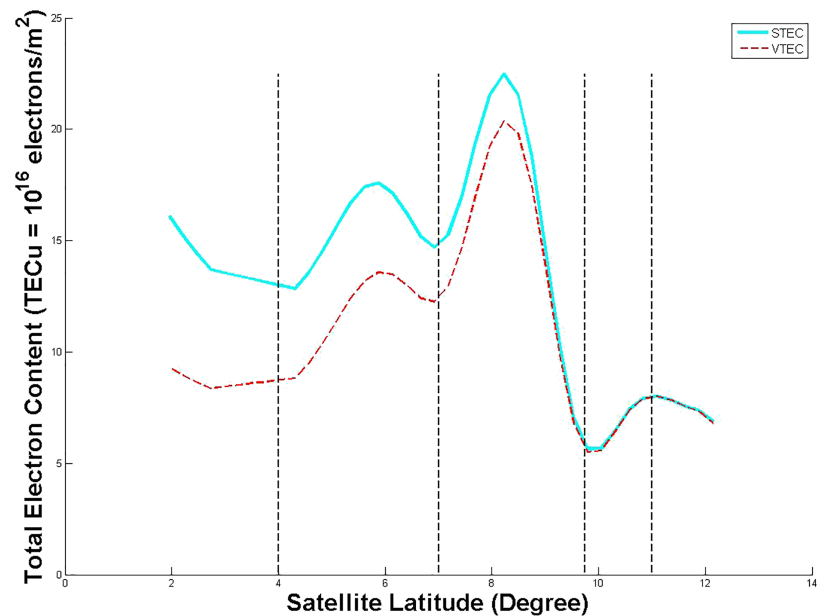
was chosen to be the interval between transmissions. This is essentially the worst case scenario for Class A ships underway. For the scenarios having mutual LOS access to Ships 1 through 5, of 7 min and 4 s (424.4 s) there would be approximately 42 rays from each ship received by the satellite for each pass.

The 2-D IRI profile that was used as an input for this scenario was generated for the corresponding date and time of 19 October 2012 at 05:25 UTCG for the position of Ship 3 at 12.87° latitude and 130°E. longitude. The uniform 2-D profile was then modified by superimposing enhancements using Gaussian distributions centered at 4°, 7°, 9.75°, and 11° latitude with relative amplitudes to the background of 2, 3, 4, and 5 and latitudinal widths of 0.25°, 1.5°, 0.25°, and 0.25° in latitude with a vertical spread of 60, 60, 90, and 60 km, at a peak altitude of 250 km.





**Figure 14.** The raw reconstructed relative electron density maps of the ray trace input shown in Figure 13 using TEC measurements and LOS path for AIS with 15 ships/transmitters (top), 30 ships (middle), and 45 ships (bottom). Regions where there is an absence of data for reconstruction is shown in white.



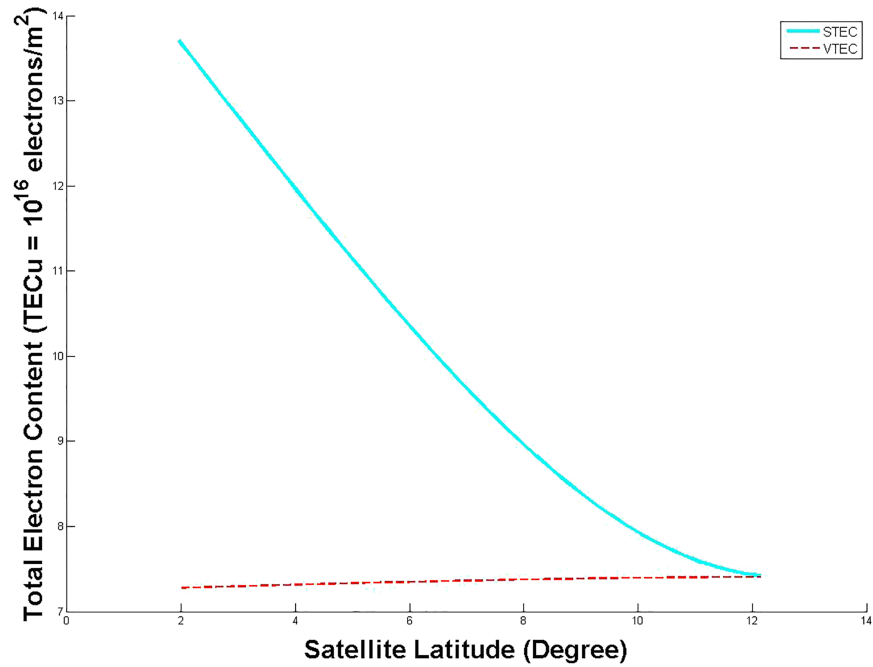
**Figure 15.** STEC and corresponding VTEC (using equation (13)) as a function of latitude obtained from the ray trace model for a ship located at  $11.3^\circ$  latitude and the ionospheric electron density map shown in Figure 13. The locations in terms of latitude of the ionospheric enhancements are denoted by dashed vertical lines.

Figure 14 shows the results for three cases: 15 ships (top panel), 30 ships (middle panel), and 45 ships (lower panel) using access conditions determined from the STK scenario for Figure 12. The top panel of Figure 14 shows the results for a scenario having 15 ships situated equally spaced between Ships 1 and 5. The middle and bottom panels show the reconstruction results using 30 and 45 ships, respectively. Based on Marine Traffic (see Figure 12), 15–45 ships would be a reasonable number of ships to be found in this region on any given day.

In Figure 14 we see an improvement in the reconstructions as the number of transmitters increases (i.e., the number of ships increased from 15 to 45). In each case, the enhancements at  $7^\circ$ ,  $9.75^\circ$ , and  $11^\circ$  latitude are reasonably reproduced. On the other hand, the enhancement at  $4^\circ$  is not quite as obvious. This is not surprising given that it is found on the edge of the reconstruction region, and it has the lowest amplitude. It may be somewhat visible in the top panel of Figure 14 only because we know it is there. It seems to be more visible in the middle and bottom panels but has approximately the same amplitude as the artifacts in the reconstructions. In addition, the original structure is situated at the far left of the reconstructed region and only has rays from transmitters that are located at less than  $\sim 5^\circ$  latitude passing through it. As a result it is not well sampled and few ray paths intersect these pixels to reconstruct the feature. If rays were considered from other ships at lower latitudes than those used in this scenario, the feature may be more defined. The same argument can be made to explain the artifacts below 100 km and the one at  $\sim 5^\circ$  latitude,  $\sim 725$ -km altitude. Few rays intersect these pixels therefore the residual electron density values from each ray are attributed to these pixels to permit the minimization of the error between the integrated values along the path and the STEC value for these rays. Nevertheless, these cases show good relative agreement between the input profile shown in Figure 13 and the reconstructions shown in Figure 14. These results suggest that given a realistic distribution of AIS transmitters, CIT is feasible. From this scenario we can say that a minimum of 30 ships would be required to perform an adequate reconstruction.

### 3.2.1. VTEC Mapping

The previous sections demonstrated that AIS data could be used as input to CIT to reconstruct the electron density distribution. However, even if there is an insufficient number of AIS transmitters to provide enough STEC measurements, measurements from a single ship can be used to map the VTEC from the STEC.



**Figure 16.** STEC and corresponding VTEC (using equation (13)) as a function of latitude obtained from the ray trace model for a ship located at 11.3° latitude and the ionospheric electron density map shown in Figure 5.

The STEC and VTEC are related by the following equation (Langley et al., 2002; Mannucci et al., 1993)

$$VTEC = STEC \times \sqrt{1 - \left( \frac{R_E \cos \alpha}{R_E + h_{max}} \right)^2} \quad (13)$$

where  $\alpha$  is the elevation angle,  $R_E = 6378$  km is the radius of the Earth, and  $h_{max} = 350$  km is the height of the ionospheric shell above the surface of the Earth. The STEC and elevation angle come from the ray trace model output.

The blue trace in Figure 15 represents the STEC as a function of the satellite receiver latitude for a ship located at 11.3° latitude for the ionospheric map shown in Figure 13. We observe three distinct peaks in the STEC, which indicates the presence of at least three enhancements. The peaks do not map directly to the enhancements in Figure 13 (denoted by dashed vertical lines in Figure 15) for several reasons but mainly because the plotted latitude corresponds to the satellite receiver and does not consider where the ray originated from. In addition, STEC is an integrated value over the entire path length so a propagation path at a lower elevation angle will have a longer path length. In comparison a vertical propagation path, would be much shorter and would result in a lower STEC measurement. The dashed red trace in Figure 15 shows the VTEC computed from equation (13) as a function of the satellite receiver latitude. The latitudinal positions of the enhancements are still not correct but are improved both in terms of latitude and relative amplitude.

To improve the alignment of the peaks, a more sophisticated mapping function (see for example ; Rao & Dutt, 2017; Xiang & Gao, 2019) may be required that is more well suited for a LEO orbit. This is beyond the scope of this work since the location of the ionospheric enhancements can be determined using tomography, which uses the STEC, not the VTEC. This would be an important consideration for supplementing VTEC maps. Figure 15 is included only to show how the enhancements are detectable in the STEC (and VTEC) data compared to a horizontally stratified ionosphere.

In contrast, Figure 16 shows the STEC (blue) and VTEC (dashed red) plotted as a function of latitude for a ship at 11.3° latitude for a horizontally stratified ionosphere, without any enhancements (shown in Figure 5). It is clear from this figure that the TEC is minimum at 11.3°, coinciding to the area where the path length is at its minimum. The curve is monotonically increasing and shows no sign of any variation due to enhancements since they are not there.

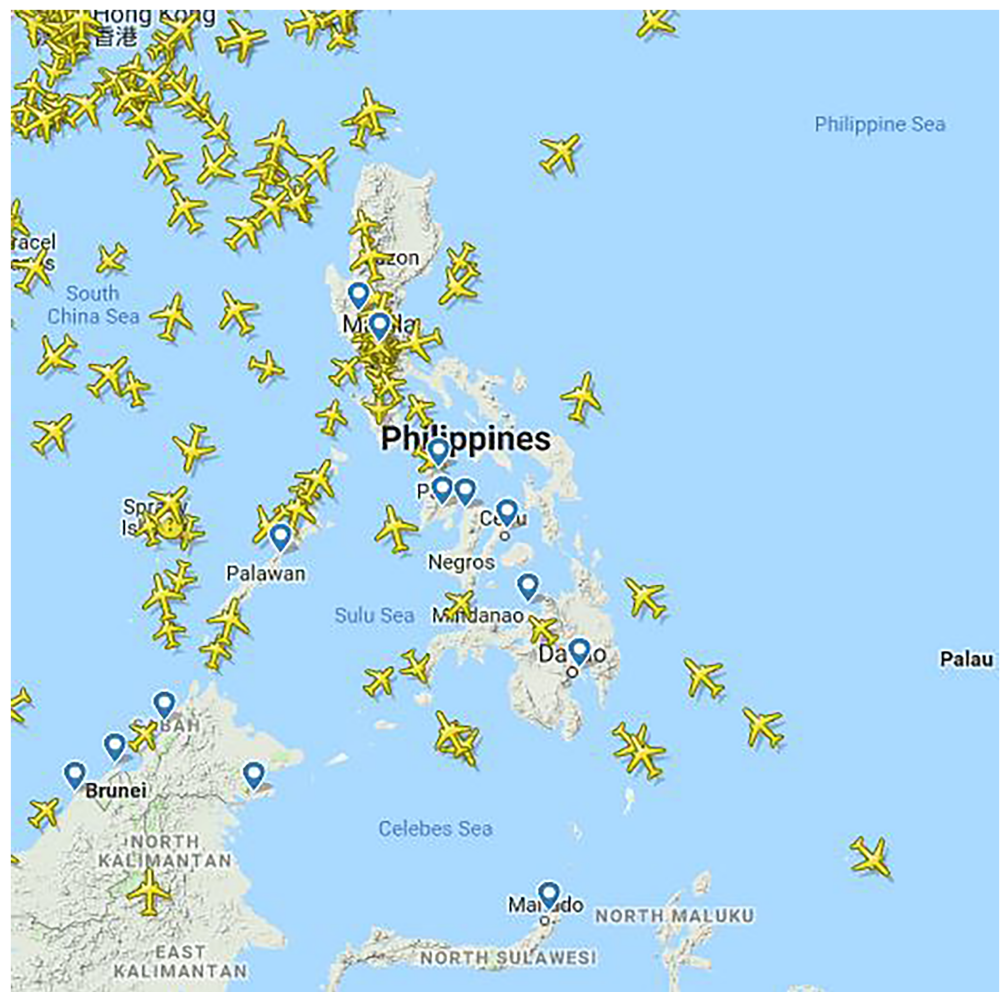


**Figure 17.** A map of the aircraft in the Philippine Sea taken from Flightradar24 29 April 2019 at 4:20 EST.

We conclude that these results demonstrate that AIS data can be useful for supplementing the current GNSS measurements used for VTEC mapping, particularly since there exists gaps in the coverage in oceanic and high-latitude regions, where AIS and ADS-B measurements are available.

### 3.2.2. Comparison of AIS and ADS-B

The next logical step was to compare the reconstructions using AIS signals with ADS-B in the Philippine Sea region. For this comparison, the ADS-B geometry was recalculated using the updated altitude of the Iridium NEXT satellite. In Cushley and Noël (2014) they simulated an ADS-B receiver on a satellite in a 1,000-km circular orbit because there was no actual space-borne ADS-B receiver at that time. However, Iridium NEXT carries both AIS and ADS-B receivers at an orbital altitude of 780 km. For this reason the access conditions for ADS-B was re-evaluated by placing aircraft at the same locations as the ships in Figure 12 and using a pass duration of 424 s (same as for AIS).

The same reconstruction procedure was used for both cases, except to maintain a grid of 100 pixels by 100 pixels, the vertical extent of the pixels was reduced to 7.8 km as opposed to 10 km used for 1,000 km. Unlike GPS CIT where the measured TEC is attributed only to a certain altitude (600 km in some studies, 1,000 or 2,000 km in others) and the contribution above this upper limit of the reconstruction region is neglected, in both the 1,000- and 780-km cases, the STEC measurements are being used to reconstruct up to the altitude of the satellite. This means that the STEC measured at 1,000 km is slightly greater than at 780 km due to the increased number of electrons integrated along the path between 780–1,000 km, but CIT reconstructs the relative density, not the absolute density giving similar results.

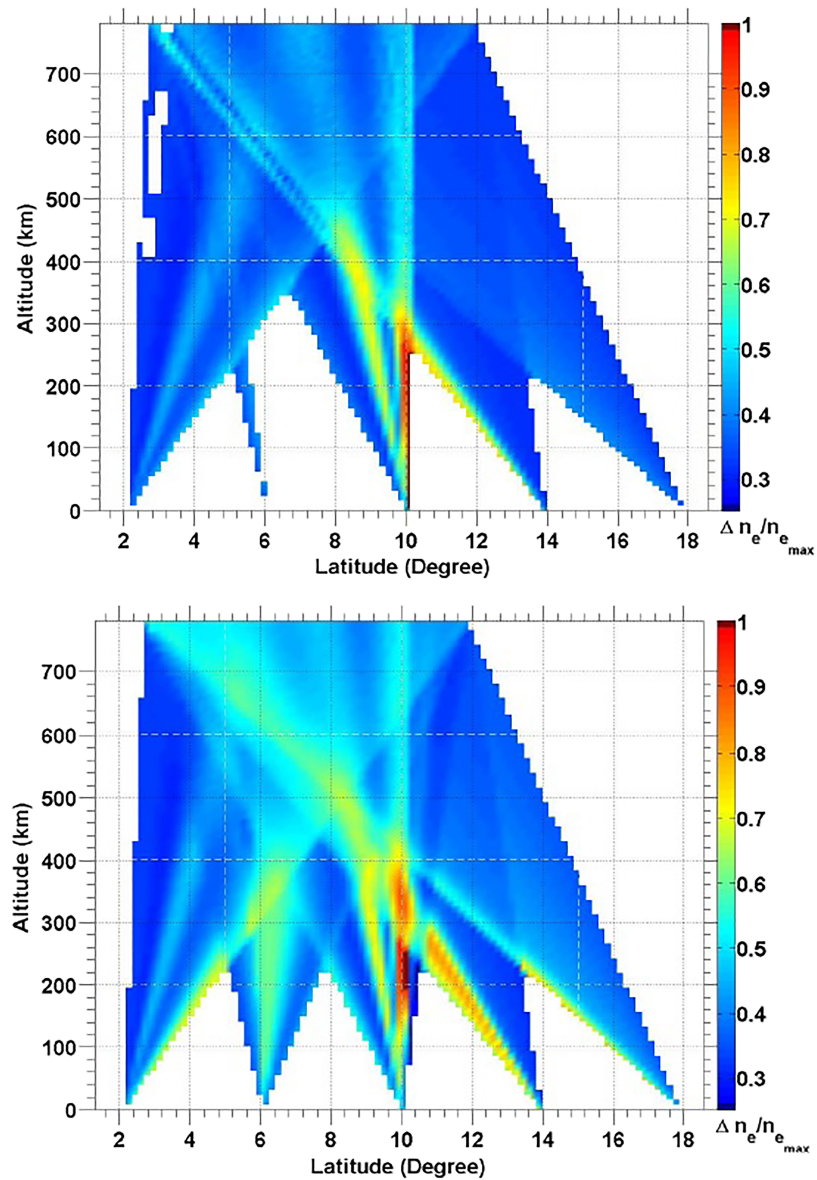


**Figure 18.** (top) Reconstructed relative electron density profile of ray trace input shown in Figure 13 using TEC measurements and LOS path for five ADS-B transmitters with 118 rays transmit per aircraft to a satellite at 1,000-km altitude. (bottom) Reconstructed relative electron density profile of the same ray trace input profile for five ADS-B transmitters with 424 rays transmit per aircraft to a satellite at 780-km altitude. Regions where there is an absence of data for reconstruction is shown in white.

ADS-B is transmitted every 0.4–0.6 s for an average of 0.5-s alternating between top and bottom-mounted quarter wave monopole antennas (Radio Technical Commission for Aeronautics, 2003). Van Der Pryt and Vincent (2016) showed that sea surface reflection and multipath signals should not be received by the receiver therefore only the top mounted antenna signals will be received by the satellite. This implies that a signal will be received approximately every second for a total of 424 signals during a single overhead pass of the satellite for each aircraft.

Using Flightradar24 (Figure 17), a live online air traffic monitor that is similar Marine Traffic, shows that it would be reasonable to assume that at least five aircraft would be within the reconstruction region between 1.3° to 18.8° latitude along a 1° longitudinal slice at 130° longitude. Hence, for this scenario the aircraft were considered to be equally spaced at an interval of 4.375° latitude from 1.3° to 18.8°.

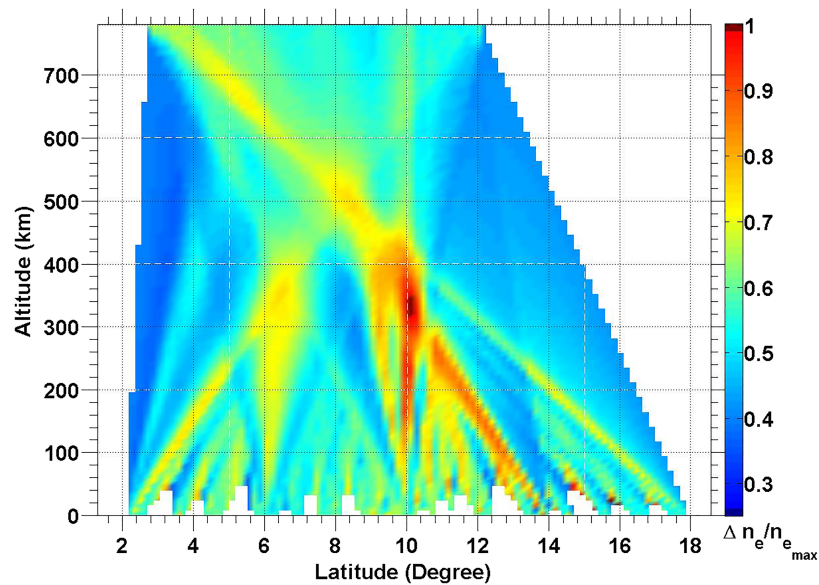


**Figure 19.** The raw reconstructed relative electron density map of the ray trace input shown in Figure 13 using TEC measurements and LOS path for combined AIS and ADS-B data from 45 ships and 5 aircraft, respectively. Regions where there is an absence of data for reconstruction is shown in white.

Figure 18 presents the reconstructions using ADS-B for a satellite orbiting at 1,000 km (top panel) and at 780 km (bottom panel) for five aircraft having the same spatial distribution as the ships in Figure 12. When the satellite is at 1,000 km and each aircraft transmits 118 rays the only discernible features from Figure 13 are enhancements at 10° latitude and ~275-km altitude. We also observe an artifact at ~9° latitude and near 350-km altitude (top panel). Although the satellite used for the reconstruction in the top panel was at a higher altitude and one would reasonably expect a longer pass length and more rays to be available to perform the reconstruction, an overly conservative estimate was used by Cushley and Noël (2014).

The bottom panel of Figure 18 shows the reconstructed electron density for the same five aircraft transmitting 424 rays per aircraft to a satellite at 780-km orbital altitude. The presence of multiple enhancements is more apparent than in the top panel, but they are still not very localized. We note that the overall reconstruction seems to be smoother (using 424 rays compared to 118), but there are broader artifacts between 8° and 14° latitude, below 300 km and above ~450 km, in the bottom panel compared to the top panel. There are also other artifacts below 250 km between 2–6°, 14–16° latitude, and 9° latitude at ~500-km altitude that were not present in the top panel. The feature located at 4° in the input profile (see Figure 13) is not resolved in the top panel of Figure 18 and appears to be situated at ~5° latitude, 225-km altitude in the bottom panel. There is the presence of an artifact at ~6° latitude, 350-km altitude. The enhancement located at 7° in the input profile is also not reproduced in the reconstruction in the top panel of Figure 18 because there are very few rays originating from the transmitters located at ~6° latitude passing through that enhancement, and few, if any rays from the transmitters at ~2° and ~10° latitude. This enhancement is resolved in the bottom panel but artifacts from the feature at 4° and a lack of ray intersections at low altitudes cause it to appear elongated in altitude. The features at 9.75° and 11° latitude in the input profile are resolved in both the top and bottom panel reconstructions, but there are artifacts at ~500 km in the bottom panel. The white pixels representing an absence of data at ~3° latitude, between 400- and 780-km altitude in the top panel have data in the bottom panel, but there is little to no benefit to the overall reconstruction since there are no features or ray intersections in this region. This shows that the sampling resolution of the rays is higher than that of the grid resolution, whereas this was obviously not the case in the top panel or these pixels would have had a minimum of one ray intersection.

From this we note that it is the distribution of the transmitters and not the number of rays transmitted to the satellite over a specified latitudinal range that seems to be the factor that affects the accuracy and ability to resolve the features. This seems to suggest that five well placed transmitter between 5° and 12° latitude

(assuming the feature at 4° latitude will not be detected) may be able to detect the three largest enhancements; however, there would be uncertainty in the location of the enhancements. Without prior knowledge of the locations of the ionospheric enhancements it is virtually impossible to distribute the transmitters judiciously to sufficiently sample the enhancements in order to perform a faithful CIT reconstruction.

### 3.2.3. Concatenating AIS and ADS-B Signals

In addition to comparing individual reconstructions for AIS signals and ADS-B signals as independent sources of TEC data, these two types of signals can also be concatenated with one another. In this case the two data sets (TEC and ray start and end locations) are simply combined using 5 planes and 45 ships.

Figure 19 shows the result of the reconstruction when AIS and ADS-B data are combined. Figure 19 shows an improvement in the reconstruction when compared to using only ADS-B data (see Figure 18) but is arguably worse than using a sufficient number (i.e., 30) of ships AIS signals (see Figure 14). There are more artifacts present in this reconstruction compared to Figure 14. Although the CIT problem remains an underdetermined mathematical problem, there may be redundant or conflicting data in the regions where data are available. The same three out of four enhancements are discernible, but we also note the presence of an increased number of artifacts at lower altitudes seen as little yellow striations between the lower boundary and ~100-km altitude. Artifacts may arise that are associated with diverse methods, operators, and algorithms. The ART algorithm is known cause more artifacts than algorithms such as MART, decomposed algebraic reconstruction technique and Simultaneous Iterative Reconstruction Technique (Kunitsyn & Tereschenko, 2003).

### 3.3. Discussion

In this work, the structures that were detected using CIT were localized electron density “blobs” of magnitudes ranging from 2 to 5 times the background density. It was found that the capability of the CIT technique to reproduce the enhancements deteriorated in regions where there were relatively few transmitters. This was particularly true at high and low altitudes. However, it performed reasonably well in the *F* region of the ionosphere. The lack of accuracy is due to a lack of vertical rays that would provide information about the pixels below ~100 km, the lowest altitude that rays from neighboring receivers will intersect one another. As shown in Figure 14, the reconstruction is improved by increasing the number of transmitters, since the number of rays per pass and number of satellites in orbit remain fixed. More rays leads to more ray intersections which improves sampling and leads to better CIT performance.

The number of intersections in a reconstruction having a specified grid size also increases proportionally to the number of transmitting aircraft, which provides more constraints on the electron density within any given pixel—that is, there are more equations that must be satisfied by a pixel value when the given pixel is intersected by an increasing number of rays. If a pixel is only intersected by a single ray, a value may be attributed to it which helps the reconstruction converge because it is not being modified by any other rays. (i.e., the STEC residual for that ray is deposited in pixels at extremely low and high altitudes to allow the pixel values intersected by other rays to converge and these pixels values are not iterated thereafter). This results in the artifacts that were discussed previously, especially at high and low altitudes, where there are fewer rays intersecting each pixel. Pixels that are not intersected by any ray have no information revealed about them and appear as white pixels in all the reconstructions.

Both of these issues can be resolved by using a priori guess to give these pixels realistic values for the initial iteration or by imposing other constraints such as additional equations that impose smoothness on the electron density field. These elaborations were not considered in this study so that the efficacy of using AIS data in the reconstruction algorithm could be evaluated without biasing the results with additional information.

The grid size could also be modified in order to improve the reconstruction and the resolution. In this study, the grid size was selected to be the same size as in Cushley and Noël (2014) so that the results of this study (Scenarios I and II) could be compared directly. In Cushley (2013) they found that in order to perform a reasonable reconstruction, the grid size had to be small enough so that it did not require days for the ray tracing program to complete its simulations or that the computer would run out of access memory.

Their results were based on ADS-B scenarios using 5 to 25 aircraft with 118 rays per aircraft. The grid size that would maximize the number of intersections and reduce the sparsity of the geometry matrix gave the best result for the reconstructions (Cushley, 2013). It was found that a grid size of 100 by 100 pixels, with each pixel 10 km in altitude and 0.25° in latitude, was sufficient to reduce the size of the matrix to be inverted but

fine enough that it gave a good resolution for the current study. Since the AIS transmitter cadence is lower than ADS-B, with only about one third of the number of rays for each ship during a given satellite pass, the pixel size may need to be increased thereby reducing the grid resolution, facilitating more ray intersections per pixel thus reducing the sparseness of the geometry matrix. Using a larger pixel size would not permit the resolution of small-scale structures since the spatial resolution would be too low.

To increase the number of pixel intersections, the number of transmitters could also be increased. In reality, in situ data will have a large variation in how ships are spatially distributed. According to the results found in this study, sectors with more than 15 ships could be amenable for CIT, although the minimum number of ships required and their spatial distribution was not studied in great detail in the current manuscript. Areas with only one or two ships may only be useful for supplementing VTEC mapping (see section 3.2.1).

To evaluate global AIS data, an algorithm will be required to bin the data into slices of longitude with sufficient ray sampling density to perform the inversion. There are other available on-line AIS tracking services other than MarineTraffic that offer similar visual products that may be useful in characterizing scenarios. For example, ShipView 2.0 by exactEarth captures thousands of open-ocean vessels with positions that are less than 1 min old. Figure 2 shows another type of visual product from MarineTraffic which shows bins containing the number of ships whose last global positions of ships were reported for 11 October 2018 at ~1pm EST. These type of products can be used to help identify areas of interest that are amenable for CIT reconstruction and others that may only be practical for VTEC mapping.

The number of rays available to perform the reconstruction undoubtedly affects the quality of the reconstruction. All of the scenarios presented in this manuscript use relatively few rays when compared to CIT using GNSS data. As a reference, the number of rays that are used in GPS CIT is typically on the order of 4,000 to  $2 \times 10^5$  rays (Choi et al., 2006). For this study, the maximum number of rays expected from the ADS-B and AIS ray geometries is 2,950 rays for 25 aircraft, or 1,800 rays for 45 ships, respectively. In scenario III we saw that at least 15 transmitters is desirable but that there was not any significant improvement in the CIT reconstruction by using 45 transmitters. In conclusion, even if there are hundreds or thousands of transmitters available, 30 well-spaced ships would be sufficient for CIT and, as a result, will reduce the computation complexity and time to perform the reconstruction.

Other aspects that can affect the reconstruction include but not limited to adverse propagation effects (e.g., some refraction at low-elevation angles, or velocity bunching), the geometry of satellite relative to both the ionospheric feature and transmitter, the enhancement scale size and relative amplitude, the satellite pointing accuracy, measurement (e.g., phase, FR, and TEC) noise, and uncertainty and interference introduced to the reconstruction caused by the relative motion between the aircraft and the satellite. By using several satellite receivers the time interval required to collect a given number of ray paths can be reduced. Alternatively, if the time interval remains constant, using more receivers would imply a greater number of ray paths would be collected for the reconstruction.

In the scenarios presented in this manuscript there is a predominantly vertical nature for the rays, potentially due to the constraints imposed of using a single overhead pass with only the ships within the reconstruction region (i.e., there are few if any rays at low-elevation angles from ships beyond the latitudes used for the reconstruction). Rays that originate and terminate within the reconstruction region cannot be horizontal so there is a lack of information about the altitude distribution of the electron content. For the future case of constellation-based data sets, the null regions on each side will be eliminated by concatenating data sets or considering data from transmitters beyond the reconstruction region.

This highlights some of the additional challenges that are imposed by using CT techniques to image the ionosphere that can usually be controlled in other applications of CT. In most applications of CT a precise apparatus is used or constructed to satisfy the requirement of generating equally spaced data, and obtaining a complete data set at the spatial interval or correlation length required. Several physical constraints of the imaging system restrict the quantity of data collected and consequently the quality of the reconstructed image. An ideal tomographic apparatus requires a finite-sized object distribution, densely packed ray paths passing at all possible angles through it, and a dense chain of coplanar receivers (Biswas & Na, 1998; Na & Lee, 1994; Na et al., 1995).

For the typical CIT scenario (e.g., GPS), unlike other applications of CT, a complete set of projection data is not available. A measurement for every sensor position moved in equal increments, whether equiangular



or equidistant, at a fixed distance (or altitude in the case of CIT) is not controlled in the CIT apparatus, as with CT. For example, the nature of a satellite pass where the data is collected in fixed increments of time will not be equidistant, nor equiangular. In CT, an instrument may be built to satisfy these specifications, but in CIT there are a great deal of other restricting considerations. From a tomographic perspective, the restricted viewing angles of the imaging system, combined with irregularity and sparsity of ground-based receiver(s) chain, makes it inherently prone to data insufficiency and the inversion process one of the most challenging examples of limited data tomography (Yeh & Raymond, 1991).

#### 4. Summary and Conclusions

GNSS, AIS, and the ADS-B are signals that exist for very specific purposes; however, they all can be used for ionospheric sounding as well as other geophysical applications such as tsunami detection (Peltier & Hines, 1976; Sanchez-Dulcet et al., 2015; Savastano et al., 2017), earthquake warning (Kelley & Heki, 2017; Fuying et al., 2011; Li et al., 2015; Pulinets, 2004; Pulinets & Boyarchuk, 2005; Xu et al., 2012), tornadoes (Hung, 1978; Nishioka et al., 2013), volcanoes (Larson, 2013), and explosions (Fitzgerald, 1997; Titheridge, 1962). Whether they are mandated and government funded or simply voluntarily constructed and operated, these networks provide data that can be used for both scientific in addition to their original operational purposes. They all rely on space weather data in order to perform their intended tasks (i.e., geospatial positioning, tracking air and marine traffic), but they can also serve as dual purpose payloads.

Given the state of the global economic environment since the global recession of 2008 and the fiscal consequences to scientific research funding both in Canada and abroad, these types of networks with their preexisting hardware offers an innovative alternative to deploying and operating new networks of instruments. Although the data from these networks may have greater uncertainties than scientific instruments that have been specifically designed to measure the electron density and TEC, they can offer supplementary observations in areas that would otherwise lack coverage. This would be particularly useful for data assimilation, modeling, and forecasting in gap regions.

Another advantage of this type of configuration is that mobile ground-based transmitters could be used, which offers more flexibility for deployment than stationary GNSS receivers.

The main objective of this work was to investigate the capability of reconstructing 2-D ionospheric electron density structures using the FR of modeled AIS signals and compare the results with those previously obtained using ADS-B. The work concentrated on modeling the effects of the ionosphere on AIS signals traveling through electron density enhancements localized in space to contribute to current methods of ionospheric electron density mapping in regions without coverage from other instruments.

To this end, using a ray tracing program, the vertically polarized waves that originated from AIS transmitters on ships and computed the expected FR that an orbiting satellite would observe was modeled. The FR was used to infer the *STEC* along the ray path. Using only a LOS ray path (from the transmitter and receiver positions) and the inferred *STEC* values as input, the ART algorithm was used to reconstruct 2-D ionospheric electron density maps.

In order to evaluate AIS signals as a potential source as input data for the CIT technique and be able to compare the results obtained using a lower carrier frequency (than either ADS-B or GNSS) with those obtained by Cushley and Noël (2014) we replicated the two scenarios presented by Cushley and Noël (2014); using 25 AIS-equipped ships as our transmitters and a single satellite acting as the receiver. In these two scenarios, the distribution of the ships, and positions of the satellite were the same as those used by Cushley and Noël (2014). Each ship produced 118 rays for a total of 2,950 rays propagating through the ionosphere from 13° to 18.8° in latitude.

In the first scenario, a single localized electron density enhancement was created as the input for the ray tracing program. The single feature was reconstructed successfully using the LOS ray paths from the transmitter and receiver positions and their associated *STEC*. Although the reconstructed electron density enhancement was still elongated in terms of its vertical extent as was the case in Cushley and Noël (2014), it was somewhat more localized vertically and its latitudinal position agreed reasonably well with the original input structure.

In Scenario II we investigated whether multiple density enhancements could be resolved using AIS. The ship distribution remained the same as the first scenario in this scenario. The input electron density map was

modified with five density enhancements of varying peak density, altitude, latitude and horizontal extent, and fixed vertical extent imposed on the same quiet background as in the first scenario. As was the case in the first scenario, the individual electron density enhancements were detectable and agreed reasonably well with the initial input electron density map.

The third scenario was used to simulate a more realistic spatial distribution of AIS-equipped ships. Based on global ship traffic the Philippine Sea was selected for this case study. The size of the reconstruction region was the same as the first two scenarios with 15–45 ships distributed within that space. Each ship produced 40 rays for a total of 600–1,800 rays crossing the ionosphere from 0.7° to 18.8° in latitude. Four Gaussian distributions of varying peak density, altitude, latitude, and horizontal extent, and fixed vertical extent were superimposed on a horizontally stratified background electron density map obtained from IRI at the middle of the scenario at 12.87° latitude and 130°. Once again, the electron density enhancements were detectable. Three of the four enhancements were conspicuous while the fourth smallest enhancement was less so. It was not as perceptible as the other enhancements owing to the sampling geometry and it had the lowest density enhancement. Overall, the reconstructed electron density map agreed reasonably well with the initial map.

From all the scenarios we note that the position and horizontal extent of the enhancement could be determined with a reasonable degree of accuracy from the raw AIS data and that data from another source would not be required. The reconstructions presented in this manuscript illustrate the feasibility of CIT using AIS data to analyze qualitative phenomena.

These results clearly demonstrate the feasibility of using CIT from AIS data, especially considering the relatively few number of rays that were used to perform the reconstruction. At a bare minimum, AIS may be a useful tool for indicating the approximate location of ionospheric features. This type of information can be used to provide a useful, and economical method to inform further observations using other ground-based assets.

This work has shown the benefit of inverting the traditional CIT models. Rather than the satellite transmitting to ground stations whose positions are restricted and confined to the surface of the Earth, the location of the transmitter(s) and receivers have been exchanged and the CIT apparatus is now inverted. In this inverted scheme, the AIS-equipped ships are the transmitters and the satellite is the receiver. The satellite is also now a LEO satellite which creates a synthetic bank of receivers during the course of a LOS pass. It should be noted that the TEC computed along a given ray path does not depend on the direction of propagation.

In conclusion, the modeled ionospheric electron density features within a given reconstruction region were successfully reconstructed using CIT techniques for AIS and ADS-B. The data used to perform the reconstructions in this study were simulated using theoretical ray trace modeling under different aircraft and ship distributions using their two respective frequencies for AIS and ADS-B. Furthermore, different geometric, geomagnetic, and density conditions were used.

Because real AIS data are not currently available, a meaningful comparison could not be made with other instruments. For this reason a comparison was made with previously simulated ADS-B signal data using the same technique. In the future, a comparison with another instrument such as GPS and using in situ a priori data from another source (e.g., ionosonde) is planned for validation, calibration, and to improve the vertical distribution.

It would be useful to acquire real data for a region where truth data can be used for comparison, validation, and calibration. A region such as Japan's coastal waters would be a good choice in conjunction with Geonet data, the largest and densest network of GNSS receivers. Another option may be to use Topex campaign data over the ocean. A limitation of current receiver systems is that they do not measure polarization. While GPS signals are transmitted with right-hand circular polarization, the same cannot necessarily be said for the signal reaching the antenna, and this difference will contain further information about the propagation path (Benton & Mitchell, 2014). This work shows how the FR of a signal can provide important information about the ionospheric electron content.

The original objective for this work was to evaluate whether the FR of AIS signals could be used to supplement GNSS VTEC maps, so the possibility of doing CIT in order to obtain 2-D and possibly higher dimensional (longitude and time) profiles is a bonus. Numerical modeling has demonstrated that AIS and ADS-B signals are subject to FR as they pass through the ionosphere. Ray tracing techniques were used to determine the characteristics of individual waves, including the wave path and the state of polarization. The

modeled FR was computed and converted to TEC along the ray paths. TEC data can be used as input for CIT in order to reconstruct electron density maps of the ionosphere.

### Acknowledgments

All values and equations used to perform the simulations presented are given in the manuscript. The authors would like to thank the Government of Canada Natural Sciences and Engineering Research Council of Canada (NSERC) [https://doi.org/10.13039/50110000038] (249806) for supporting this research. The electron density values were determined using the IRI model available at [http://omniweb.gsfc.nasa.gov/vitmo/iri\\_vitmo.html](http://omniweb.gsfc.nasa.gov/vitmo/iri_vitmo.html) website, and the values for the geomagnetic field were computed using the IGRF model available online (<https://www.ngdc.noaa.gov/IAGA/vmod/igrf.html>). The authors acknowledge the significant contributions of R. Gillies (University of Saskatchewan) for providing the ray tracing program used to model FR and TEC measurement data used as input for this investigation. We thank DLR who is maintaining the Ionosphere Monitoring and Prediction Center (IMPC) services used to produce global VTEC maps available at <https://impc.dlr.de/products/total-electron-content/forecast-tec/1-h-fc-tec-global/> website. The IMPC is operated by the German Aerospace Center (DLR) at the Neustrelitz location.

### References

- Amos, J. (2012). Ahoy! your ship is being tracked from orbit. *Electronic*.
- Anderson, J. P., Phelps, E. B., Erickson, P. J., Lind, F. D., Coster, A. J., & Langston, G. I. (2011). Characterization of system calibration parameters for high gain dual polarization satellite beacon diagnostics of ionospheric variations. *Radio Science*, 46, RS5017. <https://doi.org/10.1029/2011RS004711>
- Appleton, E. V., & Builder, G. (1933). The ionosphere as a doubly refracting medium. *Proceedings of the Physical Society*, 45, 208.
- Atkinson, C. H., & Soria, J. (2007). Algebraic reconstruction techniques for tomographic particle image velocimetry, *16th Australasian Fluid Mechanics Conference, laboratory for turbulence research in aerospace and combustion Department of Mechanical Engineering*. Crown Plaza, Gold Coast, Australia: Monash University, Victoria, 3800 AUSTRALIA.
- Austen, J., Franke, S., Liu, C., & Yeh, K. (1986). Application of computerized tomography techniques to ionospheric research. In A. Taurainen (Ed.), *URSI and COSPAR International Beacon Satellite Symp. on radio beacon contribution to the study of ionization and dynamics of the ionosphere and to corrections to geodesy and technical workshop* (Vol. 1, pp. 25–35). Oulu, Finland: University of Oulu.
- Benton, C. J., & Mitchell, C. N. (2014). Method to measure the Stokes parameters of GPS signals. *Radio Science*, 49, 7–18. <https://doi.org/10.1002/2013RS005160>
- Bilitza, D. (2007). IRI-2007: Online computation and plotting through IRI-2007web.
- Bilitza, D., McKinnell, L.-A., Reinisch, B., & Fuller-Rowell, T. (2011). The International Reference Ionosphere today and in the future. *Journal of Geodesy*, 85, 909–920.
- Biswas, C., & Na, H. (1998). Three-dimensional computerized ionospheric tomography using volumetric constraints. *Radio Science*, 33(6), 1793–1805.
- Budden, K. G. (1961). *Radio waves in the ionosphere: The mathematical theory of the reflection of radio waves from stratified ionised layers*. UK: Cambridge University Press.
- Campbell, R. (1999). Ionospheric corrections via PIM and real-time data. *New Astronomy Reviews*, 43, 617–199. <https://arxiv.org/abs/astro-ph/9907412>
- Canada Centre For Remote Sensing (2007). Radar polarimetry; advanced radar polarimetry tutorial.
- Chen, F. F. (1984). *Introduction to plasma physics and controlled fusion, Volume 1: Plasma physics* (2nd ed.). New York: Plenum Press.
- Choi, B.-K., Park, J.-U., & Chung, J.-K. (2006). Ionospheric tomography using a regional GPS network over South Korea. *Journal of Global Positioning Systems*, 5(1-2), 47–51. <https://doi.org/10.5194/angeo-31-75-2013>
- Cushley, A. (2013). Ionospheric tomography using Faraday rotation of Automatic Dependent Surveillance Broadcast (UHF) signals. Physics, Royal Military College of Canada.
- Cushley, A. (2015). The potential of using ADS-B and other signals of opportunity in the construction of ionospheric electron density maps.
- Cushley, A., Kabin, K., & Noël, J.-M. A. (2017). Faraday rotation of Automatic Dependent Surveillance Broadcast (ADS-B) signals as a method of ionospheric characterization. *Radio Science*. <https://doi.org/10.1002/2017RS006319>
- Cushley, A., & Noël, J.-M. A. (2014). Ionospheric tomography using (ADS-B) signals. *Radio Science*, 49(7), 549–563. <https://doi.org/10.1002/2013RS005354>
- Cushley, A., Noël, J.-M. A., & Kabin, K. (2017). Faraday rotation, total electron content, and their sensitivity to the average parallel component of the magnetic field. *Radio Science*, 53, 1075–1088. <https://doi.org/10.1029/2018RS006667>
- Dahlgren, H., Perry, G. W., Semeter, J. L., St-Maurice, J.-P., Hosokawa, K., Nicolls, M. J., et al. (2012). Space-time variability of polar cap patches: Direct evidence for internal plasma structuring. *Journal of Geophysical Research*, 117, A09312. <https://doi.org/10.1029/2012JA017961>
- de Selding, P. B. (2105). Harris, exactearth aim to ride iridium next to growth in AIS.
- Dhar, B., Vadher, N. M., & Deshpande, M. R. (1977). An equipment to measure Faraday rotation angle of VHF waves received from a geostationary satellite. *IETE Journal of Research*, 23(12), 708–711. <https://doi.org/10.1080/03772063.1977.11451514>
- Ros, E., Marcaide, J., Guirado, J., Sardón, E., & Shapiro, I. I. (2000). 356, A GPS-based method to model the plasma effects in VLBI observations. *Astronomy & Astrophysics*, 356, 357.
- Elsinga, G., Scarano, F., Wieneke, B., & van Oudheusden, B. (2006). Tomographic particle image velocimetry. *Experiments in Fluids*, 41, 933–947.
- Erickson, W. C., Perley, R. A., Flatters, C., & Kassim, N. E. (2001). Ionospheric corrections for VLA observations using local GPS data. *Astronomy and Astrophysics*, 366(3), 1071–1080.
- exactEarth (2015). exactEarth launches advanced equatorial AIS satellite.
- exactEarth (2016). exactView RT powered by Harris info sheet: Real-time advanced ship tracking solution. Cambridge, Ontario, Canada: exactEarth. Retrieved from <https://cdn2.hubspot.net/hubfs/183611/Landing Page Documents/exactView RT Slick Sheet.pdf>
- Fitzgerald, T. (1997). Observations of total electron content perturbations on GPS signals caused by a ground level explosion. *Journal of Atmospheric and Solar-Terrestrial Physics*, 59(7), 829–834.
- Francis, R., Vincent, R., Noël, J., Tremblay, P., Desjardins, D., Cushley, A., & Wallace, M. (2011). The flying laboratory for the observation of ADS-B signals. *International Journal of Navigation and Observation*, A2, 5. <https://doi.org/10.1155/2011/973656>
- Frissell, N. A., Baker, J. B. H., Ruohoniemi, J. M., Greenwald, R. A., Gerrard, A. J., Miller, E. S., & West, M. L. (2016). Sources and characteristics of medium-scale traveling ionospheric disturbances observed by high-frequency radars in the north american sector. *Journal of Geophysical Research: Space Physics*, 121, 3722–3739. <https://doi.org/10.1002/2015JA022168>
- Fuying, Z., Yun, W., Yiyan, Z., & Jian, L. (2011). A statistical investigation of pre-earthquake ionospheric TEC anomalies. *Geodesy and Geodynamics*, 2(1), 61–65.
- Gillies, R. G. (2006). Modelling of transionospheric HF radio wave propagation for the ISIS II and ePOP satellites (Master's thesis), University of Saskatchewan.
- Gillies, R. (2010). Transionospheric signal modelling for ePOP and SuperDARN (Ph.D. thesis), University of Saskatchewan.
- Gillies, R., Hussey, G., James, H., Sofko, G., & André, D. (2007). Modelling and observation of transionospheric propagation results from ISIS II in preparation for ePOP. *Annales Geophysicae*, 25, 87–97.
- Gillmor, C. S. (1982). Wilhelm Altar, Edward Appleton, and the magneto-ionic theory. *Proceedings of the American Philosophical Society*, 126(5), 395–440.

- Gondarenko, N. A., & Guzdar, P. N. (1999). Gradient-drift instability in high-latitude plasma patches: Ion inertial effects. *Geophysical Research Letters*, *26*, 3345–3348.
- Gondarenko, N. A., & Guzdar, P. N. (2001). Three-dimensional structuring characteristics of high-latitude plasma patches. *Journal of Geophysical Research*, *106*, 24,611–24,620.
- Greidanus, H. (2005). Assessing the operationality of ship detection from space, in *Presented at EURISY symposium new space services for maritime users: The impact of satellite technology on maritime legislation Paris 21-23*. Ispra (VA), Italy: European Commission Joint Research Centre.
- Hackbusch, W. (1994). *Iterative solution of large sparse systems of equations*. New York: Springer-Verlag.
- Haque, J., Altan, H., Malaga, A., Parmet, D., & Tabor, D. (2013). *Systems and methods for receiving aircraft position reports*. FL: US Patent App. 13/316,052 Clearwater.
- Hartmann, G., & Leitinger, R. (1984). Range errors due to ionospheric and tropospheric effects for signal frequencies above 100 MHz. *Bulletin g'eodésique*, *58*, 109–136.
- Hartree, D. R. (1929). The propagation of electromagnetic waves in a stratified medium. *Proceedings of the Cambridge Philosophical Society*, *25*, 97.
- Haselgrove, J. (1963). The Hamiltonian ray path equations. *Journal of Atmospheric and Solar-Terrestrial Physics*, *25*, 397–399.
- Hung, R. J., Phan, T., & Smith, R. E. (1978). Observation of gravity waves during the extreme tornado outbreak of 3 April 1974. *Journal of Atmospheric and Terrestrial Physics*, *40*, 831–843. [https://doi.org/10.1016/0021-9169\(78\)90033-8](https://doi.org/10.1016/0021-9169(78)90033-8)
- Hunsucker, R., & Hargreaves, J. (2003). *The high-latitude ionospheres and its effects on radio propagation*. UK: Cambridge University Press.
- International association of geomagnetism and aeronomy, Working Group V-MOD (2010). International Geomagnetic Reference Field: The eleventh generation. *Geophysical Journal International*, *183*(3), 1216–1230. <https://doi.org/10.1111/j.1365-246X.2010.04804.x>. Participating members: C. C. Finlay, S. Maus, C. D. Beggan, T. N. Bondar, A. Chambodut, T. A. Chernova, A. Chulliat, V. P. Golovkov, B. Hamilton, M. Hamoudi, R. Holme, G. Hulot, W. Kuang, B. Langlais, V. Lesur, F. J. Lowes, H. Luhr, S. Macmillan, M. Mandea, S. McLean, C. Manoj, M. Menvielle, I. Michaelis, N. Olsen, J. Rauberg, M. Rother, T. J. Sabaka, A. Tangborn, L. Toffner-Clausen, E. Thebault, A. W. P. Thomson, I. Wardinski Z. Wei, T. I. Zvereva.
- Jakowski, N., Mayer, C., Hoque, M. M., & Wilken, V. (2011). Total electron content models and their use in ionosphere monitoring. *Radio Science*, *46*(RS0D18), 1–11. <https://doi.org/10.1029/2010RS004620>
- Jehle, M., Rüegg, M., Zuberbühler, L., Small, D., & Meier, E. (2009). Measurement of ionospheric Faraday rotation in simulated and real spaceborne SAR data. *IEEE Transactions on Geoscience and Remote Sensing*, *47*(5), 1512–1523.
- Jin, S., Park, J., Wang, J., Choi, B., & Park, P. (2006). Electron density profiles derived from ground-based GPS observations. *The Journal of Navigation*, *59*(3), 395–401. <https://doi.org/10.1017/S0373463306003821>
- Kak, A., & Slaney, M. (1988). *Principles of computerized tomographic imaging*. University City, Philadelphia.
- Kelley, W. E. S. M. C., & Heki, K. (2017). Apparent ionospheric total electron content variations prior to major earthquakes due to electric fields created by tectonic stresses. *Journal of Geophysical Research: Space Physics*, *122*, 6689–6695. <https://doi.org/10.1002/2016JA023601>
- Klobuchar, J. A., & Liu, C. (1989). *World ionosphere modern total electron content measurement ionosphere/thermosphere study*. Urbana, IL: SCOSTEP Secretariat.
- Kraus, J. (1966). *Radio astronomy*. New York: McGraw Hill.
- Kunitsyn, V. E., Andreeva, E. S., Popov, A. Y., & Razinkov, O. G. (1995). Methods and algorithms of ray radiotomography for ionospheric research. *Annales Geophysicae*, *13*, 1421–1428.
- Kunitsyn, V., & Tereshchenko, E. (2003). *Ionospheric tomography*. Berlin: Springer.
- Kunitsyn, V., Tereshchenko, E. D., Andreeva, E. S., & Razinkov, O. G. (1994). Phase and phase-difference ionospheric radio tomography. *International Journal of Imaging Systems and Technology*, *5*, 128–140.
- Kyovtorov, V., Vespe, M., Fortuny, G., Tarchi, D., Giuliani, R., & Broussolle, J. (2012). Passive automatic identification system for maritime surveillance. Publications Office of the European Union.
- Langley, R., Fedrizzi, M., Paula, E., Santos, M., & Komjathy, A. (2002). Mapping the low latitude ionosphere with GPS. *GPSWorld*, *13*, 41–46.
- Larson, K. M. (2013). A new way to detect volcanic plumes. *Geophysical Research Letters*, *40*, 2657–2660. <https://doi.org/10.1002/grl.50556>
- Li, J., Meng, G., You, X., Zhang, R., Shi, H., & Han, Y. (2015). Ionospheric total electron content disturbance associated with May 12, 2008, Wenchuan earthquake. *Geodesy and Geodynamics*, *6*(2), 126–134. <https://doi.org/10.1016/j.geog.2015.01.003>
- Mannucci, A. J., Wilson, B. D., & Edwards, C. D. (1993). A new method for monitoring the Earth's ionospheric total electron using the GPS global network, in *Proceedings of the institute of navigation GPS-93* (pp. 1323). Alexandria, VA: Inst. of Navig.
- Marine, M. (2018). Frequently asked questions: What kind of information is broadcast for each ship and how often is it updated?
- Max van de Kamp, M. (2012). Medium-scale 4D ionospheric tomography using a dense GPS network. *Annales Geophysicae*, *31*, 75–89. <https://doi.org/10.5194/angeo-31-75-2013>
- Miller, P. (2016). Why are our satellites in low Earth orbit?
- NASA Jet Propulsion Laboratory California Institute of Technology (2014). Real-time ionospheric maps. Website.
- Na, H., Hall, B., & Sutton, E. (1995). Ground station spacing effects in ionospheric tomography. *Annales Geophysicae*, *13*(12), 1288–1296.
- Na, H., & Lee, H. (1994). Resolution degradation parameters of ionospheric tomography. *Radio Science*, *29*(1), 115–125.
- Nishioka, M., Tsugawa, T., Kubota, M., & Ishii, M. (2013). Concentric waves and short-period oscillations observed in the ionosphere after the 2013 Moore EF5 tornado. *Geophysical Research Letters*, *40*, 5581–5586. <https://doi.org/10.1002/2013GL057963>
- Orfanidis, S. J. (2008). *Electromagnetic waves and antennas*, pp. 8854–8058. NJ: Rutgers University, 94 Brett Road Piscataway.
- Parsons, G., Youden, J., & Fowler, C. (2013). Satellite Automatic Identification System (SAIS) performance modelling and simulation (*Tech. rep.*) Ottawa, ON.
- Peltier, W. R., & Hines, C. O. (1976). On the possible detection of tsunamis by a monitoring of the ionosphere. *Journal of Geophysical Research*, *81*(12), 1995–2000.
- Pulinets, S. (2004). Ionospheric precursors of earthquakes; recent advances in theory and practical applications. *Terrestrial, Atmospheric and Oceanic sciences journal*, *15*(3), 413–435.
- Pulinets, S., & Boyarchuk, K. (2005). *Ionospheric precursors of earthquakes* (Vol. XIII, pp. 315). Berlin Heidelberg: Springer-Verlag. <https://doi.org/10.1007/b137616>
- Radio Technical Commission for Aeronautics (2003). (DO-260) minimum operational performance standards for 1090 MHz Extended Squitter Automatic Dependent Surveillance- Broadcast (ADS-B) and Traffic Information Services -Broadcast (TIS-B).
- Rao, K. D., & Dutt, V. S. I. (2017). An assessment of mapping functions for VTEC estimation using measurements of low latitude dual frequency GPS receiver. *International Journal of Applied Engineering Research*, *12*(4), 422–427.

- Rogers, N. C., & Quegan, S. (2014). The accuracy of Faraday rotation estimation in satellite synthetic aperture radar images. *IEEE Transactions on geoscience and remote sensing*, *52*(8), 4799–807.
- Ruzmaikin, A., & Sokoloff, D. (1979). The calculation of faraday rotation measure of cosmic radio sources. *Astronomy & Astrophysics*, *78*, 1–6.
- Sanchez-Dulcet, F., Rodríguez-Bouza, M., Silva, H., Herraiz, M., Bezzeghoud, M., & Biagi, P. (2015). Analysis of observations backing up the existence of VLF and ionospheric TEC anomalies before the Mw6.1 earthquake in Greece, January 26, 2014. *Physics and Chemistry of the Earth Parts A/B/C*, *85*, 150–166. <https://doi.org/10.1016/j.pce.2015.07.002>
- Savastano, G., Komjathy, A., Verkhoglyadova, O., Mazzoni, A., Crespi, M., Wei, Y., & Mannucci, A. J. (2017). Real-time detection of tsunami ionospheric disturbances with a stand-alone GNSS receiver: A preliminary feasibility demonstration. *Scientific Reports*, *7*, 46607.
- Schunk, R. W., & Nagy, A. F. (2000). *Ionospheres. Physics, plasma physics, and chemistry*. Cambridge, United Kingdom: Cambridge atmospheric and space science series, Cambridge University Press.
- Soicher, H., & Gorman, F. (2012). Seasonal and day-to-day variability of total electron content and mid-latitudes near solar maximum. *Radio Science*, *20*, 383–387. <https://doi.org/10.1029/RS020i003p00383>
- Sotomayor-Beltran, C., Sobey, C., Hessels, J. W. T., de Bruyn, G., Noutsos, A., Alexov, A., et al. (2013). Calibrating high-precision Faraday rotation measurements for LOFAR and the next generation of low-frequency radio telescopes. *Astronomy & Astrophysics*, *552*, A58. <https://doi.org/10.1051/0004-6361/201220728>
- Tessa, V. H., Sarah, W., Maggie, G., Joost, B. K., & Jan, S. (2007). The implementation of iterative reconstruction algorithms in MatLab. iterative Reconstruction Algorithms.
- The International Telecommunications Union (1998). Recommendation ITU-R M 1371 technical characteristics for a universal shipborne Automatic Identification System using time division multiplex access in the vhf maritime mobile band, The ITU Radiocommunication Assembly.
- The International Telecommunications Union, Ionospheric propagation data and prediction method required for the design of satellite services and systems (2003). Recommendation ITU-R P.531-7. The ITU Radiocommunication Assembly.
- Tikhonov, A., & Arsenin, V. (1977). *Solutions of ill-posed problems*. New York: Wiley.
- Tikhonov, A., & Goncharsky, A. (1987). *Ill-posed problems in the natural sciences*. Moscow: MIR.
- Titheridge, J. E. (1962). Variations in the total electron content of the ionosphere after the high-altitude nuclear explosion. *New Zealand Journal of Geology and Geophysics*, *5*(6), 1003–1008. <https://doi.org/10.1080/00288306.1962.10420056>
- Van Der Pryt, R., & Vincent, R. (2016). A simulation of reflected ADS-B signals over the North Atlantic for a spaceborne receiver. *Positioning*, *7*, 51–62.
- Wahi, R., Dubey, S., & Gwal, A. K. (2005). Ionospheric total electron content measurement in Malaysian region during high solar activity using GPS receiver. *Indian Journal of Radio and Space Physics*, *34*, 399–401.
- Xiang, Y., & Gao, Y. (2019). An enhanced mapping function with ionospheric varying height. *Remote Sensing*, *11*, 1497. <https://doi.org/10.3390/rs11121497>
- Xu, T.-L., Jin, H., & Guo, P. (2012). Preliminary analysis of ionospheric anomaly preceding the great east japan earthquake. *Earthquake*, *32*(4), 131–139.
- Yeh, K., & Raymond, T. (1991). Limitations of ionospheric imaging by tomography. *Radio Science*, *26*, 136–1380.
- Yueh, S. (1999). Estimates of Faraday rotation with passive microwave polarimetry for micro-wave remote sensing of Earth surfaces. Jet Propulsion Laboratory, California Institute of Technology.
- Zhao, B., Wan, W., Liu, L., & Ren, Z. (2009). Characteristics of the ionospheric total electron content of the equatorial ionization anomaly in the Asian-Australian region during 1996-2004. *Annales Geophysicae*, *27*, 3861–3873.

## Conclusions and Future Work

### 8.1 Overview

This chapter summarizes the main results from the thesis and proposes additional work that could be undertaken in the future.

### 8.2 Summary

The ionosphere is driven primarily by solar and geomagnetic activity. There exists a strong coupling between the physical processes on the Sun and the Earth's ionosphere. The state of the ionosphere is characterized by a wide range of empirical and physics-based models as well as remote and in-situ observations. However, observations at high latitudes and oceanic regions are sparse, and models do not always represent the high latitude and polar regions well due to the complex nature of the region. High latitude dynamics in turn, can drive geospace dynamics at other latitudes. As a consequence, additional regular high latitude observations are particularly important for improving our understanding of Earth's open magnetic-field regions, particularly for Canada [*Semeter*, 2015].

Accurate forecasting of space weather conditions in the near-Earth space environment is essential to protect the electronics and inhabitants of Earth, aircrew and passengers on trans-polar flights, spacecrew as well as orbiting spacecraft. Northern Polar routes have been used more often since the beginning of the 21st Century due to the fuel and time savings. Unfortunately this region is highly active in a geomagnetic sense, making those travellers susceptible to receiving significant radiation doses [*Lewis et al.*, 2001; *Perron*, 2014].

Measurements of the electron content are needed in order to better understand the basic atmospheric and ionospheric structures, time constants of physical and chemical processes, and other pertinent properties of the atmosphere and ionosphere such as

the energetics of the ionosphere. This data can be used to analyse the sensitivity of the ionosphere to various physical and/or chemical processes [De *et al.*, 1988]. The IEDs which can be inferred using GPS CIT among other methods, plays a critical role in understanding phenomena such as hemispheric conjugacy in addition to more practical applications oriented towards safeguarding technological assets e.g. the power grid, telecommunications as well as space-based assets.

Observations of the upper atmosphere using networked instrumentation allow multiple locations to be monitored simultaneously in order to capture the system dynamics on a global-scale. When these networks are established for an extended period of time, the data may be examined for temporal variations as well as being available for stochastic events such as large solar disturbances, which are less likely to be measured in a short-term campaign. In aeronomy and magnetospheric sciences, such networks provide the insight and validation required to understand global-scale processes such as travelling ionospheric disturbances (TIDs), the transport of energy during storm periods, vertical coupling between different atmospheric regions, along with associated global-scale variability. These scientific advancements in terms of magneto-ionic theory are enabled by observations of large-scale processes. Therefore new observational networks to provide data to the modelling community are important types of input so that they can improve their research and help constrain their numerical models [Bhatt, 2014].

CIT is a powerful tool for producing images of the electron density distribution in the ionosphere as a function of latitude and altitude in 2D. Reconstructions are based on measured signals of integrated parameters over many directions between satellites and traditionally ground receiving stations. Although tomography is a relatively new technique applied to space physics and the ionosphere [Austen *et al.*, 1986] it has been successfully applied to monitor radio transmission from GPS and has shown great promise as a relatively low-cost alternative to many ground-based instruments such as vertical sounding ionosondes and ISR.

The study of the ionosphere by means of satellite radio tomography has several other advantages to ground based instrumentation. Generally, tomography is inex-

pensive, if the cost of the constellation of receiving satellites can be neglected. The satellites operational purpose in the case of GPS and ADS-B is navigation, thus the cost of the satellite for CIT can be neglected when no further requirement to the satellite design is required to perform its main objective. For ADS-B specifically, the goal is to demonstrate enhanced flight safety globally. Phase measurements are redundant for ATC and as a space weather instrument it would simply be the additional cost of computers to perform the CIT that would be required. This cost could be considered negligible when compared to the financial and environmental costs of setting up, operating, and maintaining an ISR, even at mid latitudes.

With the potential viability of global CIT using Iridium NEXT for the additional capability of monitoring global ship and air traffic, CIT is a scientifically, economically, and environmentally practical architecture for IED mapping. This method is considered to be far less expensive than other instruments deployed on a global scale, given the ADS-B receiver is primarily designed as a flight safety system and the science is an added bonus. Accurate orbit determination and pointing is already essential for the primary mission, particularly for characterizing the signal strength and phase for anti-spoofing and other undesirable effects e.g. sea-surface reflection, multi-path duplicate signals. It is also very important for tomography.

The goal of this thesis was to investigate the feasibility of ionospheric sounding using signals of opportunity namely ADS-B and AIS. The modelled ionospheric electron densities within a given region was successfully reconstructed using CIT techniques and synthetic data. The data was simulated using theoretical modelling under a variety of geometric, geomagnetic, and density conditions using a pre-existing ray-tracing program. The ray-trace code was used to produce synthetic data that was used as input to the ART pixel-based method of CT, which in turn was used to reconstruct electron density maps. The reconstructions were compared to the corresponding original input  $n_e$  profile to study the effectiveness of the reconstruction. It was found that the reconstructions showed good relative agreement thereby indicating the potential of CIT using ADS-B and AIS data.

Two other topics that support CIT research were also discussed: improvements



to the estimate of STEC from FR which is used as an input to CIT, and a method to generate ionospheric profiles from ionospheric parameters which can be used as an *a priori* estimate for the first iteration of the reconstruction procedure.

The novelty of the CIT techniques discussed in Chapters 4 and 7, aside from using the FR of the new signals to obtain TEC data, is that the process is considered to be inverted. In this thesis the sources are ground-based while the receiver is in space. This is in contrast of having constellations of satellite transmitters and ground-based receivers in regions where it is convenient due to existing infrastructure and a moderate climate as it is currently done. We essentially have relatively unconstrained transmitters on land, air and sea being used in conjunction with a constellation of satellite receivers in order to achieve true global coverage.

The proposed networks must have a sufficiently high number of transmitters, high transmission rates and as a result a high ray density to be considered for use with individual satellites. Eventually a constellation with global coverage can be used, from which CIT at higher dimensions and/or possibly higher resolution may be realized. This was not possible when this work started because an ADS-B concept demonstrator had yet to be launched while AIS satellites were not launched until 2015, and finally the Iridium NEXT constellation was not completed until February of 2019.

CIT using ADS-B and AIS signals received by Iridium NEXT constellation satellites data could give global reconstruction to a more accurate degree in some remote regions, while potentially providing reconstructions of all regions on a greater temporal scale than current methods due to constant monitoring. Temporal constraints will occur because of how the users store the data in time, or for sparse air traffic, the integration dwell time to collect the minimum data for the quality of the reconstruction required.

The orbit of a LEO satellite, with a shorter LOS access time compared to higher altitude orbits could be appropriate for imaging structures that evolve on shorter time-scales, especially for a constellation of satellites with polar convergence. Particular scientific benefits may be realized by using data obtained over shorter time-scales

in order to observe and study events that may not be observable over longer time intervals. For example, a rocket passing through the ionosphere may cause a depletion from the rocket exhaust. By using data over shorter time intervals, the event may be observed over consecutive reconstructions to obtain a better understanding of how the ionosphere responds compared to a single point measurement in time.

GPS CIT does not reconstruct the full region through which the signals propagate. GPS methods tend to neglect a significant region between the satellite and what they assume is the upper extent of the ionosphere. They assume that the electron density above  $\sim 2000$  km does not contribute significantly to the TEC. This introduces a systematic uncertainty when integrating the TEC from the GPS satellite altitude (20 200 km) and reconstructing the ionospheric electron density at altitudes below 1000 km from the data. In other words there is a systematic overestimation of the TEC in the area of interest. While using a cut off below 60 km is acceptable since the troposphere is considered not to contribute significantly to the TEC measurement, the common upper altitude cut-off at 800 km should not be neglected. In reality, the plasmasphere may contribute significantly to the TEC. If the plasmaspheric content was considered in the TEC data, there is the added step of removing the plasmaspheric electron content presumably by using numerical models. This type of correction introduces an additional source of uncertainty to the data and the resulting reconstruction as a consequence. This is not the case for CIT using LEO satellites, which measures and reconstructs TEC from the transmitter to the receiver at 780 km altitude.

This work largely neglects the equatorial ionosphere due to the existence of numerous types of sensors that may be deployed and the relative wealth of knowledge regarding the equatorial and low-latitude ionosphere. It is more challenging to deploy equipment at higher latitudes, like the polar caps or oceanic regions due to the lack of infrastructure, maintenance personnel, harsh conditions and/or for lack of a stable platform (e.g. an ISR deployed aboard a ship). Another reason it was neglected is that the Earth's magnetic field is also largely horizontal and while many unique and interesting phenomena occur at equatorial regions, the lack of a strong parallel component of the magnetic field does not make this region amenable to making ob-

servations of FR. For a signal transmitted vertically, the geomagnetic field becomes increasingly aligned with increasing latitude, which makes measurement of the TEC using FR most conducive at higher latitudes.

The main focus of this work was advancing the understanding of magneto-ionic wave propagation and investigating the feasibility of various pre-existing networks for ionospheric sounding measurements and data assimilation, in the high latitude  $F$ -region. The benefits of this work is two-fold. Firstly, the results will benefit those studying space physics, primarily the near-Earth space-environment. Secondly, the direct application of improved methods for global electron density mapping may improve electronic communications and navigation for satellites as well as ground-based HF and GPS positioning.

Accurately mapping the electron density structures using a new source of data will supplement current methods of characterizing and modelling of the ionosphere. Two dimensional maps give a much better representation of the ionosphere for numerical models than simple vertical profiles. The broader aim of this research was to develop a novel technique to remote sense the ionosphere in order to obtain a better understanding of the physics of the near-Earth space environment and the mechanisms of the Sun-Earth system.

### 8.3 Key Findings

Of the numerous features that were reconstructed over the course of this thesis, the majority were identifiable in the numerical reconstructions. The visibility of these features varied as a function of the transmitter density that were simulated, the size of the reconstruction grid and the location of the ionospheric electron density features.

All ionospheric features observed during the analysis are displayed as either a relatively bright or dark feature on the corresponding colour-scale. The visibility of a feature, or a combination of enhancements and depletions in the reconstructed ionospheric electron densities agreed well with the initial electron density profiles. The reconstructions showed that using only the STEC and no *a priori* estimate, the presence of electron density enhancements or depletions were discernible. The

resulting electron density structures were located near their initial location. The results demonstrated the capability of ADS-B and AIS signals in CIT to highlight regions of interest.

Small to medium (25 km to 2000 km) features with relatively large magnitude relative to a quiet background within the reconstruction region were more likely to be observed due to steeper gradients in the electron densities [Marcio T.A.H. Muella *et al.*, 2011]. Gradients are important in images of any kind [Elachi and van Zyl, 2006]. For example, white (or even ivory or yellow) text and diagrams printed on white paper does not convey much information, while black text creates the steepest gradient and clearly conveys the information. Furthermore, larger spatial features were intersected by many rays, independent of elevation angle and as a result had less variation in the TEC output.

Results also showed that the features were masked at low altitudes ( $< 200$  km) because the  $F$ -region contributes much more to the TEC measurement, which is an integrated value and therefore smooths out lower amplitude ( $D$ - and  $E$ -region) features along the path. One way to fill the gaps in coverage below 200 km is to increase the transmitter density. By increasing the number of transmitters, the coverage below 200 km is increased to fill the gaps, but this may not matter since the CIT technique works best for the  $F$ -region.

From the results, the transmitter density was found to be the most important factor that contributed to the visibility of the features. The accuracy of the inversion process increased with the number of available measurements on crossing paths. This indicated that it is beneficial to use as many transmitters and satellite receivers as possible [Max van de Kamp, 2012]. Using these types of signals of opportunity for CIT is advantageous compared to other types such as GPS since it may not be feasible to deploy an increasing number of ground based receiving stations. It was observed that the results over the course of this thesis agreed well with the published results of other researchers as discussed in section 3.4.4.3 of Chapter 3.

Although the absolute electron density could not be confirmed, the reconstructions showed good relative agreement with their respective initial profiles input to the ray

trace program. There is in fact an overestimation of error when collecting data over a short period in comparison with an empirical model such as the Chapman or IRI models. CIT using signals of opportunity from a single satellite would enable the study on time-scales which are much shorter and are not empirically modelled. Quantitative prediction may not be reliable from a standard model run, regardless of the model. Real data integration techniques are required for more reliable predictions [Anderson *et al.*, 1998].

Most of the work that refer to LEO satellites in the context of CIT dismiss the possibility due to the large number of ground based receivers required in the GPS ground based paradigm. This would indeed prove inefficient, uneconomical and not practical. Andreeva *et al.* [2001], and many other independent investigations found the geometry too narrow for adequate resolution of features given the confinement of a limited number of ground-based receivers. Other literature sources that use LEO satellites for CIT consider only occulting rays to other LEO satellites, or the LEO satellites functioning as mobile GPS receivers. This approach neglects the electron content below the LEO satellites altitude.

Contrary to many literature sources, Cushley [2013]; Cushley and Noël [2014] and a paper accepted by Radio Science in December 2019 found that LEO satellites are useful for CIT for regions having a similar size used for CIT by GPS. By inverting the geometry with many transmitters below the ionosphere and using space-borne receiver(s) travelling at large relative velocity, a synthetic bank of receivers along the orbital plane is formed. The inverted model permits sufficient rays but it required *a priori* vertical distribution of the electron density like GPS.

Although CIT using LEO satellites may suffer from a reduction in vertical resolution the optimization of the number of sampling paths outweigh these other cons, hopefully revolutionizing the concept of CIT and satellite design possibilities for secondary purposes.

This work has also shown that the ray-trace model is a useful tool for generating CT input. In-situ data does not permit the same medium to be imaged by different sampling geometries, or different mediums to be imaged by the identical geometry

due to the ever-changing ionosphere. Ray trace output allowed for parameters to be controlled in a variety of fashions, with the opportunity to try different sampling geometries for the same medium, and different mediums for the same geometries. The only way this could be conducted with in-situ data is using sub-sets of large datasets.

### 8.3.1 Summary of Important Results

To briefly summarize, the reconstruction results that were presented in Chapters 4 and 7 are improved with:

- Mesoscale electron density structures can be reconstructed.
- An increase in transmitter density and consequential increase in the number of rays used;
- A grid which optimizes intersections and reduces the sparsity of the geometry matrix;
- Structures having scale sizes larger than the grid resolution, but much smaller than the width of reconstruction region;
- Steep gradients in the features, and larger variations in TEC for reconstruction;
- A wide range of elevation angles and slant ranges;

The work presented in Chapter 5 showed how a relatively simple model can be used to characterize the ionosphere using three tunable parameters that can be adjusted to produce electron density profiles that agree with FR and TEC measurements simultaneously. These could be used as various *a priori* estimates for the first iteration of CIT. These estimates would be based on data rather than electron density models, which could provide an improved representation of the ionosphere especially during ionospheric disturbances.

The work presented in Chapter 6 showed how sensitive the conversion of TEC to FR and vice versa is to different characteristic values for the average magnetic field along the path. The previous assumption that an average value may be used to remove

$B$  from inside the integral in Eqn. 2.11 may have led to results that were sufficient for earlier applications such as estimation of FR fading of signals, but a method to improve the calculation for the average value for the magnetic field along a signal path is needed for modern applications such as CIT or precision SAR image correction. The method presented in the paper can be used to more accurately determine the TEC along a path from FR measurements and produce more accurate TEC input for the reconstruction procedure.

In summary, the thesis results supports using signals of opportunity for ionospheric sounding, which will have economical and environmental benefits. This work demonstrates that signals of opportunity can be used for the purpose of ionospheric sounding and characterization in addition to their original intended purpose of monitoring air space and marine traffic.

## 8.4 Future Work

As stated earlier, the main focus of this work was to use available signals of opportunity such as ADS-B, AIS, and HAM radio signals like APRS to supplement VTEC mapping, CIT and improve ionospheric characterization. The future work ultimately aims to fuse information extracted from IRI, ionosondes, radars, or any other methods to compare with independent static and dynamic information acquired from signals of opportunity in order to characterize IED on a large scale in 4D (latitude, longitude, altitude, and time) in an automated manner. There is a great deal of work to be done in order to accomplish this; too much to be described in any great detail here.

Preliminary studies were undertaken and have yet to be published. Some of the areas of research have been de-prioritized either because they were computationally intensive and not required for current studies or only provided marginal benefits. Two examples include: the 3D CIT (see Fig. 8.1) and improvements to the geometry matrix by considering the length of a ray passing through a given pixel relative to other pixels.

The most basic form of the geometry matrix is a logical matrix and it was discussed in section 3.4. The elements of the logical geometry matrix are one if a ray contributes

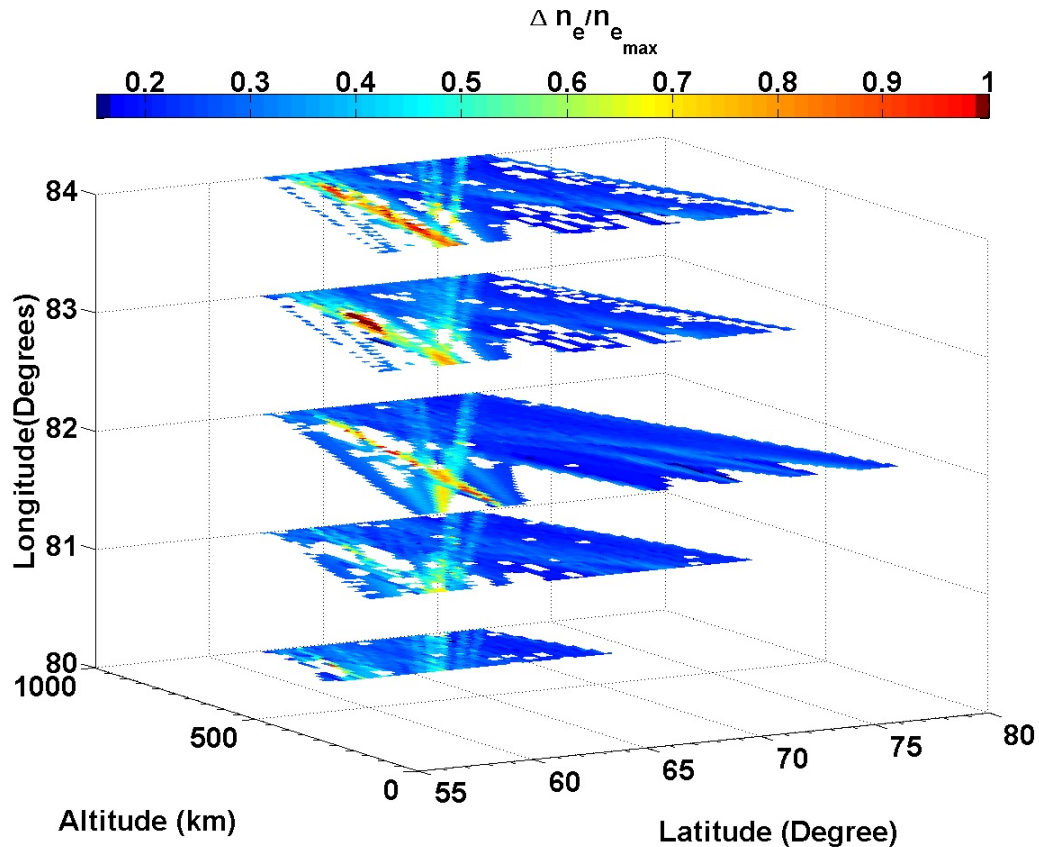


Figure 8.1: 3D reconstruction in slices of longitude.

to a given pixel, and zero otherwise. This does not account for the degree which a particular ray contributes to the pixel value relative to another pixel for a ray intersecting the pixels shown in Fig. 8.2. Using a logical index the red ray illuminated pixels 2, 3, and 4 and each of them were assigned a value of 1. Pixel 1 was assigned a value of 0. It is obvious from this figure that the contribution to the STEC of the ray are not equal. It is greatest for pixel 2 and least from pixel 4 but in our current work they were considered to be equal.

Following the initial success with the ART algorithm in *Cushley* [2013]; *Cushley and Noël* [2014] it was used to maintain a direct comparison for the research presented in Chapter 7. In the future, different reconstruction algorithms will be used to evaluate their respective benefits and shortcomings, both qualitatively and quantitatively. For example, MART has been shown in other applications to be preferable to that of additive ART which leaves artefacts or tracer in the reconstructed field [*Atkinson*



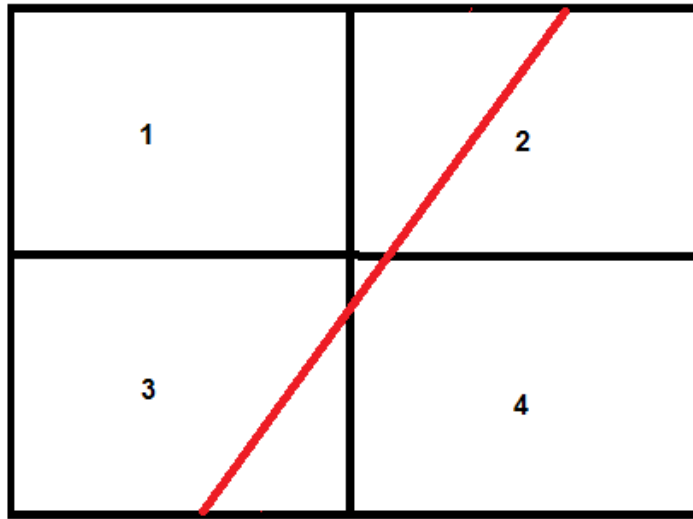


Figure 8.2: Diagram showing the problem with the formation of the geometry matrix using a logical index.

and Soria, 2007; Elsinga et al., 2006], as we saw in Chapters 4 and 7. Additional areas for further research could include, in no particular order:

- Improving the formulation of the geometric matrix to consider the relative contribution to each pixel rather than a logical index.
- Exploring adaptive grid size for reconstructions.
- 3D CIT using ADS-B (see Fig. 8.1).
- Simulating electron density depletions such as those in *Cushley* [2013].
- Using AIS and ADS-B as *a priori* information for one another.
- Comparing different VTEC mapping functions to plot VTEC as a function of latitude using STEC more accurately.
- VTEC mapping using AIS, ADS-B and APRS signals. It was found the ray density from APRS was not sufficient for CIT, but could be amalgamated with AIS and ADS-B data like in Chapter 7.

- Optimization of the relaxation parameter. The relaxation parameter is related to the increment that pixel values are changed in each iteration and time for convergence.
- Using *a priori* information from different sources including: the method discussed in Chapter 5, different models, or another instruments.
- Study the robustness of the technique to bad *a priori* guesses.
- Comparing CIT results using *a posteriori* and *a priori* information.
- Generating more dynamic electron density profiles (e.g. gradients) as input to the ray trace model as well as *a priori* data or constraints for the reconstruction procedure.
- Applying and validating the method of obtaining a more accurate characteristic value for the parallel component of the magnetic field discussed in Chapter 6 to estimate of TEC from FR.
- Comparing various reconstruction algorithms such as SIRT, SART, MART, Bayesian, etc.
- Comparing other ray trace models for example the PHaRLAP and DaVIT-py rayDARN HF raytrace models [*Cervera and Harris, 2014; de Larquier, 2011*].
- Getting access and processing real observations. Currently there exists an archive of AIS data, which includes the full waveform [*Ian D'Souza, Arunas Macikunas, Balaji Kumar - personal communication*] covering approximately the past decade. Discussions are ongoing to get access to the data from the product provider.

## References

- Abdu, M. A., Equatorial spread F development and quiet time variability under solar minimum conditions, *Indian Journal of Radio & Space Physics*, 41, 168–183, 2012.
- Abe, T., and J. Moen, In-situ measurement of electron density perturbation in the ionospheric cusp region during IC I-2 campaign, Proc. 20th ESA Symposium on European Rocket and Balloon Programmes and Related Research (ESA SP-700), 2011.
- ADS-B-Technologies, Welcome, ADS-B-Technologies, LLC, Anchorage, AK. Available at: <http://www.ads-b.com/>, 2011.
- Aireon, Aireon<sup>SM</sup> ADS-B payloads installed on first Iridium Next satellites, News and Updates. Aireon, McLean, VA. Available at: <http://aireon.com/2015/06/01/aireon2015>.
- AirNav-Systems, *AirNav Radar Box Manual*, AirNav Systems LLC, 2008.
- Alminde, L. K., A. Midtgaard, M. Brisgard, M. Jensen, B. Gosvig, A. Birklykke, P. Koch, and Y. L. Moullec, GomX-1: A nano-satellite mission to demonstrate improved situational awareness for air traffic control, in *26th Annual AIAA/USU Conference on Small Satellites*, SSC12-I-6, pp. 1–7, Aalborg, Denmark, 2012.
- Alminde, L. K., K. Kaas, M. Brisgard, M. Brisgard, J. Chistiansen, and D. Gerhard, GomX-1: Flight experience and air traffic monitoring results, in *26th Annual AIAA/USU Conference on Small Satellites*, SSC14-XII-7, pp. 1–7, Aalborg, Denmark, 2014.
- Amos, J., Ahoy! Your ship is being tracked from orbit, BBC News, London, United Kingdom. Available at: <https://www.bbc.com/news/science-environment-18889594>, 2012.
- Anderson, D., and T. Fuller-Rowell, The ionosphere, *NOAA Space Environment Topics*, p. 14, 1999.
- Anderson, D., et al., Intercomparison of physical models and observations of the ionosphere, *Journal of Geophysical Research*, 103(A2), 2179–92, 1998.
- Andreeva, E., S. Franke, K. Yeh, V. Kunitsyn, and I. Nesterov, On generation of an assembly of image in ionospheric tomography, *Radio Sci.*, 36 Issue 2, 299–309, 2001.
- Appleton, E. V., and G. Builder, The ionosphere as a doubly refracting medium, *Proc. Phys. Soc*, 45, 208–220, 1933.

- Atkinson, C. H., and J. Soria, Algebraic reconstruction techniques for tomographic particle image velocimetry, in *16th Australasian Fluid Mechanics Conference*, Laboratory for Turbulence Research in Aerospace and Combustion Department of Mechanical Engineering, Monash University, Victoria, 3800 Australia, Crown Plaza, Gold Coast, Australia, 2007.
- Aurora Service, Aurora forecast, Hourly Forecast, Utsjoki, Finland. Available at: <http://www.aurora-service.eu/aurora-forecast/>, 2016.
- Austen, J., S. Franke, C. Liu, and K. Yeh, Application of computerized tomography techniques to ionospheric research, in *URSI and COSPAR International Beacon Satellite Symposium on Radio Beacon Contribution to the Study of Ionization and Dynamics of the Ionosphere and to Corrections to Geodesy and Technical Workshop*, edited by A. Tauriainen, 1, pp. 25–35, University of Oulu, Oulu, Finland, 1986.
- Austen, J., S. Franke, and C. Liu, Ionospheric imaging using computerized tomography, *Radio Science*, 23(3), 299–307, 1988.
- Bauer, S., *Physics of planetary ionospheres*, Physics and chemistry in space, Springer, 1973.
- BBC News, Monster radiation burst from sun, BBC News, London, United Kingdom. Available at: <https://www.bbc.com/news/science-environment-22525233>, 2013.
- Bellan, P., *Fundamentals of Plasma Physics*, Cambridge University Press, 2008.
- Bennett, P. A. C. B., I., and R. Zee, Nanosatellite aircraft tracking: Simulation and design of the CanX-7 ADS-B, in *The Canadian SmallSat Conference , Toronto, 2-3 February 2016.*, 2016.
- Benton, C. J., and C. N. Mitchell, Method to measure the Stokes parameters of GPS signals, *Radio Sci.*, 49(1), 7–18, doi:10.1002/2013RS005160, 2014.
- Bhatt, A., Cedar email: AGU session: Upper atmospheric research through ground-based networked instrumentation, 2014.
- Bilitza, D., IRI-2007: Online computation and plotting through IRI-2007web, NASA/Goddard Space Flight Center, Heliospheric Physics Lab, Greenbelt, Md. Available at: [http://omniweb.gsfc.nasa.gov/vitmo/iri\\_vitmo.html](http://omniweb.gsfc.nasa.gov/vitmo/iri_vitmo.html), 2007.
- Bilitza, D., L.-A. McKinnell, B. Reinisch, and T. Fuller-Rowell, The international reference ionosphere today and in the future, *J. Geodesy*, 85, 909–920, 2011.
- Birkeland, K., *The Norwegian Aurora Polaris Expedition 1902-1903, vol. 1, 1st sect. Pitman, London*, 1908.
- Biswas, C., and H. Na, Three-dimensional computerized ionospheric tomography using volumetric constraints, *Radio Science*, 33(6), 1793–1805, 1998.

- Brown, S. J., and T. L. Hendricks, Automatic Dependent Surveillance Broadcast (ADS-B) In Aviation Rulemaking Committee (ARC) recommendations to define a strategy for incorporating ADS-B in technologies into the National Airspace System (NAS), *A report from the ADS-B In ARC to the FAA*, ADS-B In ARC, Washington, DC, 2011.
- Browne, I., J. V. Evans, J. K. Hargreaves, and W. Murray, Radio echoes from the Moon, *Prop, Phys.*, 60, 901–20, 1956.
- Bruninga (WB4APR), B., Automatic AX.25 position and status reporting, in *ARRL Amateur Radio 11th Computer Networking Conference Teaneck*, New Jersey, 1992.
- Bruninga (WB4APR), B., APRS satellite tracking and reporting system, Available at: <http://www.aprs.org/astars.html>, 2006.
- Budden, K., *Radio waves in the ionosphere: The mathematical theory of the reflection of radio waves from stratified ionised layers*, Cambridge University Press, UK, 1961.
- Budden, K., Effect of electron collisions on the formulas of magneto-ionic theory, *Radio Sci.*, 69D(2), 191–211, 1965.
- Burchill, J. K., D. J. Knudsen, B. J. J. Bock, R. F. Pfaff Jr., D. D. Wallis, J. H. Clemmons, S. R. Bounds, and H. Stenbaek-Nielsen, Core ion interactions with BB ELF, lower hybrid, and Alfvén waves in the high-latitude topside Ionosphere, *Journal of Geophysical Research*, 109, 15, doi:10.1029/2003JA010073, 2004.
- Burridge, C., private communication, NavCanada, 2009.
- Bust, G. S., G. Crowley, T. W. Garner, T. L. Gaussiran II, R. W. Meggs, C. N. Mitchell, P. S. J. Spencer, P. Yin, and B. Zapfe, Four-dimensional GPS imaging of space weather storms, *Space Weather*, S02003, 5, doi:10.1029/2006SW000237, 2007.
- Campbell, R., Ionospheric corrections via PIM and real-time data, *New Astron. Rev.*, 43, 617, 1999.
- Canada Centre For Remote Sensing, Advanced radar polarimetry tutorial: Radar polarimetry, Natural Resources Canada, Ottawa, Ontario, Canada. Available at: <http://www.nrcan.gc.ca/sites/www.nrcan.gc.ca.earth-sciences/files/pdf/resource/tutor/polarim/pdf/polarim.e.pdf>, 2007.
- Cannon, M., Satellite positioning, *ENGO*, p. 561, 1997.
- Carrington, R., Description of a singular appearance seen in the Sun on September 1, 1859, *Monthly Notices of the Royal Astronomical Society*, 20, 13–15, 1859.
- Castillo, J., M. Earl, M. Baskey, D. Stolzman, M. Grieve, R. Vincent, R. Van Der Pryt, and A. Cushley, Canadian Satellite Design Competition Proposal: SABRE, The deployment of a space based sensor for the collection of Automatic

- Dependent Signal-Broadcast transponder transmissions from commercial aircraft operating over Hudson Bay, *Tech. rep.*, Royal Military College of Canada, Kingston, ON, 2012.
- Cervera, M. A., and T. Harris, Modeling ionospheric disturbance features in quasi-vertically incident ionograms using 3-D magnetoionic ray tracing and atmospheric-gravity waves, *Journal of Geophysical Research: Space Physics*, 119, 431–440, doi:10.1002/2013JA019247, 2014.
- Chen, F. F., *Introduction to plasma physics and controlled fusion, Volume 1: plasma physics*, second ed., Plenum Press, New York, 1984.
- Chen, J., Z. Li, and C. S. Li, A novel strategy for topside ionosphere sounder based on spaceborne MIMO radar with FDCD, *Progress In Electromagnetics Research*, 116, 381–393, 2011.
- Choi, B.-K., J.-U. Park, and J.-K. Chung, Ionospheric tomography using a regional GPS network over South Korea, *Journal of Global Positioning Systems*, 5(1-2), 47–51, doi:10.5194/angeo-31-75-2013, 2006.
- Comberiate, J., and L. Paxton, Coordinated space-based observations of equatorial plasma bubbles using TIMED/GUVI and DMSP, in *JHUAPL (ISEA Presentation)*, 2009.
- Compston, D., International reference ionosphere (IRI) model, Stanford University, Stanford, CA. MatLab Central. Available at: <http://www.mathworks.com/matlabcentral/fileexchange/34863-international-reference-ionosphere-iri-model/content/iritest.m>, 2012.
- CSEW6 steering committee, Canadian scientific priorities for the global exploration strategy, in *Proceedings of the 6th Canadian Space Exploration Workshop, Dec 1-3 2008, St-Hubert, Quebec, Canada*, 2009.
- Cushley, A., *VE3RMC Amateur Satellite Communications Ground Station*, Royal Military College of Canada, Kingston, ON, 1.0 ed., 2010.
- Cushley, A., Ionospheric tomography using Faraday rotation of Automatic Dependent Surveillance Broadcast (UHF) signals (Master's thesis), Physics, Royal Military College of Canada, Kingston, ON, 2013.
- Cushley, A., The potential of using ADS-B and other signals of opportunity in the construction of ionospheric electron density maps (PhD thesis proposal), royal Military College of Canada, Kingston, ON, 2015.
- Cushley, A., and J.-M. A. Noël, Ionospheric tomography using (ADS-B) signals, *Radio Science*, 49(7), 549–563, doi:10.1002/2013RS005354, 2014.

- Cushley, A., and J.-M. A. Noël, Ionospheric sounding opportunities using signal data from preexisting amateur radio and other networks (SH11A-2378), in *American Geophysical Union Fall Meeting 2015 At: San Francisco, CA*, 2015.
- Cushley, A., K. Kabin, and J.-M. A. Noël, Faraday rotation of Automatic Dependent Surveillance Broadcast (ADS-B) signals as a method of ionospheric characterization, *Rad. Sci.*, *52*, 1293–1300, doi:10.1002/2017RS006319, 2017.
- Cushley, A., J.-M. A. Noël, and K. Kabin, Faraday rotation, total electron content, and their sensitivity to the average parallel component of the magnetic field, *Rad. Sci.*, *53*, 1075–1088, doi:10.1029/2018RS006667, 2018.
- Dahlgren, H., G. W. Perry, J. L. Semeter, J.-P. St.-Maurice, K. Hosokawa, M. J. Nicolls, M. Greffen, K. Shiokawa, and C. Heinselman, Space-time variability of polar cap patches: Direct evidence for internal plasma structuring, *Journal of Geophysical Research*, *117*(A09312), 1–15, doi:10.1029/2012JA017961, 2012.
- De, S., S. Adhikari, and B. Sarkar, Non-linear RF heating of ionospheric plasma, *Earth, Moon, and Planets*, *41*(3), 217–222, doi:10.1007/BF00113984, 1988.
- de Larquier, S., rayDARN, Virginia Tech SuperDARN Lab, Blacksburg, VA. GitHub executable file available at: <https://github.com/vtsuperdarn/davitpy/blob/master/davitpy/models/raydarn/>, 2011.
- de Selding, P. B., Harris, exactEarth aim to ride Iridium Next to growth in AIS, SpaceNews, Alexandria, VA. Available at: <https://spacenews.com/harris-exactearth-aim-to-ride-iridium-next-to-growth-in-ais/>, 2015.
- Dhar, B., N. M. Vadher, and M. R. Deshpande, An equipment to measure Faraday rotation angle of VHF waves received from a geostationary satellite, *IETE Journal of Research*, *23*(12), 708–711, doi:10.1080/03772063.1977.11451514, 1977.
- El-Naggar, A. M., Enhancing the accuracy of gps point positioning by converting the single frequency data to dual frequency data, *Alexandria Engineering Journal*, *50*(3), 237–243, doi:10.1016/j.aej.2011.03.003, 2011.
- Elachi, C., and J. van Zyl, *Introduction to the Physics and Techniques of Remote Sensing*, second ed., John Wiley and Sons, Inc., Hoboken, NJ, 2006.
- Elsinga, G., F. Scarano, B. Wieneke, and B. van Oudheusden, Tomographic particle image velocimetry, *Experiments in Fluids*, *41*, 933–947, 2006.
- Erickson, W., R. Perley, C. Flatters, and N. Kassim, Ionospheric corrections for VLA observations using local GPS data, *Astronomy and Astrophysics*, *366*(3), 1071–80, 2001.

European Space Agency, Tracking aircraft from orbit, Available at: [http://www.esa.int/Our\\_Activities/Technology/Proba\\_Missions/Tracking\\_aircraft\\_from\\_orbit](http://www.esa.int/Our_Activities/Technology/Proba_Missions/Tracking_aircraft_from_orbit), 2013a.

European Space Agency, Hitching a ride, Available at: [http://www.esa.int/Our\\_Activities/Technology/Proba\\_Missions/Hitching\\_a\\_ride](http://www.esa.int/Our_Activities/Technology/Proba_Missions/Hitching_a_ride), 2013b.

exactEarth, exactEarth launches advanced equatorial AIS satellite, exactEarth, Cambridge, Ontario, Canada. Available at: <http://www.exactearth.com/media-centre/recent-news/287-exactearth-launches-advanced-equatorial-ais-satellite>, 2015.

exactEarth, exactView RT powered by Harris info sheet: Real-time advanced ship tracking solution, exactEarth, Cambridge, Ontario, Canada. Available at: [https://cdn2.hubspot.net/hubfs/183611/Landing\\_Page\\_Documents/exactView\\_RT\\_Slick\\_Sheet.pdf](https://cdn2.hubspot.net/hubfs/183611/Landing_Page_Documents/exactView_RT_Slick_Sheet.pdf), 2016.

Feeman, T., *The Mathematics of Medical Imaging*, Springer Undergraduate Texts 11 in Mathematics and Technology, Springer Science Business Media, LLC, doi:10.1007/978-0-387-92712-1\_2, 2010.

Felgenhauer, B., and F. Jarvis, Enumerating possible sudoku grids, available at: <http://www.afjarvis.staff.shef.ac.uk/sudoku/sudoku.pdf>, 2005.

Fitzgerald, T., Observations of total electron content perturbations on GPS signals caused by a ground level explosion, *Journal of Atmospheric and Solar-Terrestrial Physics*, 59(7), 829–834, 1997.

Francis, R., Detection of Automatic Dependent Surveillance - Broadcast signals using stratospheric and orbital platforms, Master's thesis, Royal Military College of Canada, Kingston, ON, 2009.

Francis, R., R. Vincent, J. Noël, P. Tremblay, D. Desjardins, A. Cushley, and M. Wallace, The flying laboratory for the observation of ADS-B signals, *International Journal of Navigation and Observation*, 2011(A2), 5, doi:10.1155/2011/973656, 2011.

Francois, M., S. Santandrea, K. Mellab, D. Vrancken, and J. Versluys, The PROBA-V mission: the space segment, *International Journal of Remote Sensing*, 35(7), 2548–2564,, doi:10.1080/01431161.2014.883098, 2014.

Freitag, K., An analysis of Automatic Dependent Surveillance - Broadcast signals received by the CanX-7 nanosatellite: Examining the North Atlantic oceanic airspace control area, Master's thesis, Royal Military College of Canada, Kingston, ON, 2017.

Fremouw, E., J. Secan, and B. Howe, Application of stochastic inverse theory to ionospheric tomography, *Radio Sci.*, 27(5), 721–732, 1992.



- Frissell, N., E. Miller, S. Kaeppler, F. Ceglia, D. Pascoe, N. Sinanis, P. Smith, R. Williams, and A. Shovkoplyas, Ionospheric sounding using real-time amateur radio reporting networks, *Space Weather*, p. 12, doi:10.1002/2014SW001132, 2014.
- Frissell, N. A., J. B. H. Baker, J. M. Ruohoniemi, R. A. Greenwald, A. J. Gerrard, E. S. Miller, and M. L. West, Sources and characteristics of medium-scale traveling ionospheric disturbances observed by high-frequency radars in the North American sector, *JGR Space Physics*, 121(4), 3722–3739, doi:10.1002/2015JA022168, 2016.
- Frougere, P., Ionospheric radio tomography using maximum entropy, 1, Theory and simulation studies, *Radio Sci.*, 30(2), 424–444, 1995.
- Fuying, Z., W. Yun, Z. Yiyan, and L. Jian, A statistical investigation of pre-earthquake ionospheric TEC anomalies, *Geodesy and Geodynamics*, 2(1), 61–65, 2011.
- Gbur, G., The discovery, rediscovery, and re-rediscovery of computed tomography, The blog covers topics in physics and optics, the history of science, classic pulp fantasy and horror fiction, and the surprising intersections between these areas. UNC Charlotte, Charlotte, NC. Available at: <http://skullsinthestars.com/2008/08/05/the-discovery-rediscovery-and-re-rediscovery-of-computed-tomography/>, 2008.
- Gillies, R. ., Transionospheric Signal Modelling for ePOP and SuperDARN, Ph.D. thesis, University of Saskatchewan, 2010.
- Gillies, R., G. Hussey, H. James, G. Sofko, and D. André, Modelling and observation of transionospheric propagation results from ISIS II in preparation for ePOP, *Ann. Geophys.*, 25, 87–97, 2007.
- Gillies, R. G., Modelling of transionospheric HF radio wave propagation for the ISIS II and ePOP satellites, Master's thesis, University of Saskatchewan, 2006.
- Gillmor, C. S., Wilhelm Altar, Edward Appleton, and the magneto-ionic theory, *Proceedings of the American Philosophical Society*, 126(5), 395–440, 1982.
- GomSpace, GomSpace GOMX-1, Aalborg, Denmark. Available at: <http://gomspace.com/index.php?p=gomx1>, 2013.
- Gondarenko, N. A., and P. N. Guzdar, Gradient-drift instability in high-latitude plasma patches: ion inertialeffects., *Geophys. Res. Lett.*, 26, 3345–3348, 1999.
- Gondarenko, N. A., and P. N. Guzdar, Three-dimensional structuring characteristics of high-latitude plasma patches, *J. Geophys. Res.*, 106, 24,611–24,620, 2001.
- Greidanus, H., Assessing the operationality of ship detection from space, in *New Space Services for Maritime Users: The Impact of Satellite Technology on Maritime Legislation, Proceedings of the conference held 21-23 February, 2005 at UNESCO HQ, Paris in France. Edited by B. Warmbein. ISBN: 92-9092-895-6. ESA-SP Vol.*

- 584, 2005, *id.6*, European Commission Joint Research Centre, Ispra (VA), Italy, 2005.
- Gurnett, D., and A. Bhattacharjee, *Introduction to Plasma Physics With Space and Laboratory Applications*, Cambridge University Press, New York, NY, 2005.
- Hackbusch, W., *Iterative Solution of Large Sparse Systems of Equations*, Springer-Verlag, New York, 1994.
- Hadamard, J., Sur les problèmes aux dérivées partielles et leur signification physique, *Princeton University Bulletin*, 13, 49–52, 1902.
- Hanslmeier, A., *The Sun and Space Weather*, Astrophysics and Space Science Library, Springer Netherlands, 2007.
- Haque, J., H. Altan, A. Malaga, D. Parmet, and D. Tabor, Systems and methods for receiving aircraft position reports, US Patent App. 13/316,052 Clearwater, FL, 2013.
- Harris Corporation, Aireon awards Harris Corporation contract for largest implementation of hosted satellite payloads; will provide global satellite-based aircraft tracking, Harris Press Release. Washington, DC/Melbourne, FL. Available at: [http://harris.com/view\\_pressrelease.asp?pr\\_id=3476](http://harris.com/view_pressrelease.asp?pr_id=3476), 2012.
- Harris Corporation, Harris Corporation completes space qualification testing of hosted payload for satellite-based global aircraft tracking system, Harris Press Release. Washington, DC/Melbourne, FL. Available at: <http://harris.com/press/article.asp?id=3681>, 2014.
- Hartmann, G., and R. Leitinger, Range errors due to ionospheric and tropospheric effects for signal frequencies above 100 MHz, *Bull Geod*, 58, 109–136, 1984.
- Hartree, D. R., The propagation of electromagnetic waves in a stratified medium, *Proc. Camb. Phil. Soc*, 25, 97, 1929.
- Haselgrove, J., The Hamiltonian ray path equations, *J. Atmos. Terr. Phys*, 25, 397–399, 1963.
- Herman, G., *Image Reconstruction From Projections-The Fundamentals of Computerized Tomography.*, Academic Press, 1980.
- Huba, J., R. Schunk, and G. Khazanov, *Modeling the Ionosphere-Thermosphere*, Geophysical Monograph Series, Wiley, 2014.
- Hung, R., T. Phan, and R. Smith, Observation of gravity waves during the extreme tornado outbreak of 3 April 1974., *J. Atmos. Terr. Phys*, 40, 831–843, doi: 10.1016/0021-9169(78)90033-8, 1978.
- Hunsucker, R., and J. Hargreaves, *The High-Latitude Ionospheres and its Effects on Radio Propagation*, Cambridge University Press, Cambridge, UK, UK, 2003.

- Inter-Agency Space Debris Coordination Committee, (IADC-02-01) Space debris mitigation guidelines, Available at: [http://www.iadc-online.org/index.cgi?item=docs\\_pub](http://www.iadc-online.org/index.cgi?item=docs_pub), 2007.
- International association of geomagnetism and aeronomy, Working Group V-MOD, International geomagnetic reference field: the eleventh generation, *Geophys. J. Int.*, *183*(3), 1216–1230, doi:10.1111/j.1365-246X.2010.04804.x., Participating members: C. C. Finlay, S. Maus, C. D. Beggan, T. N. Bondar, A. Chambodut, T. A. Chernova, A. Chulliat, V. P. Golovkov, B. Hamilton, M. Hamoudi, R. Holme, G. Hulot, W. Kuang, B. Langlais, V. Lesur, F. J. Lowes, H. Luhr, S. Macmillan, M. Mandea, S. McLean, C. Manoj, M. Menvielle, I. Michaelis, N. Olsen, J. Rauberg, M. Rother, T. J. Sabaka, A. Tangborn, L. Toffner-Clausen, E. Thebault, A. W. P. Thomson, I. Wardinski Z. Wei, T. I. Zvereva., 2010.
- IONOLAB Ionospheric Research Laboratory, Computerized ionospheric tomography (CIT), Available at: <http://ionolab.org/index.php?page=cit&language=en>.
- Ippolito, L., *Satellite Communications Systems Engineering: Atmospheric Effects, Satellite Link Design and System Performance*, wireless communications and mobile computing, West Sussex, UK: Wiley, 2008.
- Jahn, R. G., *Physics of Electric Propulsion*, McGraw-Hill Series in Missile and Space Technology, New York: McGraw-Hill Book Company., 1968.
- Jakowski, N., C. Mayer, M. M. Hoque, and V. Wilken, Total electron content models and their use in ionosphere monitoring, *Rad. Sci.*, *46*(RS0D18), 1–11, doi:10.1029/2010RS004620, 2011.
- Jayachandran, P., et al., The canadian high arctic ionospheric network (CHAIN), *Radio Sci.*, *44*(RS0A03), doi:10.1029/2008RS004046, 2009.
- Jehle, M., M. Rüegg, L. Zuberbühler, D. Small, and E. Meier, Measurement of ionospheric Faraday rotation in simulated and real spaceborne SAR data, *IEEE Transactions on Geoscience and Remote Sensing*, *47*(5), 1512–23, 2009.
- Jin, S., J. Park, J. Wang, B. Choi, and P. Park, Electron Density Profiles Derived From Ground-Based GPS Observations, *The Journal Of Navigation*, *59*(3), 395–401, doi:10.1017/S0373463306003821, 2006.
- Kak, A., and M. Slaney, *Principles of Computerized Tomographic Imaging*, IEEE Press, 1988.
- Kelley, M., W. Swartz, and K. Heki, Apparent ionospheric total electron content variations prior to major earthquakes due to electric fields created by tectonic stresses, *J. Geophys. Res. Space Physics*, *122*, 66896695, doi:10.1002/2016JA023601, 2017.
- Kelley, M. C., *The Earth's Ionosphere, International Geophysics Series*, vol. 43, Academic Press, San Diego, California 92101, 1989.

- Kelley, M. C., *The Earth's Ionosphere: Plasma Physics and Electrodynamics, Second Edition*, Elsevier Inc, San Diego, 2009.
- Kersley, I., J. Heatyon, S. Pryse, and T. Raymund, Experimental ionospheric tomography with ionosonde input and EISCAT verification, *Anns. Geophys.*, *11*, 1064–74, 1993.
- Kleimenova, N., O. Kozyreva, M. Kubicki, and S. Michnowski, Substorm effects in the polar latitude atmospheric electric field disturbances, *Physics of Auroral Phenomena, Proc. XXXIII Annual Seminar, Apatity*, pp. 167–170, 2011.
- Klobuchar, J. A., and C. Liu, *World Ionosphere Modern Total Electron Content Measurement Ionosphere/Thermosphere Study*, SCOSTEP Secretariat, Urbana, IL, 1989.
- Klobuchar, J. A., J. Aarons, M. Mendillo, R. S. Allen, a John P. Mullen, D. R. Seeman, and S. Basu, Total electron content studies of the ionosphere, *Tech. rep.*, Ionospheric Physics Laboratory- Air Force Cambridge Research Laboratories-L. G. Hanscom Field, Bedford, Massachusetts, 1973.
- Kraus, J., *Radio astronomy*, New York: McGraw Hill, 1966.
- Kuklinsky, W., Ionospheric tomography via iterative cross-entropy minimization, *Radio Sci.*, *32*(3), 1037–1049, 1997.
- Kunitsyn, V., and E. Tereschenko, *Ionospheric Tomography*, Springer, Berlin, 2003.
- Kunitsyn, V., E. D. Tereshchenko, E. S. Andreeva, , and O. G. Razinkov, Phase and phase-difference ionospheric radio tomography, *Int. J. Imag. Sys. Technol.*, *5*, 128140, 1994.
- Kunitsyn, V. E., E. S. Andreeva, A. Y. Popov, and O. G. Razinkov, Methods and algorithms of ray radiotomography for ionospheric research, *Ann. Geophys*, *13*, 14211428, 1995.
- Kyovtorov, V., M. Vespe, G. Fortuny, D. Tarchi, R. Giuliani, and J. Broussolle, Passive Automatic Identification System for maritime surveillance, Publications Office of the European Union, 2012.
- Langley, R., M. Fedrizzi, E. Paula, M. Santos, and A. Komjathy, Mapping the low latitude ionosphere with GPS, *GPSWorld*, *13*, 41–46, 2002.
- Lanyi, G., and T. Roth, A comparison of mapped and measured total ionospheric electron content using global positioning system and beacon satellite observations, *Radio Science*, pp. 483–492, 1998.
- Larson, K. M., A new way to detect volcanic plumes, *Geophys. Res.Lett.*, *40*, 26572660, doi:10.1002/grl.50556, 2013.

- Lavalle, M., Full and compact polarimetric radar interferometry for vegetation remote sensing. Signal and image processing, Ph.D. thesis, Université Rennes, English. <tel-00480972>, 2009.
- Lawrence, R. S., D. J. Posakony, O. K. Garriott, and S. C. Hall, The total electron content of the ionosphere at middle latitudes near the peak of the solar cycle, *Journal of Geophysical Research*, 68(7), 1889–1898, doi:10.1029/JZ068i007p01889, 1963.
- Leitinger, R., Data from orbiting navigation satellites for tomographic reconstructions, *Int. J. Imaging Syst. Technol.*, 5, 86–96, 1994.
- Leitinger, R., M.-L. Zhang, and S. M. Radicella, An improved bottomside for the ionospheric electron density model NeQuick, *Annals of Geophysics*, 48(3), 525–34, 2005.
- Lewis, B., M. McCall, A. Green, L. Bennett, M. Pierre, U. Schrewe, K. O'Brien, and E. Felsberger, Aircrew exposure from cosmic radiation on commercial airline routes, *Radiat Prot Dosimetry*, 93, 293–314, 2001.
- Li, J., G. Meng, X. You, R. Zhang, H. Shi, and Y. Han, Ionospheric total electron content disturbance associated with May 12, 2008, Wenchuan earthquake, *Geodesy and Geodynamics*, 6(2), 126 – 134, doi:http://dx.doi.org/10.1016/j.geog.2015.01.003, 2015.
- Lilensten, J., L. R. Cander, M. T. Rietveld, P. S. Cannon, and M. Barthelemy, Comparison of EISCAT and ionosonde electron densities: application to a ground-based ionospheric segment of a space weather programme, *Annales Geophysica*, 23, 183–189, 2005.
- Liu, Z., and Y. Gao, Ionospheric Tomography Using GPS Measurements, in *Proceedings of KIS-2001, Banff, Alberta, Canada*, 2001.
- Lodge, O., Mr. Marconi's results in day and night wireless telegraphy, *Nature*, 222, 66, 1902.
- Mannucci, A. J., B. D. Wilson, and C. D. Edwards, A new method for monitoring the Earth's ionospheric total electron using the GPS global network, in *Proceedings of the Institute of Navigation GPS-93*, p. 1323, *Inst. of Navig., Alexandria, Va.*, 1993.
- Marcio T.A.H. Muella, M., de Paula E.R., C. Mitchell, P. Kintner, R. Paes, and I. Batista, Tomographic Imaging of the Equatorial and Low-latitude Ionosphere Over Central-eastern Brazil, *Earth Planets Science*, 63, 129–138, 2011.
- Marković, M., Determination of total electron content in the ionosphere using GPS technology, *Geonauka*, 2(2), 1–9, 2014.

- Marsh, G., European air traffic surveillance, Avionics Today, Danbury, CT. Available at: [http://www.aviationtoday.com/av/air-traffic-control/European-Air-Traffic-Surveillance-A-Combination-Approach\\_1104.html#.U9ACorFn3qc](http://www.aviationtoday.com/av/air-traffic-control/European-Air-Traffic-Surveillance-A-Combination-Approach_1104.html#.U9ACorFn3qc), 2006.
- Martinis, C., J. Baumgardner, J. Wroten, and M. Mendillo, All-sky imaging observations of conjugate medium-scale traveling ionospheric disturbances in the American sector, *Journal of Geophysical Research*, 116(A05326), doi:10.1029/2010JA016264, 2011.
- Maus, S., et al., The 10th generation international geomagnetic reference field, *Phys. Earth Planet. Inter.*, 151, 320322., 2005.
- Max van de Kamp, M., Medium-scale 4D ionospheric tomography using a dense GPS network, *Annales Geophysicae*, 31, 75–89, doi:10.5194/angeo-31-75-2013, 2012.
- McClure, J. P., S. Singh, D. Bamgboye, R. Johnson, and H. Kil, Plasma bubbles and irregularities in the equatorial ionosphere, *J. Geophys. Res.*, 82, 2650–2656, 1977.
- Meggs, R. W., C. N. Mitchell, and P. S. J. Spencer, *Radio Sci.*, 39(1), 1–8, 2004.
- Miller, P., Why are our satellites in low earth orbit?, exactEarth, Cambridge, Ontario, Canada. Available at: <http://blog.exactearth.com/blog/why-are-our-satellites-in-low-earth-orbit>, 2016.
- Mills, C. E., Xastir & mdash; open-source client for the Automatic Packet Reporting System, Linux Journal available at: <http://www.linuxjournal.com/magazine/xastirmdashopen-source-client-automatic-packet-reporting-system>, 2010.
- Milltech Marine, Frequently asked questions: What kind of information is broadcast for each ship and how often is it updated?, Milltech Marine, Port Orchard, WA. Available at: <https://www.milltechmarine.com/faq.htm>, 2018.
- Mitchell, C. N., D. G. Jones, L. Kersley, S. E. Pryse, and I. K. Walker, Imaging of field-aligned structures in the auroral ionosphere, *Ann. Geophysicae*, 13, 1311–1319, 1997a.
- Mitchell, C. N., L. Kersley, J. A. T. Heaton, and S. E. Pryse, De-termination of the vertical electron-density profile in ionospheric tomography: experimental results, *Ann. Geophys*, 15, 747,752, doi:10.1007/s00585-997-0747-1, 1997b.
- Molmud, P., Langevin equation and the A.C. conductivity of non-Maxwellian plasmas, *Phys. Rev.*, 114, 29, 1959.
- Musa, T., Residual analysis of atmospheric delay in low latitude region using network-based GPS positioning, Ph.D. thesis, School of Surveying & Spatial Information Systems, University of New South Wales, 2007.

- Mushini, S., P. T. Jayachandran, R. B. Langley, and J. W. MacDougall, Use of varying shell heights derived from ionosonde data in calculating vertical total electron content (TEC) using GPS. New method, *J. Adv. Space Res.*, 015, 10, 2009.
- Na, H., High resolution computerized ionospheric tomography systems., *Tech. rep.*, University of Iowa, 1996.
- Na, H., and C. Biswas, A localized space-frequency algorithm for computerized ionospheric tomography, *Radio Sci.*, 31(6), 1555–1565, 1996.
- Na, H., and H. Lee, Resolution degradation parameters of ionospheric tomography, *Radio Sci.*, 29(1), 115–125, 1994.
- Na, H., B. Hall, and E. Sutton, Ground station spacing effects in ionospheric tomography, *Ann. Geophys.*, 13(12), 1288–1296, 1995.
- NASA Jet Propulsion Laboratory California Institute of Technology, Real-time ionospheric maps, NASA JPL Caltech, Pasadena CA. Available at: [http://iono.jpl.nasa.gov/latest\\_rti\\_global.html](http://iono.jpl.nasa.gov/latest_rti_global.html), 2014.
- National Aeronautics and Space Administration, *Process for Limiting Orbital Debris*, Washington, DC. Available at: [https://explorers.larc.nasa.gov/APMIDEX2016/MO/pdf\\_files/NHBK871914.pdf](https://explorers.larc.nasa.gov/APMIDEX2016/MO/pdf_files/NHBK871914.pdf), 2012.
- National Geodetic Survey, Continuously Operating Reference Station (CORS) map, National Geodetic Survey, Silver Spring, MD, USA. Available at: [http://www.ngs.noaa.gov/CORS\\_Map/](http://www.ngs.noaa.gov/CORS_Map/), 2015.
- Nava, B., P. Coisson, and S. Radicella, A new version of the NeQuick ionosphere electron density model, *Journal of Atmospheric and Solar-Terrestrial Physics*, 70, 1856–1862, doi:10.1016/j.jastp.2008.01.015., 2008.
- NavCanada, Hudson Bay implementation, NavCanada, Ottawa, ON. Brochure available at: [http://www.navcanada.co/ContentDefinitionFiles/Services/ANSPrograms/ADS-B/ADSB\\_Brochure\\_EN.pdf](http://www.navcanada.co/ContentDefinitionFiles/Services/ANSPrograms/ADS-B/ADSB_Brochure_EN.pdf), Ottawa, ON, 2008.
- NavCanada, Nav Canada vice president of operations Nav Canada, p. 1, navCanada, Ottawa, ON. Available at: <http://www.airtrafficmanagement.net/2012/07/go-adsb/>, 2010.
- NavCanada, Services-ANS programs: ADS-B, NavCanada, Ottawa, ON. Available at: <http://www.navcanada.ca/navcanada.asp>, 2011.
- Nishioka, M., T. Tsugawa, M. Kubota, and M. Ishii, Concentric waves and short-period oscillations observed in the ionosphere after the 2013 Moore EF5 tornado, *Geophysical Research Letters*, 40, 5581–5586, doi:10.1002/2013GL057963, 2013.

- Office of Information Technology, IT update-security malware detection and prevention, University of Alaska, Anchorage AK. Available at: [http://www.alaska.edu/files/bor/130411Ref30\\_IT\\_Security\\_Update.pdf](http://www.alaska.edu/files/bor/130411Ref30_IT_Security_Update.pdf), 2013.
- Orfanidis, S. J., *Electromagnetic waves and antennas*, Rutgers University, 94 Brett Road Piscataway, NJ 08854-8058, 2008.
- Parsons, G., J. Youden, and C. Fowler, Satellite Automatic Identification System (SAIS) performance modelling and simulation, *Tech. rep.*, Defence Research and Development Canada, Ottawa, ON, 2013.
- Peltier, W. R., and C. O. Hines, On the possible detection of tsunamis by a monitoring of the ionosphere, *J. Geophys. Res.*, *81*(12), 19952000, 1976.
- Perron, P., Space weather situational awareness and its effects upon a joint, interagency, domestic, and Arctic environment, *Canadian Military Journal*, *14*(4), 18–27, 2014.
- Pokhotelov, D., C. N. Mitchell, P. S. J. Spencer, M. R. Hairston, and R. A. Heelis, Ionospheric storm time dynamics as seen by GPS tomography and in situ spacecraft observations, *Journal of Geophysical Research*, *113*(A00A16), doi:10.1029/2008JA013109, 2008.
- Pokhotelov, D., P. T. Jayachandran, C. N. Mitchell, J. MacDougall, and M. H. Denton, GPS tomography in the polar cap: comparison with ionosondes and in situ spacecraft data, *GPS Solutions*, *15*, 7987, 2011.
- Press, W. H., S. A. Teukolsky, W. T. Vetterling, and B. P. Flannery, *Numerical Recipes 3rd Edition: The Art of Scientific Computing*, Cambridge University Press, New York, NY, USA, 2007.
- Pryse, S., and L. Kersley, A preliminary experimental test of ionospheric tomography, *J. Atmos. Terr. Phys.*, *54*(6), 1007–12, 1992.
- Pryse, S., L. Kersley, D. Rice, C. Russell, and I. Walker, Tomographic imaging of the ionospheric mid-latitude trough, *Ann. Geophys.*, pp. 144–49, 1993.
- Pryse, S. E., Radio tomography: A new experimental technique, *Surv. Geophys.*, *24*(1), 1–38, 2003.
- Pulinets, S., Ionospheric precursors of earthquakes; recent advances in theory and practical applications, *Terrestrial, Atmospheric and Oceanic sciences journal*, *15*(3), 413–435, 2004.
- Pulinets, S., and K. Boyarchuk, *Ionospheric Precursors of Earthquakes*, XIII, 315 pp., Springer-Verlag Berlin Heidelberg, doi:10.1007/b137616, 2005.
- Radicella, S. M., and M. L. Zhang, The improved DGR analytical model of electron density height profile and total electron content in the ionosphere, *Annals of Geophysics*, *38*(1), 35–41, 1995.



- Radio Technical Commission for Aeronautics, (DO-260) minimum operational performance standards for 1090 MHz Extended Squitter Automatic Dependent Surveillance- Broadcast (ADS-B) and Traffic Information Services -Broadcast (TIS-B), 2003.
- Radon, J., *Medical Imaging, IEEE Transactions on*, vol. 5, IEEE, 1986.
- Rao, K. D., and V. S. I. Dutt, An assessment of mapping functions for VTEC estimation using measurements of low latitude dual frequency GPS receiver, *International Journal of Applied Engineering Research*, 12(4), 422–427, 2017.
- Ratcliffe, J., The ionosphere and the engineer, *Proc. Inst. Elec. Eng. (London)*, 1, 114, 1967.
- Rawer, K., *Propagation of decameter waves (HF band), in Meteorological and Astronomical Influences on Radio Wave Propagation*, New York Academic Press, 221–250., 1963.
- Rawer, K., *Wave Propagation in the Ionosphere*, Kluwer Acad. Publ., Dordrecht, ISBN 0-7923-0775-5, 1993.
- Raymund, T., Ionospheric tomography algorithms, *Int. J. Imaging Systems*, 54(6), 75–85, 1994.
- Rishbeth, H., H. Kohl, and L. Barclay, *A History of Ionospheric Research and Radio Communications, in Modern Ionospheric Science*, Katlenburg-Lindau, FRG, 1996.
- Rogers, N. C., and S. Quegan, The accuracy of Faraday rotation estimation in satellite synthetic aperture radar images, *IEEE Transactions on geoscience and remote sensing*, 52(8), 4799–807, 2014.
- Ros, E., J. Marcaide, J. Guirado, E. Sardón, and I. Shapiro, A GPS-based method to model the plasma effects in VLBI observations, *Astronomy & Astrophysics*, 356, 357, 2000.
- Rose, D. J., and M. Clark Jr., Plasmas and controlled fusion, *Acta Physica Academiae Scientiarum Hungaricae*, 15(4), 361–362, doi:10.1007/BF03158417, 1963.
- Ross, W., The determination of ionospheric electron content from satellite Doppler measures 1 and 2, *J. Geophys. Res*, 65(9), 2601–15, 1960.
- Royal Observatory of Belgium, Ionosphere : Tutorial, Royal Observatory of Belgium GNSS Research Group, Brussels, Belgium. Available at: [http://gnss.be/ionosphere\\_tutorial.php](http://gnss.be/ionosphere_tutorial.php), 2014.
- Rubio, P., The Canadian Satellite Design Challenge, The Canadian Satellite Design Challenge Management Society Inc., Vancouver, BC. Available at: <http://www.csdcms.ca/>, 2010.

- Ruzmaikin, A., and D. Sokoloff, The calculation of Faraday rotation measure of cosmic radio sources, *Astronomy & Astrophysics*, 78, 1–6, 1979.
- Saito, A., Total electron content detected by GeoNet in Japan.
- Sanchez-Dulcet, F., M. Rodríguez-Bouza, H. Silva, M. Herraiz, M. Bezzeghoud, and P. Biagi, Analysis of observations backing up the existence of VLF and ionospheric TEC anomalies before the Mw6.1 earthquake in Greece, January 26, 2014, *Physics and Chemistry of the Earth Parts A/B/C*, 85, 150–166, doi:10.1016/j.pce.2015.07.002, 2015.
- Sangalli, L., D. J. Knudsen, M. F. Larsen, T. Zhan, R. F. Pfaff, and D. Rowland, Rocket-based measurements of ion velocity, neutral wind, and electric field in the collisional transition region of the auroral ionosphere, *Journal of Geophysical Research (Space Physics)*, 114, 10, doi:10.1029/2008JA013757, 2009.
- Saranya, P., D. Prasad, K. Niranjan, and P. R. Rao, Short term variability in foF2 and TEC over low latitude stations in the Indian sector, *Indian Journal of Radio & Space Physics*, 44, 14–27, 2015.
- Savastano, G., A. Komjathy, O. Verkhoglyadova, A. Mazzoni, M. Crespi, Y. Wei, and A. J. Mannucci, Real-time detection of tsunami ionospheric disturbances with a stand-alone GNSS receiver: A preliminary feasibility demonstration, *Scientific Reports*, 7(46607), 2017.
- Schunk, R., D. Anderson, D. Rees, B. Reinisch, and D. McEwen, The high latitudes in the International Reference Ionosphere (IRI), in *COSPAR Scientific Assembly Meeting Report*, Hamburg, FRG, 1994.
- Schunk, R. W., and A. F. Nagy, *Ionospheres. Physics, plasma physics, and chemistry*, Cambridge atmospheric and space science series, Cambridge University Press, Cambridge, United Kingdom, 2000.
- Selcher, C. A., Three-dimensional, high resolution, computerized ionospheric tomographic imaging and computational modeling of an artificial ionospheric cavity (PhD thesis), Ph.D. thesis, Eberly College of Arts and Sciences at West Virginia University, Morgantown, West Virginia, 2007.
- Semeter, J. L., CEDAR email: CEDAR session: The high-latitude geospace system (wed, 6/24, 10-12), 2015.
- Sen, H., and A. A. Wyller, On the generalization of the Appleton-Hartree magnetoionic formulas, *J. Geophys. Res.*, 65, 3931, 1960.
- Setty, C., Electronic collision frequency in ionospheric layers, *Indian Journal of Radio and Space Physics*, pp. 38–51, 1972.
- Shepp, L., and B. Logan, The Fourier reconstruction of a head section, *IEEE Transactions on Nuclear Science*, 26(3), 21–43, 1974.

- Sheriff, R., and Y. Hu, *Mobile satellite communication networks*, Wiley, 2003.
- Shmuel, B., J. Hiemstra, V. Tarantini, F. Singarayar, G. Bonin, and R. E. Zee, The Canadian Advanced Nanospace eXperiment 7 (CanX-7) demonstration mission: De-orbiting nano- and microspacecraft, in *26th Annual AIAA/USU Conference on Small Satellites*, UTIAS Space Flight Laboratory, 4925 Dufferin St., Toronto, ON, Canada, M3H5T, 2012.
- Siefring, C. L., P. A. Bernhardt, H. G. James, and R. T. Parris, The CERTO beacon on CASSIOPE/e-POP and experiments using high-power HF ionospheric heaters, *Space Science Reviews*, *189*(1), 107–122, doi:10.1007/s11214-014-0110-2, 2015.
- Silver, H. W., HamSCI: Ham radio science citizen investigation, *QST*, *100*(8), 68–71, 2016.
- Soicher, H., and F. Gorman, Seasonal and day-to-day variability of total electron content and mid-latitudes near solar maximum, *Radio Science*, *20*(3), 383–387, doi:10.1029/RS020i003p00383, 2012.
- Sotomayor-Beltran, C., et al., Calibrating high-precision Faraday rotation measurements for LOFAR and the next generation of low-frequency radio telescopes, *Astronomy & Astrophysics*, *552*, A58, doi:10.1051/0004-6361/201220728, 2013.
- Spencer, P. S. J., and C. N. Mitchell, Imaging of fast moving electron-density structures in the polar cap, *Annals of Geo- physics*, *50*(3), 427,434, 2007.
- St-Maurice, J., Non-Maxwellian ionospheric velocity distribution in large departures from thermodynamic equilibrium, *Physics in Canada*, pp. 302–315, 1998.
- Stankov, S., and R. Warnant, Ionospheric slab thickness - analysis, modelling and monitoring, *Advances in Space Research*, *44*(11), 1295–1303, 2009.
- Stankov, S. M., N. Jakowski, S. Heise, P. Muhtarov, I. Kutiev, and R. Warnant, A new method for reconstruction of the vertical electron density distribution in the upper ionosphere and plasmasphere, *Journal of Geophysical Research*, *108*(A5), 1164, doi:10.1029/2002JA009570, 2003.
- Stix, T. H., *Waves in Plasmas*, AIP Press, 1992.
- Subirana, J. S., J. J. Zornoza, and M. Hernández-Pajares, Ionospheric delay, Technical University of Catalonia, Spain. Available at: [http://www.navipedia.net/index.php/Ionospheric\\_Delay](http://www.navipedia.net/index.php/Ionospheric_Delay), 2016.
- Sutton, E., and H. Na, A block iterative algorithm for tomographic reconstruction of the ionospheric electron density, *J. Atmos. Sol. Terr. Phys.*, *54*(6), 1007–1012, 1996.
- Sutton, E., and H. Na, Ionospheric tomography using the residual correction method, *Radio Sci.*, *26*(6), 1361–1380, 1996b.

- Tanskanen, E. I., J. A. Slavin, A. J. Tanskanen, A. Viljanen, T. I. Pulkkinen, H. E. J. Koskinen, A. Pulkkinen, and J. Eastwood, Magnetospheric substorms are strongly modulated by interplanetary high-speed streams, *Geophys. Res. Lett.*, 32(L16104), 1–4, doi:10.1029/2005GL023318, 2005.
- Taranenko, Y., U. Inan, and T. Bell, Interaction with the lower ionosphere of EM pulses from lightning: heating, attachment and ionization, *Geophysical Research Letters*, 20(15), 1539–1542, 1993.
- Tessa, V. H., W. Sarah, G. Maggie, B. K. Joost, and S. Jan, The implementation of iterative reconstruction algorithms in MatLab, *iterative Reconstruction Algorithms*, 2007.
- Tewarson, R., *Sparse Matrices*, New York: Academic Press, 1973.
- The International Telecommunications Union, Recommendation ITU-R M 1371 - Technical characteristics for a universal shipborne automatic identification system using time division multiplex access in the VHF maritime mobile band, *Tech. rep.*, The ITU Radiocommunication Assembly, 1998.
- The International Telecommunications Union, Ionospheric propagation data and prediction method required for the design of satellite services and systems, *Recommendation ITU-R P.531-7*, The ITU Radiocommunication Assembly, 2003.
- Thurber, M., ADS-B is insecure and easily spoofed, say hackers, Aviation International News online available at: <http://www.ainonline.com/aviation-news/aviation-international-news/2012-09-03/ads-b-insecure-and-easily-spoofed-say-hackers>, 2012.
- Tikhonov, A., and V. Arsenin, *Solutions of Ill-Posed Problems*, New York: Wiley, 1977.
- Tikhonov, A., and A. Goncharsky (Eds.), *Ill-Posed Problems in the Natural Sciences*, Moscow: MIR, 1987.
- Titheridge, J. E., Variations in the total electron content of the ionosphere after the high-altitude nuclear explosion, *New Zealand Journal of Geology and Geophysics*, 5(6), 1003–1008, doi:10.1080/00288306.1962.10420056, 1962.
- TransportCanada, *RAC 2.0 airspace requirements and procedures*, Transport Canada, AIM, 2012.
- Tremblay, P., R. Francis, A. Cushley, D. Desjardins, and M. Wallace, FLOAT: Flying Laboratory for Observation of ADS-B Transmissions, *Tech. rep.*, Royal Military College of Canada, Kingston, ON, FLOAT-RP-RMC-0001 Issue 1.0, 2009.
- Treumann, R., and W. Baumjohann, *Basic space plasma physics*, Imperial College Press, 1996.

- Treumann, R., and W. Baumjohann, *Advanced Space Plasma Physics*, Imperial College Press, UK, 1997.
- Tucker, A. J., Computerized ionospheric tomography, *John Hopkins APL Technical Digest*, 19(1), 66–71, 1998.
- Turner, A., Unmanned ADS-B first for NASA, Keypublishing, Stamford, UK. Available at: <http://www.airtrafficmanagement.net/2012/03/unmanned-adsb-first-for-nasa/>, 2012.
- University of Toronto Institute for Aerospace Studies Space Flight Laboratory, Nanosatellites: CanX-7, UTIAS SFL News. Toronto, ON. Available at: <http://utias-sfl.net/?page;d=210>, 2014.
- van der Merwe, S. J., Characterization of the ionosphere over the South Atlantic Anomaly by using a ship-based dual-frequency GPS receiver (Master's thesis), Master's thesis, University of Pretoria, 2011.
- Van Der Pryt, R., Modelling aircraft Automatic Dependent Surveillance- Broadcast (ADS-B) signals received by a low-earth-orbiting satellite: Examining the North Atlantic oceanic airspace control areas (Master's thesis), Master's thesis, Royal Military College of Canada, Kingston, ON, 2014.
- Van Der Pryt, R., and R. Vincent, A simulation of the reception of Automatic Dependent Surveillance-Broadcast signals in low Earth orbit, *International Journal of Navigation and Observation*, pp. 1–11, doi:10.1155/2015/567604, 2015a.
- Van Der Pryt, R., and R. Vincent, A simulation of signal collisions over the North Atlantic for a spaceborne ADS-B receiver using Aloha protocol, *Positioning*, 6(3), 23–31, doi:10.4236/pos.2015.63003, 2015b.
- Van Der Pryt, R., and R. Vincent, A simulation of reflected ADS-B signals over the North Atlantic for a spaceborne receiver, *Positioning*, 7, 51–62, 2016.
- Vijayalakshmi, G., and P. Vindhya, Comparison of algebraic reconstruction methods in computed tomography, *International Journal of Computer Science and Information Technologies*, 5(5), 6007–6009, 2014.
- Vincent, R., and R. Van Der Pryt, The CanX-7 nanosatellite ADS-B mission: A preliminary assessment, *Positioning*, 8, 1–11, doi:10.4236/pos.2017.81001, 2017.
- Wahi, R., S. Dubey, and A. K. Gwal, Ionospheric total electron content measurement in Malaysian region during high solar activity using GPS receiver, *Indian Journal of Radio and Space Physics*, 34, 399–401, 2005.
- Wen, D., Y. Yuan, J. Ou, and K. Zhang, Ionospheric response to the geomagnetic storm on August 21, 2003 over China using GNSS-based tomographic technique, *IEEE Trans. Geosci. Remote Sens.*, 48(3), 3212–17, 2010.

- William Collins Sons & Co. Ltd 1979, *Collins English Dictionary Complete and Unabridged 6th Edition*, Harper Collins Publishers, 2003.
- Wright, J. W., A model of the F-region above hmaxF2, *J. Geophys. Res.*, *65*(1), 185–91, 1960.
- Wright, P. A., S. Quegan, N. S. Wheadon, and C. D. Hall, Faraday rotation effects on L-band spaceborne SAR data, *IEEE Trans. Geosci. Remote Sens.*, *41*(12), 2735–2744, 2003.
- Xiang, Y., and Y. Gao, An enhanced mapping function with ionospheric varying height, *Remote Sensing*, *11*, 1497, doi:10.3390/rs11121497, 2019.
- Xu, T.-L., H. Jin, and P. Guo, Preliminary analysis of ionospheric anomaly preceding the great East Japan earthquake, *Earthquake*, *32*(4), 131–139, 2012.
- Yeh, K., and T. Raymund, Limitations of ionospheric imaging by tomography, *Radio Sci.*, *26*, 1361–1380, 1991.
- Yin, P., C. N. Mitchell, P. Spencer, I. McCrea, and T. Pedersen, A multi-diagnostic approach to understanding high-latitude plasma transport during the halloween 2003 storm, *Ann. Geophys.*, *26*, 2739–2747, 2008.
- Yizengaw, E., P. Dyson, and E. A. Essex., Tomographic reconstruction of the ionosphere using ground-based GPS data in the Australian region, *Tech. rep.*, CRC for Satellite Systems. Department of Physics, 2004.
- Yueh, S., *Estimates of Faraday Rotation with Passive Microwave Polarimetry for Micro-wave Remote Sensing of Earth Surfaces.*, Jet Propulsion Laboratory, California Institute of Technology., 1999.
- Zetter, K., Air traffic controllers pick the wrong week to quit using radar, Wired.com, Boone, IA. Available at: <http://www.wired.com/2012/07/adsb-spoofing/>, 2012.
- Zhao, B., W. Wan, L. Liu, and Z. Ren, Characteristics of the ionospheric total electron content of the equatorial ionization anomaly in the Asian-Australian region during 1996-2004, *Ann. Geophys.*, *27*, 3861–3873, 2009.
- Zhen, Z., H. Xiong, Z. Xun-Jie, and W. Wei-Xing, Inversion methods for ionospheric occultation from GPS observation data, *Chinese Journal of Geophysics*, *47*(4), 660–666, 2004.
- Zolesi, B., and L. R. Cander, *Ionospheric Prediction and Forecasting*, Springer Science & Business Media, 2013.

## Copyright Agreements

---

The solution of pixels  $x_i$  from the numerical example of CT in Chapter 3:

$$x_i = 0, 2, 1, 1, 3, 0, 2, 1, 2.$$

---

**JOHN WILEY AND SONS LICENSE  
TERMS AND CONDITIONS**

May 15, 2019

---

---

This Agreement between Royal Military College of Canada ("You") and John Wiley and Sons ("John Wiley and Sons") consists of your license details and the terms and conditions provided by John Wiley and Sons and Copyright Clearance Center.

License Number	4590250483508
License date	May 15, 2019
Licensed Content Publisher	John Wiley and Sons
Licensed Content Publication	Radio Science
Licensed Content Title	Ionospheric tomography using ADS-B signals
Licensed Content Author	A. C. Cushley, J.-M. Noël
Licensed Content Date	Jul 30, 2014
Licensed Content Volume	49
Licensed Content Issue	7
Licensed Content Pages	15
Type of use	Dissertation/Thesis
Requestor type	Author of this Wiley article
Format	Print and electronic
Portion	Full article
Will you be translating?	No
Title of your thesis / dissertation	Ionospheric Tomography Using the Faraday Rotation of Signals of Opportunity
Expected completion date	Sep 2019
Expected size (number of pages)	150
Requestor Location	Royal Military College of Canada 13 General Crerar Crescent  Kingston, ON K7K 7B4 Canada Attn: Royal Military College of Canada
Publisher Tax ID	EU826007151
Total	0.00 CAD
Terms and Conditions	

**TERMS AND CONDITIONS**

This copyrighted material is owned by or exclusively licensed to John Wiley & Sons, Inc. or one of its group companies (each a "Wiley Company") or handled on behalf of a society with which a Wiley

[Print This Page](#)



**JOHN WILEY AND SONS LICENSE  
TERMS AND CONDITIONS**

May 15, 2019

---

---

This Agreement between Royal Military College of Canada ("You") and John Wiley and Sons ("John Wiley and Sons") consists of your license details and the terms and conditions provided by John Wiley and Sons and Copyright Clearance Center.

License Number	4590250822343
License date	May 15, 2019
Licensed Content Publisher	John Wiley and Sons
Licensed Content Publication	Radio Science
Licensed Content Title	Faraday Rotation, Total Electron Content, and Their Sensitivity to the Average Parallel Component of the Magnetic Field
Licensed Content Author	A. C. Cushley, J.-M. Noël, K. Kabin
Licensed Content Date	Sep 14, 2018
Licensed Content Volume	53
Licensed Content Issue	9
Licensed Content Pages	14
Type of use	Dissertation/Thesis
Requestor type	Author of this Wiley article
Format	Print and electronic
Portion	Full article
Will you be translating?	No
Title of your thesis / dissertation	Ionospheric Tomography Using the Faraday Rotation of Signals of Opportunity
Expected completion date	Sep 2019
Expected size (number of pages)	150
Requestor Location	Royal Military College of Canada 13 General Crerar Crescent  Kingston, ON K7K 7B4 Canada Attn: Royal Military College of Canada
Publisher Tax ID	EU826007151
Total	0.00 CAD
Terms and Conditions	

**TERMS AND CONDITIONS**

This copyrighted material is owned by or exclusively licensed to John Wiley & Sons, Inc. or one of its group companies (each a "Wiley Company") or handled on behalf of a society with which a Wiley



**involve the separate exploitation of the permitted figures or extracts,** You may not alter, remove or suppress in any manner any copyright, trademark or other notices displayed by the Wiley Materials. You may not license, rent, sell, loan, lease, pledge, offer as security, transfer or assign the Wiley Materials on a stand-alone basis, or any of the rights granted to you hereunder to any other person.

- The Wiley Materials and all of the intellectual property rights therein shall at all times remain the exclusive property of John Wiley & Sons Inc, the Wiley Companies, or their respective licensors, and your interest therein is only that of having possession of and the right to reproduce the Wiley Materials pursuant to Section 2 herein during the continuance of this Agreement. You agree that you own no right, title or interest in or to the Wiley Materials or any of the intellectual property rights therein. You shall have no rights hereunder other than the license as provided for above in Section 2. No right, license or interest to any trademark, trade name, service mark or other branding ("Marks") of WILEY or its licensors is granted hereunder, and you agree that you shall not assert any such right, license or interest with respect thereto
- NEITHER WILEY NOR ITS LICENSORS MAKES ANY WARRANTY OR REPRESENTATION OF ANY KIND TO YOU OR ANY THIRD PARTY, EXPRESS, IMPLIED OR STATUTORY, WITH RESPECT TO THE MATERIALS OR THE ACCURACY OF ANY INFORMATION CONTAINED IN THE MATERIALS, INCLUDING, WITHOUT LIMITATION, ANY IMPLIED WARRANTY OF MERCHANTABILITY, ACCURACY, SATISFACTORY QUALITY, FITNESS FOR A PARTICULAR PURPOSE, USABILITY, INTEGRATION OR NON-INFRINGEMENT AND ALL SUCH WARRANTIES ARE HEREBY EXCLUDED BY WILEY AND ITS LICENSORS AND WAIVED BY YOU.
- WILEY shall have the right to terminate this Agreement immediately upon breach of this Agreement by you.
- You shall indemnify, defend and hold harmless WILEY, its Licensors and their respective directors, officers, agents and employees, from and against any actual or threatened claims, demands, causes of action or proceedings arising from any breach of this Agreement by you.
- IN NO EVENT SHALL WILEY OR ITS LICENSORS BE LIABLE TO YOU OR ANY OTHER PARTY OR ANY OTHER PERSON OR ENTITY

FOR ANY SPECIAL, CONSEQUENTIAL, INCIDENTAL, INDIRECT, EXEMPLARY OR PUNITIVE DAMAGES, HOWEVER CAUSED, ARISING OUT OF OR IN CONNECTION WITH THE DOWNLOADING, PROVISIONING, VIEWING OR USE OF THE MATERIALS REGARDLESS OF THE FORM OF ACTION, WHETHER FOR BREACH OF CONTRACT, BREACH OF WARRANTY, TORT, NEGLIGENCE, INFRINGEMENT OR OTHERWISE (INCLUDING, WITHOUT LIMITATION, DAMAGES BASED ON LOSS OF PROFITS, DATA, FILES, USE, BUSINESS OPPORTUNITY OR CLAIMS OF THIRD PARTIES), AND WHETHER OR NOT THE PARTY HAS BEEN ADVISED OF THE POSSIBILITY OF SUCH DAMAGES. THIS LIMITATION SHALL APPLY NOTWITHSTANDING ANY FAILURE OF ESSENTIAL PURPOSE OF ANY LIMITED REMEDY PROVIDED HEREIN.

- Should any provision of this Agreement be held by a court of competent jurisdiction to be illegal, invalid, or unenforceable, that provision shall be deemed amended to achieve as nearly as possible the same economic effect as the original provision, and the legality, validity and enforceability of the remaining provisions of this Agreement shall not be affected or impaired thereby.
- The failure of either party to enforce any term or condition of this Agreement shall not constitute a waiver of either party's right to enforce each and every term and condition of this Agreement. No breach under this agreement shall be deemed waived or excused by either party unless such waiver or consent is in writing signed by the party granting such waiver or consent. The waiver by or consent of a party to a breach of any provision of this Agreement shall not operate or be construed as a waiver of or consent to any other or subsequent breach by such other party.
- This Agreement may not be assigned (including by operation of law or otherwise) by you without WILEY's prior written consent.
- Any fee required for this permission shall be non-refundable after thirty (30) days from receipt by the CCC.
- These terms and conditions together with CCC's Billing and Payment terms and conditions (which are incorporated herein) form the entire agreement between you and WILEY concerning this licensing transaction and (in the absence of fraud) supersedes all prior agreements and representations of the parties, oral or written. This Agreement may not be amended except in writing signed by both parties. This Agreement shall be binding upon and inure to the benefit of the parties' successors, legal representatives,

and authorized assigns.

- In the event of any conflict between your obligations established by these terms and conditions and those established by CCC's Billing and Payment terms and conditions, these terms and conditions shall prevail.
- WILEY expressly reserves all rights not specifically granted in the combination of (i) the license details provided by you and accepted in the course of this licensing transaction, (ii) these terms and conditions and (iii) CCC's Billing and Payment terms and conditions.
- This Agreement will be void if the Type of Use, Format, Circulation, or Requestor Type was misrepresented during the licensing process.
- This Agreement shall be governed by and construed in accordance with the laws of the State of New York, USA, without regards to such state's conflict of law rules. Any legal action, suit or proceeding arising out of or relating to these Terms and Conditions or the breach thereof shall be instituted in a court of competent jurisdiction in New York County in the State of New York in the United States of America and each party hereby consents and submits to the personal jurisdiction of such court, waives any objection to venue in such court and consents to service of process by registered or certified mail, return receipt requested, at the last known address of such party.

## **WILEY OPEN ACCESS TERMS AND CONDITIONS**

Wiley Publishes Open Access Articles in fully Open Access Journals and in Subscription journals offering Online Open. Although most of the fully Open Access journals publish open access articles under the terms of the Creative Commons Attribution (CC BY) License only, the subscription journals and a few of the Open Access Journals offer a choice of Creative Commons Licenses. The license type is clearly identified on the article.

### **The Creative Commons Attribution License**

The Creative Commons Attribution License (CC-BY) allows users to copy, distribute and transmit an article, adapt the article and make commercial use of the article. The CC-BY license permits commercial and non-

### **Creative Commons Attribution Non-Commercial License**

The Creative Commons Attribution Non-Commercial (CC-BY-NC) License permits use, distribution and reproduction in any medium, provided the original work is properly cited and is not used for commercial purposes.(see below)

**Creative Commons Attribution-Non-Commercial-NoDerivs License**

The Creative Commons Attribution Non-Commercial-NoDerivs License (CC-BY-NC-ND) permits use, distribution and reproduction in any medium, provided the original work is properly cited, is not used for commercial purposes and no modifications or adaptations are made. (see below)

**Use by commercial "for-profit" organizations**

Use of Wiley Open Access articles for commercial, promotional, or marketing purposes requires further explicit permission from Wiley and will be subject to a fee.

Further details can be found on Wiley Online Library

<http://olabout.wiley.com/WileyCDA/Section/id-410895.html>

**Other Terms and Conditions:****v1.10 Last updated September 2015**

Questions? [customer care@copyright.com](mailto:customer care@copyright.com) or +1-855-239-3415 (toll free in the US) or +1-978-646-2777.



**JOHN WILEY AND SONS LICENSE  
TERMS AND CONDITIONS**

May 15, 2019

This Agreement between Royal Military College of Canada ("You") and John Wiley and Sons ("John Wiley and Sons") consists of your license details and the terms and conditions provided by John Wiley and Sons and Copyright Clearance Center.

License Number	4590250733944
License date	May 15, 2019
Licensed Content Publisher	John Wiley and Sons
Licensed Content Publication	Radio Science
Licensed Content Title	Faraday Rotation of Automatic Dependent Surveillance-Broadcast (ADS-B) Signals as a Method of Ionospheric Characterization
Licensed Content Author	A. C. Cushley, K. Kabin, J.-M. Noël
Licensed Content Date	Oct 19, 2017
Licensed Content Volume	52
Licensed Content Issue	10
Licensed Content Pages	8
Type of use	Dissertation/Thesis
Requestor type	Author of this Wiley article
Format	Print and electronic
Portion	Full article
Will you be translating?	No
Title of your thesis / dissertation	Ionospheric Tomography Using the Faraday Rotation of Signals of Opportunity
Expected completion date	Sep 2019
Expected size (number of pages)	150
Requestor Location	Royal Military College of Canada 13 General Crerar Crescent  Kingston, ON K7K 7B4 Canada Attn: Royal Military College of Canada
Publisher Tax ID	EU826007151
Total	0.00 CAD
Terms and Conditions	

**TERMS AND CONDITIONS**

This copyrighted material is owned by or exclusively licensed to John Wiley & Sons, Inc. or one of its group companies (each a "Wiley Company") or handled on behalf of a society with which a Wiley

Company has exclusive publishing rights in relation to a particular work (collectively "WILEY"). By clicking "accept" in connection with completing this licensing transaction, you agree that the following terms and conditions apply to this transaction (along with the billing and payment terms and conditions established by the Copyright Clearance Center Inc., ("CCC's Billing and Payment terms and conditions"), at the time that you opened your RightsLink account (these are available at any time at <http://myaccount.copyright.com>).

## Terms and Conditions

- The materials you have requested permission to reproduce or reuse (the "Wiley Materials") are protected by copyright.
- You are hereby granted a personal, non-exclusive, non-sub licensable (on a stand-alone basis), non-transferable, worldwide, limited license to reproduce the Wiley Materials for the purpose specified in the licensing process. This license, **and any CONTENT (PDF or image file) purchased as part of your order**, is for a one-time use only and limited to any maximum distribution number specified in the license. The first instance of republication or reuse granted by this license must be completed within two years of the date of the grant of this license (although copies prepared before the end date may be distributed thereafter). The Wiley Materials shall not be used in any other manner or for any other purpose, beyond what is granted in the license. Permission is granted subject to an appropriate acknowledgement given to the author, title of the material/book/journal and the publisher. You shall also duplicate the copyright notice that appears in the Wiley publication in your use of the Wiley Material. Permission is also granted on the understanding that nowhere in the text is a previously published source acknowledged for all or part of this Wiley Material. Any third party content is expressly excluded from this permission.
- With respect to the Wiley Materials, all rights are reserved. Except as expressly granted by the terms of the license, no part of the Wiley Materials may be copied, modified, adapted (except for minor reformatting required by the new Publication), translated, reproduced, transferred or distributed, in any form or by any means, and no derivative works may be made based on the Wiley Materials without the prior permission of the respective copyright owner. **For STM Signatory Publishers clearing permission under the terms of the STM Permissions Guidelines only, the terms of the license are extended to include subsequent editions and for editions in other languages, provided such editions are for the work as a whole in situ and does not**



**involve the separate exploitation of the permitted figures or extracts,** You may not alter, remove or suppress in any manner any copyright, trademark or other notices displayed by the Wiley Materials. You may not license, rent, sell, loan, lease, pledge, offer as security, transfer or assign the Wiley Materials on a stand-alone basis, or any of the rights granted to you hereunder to any other person.

- The Wiley Materials and all of the intellectual property rights therein shall at all times remain the exclusive property of John Wiley & Sons Inc, the Wiley Companies, or their respective licensors, and your interest therein is only that of having possession of and the right to reproduce the Wiley Materials pursuant to Section 2 herein during the continuance of this Agreement. You agree that you own no right, title or interest in or to the Wiley Materials or any of the intellectual property rights therein. You shall have no rights hereunder other than the license as provided for above in Section 2. No right, license or interest to any trademark, trade name, service mark or other branding ("Marks") of WILEY or its licensors is granted hereunder, and you agree that you shall not assert any such right, license or interest with respect thereto
- NEITHER WILEY NOR ITS LICENSORS MAKES ANY WARRANTY OR REPRESENTATION OF ANY KIND TO YOU OR ANY THIRD PARTY, EXPRESS, IMPLIED OR STATUTORY, WITH RESPECT TO THE MATERIALS OR THE ACCURACY OF ANY INFORMATION CONTAINED IN THE MATERIALS, INCLUDING, WITHOUT LIMITATION, ANY IMPLIED WARRANTY OF MERCHANTABILITY, ACCURACY, SATISFACTORY QUALITY, FITNESS FOR A PARTICULAR PURPOSE, USABILITY, INTEGRATION OR NON-INFRINGEMENT AND ALL SUCH WARRANTIES ARE HEREBY EXCLUDED BY WILEY AND ITS LICENSORS AND WAIVED BY YOU.
- WILEY shall have the right to terminate this Agreement immediately upon breach of this Agreement by you.
- You shall indemnify, defend and hold harmless WILEY, its Licensors and their respective directors, officers, agents and employees, from and against any actual or threatened claims, demands, causes of action or proceedings arising from any breach of this Agreement by you.
- IN NO EVENT SHALL WILEY OR ITS LICENSORS BE LIABLE TO YOU OR ANY OTHER PARTY OR ANY OTHER PERSON OR ENTITY

FOR ANY SPECIAL, CONSEQUENTIAL, INCIDENTAL, INDIRECT, EXEMPLARY OR PUNITIVE DAMAGES, HOWEVER CAUSED, ARISING OUT OF OR IN CONNECTION WITH THE DOWNLOADING, PROVISIONING, VIEWING OR USE OF THE MATERIALS REGARDLESS OF THE FORM OF ACTION, WHETHER FOR BREACH OF CONTRACT, BREACH OF WARRANTY, TORT, NEGLIGENCE, INFRINGEMENT OR OTHERWISE (INCLUDING, WITHOUT LIMITATION, DAMAGES BASED ON LOSS OF PROFITS, DATA, FILES, USE, BUSINESS OPPORTUNITY OR CLAIMS OF THIRD PARTIES), AND WHETHER OR NOT THE PARTY HAS BEEN ADVISED OF THE POSSIBILITY OF SUCH DAMAGES. THIS LIMITATION SHALL APPLY NOTWITHSTANDING ANY FAILURE OF ESSENTIAL PURPOSE OF ANY LIMITED REMEDY PROVIDED HEREIN.

- Should any provision of this Agreement be held by a court of competent jurisdiction to be illegal, invalid, or unenforceable, that provision shall be deemed amended to achieve as nearly as possible the same economic effect as the original provision, and the legality, validity and enforceability of the remaining provisions of this Agreement shall not be affected or impaired thereby.
- The failure of either party to enforce any term or condition of this Agreement shall not constitute a waiver of either party's right to enforce each and every term and condition of this Agreement. No breach under this agreement shall be deemed waived or excused by either party unless such waiver or consent is in writing signed by the party granting such waiver or consent. The waiver by or consent of a party to a breach of any provision of this Agreement shall not operate or be construed as a waiver of or consent to any other or subsequent breach by such other party.
- This Agreement may not be assigned (including by operation of law or otherwise) by you without WILEY's prior written consent.
- Any fee required for this permission shall be non-refundable after thirty (30) days from receipt by the CCC.
- These terms and conditions together with CCC's Billing and Payment terms and conditions (which are incorporated herein) form the entire agreement between you and WILEY concerning this licensing transaction and (in the absence of fraud) supersedes all prior agreements and representations of the parties, oral or written. This Agreement may not be amended except in writing signed by both parties. This Agreement shall be binding upon and inure to the benefit of the parties' successors, legal representatives,

and authorized assigns.

- In the event of any conflict between your obligations established by these terms and conditions and those established by CCC's Billing and Payment terms and conditions, these terms and conditions shall prevail.
- WILEY expressly reserves all rights not specifically granted in the combination of (i) the license details provided by you and accepted in the course of this licensing transaction, (ii) these terms and conditions and (iii) CCC's Billing and Payment terms and conditions.
- This Agreement will be void if the Type of Use, Format, Circulation, or Requestor Type was misrepresented during the licensing process.
- This Agreement shall be governed by and construed in accordance with the laws of the State of New York, USA, without regards to such state's conflict of law rules. Any legal action, suit or proceeding arising out of or relating to these Terms and Conditions or the breach thereof shall be instituted in a court of competent jurisdiction in New York County in the State of New York in the United States of America and each party hereby consents and submits to the personal jurisdiction of such court, waives any objection to venue in such court and consents to service of process by registered or certified mail, return receipt requested, at the last known address of such party.

## **WILEY OPEN ACCESS TERMS AND CONDITIONS**

Wiley Publishes Open Access Articles in fully Open Access Journals and in Subscription journals offering Online Open. Although most of the fully Open Access journals publish open access articles under the terms of the Creative Commons Attribution (CC BY) License only, the subscription journals and a few of the Open Access Journals offer a choice of Creative Commons Licenses. The license type is clearly identified on the article.

### **The Creative Commons Attribution License**

The Creative Commons Attribution License (CC-BY) allows users to copy, distribute and transmit an article, adapt the article and make commercial use of the article. The CC-BY license permits commercial and non-

### **Creative Commons Attribution Non-Commercial License**

The Creative Commons Attribution Non-Commercial (CC-BY-NC) License permits use, distribution and reproduction in any medium, provided the original work is properly cited and is not used for commercial purposes.(see below)

**Creative Commons Attribution-Non-Commercial-NoDerivs License**

The Creative Commons Attribution Non-Commercial-NoDerivs License (CC-BY-NC-ND) permits use, distribution and reproduction in any medium, provided the original work is properly cited, is not used for commercial purposes and no modifications or adaptations are made. (see below)

**Use by commercial "for-profit" organizations**

Use of Wiley Open Access articles for commercial, promotional, or marketing purposes requires further explicit permission from Wiley and will be subject to a fee.

Further details can be found on Wiley Online Library

<http://olabout.wiley.com/WileyCDA/Section/id-410895.html>

**Other Terms and Conditions:****v1.10 Last updated September 2015**

Questions? [customercare@copyright.com](mailto:customercare@copyright.com) or +1-855-239-3415 (toll free in the US) or +1-978-646-2777.



## Radio Science

Published by Wiley on behalf of American Geophysical Union (the "Owner")

### COPYRIGHT TRANSFER AGREEMENT

Date: December 24, 2019

Contributor name: Alex Cushley

Contributor address:

Manuscript number: 2019RS006872

Re: Manuscript entitled Ionospheric sounding and tomography using Automatic Identification System (AIS) and other signals of opportunity (the "Contribution")

for publication in Radio Science (the "Journal")

published by Wiley Periodicals, Inc. ("Wiley")

Dear Contributor(s):

Thank you for submitting your Contribution for publication. In order to expedite the editing and publishing process and enable the Owner to disseminate your Contribution to the fullest extent, we need to have this Copyright Transfer Agreement executed.

**Publication cannot proceed without a signed copy of this Agreement.**

---

#### INFORMATION CONCERNING YOUR COPYRIGHT

The Copyright Law enacted in 1978 requires the American Geophysical Union to obtain specific rights to articles published. This legal requirement does not alter in any way the long-standing relationship between AGU and its authors, nor does it change the philosophy behind our practice of copyrighting our journals and books.

AGU's philosophy recognizes the need to ensure that authors have a say in how their works are used and the necessity to foster broad dissemination of scientific literature while protecting the viability of the publication system. Authors still retain all proprietary rights other than copyright (such as patent rights), the right to present the material orally, the right to reproduce figures, tables, and extracts properly cited.

**Permission to Deposit an Article in an Institutional Repository**

AGU allows authors to deposit their journal articles if the version is the final published citable version of record, the AGU copyright statement is clearly visible on the posting, and the posting is made 6 months after official publication by the AGU.

### **Public Domain**

Work prepared by U.S. Government employees in their official capacities is not subject to copyright in the United States. Such authors may place their papers in the public domain, which means that it may be freely copied, republished, and redistributed. In order for the work to be placed in the public domain, all authors must be official U.S. Government employees. If at least one author of the work was privately employed, copyright should be transferred to AGU by any of the privately employed authors.

### **Works Prepared by Both Privately Employed Persons and Official U.S. Government Employees**

To ensure that we can continue to promote wide availability of our publications, AGU requests all non-U.S. Government employees to transfer copyright to us. This transfer permits us to continue publishing our journals and books in all their various formats, to grant permission to abstracting and indexing services to cover our publications, and to grant permission for photocopying beyond the limits defined in the law. In instances where authorship consists of both U.S. Government and privately employed individuals, we require at least one privately employed author to transfer copyright to AGU. This kind of transfer provides ultimate protection and broad dissemination of the work.

### **Rights Other Than Copyright**

Privately employed authors who have written articles in their official capacities as employees should also transfer copyright to AGU. The author's employer retains the same rights as individual authors. AGU claims no right to the work other than copyright; the author's employer retains all other rights such as patent rights.

### **Works Supported by U.S. Government Grants or Contracts**

Authors who are publishing works supported by a U.S. Government grant or contract are requested to transfer copyright to AGU. This kind of transfer permits the broad dissemination of the work while recognizing the U.S. Government's prior license to use the work for noncommercial purposes.

### **Copyright Permission for Reprinted/Modified Figures/Tables**

If any of the figures/tables in your article are reprinted or modified from another source (this includes any that were redrawn but are basically unaltered or have only slight modifications), you must obtain and provide AGU with original letter(s) (fax or e-mail not acceptable) from the copyright holder(s) granting permission to use them in your article before your article may be published. If the original copyright holder has given blanket permission for reuse with credit, a copy of the published permission statement is sufficient. If the material is in the public domain, please provide confirmation of this in an original letter. Material originally published in AGU publications does not require copyright permission as long as proper credit is given.

---

**[ X ]** I agree to the COPYRIGHT TRANSFER AGREEMENT as shown above and have obtained written permission from all other contributors to execute this Agreement on their behalf.

Contributor's signature (type name here): Alex Cushley

Date: December 24, 2019

---

**SELECT FROM OPTIONS BELOW:**

**Contributor-owned work**

**Certification of U.S. Government work**

*Note to U.S. Government Employees*

*Select this option and type Contributor name into the Contributor's signature section above only if ALL authors were U.S. Government employees at the time the work was prepared. (See above for explanation.) I certify that the article referenced above was prepared solely by U.S. Government employees as part of their official duties and therefore legally cannot be copyrighted. I confirm that this article has not been published previously elsewhere, nor is it under consideration by any other publisher.*

**Certification of Crown Government Copyright Reserve**

*Note to Crown government Employees*

**For Crown Copyright this form cannot be completed electronically and should be printed off, signed in the Contributor's signatures section above by the appropriately authorised individual and uploaded to the Wiley Author Services Dashboard.** For production editor contact details please visit the Journal's online author guidelines.

This is to certify that ALL authors are or were bona fide officers of a Crown government which reserves its own copyright under national law, and the work was prepared on behalf of the \_\_\_\_\_ (Government or Agency Name) as part of their official duties. Copyright in the paper is therefore reserved and may not be transferred.

The following nonexclusive rights are hereby given to the American Geophysical Union (AGU).

1. The right to use, print, and/or publish in any language the above-mentioned work or any part thereof, provided that the name of the author(s) and the Crown government affiliation are clearly indicated.
2. The right to grant the same rights to others to print and publish the work subject to the above proviso.
3. The right to collect royalty fees.

In return for these rights, AGU hereby certifies that whenever approached by third parties for individual permission to use, reprint, or republish specified full articles (except for classroom use, library reserve, or to reprint in a collective work of the AGU) the corresponding author's or employer's permission will also be required. AGU is not obligated to print the Crown government copyright credit line. *If your status as a government employee legally prevents you from signing this Agreement, please contact the Journal production editor.*

**Other**

Including Other Government work or Non-Governmental Organisation work

*Note to Non-U.S., Non-U.K. Government Employees or Non-Governmental Organisation Employees*

**For Other Government or Non-Governmental Organisation work this form cannot be completed electronically and should be printed off, signed in the Contributor's signatures section above by the appropriately authorised individual and uploaded to the Wiley Author Services Dashboard.** For production editor contact details please visit the Journal's online author guidelines. *If your status as a government or non-governmental organisation employee legally prevents you from signing this Agreement, please contact the Journal production editor.*

Name of Government/Non-Governmental Organisation:

---

**Company/institution owned work (made for hire in the course of employment)**

**For "work made for hire" this form cannot be completed electronically and should be printed off, signed and uploaded to the Wiley Author Services Dashboard.** For production editor contact details please visit the Journal's online author guidelines.

Name of Company/Institution:

---

Authorized Signature of Employer:

---

Date:

---

Signature of Employee:

---

Date:

---



## Co-authorship statement

### Paper 1 – Ionospheric tomography using ADS-B signals

A.C. Cushley and J.-M. A. Noël conceived the idea of using the FR of ADS-B signals as input to computerized tomography in order to reconstruct the ionospheric electron content. A.C. Cushley planned and carried out the simulations to produce the synthetic data using ray tracing and reconstructions using computerized tomography. A.C. Cushley took the lead in writing the manuscript and was the corresponding author for submission and manuscript revisions. J.-M. A. Noël provided critical feedback and helped shape the research, analysis and manuscript. J.-M. A. Noël supervised the project.

### Paper 2 – Faraday rotation of Automatic Dependent Surveillance-Broadcast (ADS-B) signals as a method of ionospheric characterization

A.C. Cushley conceived the idea of using the shape of ionospheric profiles as an *a priori* guess for the reconstruction method applied to *Cushley* [2013]; *Cushley and Noël* [2014] and conceived the idea for this research as future work within *Cushley* [2013] and proposed the work within *Cushley* [2015]. K. Kabin encouraged A.C. Cushley to investigate whether a few simple, common ionospheric parameters could be used to create vertical electron density profiles that could be used for this purpose and wrote preliminary code specifically using the parameters used by the NeQuick model (which is based on the Epstein formalism). A.C. Cushley expanded the code, planned and carried out the experiments to produce the results. A.C. Cushley took the lead in writing the manuscript and was the corresponding author for submission and manuscript revisions. K. Kabin and J.-M. A. Noël provided critical feedback and helped shape the research, analysis and manuscript. A.C. Cushley wrote the manuscript in consultation with K. Kabin and J.-M. A. Noël. J.-M. A. Noël and K. Kabin supervised the project.

### Paper 3 – Faraday Rotation, Total Electron Content, and Their Sensitivity to the Average Parallel Component of the Magnetic Field

A.C. Cushley conceived the idea of using a more accurate value for the magnetic field than a simple arithmetic average when converting FR measurements to TEC estimates to be used as input to the reconstruction method applied to *Cushley* [2013]; *Cushley and Noël* [2014]. This was presented as future work within *Cushley* [2013] and proposed the work as a section within *Cushley* [2015]. A.C. Cushley performed numerical simulations, took the lead in writing the manuscript and was the corresponding author for submission and manuscript revisions. J.-M. A. Noël and K. Kabin provided critical feedback and helped shape the research, analysis and manuscript. J.-M. A. Noël and K. Kabin supervised the project.

### Paper 4 – Ionospheric sounding and tomography using Automatic Identification System (AIS) and other signals of opportunity

A.C. Cushley conceived the idea of using the FR of AIS signals as input to computerized tomography in order to reconstruct the ionospheric electron content, similar to *Cushley* [2013]; *Cushley and Noël* [2014]. This idea was proposed by *Cushley* [2015]. A.C. Cushley planned and carried out the simulations to produce the synthetic data using ray tracing and reconstructions using computerized tomography. A.C. Cushley took the lead in writing the manuscript and was the corresponding author for submission and manuscript revisions. J.-M. A. Noël provided critical feedback and helped shape the research, analysis and manuscript. J.-M. A. Noël supervised the project.

## CURRICULUM VITAE

Name: Alex Clay Cushley  
Place of birth: Sault Ste. Marie, Ontario, Canada.  
Date of birth: 2 September 1986.  
Email: acushley[at]gmail.com  
Website: [https://www.researchgate.net/profile/Alex\\_Cushley](https://www.researchgate.net/profile/Alex_Cushley)

Alex Cushley is a veteran of the Canadian Forces (CF), and currently a graduate student, and teaching assistant at the Royal military College of Canada (RMC). He enrolled in the CF in 2003 as a weapons technician in the CF primary reserves. In 2005 he transferred to the regular force, and obtained his undergraduate degree in Space Science at RMC in 2009.

In the winter semester of 2009 he worked with two other graduate students and helped supervise three undergraduate students to design a high altitude balloon mission as part of the Space Mission Design course. The aim of this mission was to detect aircraft transmissions (Automatic Dependent Surveillance - Broadcast, or ADS-B) from the stratosphere. The balloon mission was a success and subsequently led to RMC's entry into the Canadian Satellite Design Challenge (CSDC).

He was released from the CF in 2009 and completed a bachelor of education at Queens University in 2010, specializing in intermediate and senior mathematics and physics. In March of 2012, he participated in another high altitude balloon mission that tested the satellite payload. As a result of this effort, the payload was integrated onto the CanX-7 satellite, which was launched in 2016 in conjunction with COM DEV, UTIAS and DRDC.

In 2013 he completed his masters of science in physics at RMC. Concurrent activities included participation as a team member in the CSDC, and playing a technical role in the development and successful operation of RMC's satellite ground station, VE3RMC.

Post-secondary  
education:

Royal Military College of Canada  
Ph.D. Physics, 2013-2019

Royal Military College of Canada  
M.Sc. Physics, 2010-2013

Queens University  
B.Ed. Intermediate/Secondary Mathematics and  
Physics, 2009-2010

Royal Military College of Canada  
B.Sc. Space Science, 2004-2009

Honours and Awards:

**Cushley, A.C.** and Noël, J.M. (2018),  
Determination of the effective parallel geomagnetic field  
along a path using Faraday rotation and total electron  
content from Automatic Dependent Surveillance Broadcast  
signals, Canadian Association of Physicists (CAP)  
Congress; Division of Atmospheric and Space Physics,  
2nd Prize Best Student Poster Presentation.

**Cushley, A.C.** and Noël, J.M. (2015),  
Ionospheric Sounding Opportunities Using Signal  
Data From Preexisting Amateur Radio And Other  
Networks, Canadian Association of Physicists (CAP)  
Congress; Division of Atmospheric and Space Physics,  
Best Student Poster Presentation.

**Cushley, A.C.** and Noël, J.M. (2014),  
Volumetric Reconstruction of the Ionospheric Electron  
Content Using Automatic Dependent Surveillance Broadcast  
(ADS-B) Signals, Canadian Association of Physicists (CAP)  
Congress; Division of Atmospheric and Space Physics,  
Honorable mention Best Student Poster Presentation.

**Cushley, A.C.** and Noël, J.M. (2013),  
Ionospheric Tomography Using Faraday Rotation of  
Automatic Dependant Surveillance Broadcast (ADS-B)  
Signals (A23A-0169), American Geophysical Union  
Outstanding Student Paper Award: Atmospheric Sciences.

**Cushley, A.C.** (2013),  
Halifax Amateur Radio Club  
Britt Fader Memorial Scholarship.

**Cushley, A.C.** and Noël, J.M. (2012),  
Ionospheric Tomography Using Faraday Rotation of  
Automatic Dependent Surveillance Broadcast UHF  
Signals, Canadian Association of Physicists (CAP)  
Congress; Division of Atmospheric and Space Physics,  
2nd Prize Best Student Oral Presentation.

**Cushley, A.C.** (2001/2002/2003),  
Bronze, Silver and Gold Duke of Edinburgh Awards  
Duke of Edinburgh's International Award

Articles published or  
accepted in refereed  
journals:

**Cushley, A.C.**, Noël, J.M. and Kabin, K. (2018),  
Faraday Rotation, Total Electron Content,  
and Their Sensitivity to the Average Parallel Component  
of the Magnetic Field. *Radio Science*. 53(9): 1075-1088.

**Cushley, A.C.**, Kabin, K. and Noël, J.M. (2017),  
Faraday rotation of ADS-B signals as a method of ionospheric  
characterization. *Radio Science*. 52: 1293-1300.

**Cushley, A.C.** and Noël, J.M.(2014),  
Ionospheric Tomography Using ADS-B Signals  
*Radio Science*. 49: 549-563.

Francis, R., Vincent, R., Noël, J.M., Tremblay,P.,  
Desjardins, D., **Cushley, A.C.**, Wallace, M. (2011),  
The Flying Laboratory for the Observation of ADS-B  
Transmissions. *International Journal of Navigation  
and Communication*. 5 pgs.

Articles accepted by  
refereed journals:

**Cushley, A.C.** and Noël, J.M.,  
Ionospheric sounding and tomography using Automatic  
Identification System (AIS) and other signals of opportunity.  
*Radio Sci.*, accepted December 2019

Dissertations:

**Cushley, A.C.** (2013),  
Ionospheric Tomography Using Faraday Rotation Of Au-  
tomatic Dependent Surveillance Broadcast (UHF) Signals:  
Ionospheric Measurement From ADS-B Signals.  
Royal Military College of Canada. Master's Thesis.  
Supervisor: Dr. Jean-Marc Noël  
<http://dx.doi.org/10.13140/RG.2.1.5174.7607>

Non-refereed  
contributions:

Francis, R., Vincent, R., Noël, J.M., Tremblay,P.,  
Desjardins, D., **Cushley, A.C.**, Wallace, M. (2009)  
The Flying Laboratory for the Observation of ADS-B  
Transmissions, RMC-RP-0001, Issue 1.0.

**Cushley, A.C.** and Noël, J.M. (2010)  
VE3RMC Amateur Satellite Communications Ground  
Station Manual, RMC-RP-0001, Issue 1.0.

Posters and  
Presentations:

**16** found at:  
[https://www.researchgate.net/profile/Alex\\_Cushley](https://www.researchgate.net/profile/Alex_Cushley)